CANADIAN THESES ON MICROFICHE

I.S.B.N.

THESES CANADIENNES SUR MICROFICHE

National Library of Canada
Collections Development Branch

Canadian Theses on
Microfiche Service

Ottawa, Canada
K1A 0N4

Bibliothèque nationale du Canada
Direction du développement des collections

Service des thèses canadiennes
sur microfiche

NOTICE

The quality of this microfiche is heavily dependent upon the quality of the original thesis submitted for microfilming. Every effort has been made to ensure the highest quality of reproduction possible.

If pages are missing, contact the university which granted the degree.

Some pages may have indistinct print especially if the original pages were typed with a poor typewriter ribbon or if the university sent us a poor photocopy.

Previously copyrighted materials (journal articles, published tests, etc.) are not filmed.

Reproduction in full or in part of this film is governed by the Canadian Copyright Act, R.S.C. 1970, c. C-30. Please read the authorization forms which accompany this thesis.

THIS DISSERTATION
HAS BEEN MICROFILMED
EXACTLY AS RECEIVED

AVIS

La qualité de cette microfiche dépend grandement de la qualité de la thèse soumise au microfilmage. Nous avons tout fait pour assurer une qualité supérieure de reproduction.

S'il manque des pages, veuillez communiquer avec l'université qui a conféré le grade.

La qualité d'impression de certaines pages peut laisser à désirer, surtout si les pages originales ont été dactylographiées à l'aide d'un ruban usé ou si l'université nous a fait parvenir une photocopie de mauvaise qualité.

Les documents qui font déjà l'objet d'un droit d'auteur (articles de revue, examens publiés, etc.) ne sont pas microfilmés.

La reproduction, même partielle, de ce microfilm est soumise à la Loi canadienne sur le droit d'auteur, SRC 1970, c. C-30. Veuillez prendre connaissance des formules d'autorisation qui accompagnent cette thèse.

LA THÈSE A ÉTÉ
MICROFILMÉE TELLE QUE
NOUS L'AVONS REÇUE

NL 339 (r. 82/08)

Canada

DISSOLUTION OF HIGH MELTING POINT ADDITIONS IN LIQUID STEEL

by

STAVROS A. ARGYROPOULOS

A thesis submitted to the Faculty of Graduate Studies
and Research in partial fulfillment of the
requirements for the degree of Doctor
of Philosophy in Metallurgy

Department of Mining and Metallurgical Engineering
McGill University
August 1981

ITHAKA

When you set out for Ithaka
pray that your road's a long one,
full of adventure, full of discovery.
Laistrygonians, Cyclops,
angry Poseidon—don't be scared of them:
you won't find things like that on your way
as long as your thoughts are exalted,
as long as a rare excitement
stirs your spirit and your body.
Laistrygonians, Cyclops,
wild Poseidon—you won't encounter them
unless you bring them along inside you,
unless your soul raises them up in front of you.

Pray that your road's a long one.
May there be many a summer morning when—
full of gratitude, full of joy—
you come into harbors seen for the first time;
may you stop at Phoenician trading centers
and buy fine things,
mother of pearl and coral, amber and ebony,
sensual perfumes of every kind,
as many sensual perfumes as you can;
may you visit numerous Egyptian cities
to fill yourself with learning from the wise.

Keep Ithaka always in mind.
Arriving there is what you're destined for.
But don't hurry the journey at all.
Better if it goes on for years
so you're old by the time you reach the island,
wealthy with all you've gained on the way,
not expecting Ithaka to make you rich.

Ithaka gave you the marvelous journey.
Without her you wouldn't have set out.
She hasn't anything else to give.

And if you find her poor, Ithaka won't have fooled you.
Wise as you'll have become, and so experienced,
you'll have understood by then what an Ithaka means.

C. P. Cavafy (1863-1933).

ABSTRACT

The kinetics of dissolution of titanium and vanadium in liquid steel has been studied. Two periods were distinguished: the steel shell period and the free dissolution period.

In the case of titanium, it is shown that the customary frozen shell of steel encases the cylinder following its initial immersion. Premature internal dissolution then begins as a result of liquid eutectic of $Fe_{0.3}Ti_{0.7}$ composition forming at the inner steel shell boundary. This phenomenon triggers an exothermic dissolution and erosion of the inner steel shell. The net result is considerable shortened shell melting times. During the free dissolution period, the temperature of the titanium dissolving at the interface increases and the dissolution process becomes self-accelerating.

During the steel shell period with pure vanadium and ferrovanadium alloys, no reaction was observed between the steel shell and vanadium. For low grade ferrovanadium alloys, the dissolution proceeds via a heat transfer mechanism. On the other hand, for high grades, ferrovanadium mass transfer mechanisms dominate.

A simplified mathematical model of the process has been developed to describe the coupled heat and mass transfer phenomena involved in the various systems studied.

RESUME

La cinétique de dissolution du titane et du vanadium dans l'acier liquide a été étudiée. Il a été distingué deux périodes: la période de la coquille d'acier et la période de la dissolution libre.

Dans le cas du titane, il a été montré que l'habituelle coquille d'acier solidifée enferme le cylindre immédiatement après son immersion. Une dissolution prématurée de la partie interne se produit consécutive à la formation d'un liquide eutectique de composition $Fe_{0.3}\ Ti_{0.7}$ sur la face interne de la coquille d'acier. Ce phénomène déclenche une dissolution exothermique et une érosion de l'intérieur de la coquille d'acier. Il en résulte des temps de dissolution de la coquille considérablement plus court. Pendant la période de dissolution libre la température du titane se dissolvant à l'interface s'accroit et le processus de dissolution devient auto-accéléré.

Pendant la période de la coquille d'acier avec du vanadium pur et des alliages de ferro-vanadium, il n'a été observé aucune réaction entre la coquille d'acier et le vanadium. Pour des alliages de ferro-vanadium faiblement alliés, la dissolution passe par un mécanisme de transfert de chaleur. Par contre, pour des alliages de ferro-vanadium fortement allié, le mécanisme de transfert de masse prédomine.

Un modèle mathématique simplifié du processus a été développé permettant de décrire simultanément le phénomène de transfert de masse et de chaleur concernant les divers systèmes étudiés.

TABLE OF CONTENTS

LIST OF FIGURES

Page

Page

Page

Page

Page

LIST OF TABLES

CHAPTER 1

INTRODUCTION

1.1 PRELIMINARY REMARKS

In recent years, the process of steel alloy development has greatly benefited from the large amount of research carried out in that area. This research has led to a much improved appreciation of the relationship between microstructure and mechanical properties, so that new alloy steels can now be developed on the basis of reasonably well understood metallurgical phenomena from the physical metallurgy viewpoint. However, at the refining stage of the alloy steelmaking route, very little is known particularly on the solution rates and solution mechanisms of solid additives in raw steel. A thorough understanding of the solution mechanisms and their kinetics is of clear importance from both the academic and industrial points of view.

1.2 ALLOY STEELS

The steels whose characteristic properties are due to some element other than carbon are called alloy steels. Although manganese and silicon are included in all plain carbon steels, they are not classified as alloy steels since the principal function of dissolved manganese and silicon is to act as deoxidizers.

There are many reasons for the addition of alloying elements into liquid steel. Some of the most important are to:

1) improve strength at ordinary temperatures;
2) improve mechanical properties at either high or low temperatures;
3) increase hardenability;
4) improve toughness at any minimum hardness of strength;
5) increase corrosion resistance;
6) increase wear resistance;
7) improve magnetic properties.

In the present study, the dissolution of titanium and vanadium in liquid steel was investigated. Some of the effects of titanium in alloy steels are that it:

1) reduces martensitic hardness and hardenability in medium-chromium steels;
2) prevents formation of austenite in high-chromium steels;
3) prevents localized depletion of chromium in stainless steel during long heating.

Vanadium is the most expensive of the common alloying elements. Some of the effects of vanadium in alloy steels are that it:

1) elevates coarsening temperature of austenite (promotes fine grain structure);
2) increases hardenability (when dissolved);
3) resists tempering and causes marked secondary hardening;
4) promotes carbide formation.

1.3 PRESENT WORK

The present work is concerned with a study of the dissolution of titanium and vanadium in liquid steel. The experimental method presently used involved the measurement of dissolution rates of cylindrical-shaped specimens immersed in stagnant steel baths.

The dissolution behaviour of these objects was carefully monitored through continuous measurement of various physical parameters. These comprised:

1) the apparent weight of the specimen;
2) temperatures of the specimen at various positions;
3) the temperature of the steel bath.

For some specimens measurement of the steel shell thicknesses were also taken. A mathematical model was developed to predict the rate of dissolution of titanium and vanadium in liquid steel.

CHAPTER 2

PREVIOUS WORK

In this chapter, previous work reported in the literature concerning studies of dissolution kinetics in liquid iron and iron-carbon alloys is reviewed. A discussion of the thermophysical and transport properties of iron and low carbon iron alloys is also included with respect to thermodynamic data and phase diagrams relevant to this study.

2.1 GENERAL CONSIDERATIONS

The solution of a solid in a liquid represents a classical example of a heterogeneous process. Although most such processes involve a rather complex set of individual reaction steps, there are certain elementary aspects which are common to a wide range of reactions.

The transfer of material from a solid to liquid can be characterized as melting or as dissolution. The first occurs by application of heat, while the latter happens when the solid material comes in contact with the liquid at temperatures below the melting point of the solid. The dissolution process may be broken into two consecutive steps. The first is the surface reaction where the solid goes through a phase change to the liquid. The second is the transport of the resulting solute atoms from the interface into the bulk liquid by diffusion through a boundary layer. Either step could be rate-controlling in the dissolution process.

Additions in liquid steel can be classified into two categories. The first are those with a melting range lower than that of liquid steel. Table 2.1 gives a list of such additions. The second category of additions are those with melting ranges higher than that of liquid steel. Examples of some of these additions are listed in Table 2.2. Figure 2.1 shows, in schematic form, the relevant thermophysical phenomena which take place when a solid addition is immersed in a bath of molten steel. The first four routes refer to low melting range additions while the fifth one depicts the case of dissolution of high melting point additions. Routes 1, 2, 3 and 5 are analyzed in a work by Guthrie[45], while route 4 is presented in great detail by the present author and Guthrie in references 46,47.

2.2 DISSOLUTION IN LIQUID IRON ALLOYS

Extensive studies on the kinetics of dissolution of solid materials in liquid iron-carbon melts have been conducted over the past twenty-five years. The great majority of these experiments were done in either high carbon iron alloy melts or carbon saturated iron alloy melts. Far fewer experiments have been conducted in low carbon and relative pure iron alloy melts.

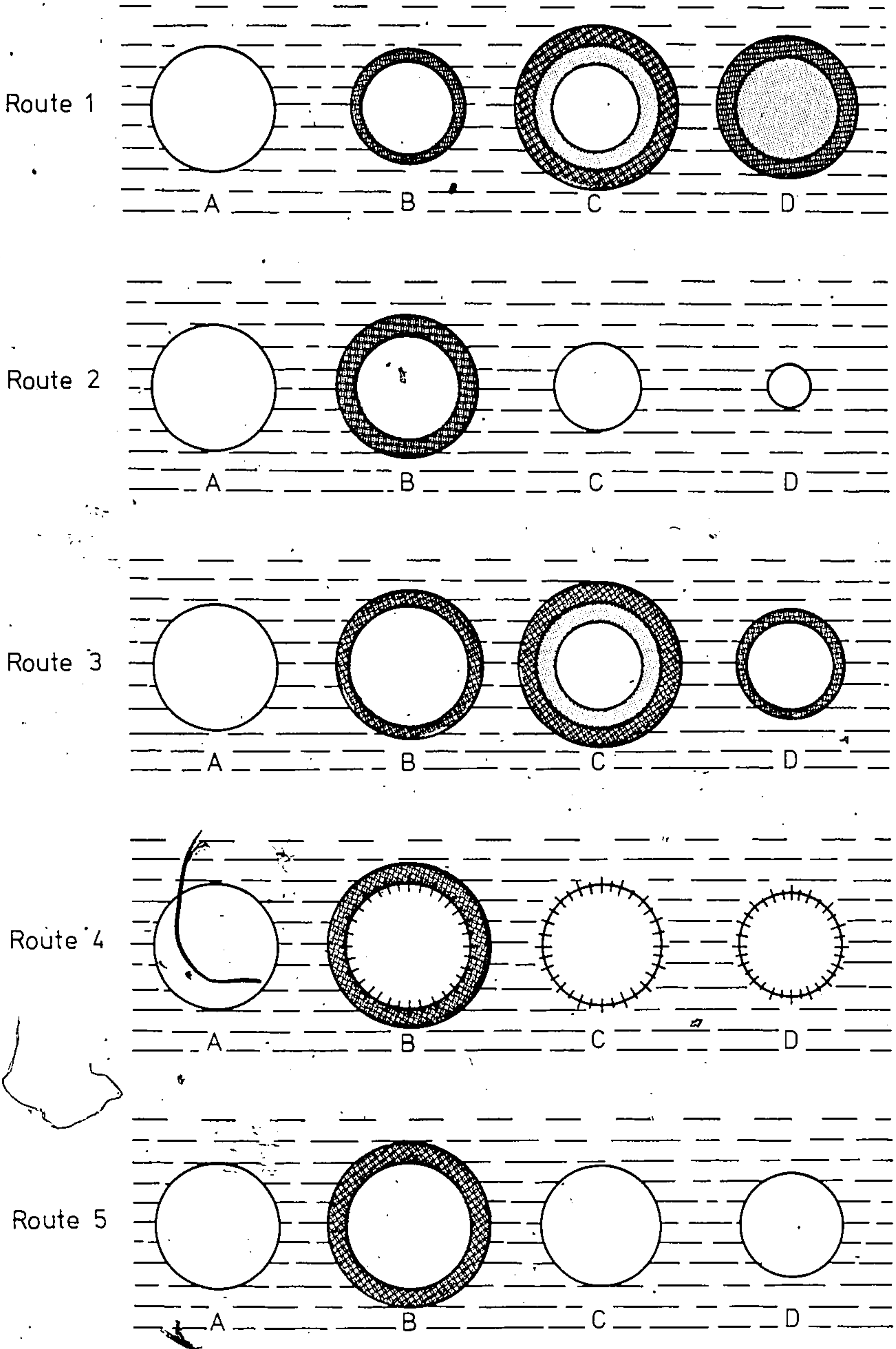

Figure 2.1 Schematic representation of the thermophysical phenomena which take place when a solid addition is immersed in liquid steel.

Routes 1, 2, 3 refer to low melting range additions. Route 4 corresponds to additions which exhibit exothermic reaction with liquid steel. Route 5 refers to high melting range additions.

Route 1	(1C) internal melting to begin and in many cases to be completed (1D) before the enclosing shell melts back. Typical examples Fe-Mn, SiMn, Al, at low steel bath superheats.
Route 2	Shows the case of an addition which after freezing the customary chill layer around it is reexposed to the bath before complete internal melting has occurred (2C). Conditions favoring such behaviour, high superheats (80-100°C) large diameters and alloys with low thermal conductivities.
Route 3	Once the solid is reexposed (3C), it is quite possible for another shell of steel (or series of shells), (3D), to form.
Route 4	Exothermic reaction starts at (3B) and steel shell melts back very fast, typical examples, Fe-Si where (3C) and (3D) are very short.
Route 5	Typical examples, Fe-V, Fe-Mo, Fe-W.

TABLE 2.1

Additions with Melting Range Lower than the Liquid Steel Melting Point

Addition	Melting Range of Melting Point	
Standard Ferromanganese	1071-1266°C	(1344-1539 K)
50% Ferrosilicon	1210-1227°C	(1483-1500 K)
Low Carbon Silicomanganese	1215-1260°C	(1488-1533 K)
75% Ferrosilicon	1204-1316°C	(1474-1589 K)
Aluminum	660°C	(993 K)
Charge Chrome 50-55% Cr	1404-1482°C	(1677-1755 K)

TABLE 2.2

Additions with Melting Range Higher than Liquid Steel Melting Point

Addition	Melting Range Melting Temperature	
Vanadium	1902°C	(2175 K)
Titanium	1667°C	(1840 K)
Niobium	2467°C	(2740 K)
Molybdenum	2615°C	(2888 K)
Tungsten	3400°C	(3673 K)
FeMo (62% Mo)	1800-1540°C	(2073-1813 K)
FeW (74% W)	2700-1640°C	(2973-1913 K)
FeNb 60% Nb		
FeV (80% V)	1670-1890°C	(1943-2163 K)

Table 2.3 lists metallic systems of solids dissolving in iron based melts for which experimental data have been reported. These experiments have been classified according to experimental mode and geometry. The experimental mode can be classified into two subgroups; static and dynamic. In the static method, the solid specimens were held motionless in liquid and natural convection influenced the dissolution rate. In the dynamic method, specimens were rotated so that forced convection affected their rate of dissolution. Most of the experiments reported used cylindrical or disk shaped specimens. Two exceptions are:

1) Biletskii and Shumikhim[10] studied the dissolution of spherical graphite particles in cast iron melt;

2) Niwa et al.[18] also used an alumina crucible to study the reaction of the alumina with carbon dissolved in molten iron. The crucibles used were either alumina or graphite apart from a few exceptions where magnesia crucibles were used.

The dissolution in liquid iron alloys was reported to be a diffusion rate controlled process under most conditions. An exception is the one reported by Karchin and Grigoryan[6] who observed that the dissolution rate of pyrographite in an iron-carbon melt was anisotropic with respect to different crystallographic faces at high rotational speeds. They found that the solution interface reaction of graphite became the controlling step at high stirring rates.

TABLE 2.3

Dissolution Experiments in Liquid Iron Alloys

Liquid	Solid	Specimen	Mode	Reference
Fe-C	Graphite	Cylinder	Static	1
Fe-C	Graphite	Cylinder	Static	2
Fe-C	Graphite	Cylinder	Static and Rotating	3
Fe-C	Graphite	Cylinder	Rotating	4
Fe-Mn	Graphite		Static	5
Fe-C	Graphite		Rotating	6
Pig Iron	Graphite	Disk	Static	7
Fe-C	Graphite	Disk	Rotating	8
Fe-Ni	Graphite	Disk	Rotating	8
Fe-P	Graphite	Disk	Rotating	8
Fe-Si	Graphite		Rotating	8
Fe-C	C			9
Cast Iron	Graphite	Spherical		10
Fe-C	Graphite			11
Fe-C	Si-C			11
Fe-C	C			12
Fe-C	Co	Disk	Rotating	13
Fe-C	Cr	Disk	Rotating	13
Fe-C	Mo	Disk	Rotating	13
Fe-C	Ni	Disk	Rotating	13
Fe-C	Si	Disk	Rotating	13
Fe-C	Ti	Disk	Rotating	13
Fe-C	W	Disk	Rotating	13
$Fe-C_{sat}$	Cr	Disk	Rotating	14
$Fe-C_{sat}$	CrC	Disk	Rotating	14
$Fe-C_{sat}$	Fe	Disk	Rotating	14
$Fe-C_{sat}$	Mo	Disk	Rotating	14

...cont.

TABLE 2.3 continued

Liquid	Solid	Specimen	Mode	Reference
Fe-C_{sat}	W	Disk	Rotating	14
Fe-C_{sat}	WC	Disk	Rotating	14
Gray Iron	SiC	Cylinder	Rotating	15
Pig Iron	C-Steel	Cylinder	Rotating and Static	16
Fe-C_{sat}	Fe	Cylinder	Rotating	17
Fe-C_{sat}	Al_2O_3	Crucible	Static	18
Fe-C	C-Steel	Cylinder	Static	19
Fe-C	C-Steel	Cylinder	Rotating and Static	20
Fe-C	Cu-Mg		Static	21
Fe-C	C-Steel	Cylinder	Static and Rotating	22
Fe-C-S	Ce		Static	23
Fe-C-Si	Ce		Static	23
FeO-Fe_2O_3	Fe	Cylinder	Rotating	24
Fe-C	Mg-Alloy		Static	25
Fe-C_{sat}	Al_2O_3	Cylinder	Static and Rotating	26
Fe-C	Fe			27
Fe-N_{sat}	BN	Disk	Static	28
Fe-B	BN	Disk	Static	28
Fe-C_{sat}	CaC_2	Cylinder	Rotating	29
Pig Iron	C-Steel	Cylinder	Static	30
Pig Iron	C-Steel	Cylinder	Static	31
Fe-C	Fe	Cylinder	Static and Rotating	32
Fe-C_{sat}	Mo	Cylinder	Rotating	33
Fe-S	Fe		Rotating	34
Fe-Cu	Fe	Cylinder	Rotating	35
Fe-C	Nb			36
Fe-C_{eutect}	Mo	Cylinder	Static	37
Cast Iron	Si	Disk	Rotating	38
Cast Iron	Ti	Disk	Rotating	38
Cast Iron	Cr	Disk	Rotating	38

...cont.

TABLE 2.3 continued

Liquid	Solid	Specimen	Mode	Reference
Cast Iron	Co	Disk	Rotating	38
Cast Iron	Ni	Disk	Rotating	38
Cast Iron	Mo	Disk	Rotating	38
Cast Iron	W	Disk	Rotating	38

Various additions relevant to steelmaking practices studied for dissolution kinetics in low carbon iron-based melts are listed in Table 2.4. In all cases and immediately following immersion a solid steel shell solidifies around the addition. The precise manner under which the steel shell behaves (i.e. freezing or melting) is very important for low melting point additives. However, its importance substantially lessens in the case of high melting point additions. In the first case, the dominant factor in the thermophysical phenomena is heat transfer, while in the latter, mass transfer becomes more important. For the dissolution of 50% ferro-silicon in liquid steel, a 'double heat effect' is applied to the steel shell such that the dissolution reaction becomes self-accelerating.[46,47]

Krupman and Yavoiskii[37] investigated the dissolution of molybdenum in Armco Iron. They distinguished two periods in the dissolution process. The first corresponded to the 'thermal' period where a solid shell freezes around the molybdenum. The second was the 'diffusion' period which began after the temperature had equalized between the bulk liquid steel and the molybdenum specimen. They proposed the following relationship for the dependence of mass transfer coefficients on temperature:

$$\log K = -\frac{14800}{T} + 4.87$$

K: cm s^{-1}
T: °K

TABLE 2.4

DISSOLUTION EXPERIMENTS IN PURE LIQUID IRON OR LOW CARBON LIQUID IRON ALLOYS

Dissolving Solid	Specimen	Experimental Mode	Reference
Ti	Disk	Rotating	38
Cr	Disk	Rotating	38
Nb	Disk	Rotating	38
Mo	Disk	Rotating	38
W	Disk	Rotating	38
FeMo (62% Mo)	Disk	Rotating	38
FeW (74% W)	Disk	Rotating	38
FeNb (60% Nb)	Disk	Rotating	38
Mo	Cylinder	Static and Vibrating	37
Mo	Cylinder	Static and Rotating	39
W	Cylinder	Static and Rotating	39
Fe-Mn	Cylinder	Static	40
Cr-Mn	Cylinder	Static	40
Fe-Cr	Cylinder	Static	40
Fe-Mn	Lumps with Isotopes	Static	41
Si-Mn	Lumps with Isotopes	Static	41
TiN		Rotating	42
Ferro-alloys			43
Fe-Mn	Cylinder	Static	44
Si-Mn	Cylinder	Static	44
Fe-Si	Cylinder	Static	44
Fe-Mn	Cylinder and Sphere	Static	45
Si-Mn	Cylinder and Sphere	Static	45
Fe-Si (50%)	Cylinder	Static	46
Fe-Si (50%)	Cylinder	Static	47
Al	Sphere	Static	48
Al	Cylinder	Rotating	49

Based on their data, an activation energy for the solution of molybdenum in liquid iron was calculated and shown to be at 273 kJ/mole or (65.1 kcal/mole). They explained this surprisingly high value of activation energy on the basis of liquid phase diffusion. However, recent work by Ershov et al.[59] and Ono et al.[51] has shown that the activation energy for the diffusion of molybdenum in liquid iron is only in the order of 59 kJ/mole (14.5 kcal/mole). Consequently their explanation based on a liquid phase diffusion controlled process must be regarded with some doubt. An attempt will be made by the present author to provide another explanation for their activation energy results in Chapter 6.

Shantarin and Shurygin[38] studied the dissolution rates of Ti, Cr, Mo, W and FeNb, FeMo, FeW in molten pure iron. They used a disk of metal rotating in liquid iron. They found that the dissolution rates in pure iron increases in the order of Mo-W-Cr-Ti and among the ferro-alloys (FeNb, 60% Nb)-(FeMo, 62% Mo) - (FeW, 74% W). They did not provide any explanation and the precise mechanisms were neither considered nor identified. They calculated diffusion coefficients from their results, which were found to be in agreement with recent work by Ershov et al.[50]

Bungardt et al.[39] studied the dissolution of molybdenum and tungsten in liquid steel under conditions of free and forced convection respectively. In the case of forced convection, they used rotation of their cylinders as well as

TABLE 2.5

Experimental Results from Brandis et al.[39]

	Dissolution Rate ($mol/m^2 \cdot s$)			Mass Transfer Coefficient
	Free Convection	350 (RPM)	Gas Flow Rate 14 lit Ar/h	Free Convection m/s
Mo	0.833	2.0	3.3	1.9×10^{-5}
W	0.325	0.66	0.675	1.82×10^{-5}

flow of Argon gas through the iron bath at a rate of $(3.8 \times 10^{-6}\ m^3/s)$. Their results are summarized in Table 2.5. They found that the dissolution rate of molybdenum was higher than that of tungsten at 1863 K (1590°C) and that the mass transfer coefficients were about the same. At temperatures below 1910 K (1637°C) the reaction of tungsten with liquid iron resulted in the intermetallic combination Fe_7W_6 whose structure permitted no conclusion as to preferred diffusibility of the constituent elements.

Terziyan[41] studied the dissolution kinetics of ferroalloys in steel ladles. He labelled the alloys with radioisotopes, immersed them in liquid steel for specific times and measured the loss in weight of the alloy and the radioactivity of metal samples from the ladle. The experiments were carried out in both quiescent and intensively stirred liquid steel baths. Data on the kinetics and mechanisms of dissolution of ferromanganese and silicomanganese were processed statistically. Regression equations were formulated for the time of dissolution as a function of lump size and metal temperature in relatively quiescent metal baths. They obtained:

$$T_p = 100 + 27.75 \cdot x_1 - 17.25 \cdot x_2 + 2 \cdot x_1^2 + 2 \cdot x_2^2 - 5.25 \cdot x_1 \cdot x_2 \qquad (2.1)$$

$$T_p = 63 + 2.5 \cdot x_1 - 12.5 \cdot x_2 + 2.7 \cdot x_1^2 + 1.4 \cdot x_2^2 - 2.5 \cdot x_1 \cdot x_2 \qquad (2.2)$$

where T_p: duration of solution (sec)

x_1: parameter characterizing the diameter of the sample d(mm) $x_1 = (d-50)/10$

x_2: parameter characterizing the temperature of the metal t°C $x_2 = (t-50)/15$.

Equation 2.1 gives the solution time for ferromanganese while equation 2.2 gives the solution time for silicomanganese. Terziyan claimed that these equations were determined with a sufficient degree of accuracy for predicting solution times of ferro-alloy lumps, measuring from 40 to 180 mm in diameter at bath temperatures ranging between 1560 and 1650°C (1833 to 1923 K).

In 1974, Gourtsoyannis et al.[48] developed a mathematical model predicting the melting history of aluminum spheres immersed suddenly into liquid steel. Their model predicted the formation of a solid shell of steel which rapidly froze around the aluminum sphere during the first seconds of immersion. The model also demonstrated how partial melting of the object can begin while still encased within the steel shell. It was shown that the enclosed object would continue to melt at a rate which depended on a) the rate of evolution of latent heat as the steel shell solidifies and b) the rate of convective heat transfer from the bath to the outer surface of the steel shell.

In previous work, the present author conducted a series of experiments to study the melting characteristics of ferromanganese and silicomanganese cylinders in molten steel baths. A detailed account of this work is given in Ref. 44. Briefly, a heat transfer model simulating the thermal events which occur when ferromanganese and silicomanganese cylinders are immersed in molten baths was developed. The experimental results were found to be in substantial agreement with model predictions. The steel bath cooling rate and superheat were shown to be significant factors on solution kinetics of these alloys, while steel bath viscosity had no significant effect. Figure 2.2 shows a cross-section of a ferromanganese cylinder (3.81 cm diameter) following immersion for a 30 second period in a steel bath whose initial superheat was 30°C.

The modification of dissolution kinetics by the high exothermic heat of dissolution to molten steel was also studied by the present author and Guthrie.[46,47] To this end, the kinetics of dissolution of solid cylinders of 50 wt% ferrosilicon in liquid steel were chosen. It was shown that the customary frozen shell of steel formed around the ferrosilicon cylinder following its initial immersion. Premature internal melting of the cylinder then began as a result of liquid eutectic of Fe_2Si compositon forming at the inner steel shell/ferrosilicon boundary. This phenomenon was shown to trigger exothermic dissolution and erosion of the steel shell at the inner surface. The outer boundary of the steel shell melted back concurrently as a result of convective heat transfer from the steel bath.

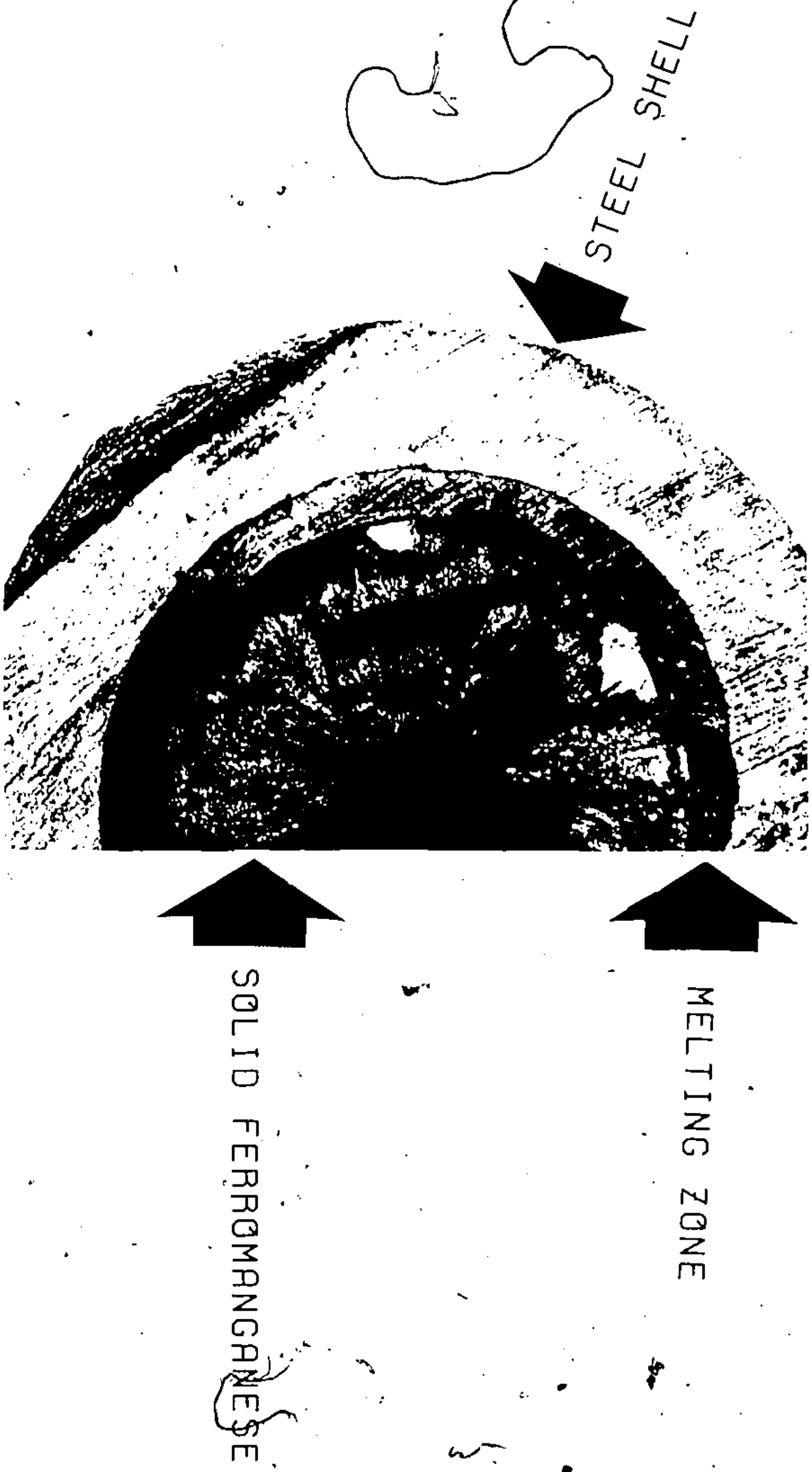

Figure 2.2 Cross section of a ferromanganese cylinder immersed for 30 seconds in a steel bath with an initial superheat 30°C.

The net result of exothermic dissolution phenomena is that considerably shortened shell dissolution times can be observed in comparison to more conventional ferro-alloy/ steel systems.

A simplified mathematical model of the process was developed and Figure 2.3 gives a schematic representation of the 'double heat effect' which is imposed on the frozen steel shell.

Povolotskii et al.[58] investigated the diffusion of deoxidants such as Al, Si, Mn in molten iron using the capillary method. The diffusion coefficients, D, and energies of activation, E, for diffusion of the deoxidants in iron containing various amounts of carbon were determined. They found that in the case of separate diffusion in a melt containing oxygen, the higher the deoxidizing capacity of the element, the greater was the activation energy of diffusion. Thus, with diffusion in an iron containing 0.003-0.010% oxygen, the energy of activation of aluminum, silicon and manganese is 145.7 kJ (34.7 kcal), 121.8 kJ (29 kcal), 101.2 kJ (24.1 kcal).

In more recent work, Mucciardi[49] has studied light alloy addition techniques in steelmaking. Aluminum wires of 6.4 to 15.9 mm in diameter were fed into steel melts while their 'apparent' weights were monitored. It was found that the maximum depth of penetration of an aluminum wire fed into molten steel can be expressed in the dimensional equation:

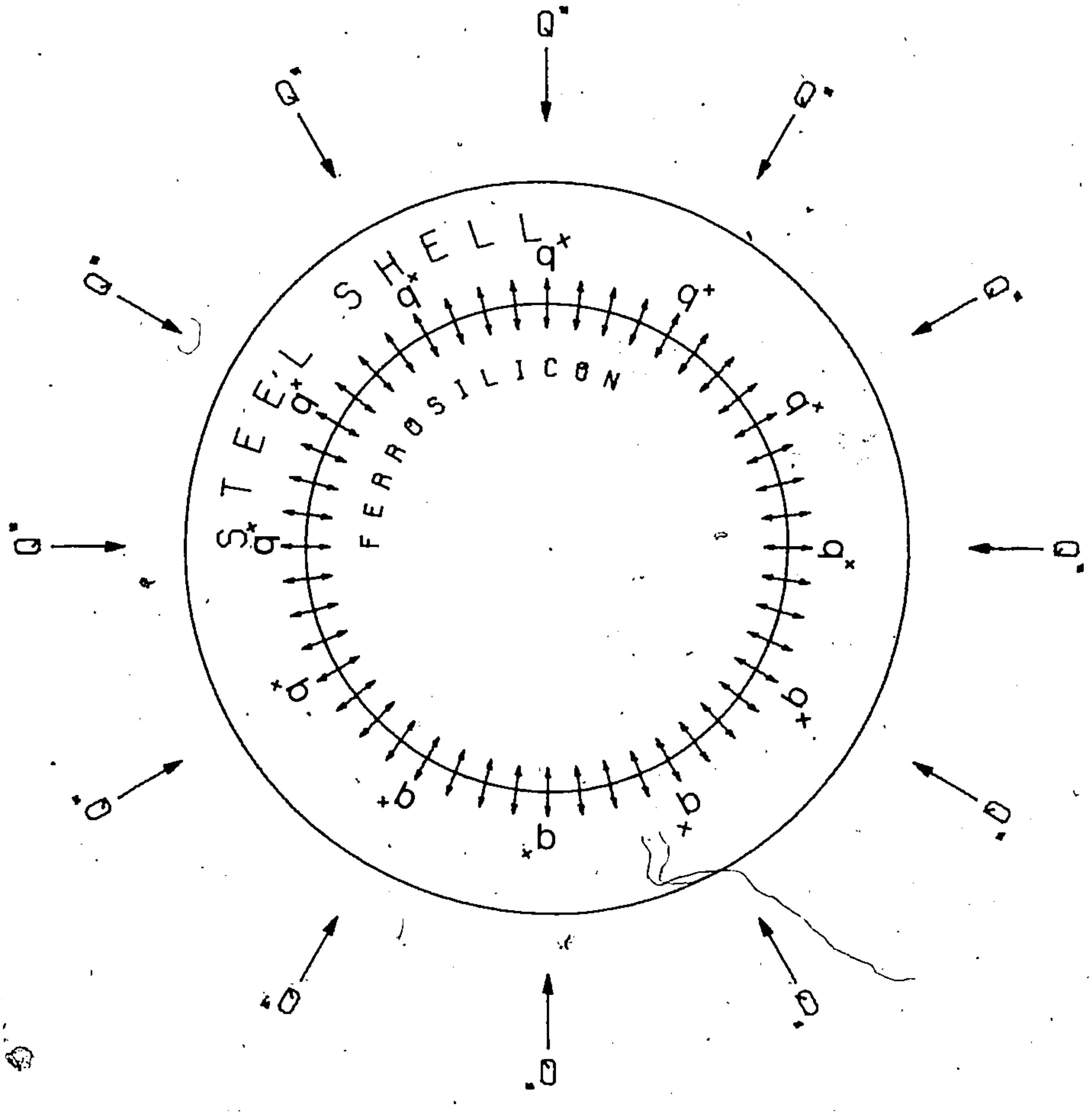

Figure 2.3 Schematic representation of the 'double heat effect' which is imposed on the frozen steel shell.

$$\text{Depth(m)} = \frac{145.5\ \text{Diameter(m)}^{0.86} \cdot \text{Velocity(m/s)}^{0.52}}{\text{Superheat(k)}^{0.34}} \qquad (2.4)$$

2.3 THERMOPHYSICAL AND TRANSPORT PROPERTIES OF LIQUID IRON

2.3.1 Phase diagram

The iron-carbon phase diagram shown in Figure 2.4 is that recorded in the Thermochemistry for Steelmaking, Vol. II, by Elliot et al.[52] The melting point of pure iron is reported to be at 1809 K (1536°C). Iron liquidus values at different temperatures ranging between 1809 K (1536°C) and 1773 K (1500°C) tabulated by Elliot et al.[52] were used to obtain:

$$T_{mp}(K) = 1809.1 - 29.55 \cdot W_c - 85.7 \cdot W_c^2 \qquad (2.5)$$

where W_c = weight percent of carbon

2.3.2 Density

The density of pure iron at various temperatures is reported in many sources including: Thermochemistry for Steelmaking, Volume II, by Elliot et al.,[52] Lucas,[53] Lange[54] and in the Metals reference book by Smithels.[55]

Smithels gives the density of liquid iron at 1809 K (1536°C) as 7015 kg m^{-3} (7.015 gr cm^{-3}). At higher temperatures, the density of liquid iron is given by equation 2.6.[55]

$$D = D_0 + (T - T_0)(dD/dT) \qquad (2.6)$$

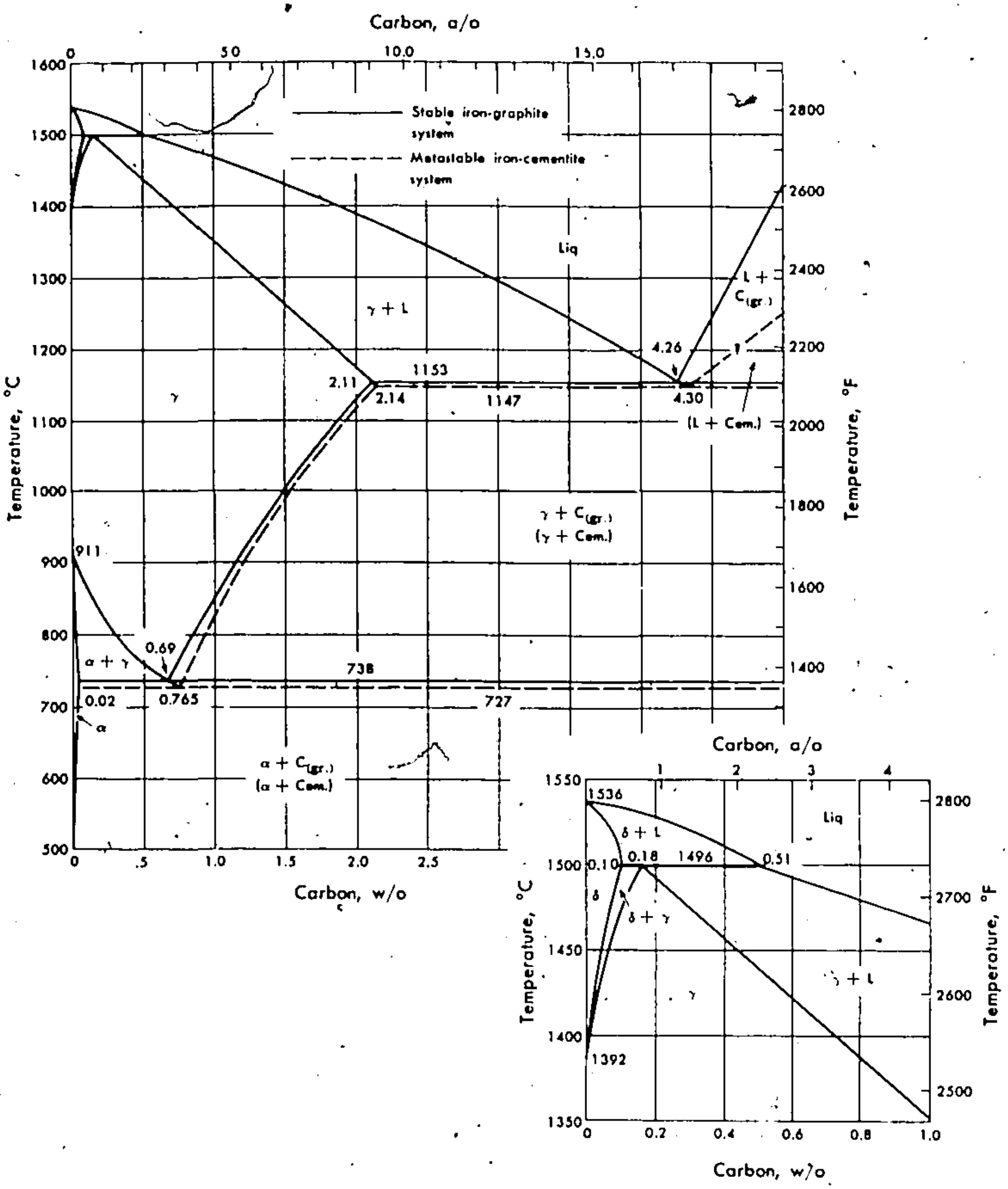

Figure 2.4 The iron-carbon phase diagram.[52]

where Do is the density of liquid iron at melting point T_o and $dD/dt = -0.887\ kg/m^3k$ (2.7)

These values have been adopted in the present text.

2.3.3 Viscosity

Turkdogan[56] has presented data for the viscosity of liquid iron at its melting point. The value quoted is $0.00495\ N\cdot S/m^2$ (4.95 CP) with E at 41.58 kJ. The variation in viscosity with temperature for liquid iron is given by Smithells.[55]

$$n = n_o \exp\left(\frac{E}{RT}\right) \qquad (2.8)$$

where n_o: 0.3699 mNS/m²

E: 41.4 kJ/mol

R: gas constant 8.3144 J/k mol

2.3.4 Thermal Conductivity

The variation in iron thermal conductivity of iron with temperature is given by Turkdogan.[56] At the melting point of pure iron, it is quoted as $30\ Wm^{-1}K^{-1}$ ($0.071\ cal\cdot cm^{-1}\cdot s^{-1}\cdot c^{-1}$), at 1873 K (1600°C) $35\ Wm^{-1}K^{-1}$ ($0.083\ cal\cdot cm^{-1}\cdot s^{-1}\cdot c^{-1}$).

2.3.5 Specific Heat and Latent Heat of Fusion

Data on iron specific heat has been summarized by Elliot et al.[52] Lange[54] also reviewed experimental data for the specific heat of pure iron. The tabulated values of specific heat were used to obtain an average over a range of temperature. The latent heat of fusion was chosen to be 15 kJ/gr-atom,[63] a value reported to range between 13.4 and 15.5 kJ/g-atom.

2.3.6 Diffusivity

Ono and Shigematsu[51] determined the diffusivity of vanadium, cobalt and molybdenum in molten iron using a coupled-diffusion method. They found the following results: for Fe-V alloys with vanadium contents up to 1.42%:

$$D_V = 3.69(\pm 0.33)\ 10^{-5}\ \text{cm}^2/\text{s} \quad \text{or}$$

$$D_V = 3.69(\pm 0.33)\ 10^{-9}\ \text{m}^2/\text{s}$$

at 1823 K (1550°C)

Iida and Morita[57] derived a series of expressions describing some properties such as diffusivity and viscosity of any liquid metal and alloy near their liquidus temperatures in terms of some basic physical quantities. They showed good agreement between calculated and experimental values for the solute diffusivity in liquid iron at 1873 K (1600°C). For the diffusivity of vanadium in liquid iron, they calculated a value of 4.4×10^{-9} m²/s (4.4×10^{-5} cm²/s) at 1873 K (1600°C).

Ershov et al.[59] studied the diffusion of various alloying elements in liquid iron over the temperature range 1823 to 1973 K (1550 to 1700°C). They used electron microprobe analysis for the determination of concentration profiles. An exponential form $D = D_o \exp(-Q/RT)$ was employed to determine the temperature dependence of the diffusivity.

$(D)\cdot10^9$ m²s^{-1}	$D\cdot10^9$ m²/s (1873 K)	$D_o\cdot10^8$ m²/s	Q kJ/mol
V	4.1	11.10	51.66
Ti	13.8	31.00	48.3

The considerable variation in diffusion coefficients between these elements was explained by microheterogeneity of the liquid iron and by features of the distribution of the diffusing elements between the structure components of the melt.

2.4 THE IRON-TITANIUM PHASE DIAGRAM

The Fe-Ti phase diagram shown in figure 2.5 was adopted from the 'Thermochemistry for Steelmaking', Vol. II, by Elliot et al.[52] One will note that two intermetallic compounds, 'FeT_i' and 'Fe_2T_i', are reported. According to Ence and Margolin,[59] the compound $FeTi_2$, not shown in this diagram, forms a peritectoid reaction between β and FeTi at the temperature of 1273 K (1000°C).

Molchanova[60] states that the '$FeTi_2$' is stable only in the presence of oxygen. The temperature range where the liquid phase could exist in the binary iron-titanium system and where this study was concentrated, was from 1843 K (1570°C) to 1923 K (1650°C). The β liquidus was given as a straight line.[52]

$$T_L(K) = 1940 - 2030.3 \cdot X_{Fe} \quad \text{or}$$

$$T_L(°C) = 1667 - 2030.3 \cdot X_{Fe}$$

2.5 THERMODYNAMIC PROPERTIES OF IRON-TITANIUM ALLOYS

There is only limited published data on the thermodynamics of liquid iron-titanium. Chipman[64] estimated the activity coefficient of titanium at infinite dilution, $\gamma^\circ_{Ti} = 0.011$ at 1873 K. More recently, Fruehan[65] calculated the activity coefficient of Ti at infinite dilution as $\gamma^\circ_{Ti} = 0.038$ at 1873 K. Since then, Kaufman and Nesor[61] derived an analytical description of the iron-titanium systems. They

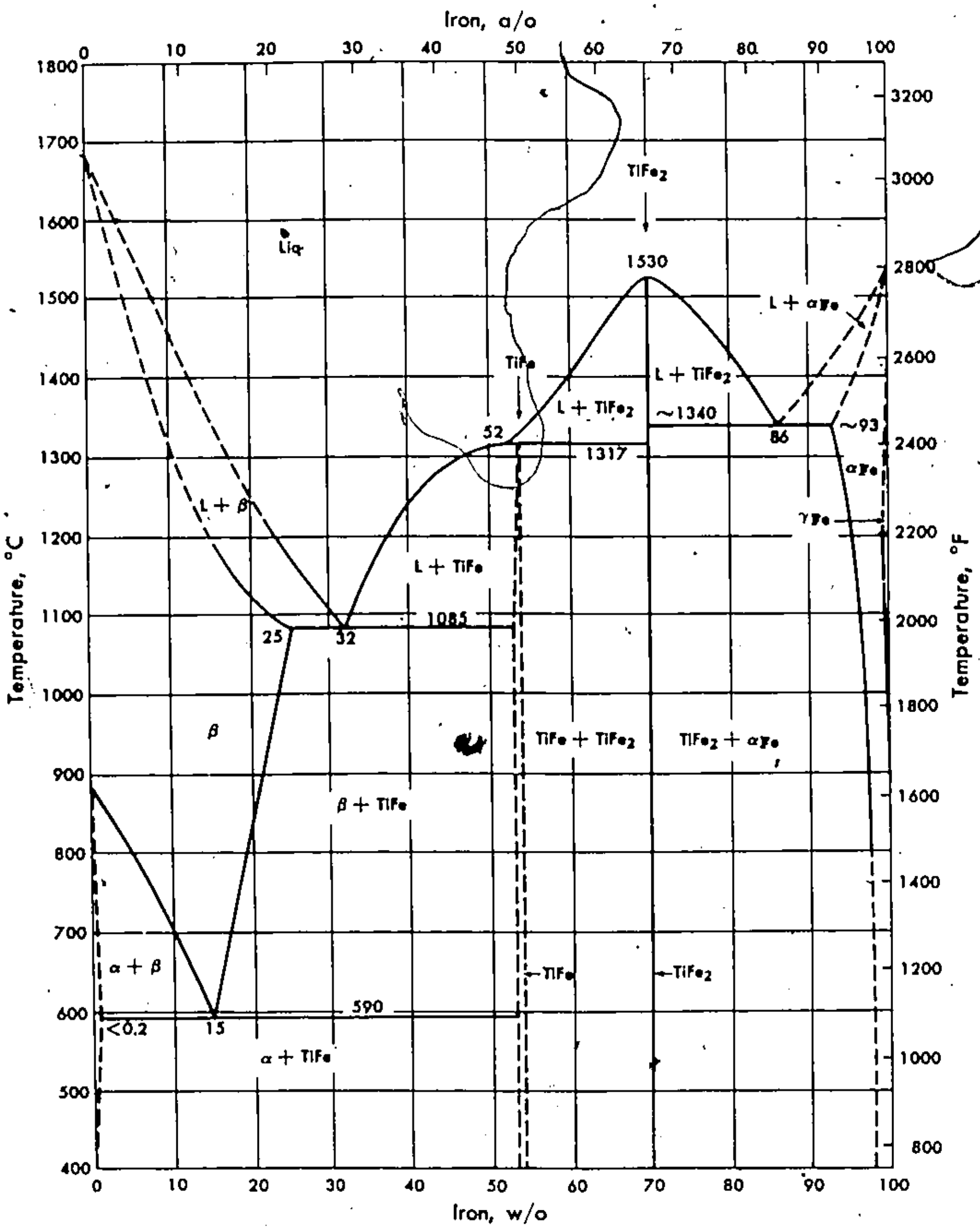

Figure 2.5 The iron-titanium phase diagram.[52]

used data published in their computations from the experimental results of Kubaschewski and Dench[62], and of Wagner and St. Pierre.[63] The integral heat of mixing for liquid iron and titanium is given in the following formula[61]:

$$\Delta H_m = X_{Fe}\, X_{Ti}\,(-62760\, X_{Fe} - 46024\, X_{Ti})$$

where X_{Fe}: iron mole fraction

X_{Ti}: titanium mole fraction

ΔH_m : J/mol

$0 \leq X_{Ti} \leq 1$: composition range

$1400 \leq T \leq 2000$: temperature range in K

2.6 THE IRON-VANADIUM PHASE DIAGRAM

The Fe-V phase diagram in Figure 2.6 was also adopted from 'Thermochemistry for Steelmaking', Vol. II by Elliot et al.[52] A compound Fe_3V which is not shown in their diagram, has also been reported.[66]

The temperature range where the liquid phase could exist in the binary iron-vanadium system and where, therefore, the present study was concentrated, ranges between 1823 K (1550°C) and 1908 K (1635°C). The liquidus can be approximated as a straight line:

$$T_L(K) = 2041 - 520 \cdot X_{Fe} \text{ or}$$

$$T_L(°C) = 1768.0 - 520 \cdot X_{Fe}$$

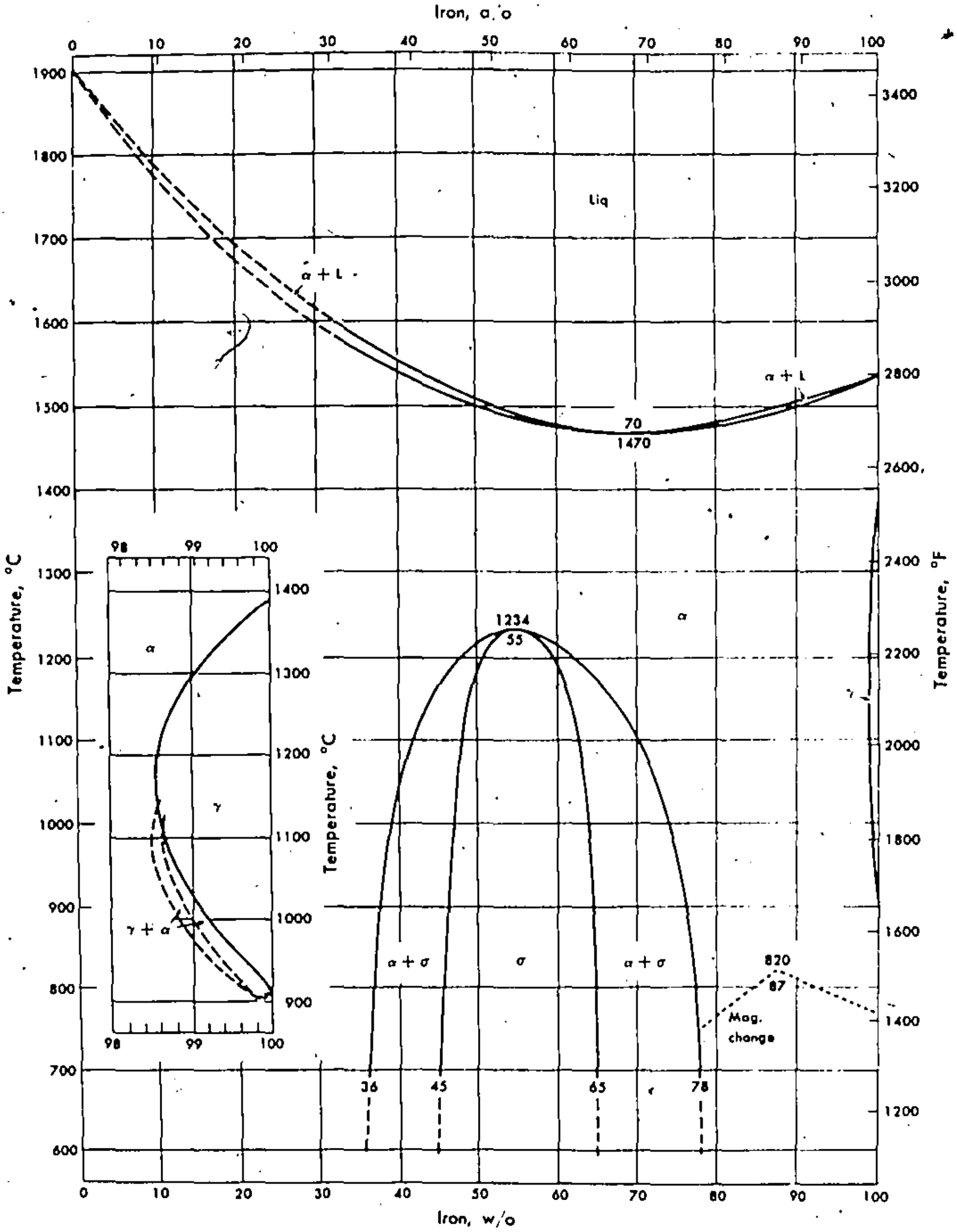

Figure 2.6 The iron-vanadium phase diagram.[52]

2.7 THERMODYNAMIC PROPERTIES OF IRON-VANADIUM ALLOYS

Elliot et al.[52] have presented the partial and molar properties of mixing of liquid iron and vanadium at 1873 K (1600°C). They derived this directly from Chipman's activity curves where he made the assumption that the entropy of mixing for the solution is ideal (regular solution behaviour). More recently Kay and Kontopoulos[67] measured Henry's law coefficient γ_V°, as being 0.23, 0.21, and 0.18 at 1823 K (1550°C), 1873 K (1600°C), 1923 K (1650°C) respectively. Based on these results and with the assumption of regular solution behaviour, the present author derived the enthalpies of mixing of liquid iron and vanadium at different temperatures. Figure 2.7 summarizes these results.

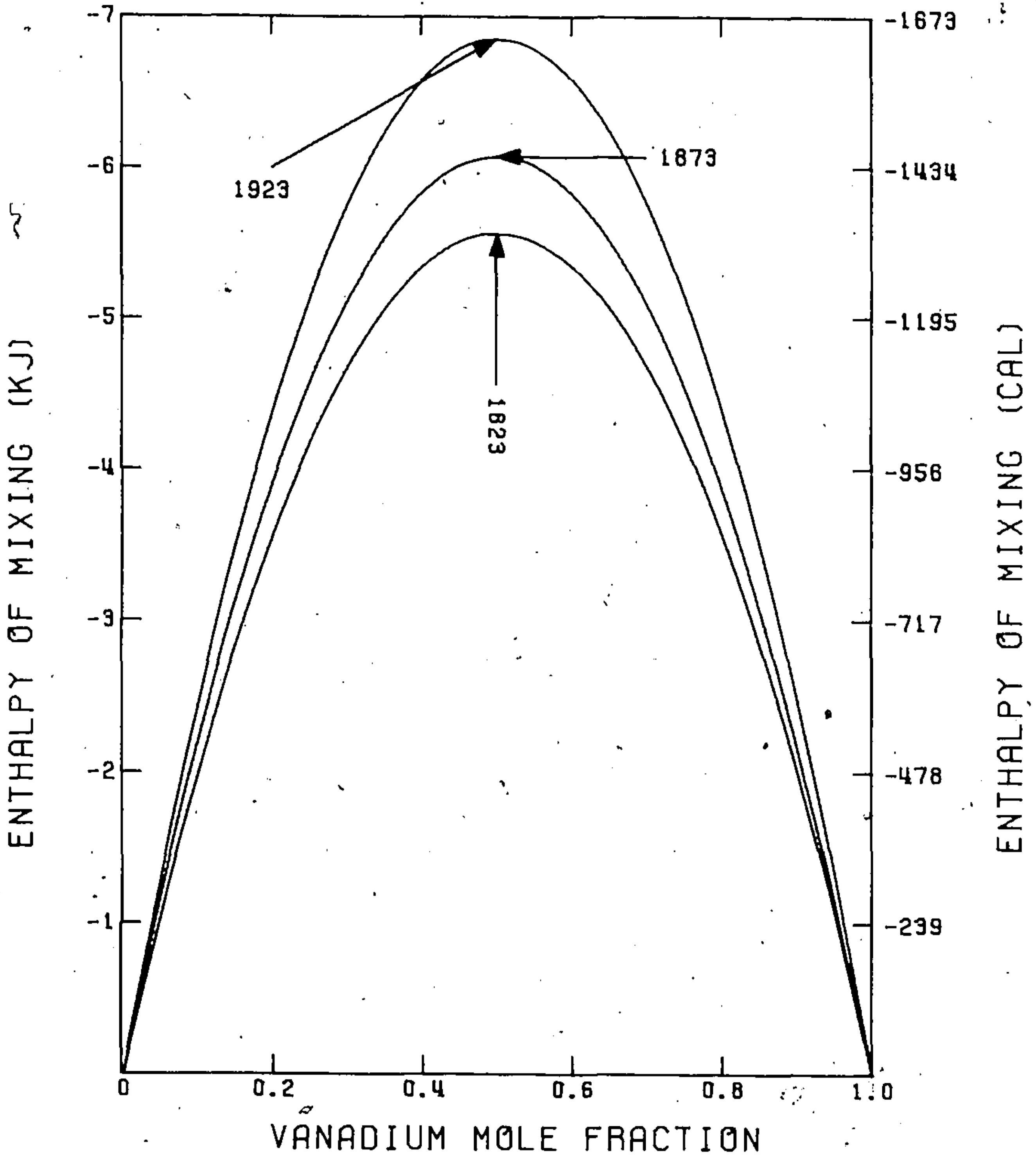

Figure 2.7 Heat of mixing of iron and vanadium at different temperatures (K).

CHAPTER 3

3.1 INTRODUCTION

In this chapter materials and experimental procedures used are presented in detail. The hardware and software aspects of a microprocessor based data acquisition system are described. This system was developed specifically for this research work.

3.2 CYLINDER IMMERSION EXPERIMENTS

The cylinder immersion tests were carried out using a Tocco meltmaster furnace to melt and contain the steel. It was a 150 kVA, 400 V, 3000 Hz unit. The inductotherm coils had 9 turns in a length of 35.6 cm, with an internal coil diameter of 33.0 cm. The alumina crucible, (90% Al_2O_3, 10% SiO_2 supplied by Engineered Ceramics), had an internal diameter of 19.7 cm and a height of 35.6 cm. The molten charge normally filled the crucible to within 2.5 cm of the top. All of the heats were made by induction remelting an initial charge of Armco iron in an alumina crucible. Figure 3.1 shows the induction furnace with its controls. During the meltdown and throughout the heat, oxidation was minimized by placing a pipe, 0.95 cm in diameter, slightly above the rim of the crucible. Argon was passed through the pipe at a flowrate of 15 c.f.h. throughout the course of the experiment.

Figure 3.1 The induction furnace with its controls.

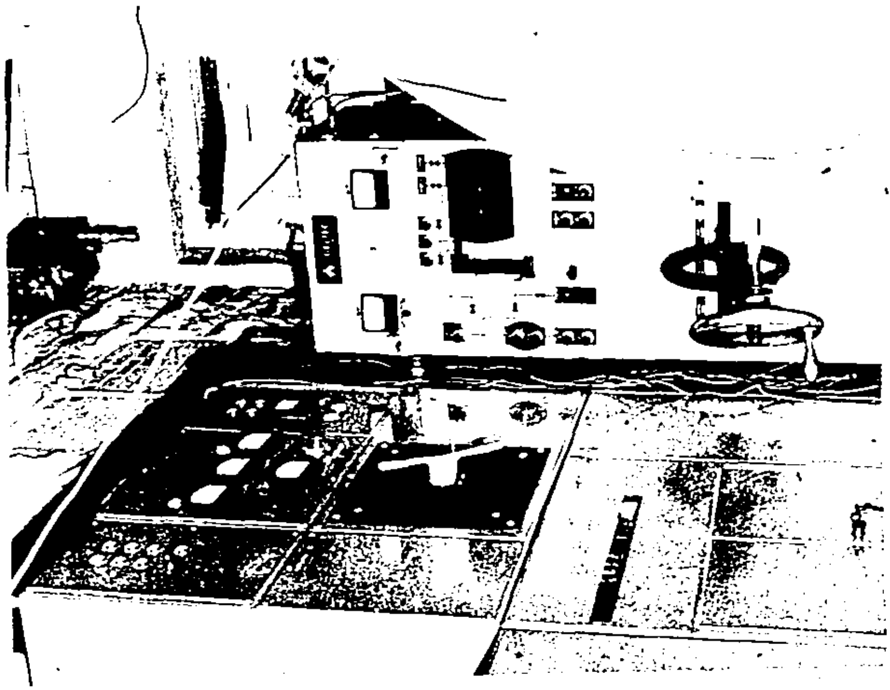

3.2.1 Materials

The titanium cylinders used, designated as ASTM B-348 GRADE 2, were purchased from Titanium Ltd., Ville St-Laurent, Quebec. The analysis certificate quotes 0.03% nitrogen, 0.10% carbon, 0.0125% hydrogen, 0.30% iron, 0.25% oxygen and titanium the balance. Thermophysical properties for this type of titanium along with their sources are presented in Table 3.1. The vanadium cylinders used were purchased from Metals and Byproducts Company, Sparta, New Jersey. The analysis certificate quotes 99.9% vanadium, 0.02% carbon, 0.04% oxygen, 0.02% nitrogen, and 0.02% iron. The properties of vanadium cylinders were estimated from similar properties of pure vanadium and are summarized in Table 3.1. High purity, iron melts were made by melting Armco iron having a nominal composition of 0.02%-0.03% carbon, 0.05% manganese, 0.007% phosphorus, 0.018%-0.01% sulphur, 0.001% silicon, and iron the balance.

In the case of titanium cylinders, the necessary thermocouple inserts were made by drilling out 0.31 cm diameter holes. For the vanadium cylinders the spark erosion technique was employed in order to make these holes. The exact position of the tips of these holes in the cylindrical body was found by x-ray radiography.

The ferrovanadium cylinders used were supplied from the Market Development Department of Metals Division of Union Carbide Corporation.

Table 3.1 Thermal and Physical Properties of Titanium, Vanadium and Armco Iron

	Property	Titanium	Vanadium	Armco Iron
Solid	Density (kg/m³)	[89] 4500 (298 K)	[89] 6100 (298 K)	[100] 7506 (1500 K)
	Heat Capacity (J/kg K)	[89] 580 (298)	[55] 498 (298)	[100] 698 (1500 K)
	Thermal Conductivity w/m K	[89] 16 (298)	[55] 31.6 (298)	[100] 32.1 (1500 K)
Melting Point (K)		[89] 1938±5	[91] 2173±25	(est) 1793
Phase Transformation (K)		[91] 1155.0	-	-
Latent Heat of Transformation (J/kg)		[91] 8874.8	-	-
Liquid	Density (kg/m³)	[55] 4100 (1938 K)	[55] 5700 (2173)	[100] 6960 (1870 K)
	Heat Capacity (J/kg K)	-	-	[100] 822 (1870 K)
	Thermal Conductivity w/m K	-	[90] 49.4 (1873 K)	[100] 41.2 (1870)
	Viscosity (Pa S)	-	-	[100] 5.1×10^{-3}
	Volumetric Coefficient of Expansion	-	-	[100] 1.4×10^{-4} (1870)
Prandtl Number		-	-	0.102
Latent Heat of Fusion (J/kg)		[91] 322,182	[91] 410,370	[63] 268,500

Figures 3.2 and 3.3 show titanium and vanadium cylinders, respectively. In order to eliminate the bottom effects in the cylinders a steel cap was placed very tightly on the bottom of the cylinders. This cap was thicker at the corners where the melting is faster.

3.2.2 Procedure for Adjusting Steel Bath Chemistry

Sixty-five kg heats of Armco iron were melted down. The bath temperature was brought up to 1600°C (1873 K) and thereafter maintained within ±20 K. For this measurement, Leeds and Northrup Dip-Tir thermocouples were used, which were type R (platinum/platinum-13% rhodium). The EMF measurements were taken with a Fluke 8600A digital voltmeter. At this stage the oxygen content of the bath was generally found to be in the range 1100-1200 ppm.

A 100 gr pure silicon addition followed for deoxidizing the steel. The lumps were stirred in the melt for about 30 seconds. Following this, 300 gr of aluminum rods 1.905 cm in diameter were immersed. Immediately after, 40 gr of lime were dispersed in the surface of the melt. At this point the accumulated slag was quite fluid and skimmed off easily. After three minutes, samples were taken with a 0.47 cm I.D. vycor tube, equipped with a rubber aspirator bulb. After deoxidation, the oxygen content of the steel bath was found to be between 40 and 60 ppm. In order to keep the titanium content of the steel bath to a minimum only a limited amount

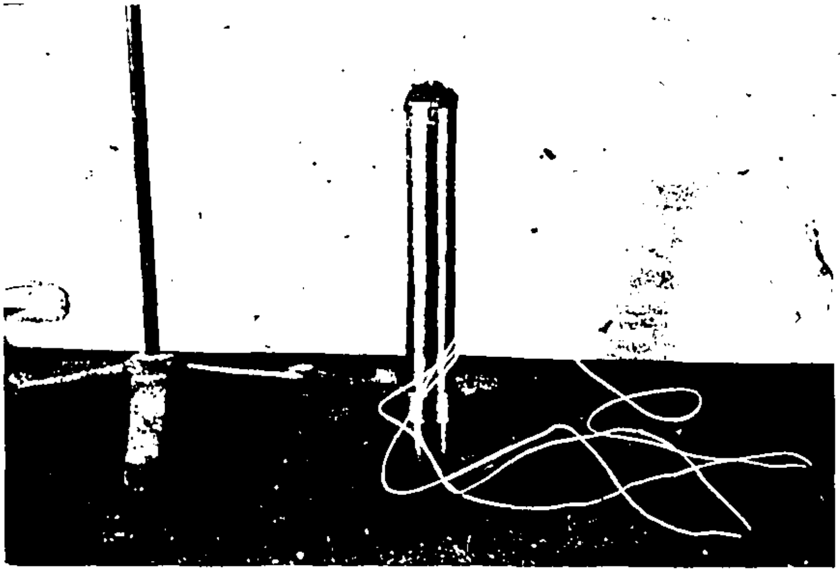

Figure 3.2 Titanium cylinder.

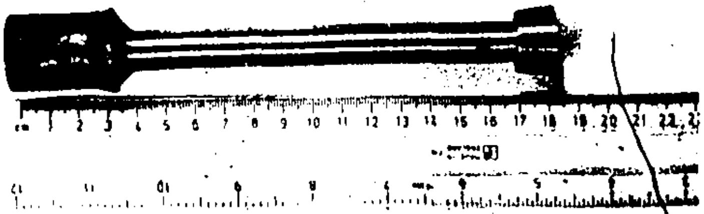

Figure 3.3 Vanadium cylinder.

of titanium cylinders were immersed in each heat. In any case, the titanium content of the steel bath never exceeded the 3.0 wt% mark. In the case of vanadium experiments each cylinder was immersed in a new steel bath.

3.2.3 Procedure for Immersing Bath Thermocouple

Once the bath chemistry had been correctly adjusted, the next step involved immersion of the bath thermocouple. As will be mentioned with the mathematical model in Chapter 4, a continuous monitoring of bath thermocouple is critical to the success of these dipping tests since melting times are normally inversely proportional to superheat temperatures ($\theta_{Bath} - \theta_{M.P.Fe}$). For typical steel plant conditions, this only amounts to at most 100°C, so for a ±5% error, instantaneous bath temperature must be known to be within ±5°C maximum.

The thermocouple system chosen was a type R (Platinum/ platinum-13% rhodium). The thermocouple wires had been appropriately placed in a 99.8% alumina double bore insulator tube (McDanel) with O.D. 2.38 mm. The whole system was contained in a 99.8% alumina sheath 5 mm I.D., 7 mm O.D., 46 cm long with one end closed. In order to prevent slag erosion (of alumina tube) at the melt surface, a cement 'collar' 9 cm long and about 3.2 cm in diameter was bound around it over the appropriate distance. Another cement collar of the same diameter and a length of 2.5 cm was placed 6.5 cm from the open end of the alumina sheath. This latter collar allowed better attachment of the alumina tube to the support stand. Figure 3.4 shows a bath thermocouple.

The whole thermocouple assembly was lowered to within 7 cm of the bath surface for about seven minutes, and it was connected with a Fluke 8600A digital voltmeter. It was then lowered to just above the melt surface for about ten minutes. When the temperature was at 1400°C (1673 K), the tip was immersed to a depth of 6 cm. The maximum life achieved for a thermocouple immersed in this way was one and a half hours at temperatures ranging between 1550°C and 1650°C (1823 K to 1923 K).

The platinum wires of bath and cylinder thermocouples were long and were connected with cold junction compensators, type CJ-R, supplied by Omega Engineering Inc., Stamford, Ct., U.S.A..

3.2.4 Weight Sensor

In this work, advantage was taken of a piece of equipment which had been constructed at McGill University. Using this equipment the apparent weight of the addition in the steel bath was monitored. Figure 3.5 shows a picture of this apparatus while full details are given in reference 49. In essence, the equipment provides a feeding mechanism driven by a 1/3 HP variable speed DC motor, plus a LEBOW 12 kg capacity load cell capable of measuring both tensile and

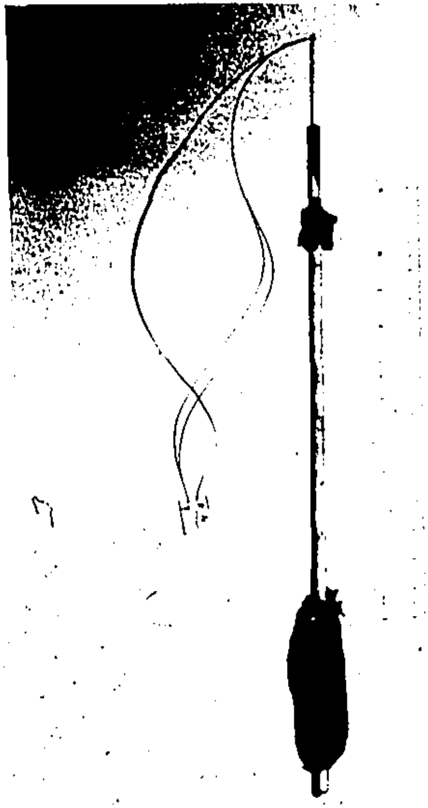

Figure 3.4
Steel bath thermocouple.

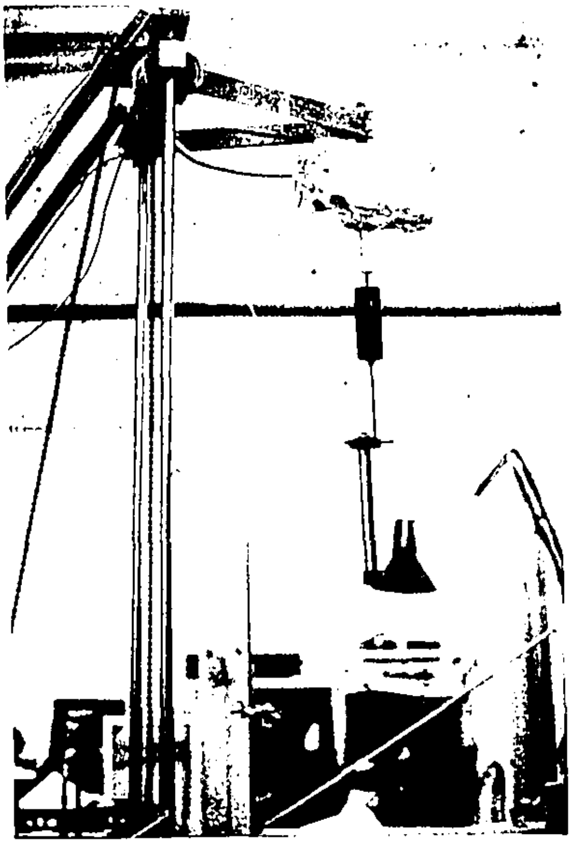

Figure 3.5
Weight sensor.

compressive loads. The load cell was calibrated by suspending known weights from it and by subsequently measuring the output signal for the input excitation voltage of 20 DC. The following mathematical expression was found to be excellent in converting analog signals to force:

$$\text{Net Downward Force (N)} = 2.778\ (\text{MIL}) - 2.996$$

or (3.1)

$$\text{Net Downward Force (gr force)} = 283.2\ (\text{MIL}) - 305.5$$

$$\text{Correlation} = 1.00$$

where MIL: the output signal in millivolts.

Figures 3.6 and 3.7 give schematic representations of the induction furnace with the bath and cylinder thermocouples and the weight sensor.

The accuracy of weight measurements by the load cell is equal to ±4 gr force or (±0.039N).

3.3 MICROPROCESSOR BASED DATA ACQUISITION SYSTEM

The monitoring of analog signals from the transducers (i.e. thermocouples and load cell) was carried out with a novel data acquisition system designed and constructed expressly for the present study. Figure 3.8 shows a schematic layout of the data acquisition and a picture of this system is presented in Figure 3.9.

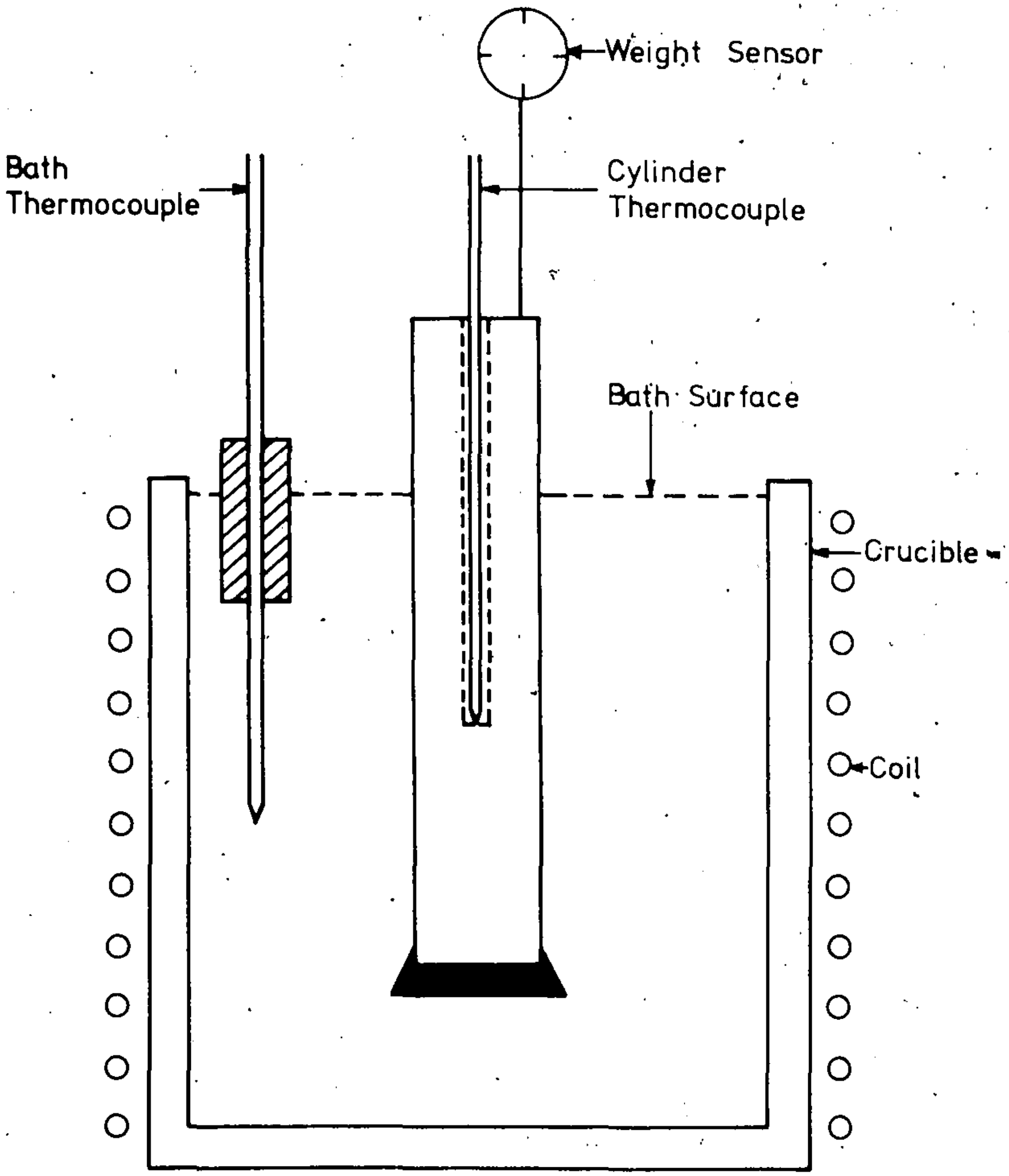

Figure 3.6 Schematic representation of induction furnace cross section with bath and one cylinder thermocouple and the weight sensor.

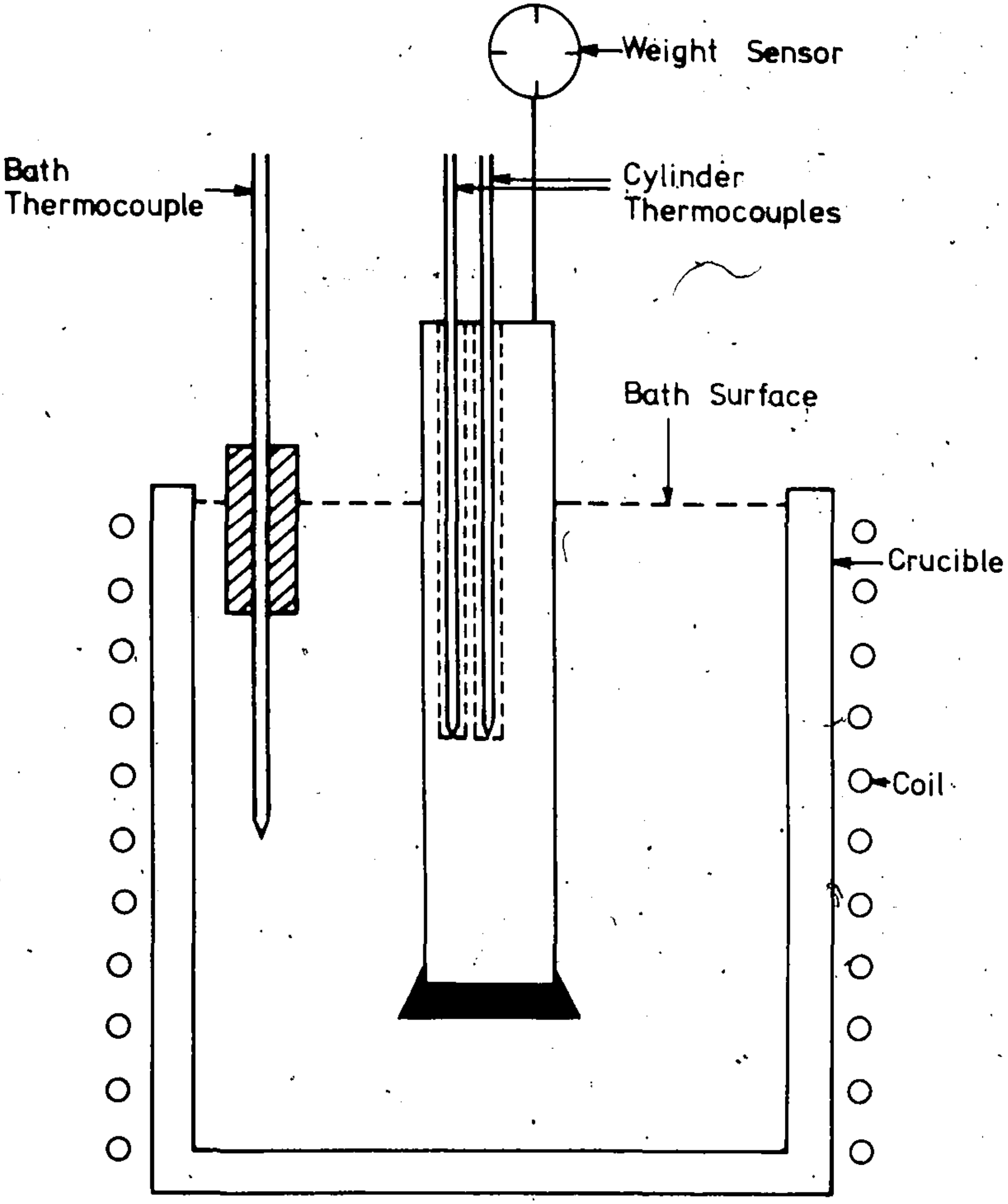

Figure 3.7 Schematic representation of induction furnace cross section with bath and two cylinder thermocouples and the weight sensor.

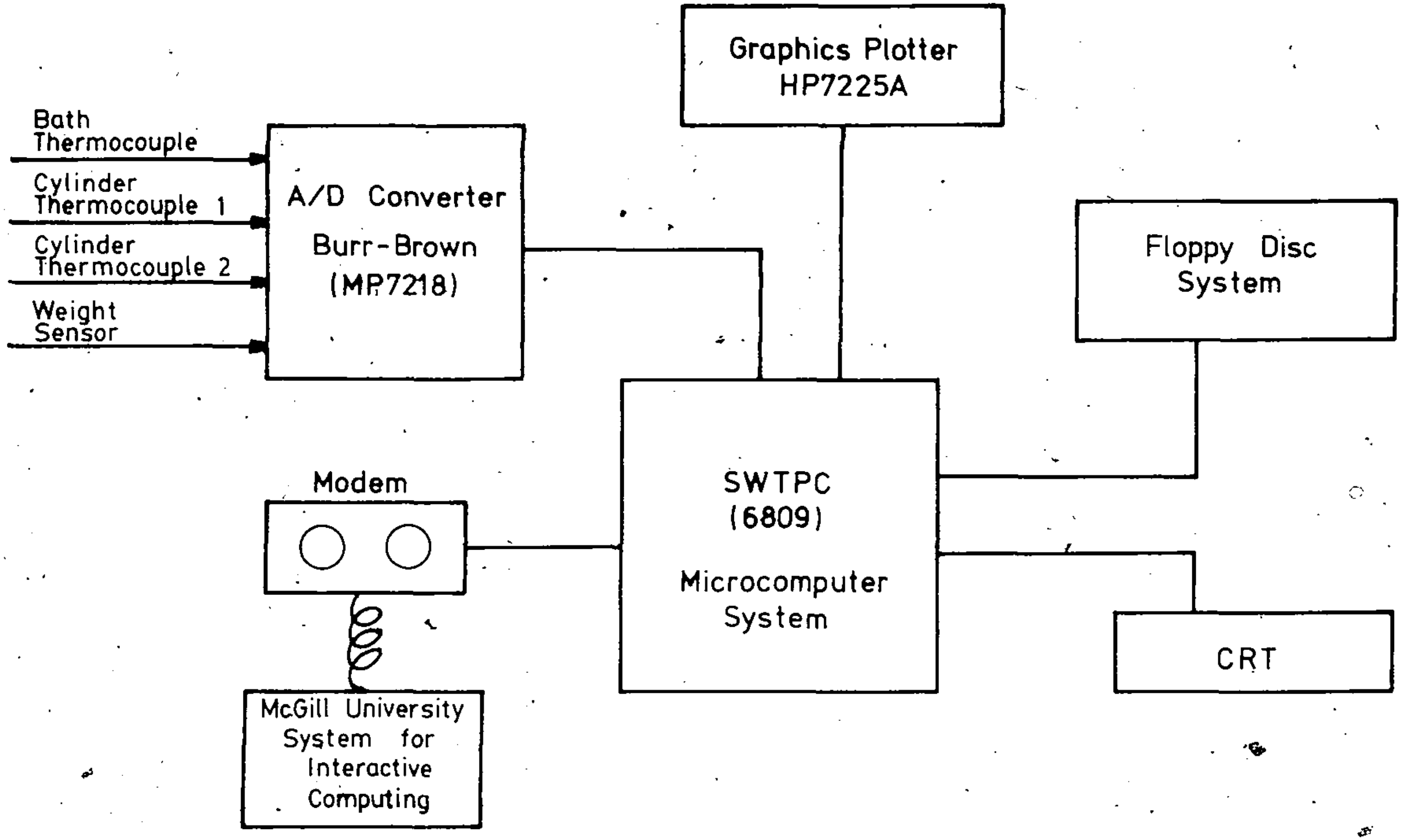

Figure 3.8 Schematic layout of the data acquisition system.

Figure 3.9 A) Microprocessor, A/D converter, floppy disk.
B) Plotter, CRT, Model M.

3.3.1 Hardware Aspects

The hardware was developed on a Southwest Technical Products Corporation computer system which uses the SS-50 bus system. The following boards were used in this computer system:

a) The MP-09 processor board. It consists of the Motorola MC6809 processor, ROM monitor, memory management system and buffering circuits;

b) Three memory boards - 32K, 16K and 8K respectively. The total number of RAM Memory is 56K;

c) Three serial interface boards MP-S;

d) One Interrupt timer MP-T board;

e) The DMAF2 Controller board;

f) A bus extension board used to bring the SS-50 bus signals to the analogue input microperipheral board.

Figure 3.10 depicts an overview of these boards. As the measured parameters are in analog form, a translator was needed to convert them into a digital form suitable for computer processing. For this purpose, a BURR-BROWN analog input microperipheral board (MP7218) was used. This microcomputer analog input system is contained on a single printed circuit board which is treated as a memory by the CPU.[101] Figure 3.11 shows this analog input board.

The board includes a 25 V input overvoltage protection, an analog multiplexer, a high gain instrumentation amplifier

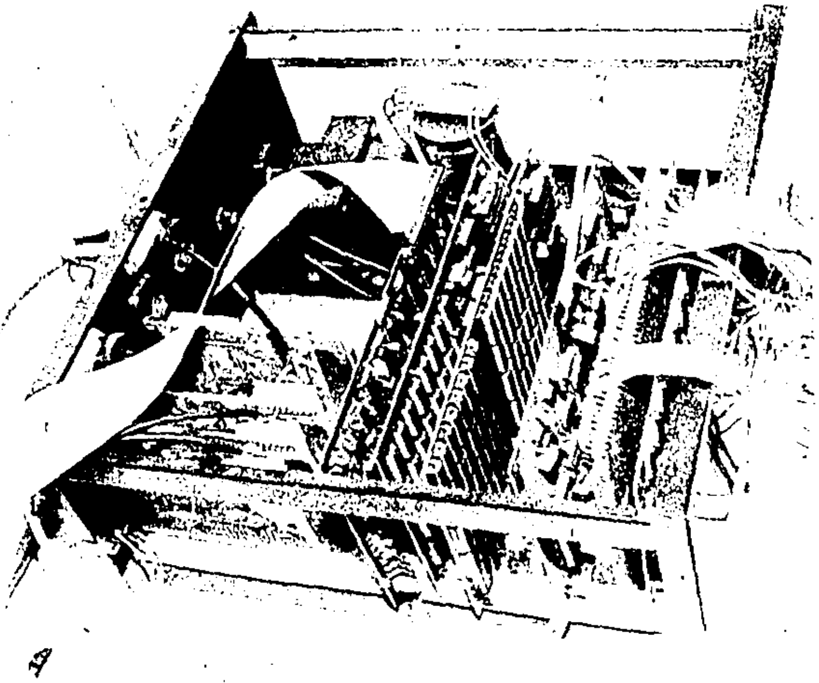

Figure 3.10 An overview of the boards of the microprocessor.

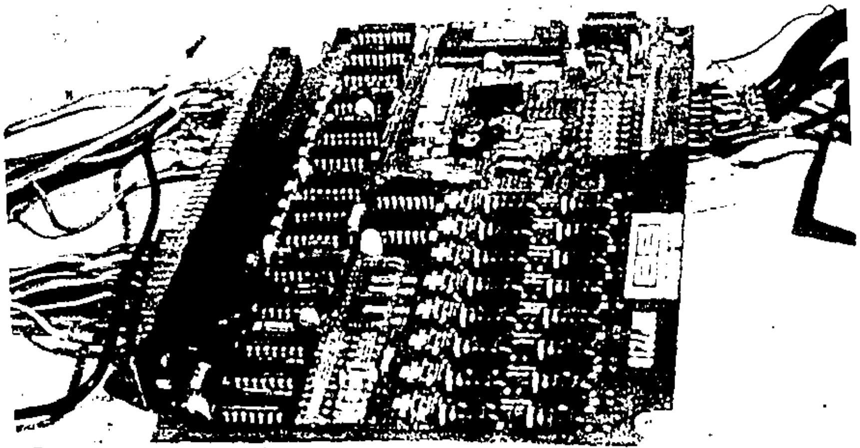

Figure 3.11 The analog input board with the A/D converter.

and a 12-bit analog to digital converter with the necessary timing, decoding and control. The analog digital converter employs the successive approximation technique. As the analog digital converter output is a 12-bit word, two 8-bit memory locations are needed for each channel. Address bits A15-A5 select the board and A4-A1 select the analog input channel to be digitized. The polling mode is used for the A/D operation. To start a conversion, the board is written using a STORE (STA) instruction. The analog input board is jumper configured so as to operate at any memory location. For this microcomputer system, the board was configured to be at location $E020_{16}$. Figure 3.12 shows the MOTOROLA assembler statements which are needed in order for the computer to perform an analog-to-digital conversion. The range of the analog input board is jumper selectable and was set at ±2.5 V. By increasing the gain of the operational amplifier by a factor of 100, the analog input board was capable of measuring the range of ±25 mV. The resolution of analog to digital conversion for the ±25 mV analog input level is ±12μV.

The interfacing of the analog input board with the microcomputer was carried out using an extension board and an 86-pin PC edge connector (SAE-43D/1-2). The signals which are required for the analog input board are supplied from the SS-50 bus. Two of them (VMA and ϕ2) are inverted in the SWTPC bus. In order to make them compatible with analog

```
   STA A $E020
      after a convert command
      is issued, the computer is not
      allowed, by software
      control, to read the board
      for 50 microseconds
CC LDA A $E020
   BIT A #$10
   BEQ   CC
    LDA B $E021
    STD   0,X++
```

Figure 3.12 MOTOROLA assembler statements which are needed in order for the computer to perform an analog-to-digital conversion.

input board requirements, external logic was used with an X inverter. In addition to this, the analog input board requirements have very small tolerance. Consequently, because the +12 V and -12 V power lines of the SWTPC system were not regulated, regulators were incorporated into the present system.

In order to increase the storage capability and the speed of data transfer, an SWTPC DMAF-2 floppy disk was connected to the computer system. This floppy disk system can accommodate two double sided and double density 8" diskettes and each diskette has storage capability of 970 K (bytes). The FLEX 9.0 operating system[102] was used in order to control all the floppy disk operations directly from the user's terminal.

A Hewlett-Packard 7225A graphics plotter, having the 17603A personality module was interfaced with the microcomputer system. The standard RS-232-C interface cable and the hardwire handshake mode of operation were used for this interface.

The microcomputer system was interfaced with the central computing facility of the McGill University System for Interactive Computing (MUSIC). The MUSIC system is supported by the large AMDAHL V7 computer. Using this interface, any type of file can be transferred from the system diskette to MUSIC input file and vice-versa.

3.3.2 Software Aspects

A real-time software package was developed for the set of experiments described above. This software was written in MOTOROLA 6809 Assembler language. It was written so that, when running, they operated in a conversational mode allowing easy usage for neophyte terminal operators. The software package, called KINET, was used for monitoring the dissolution kinetics of solids in liquid steel. The flow chart for this program is given in Figure 3.13. As seen, eight steps are included. In the first step, the program requests the immersion time (i.e. the length of time that measurements are to be recorded), then the frequency of measurements per second. Following this, the steel bath temperature (°C), below which measurements will start is requested. The program then calls for the number of channels to be scanned (i.e. the number of input analog signals to be monitored). Finally, the program checks with the user that the above data have been entered correctly, looping back or proceeding, as appropriate. The program finally determines whether the user wishes to wait. If not, the system starts monitoring bath temperatures every tenth of a second. Once this falls to that specified, the computer informs, with the message 'Time for immersion when you are ready press R'. Before the cylinder is immersed in the molten steel, the user presses R and scanning starts. At the end of scanning, the computer prints the location for the first and last BYTE of data.

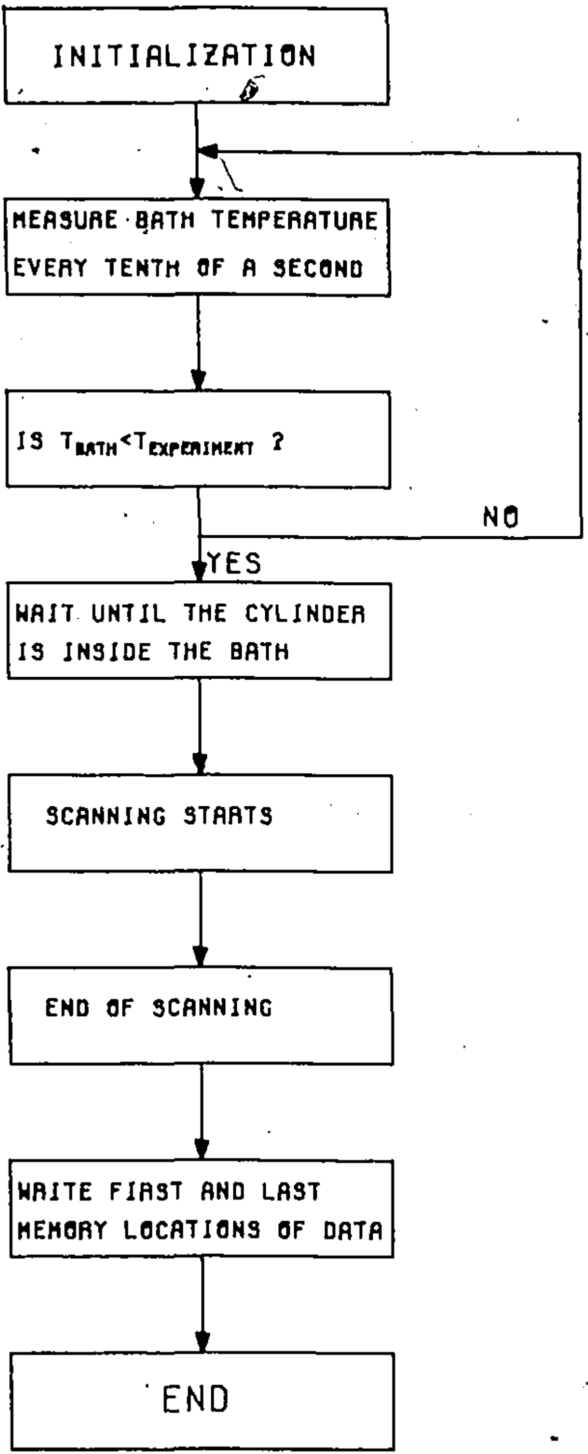

Figure 3.13 Flow chart of the program KINET.

Figure 3.14 shows a typical conversational session. The experimental results could be transferred either to floppy disk or to a disk file of McGill's large computer equivalent to the AMDAHL V7. Finally, the retrieval and conversion of raw data was carried out using a simple FORTRAN program. The software for the Hewlett-Packard 7255A Graphics Plotter was developed in BASIC high level language. An assembler listing of program KINET along with the generated code is given in Appendix IV.

In addition to the above mentioned software, another software package has been developed which enables the user of this system to monitor solidification rates of ingots. Full details about this software package are presented in reference 104.

3.3.3 Calibration of Analog to Digital Converter

Calibration was performed by connecting a precision voltage source to channel zero. A Leeds Northrup 8691-2 millivolt potentiometer was used as a voltage source. The output voltage was measured with a 8810A digital voltmeter made by FLUKE. The offset and gain adjustments were made while applying the voltages -24.994 mV and +24.981 mV, respectively. The offset adjustment is made first by using the appropriate offset calibration voltage and the program OFFSET which is listed in Appendix IV.

```
INSERT IMMERSION TIME IN SECONDS
60
INSERT NUMBER OF MEASUREMENTS PER SECOND
10
INSERT BATH TEMPERATURE IN DEGREES CELSIUS
1600
HOW MANY CHANNELS ARE GOING TO BE SCANNED ?
3
IS THE ABOVE DATA CORRECT ?
NO
INSERT IMMERSION TIME IN SECONDS
60
INSERT NUMBER OF MEASUREMENTS PER SECOND
10
INSERT BATH TEMPERATURE IN DEGREES CELSIUS
1620
HOW MANY CHANNELS ARE GOING TO BE SCANNED ?
8
IS THE ABOVE DATA CORRECT ?
Y
DO YOU WANT TO WAIT ?
N
TIME OF IMMERSION NOW

WHEN YOU ARE READY , PRESS R
R
END OF SCANNING

FIRST DATA WAS STORED AT 0000

LAST DATA WAS STORED AT  2581
```

Figure 3.14 Typical conversational session.

The OFFSET calibration program was loaded to the memory and run. After 100 conversions the program was halted at the breakpoint and the contents of the accumulator B was 32_{16}. If a difference of more than 10_{16} was present then the offset trimmer resistor would have been slightly readjusted and the program restarted again. This procedure was repeated again until the contents of the accumulator were within 10_{16} of each other. The gain adjustment was made in much the same manner using the proper gain calibration voltage and the program GAIN which is listed in Appendix IV.

3.3.4 Calibration of Interrupt Timer

The actual oscillator frequency of the Interrupt Timer was adjusted by trimming the capacitor C4.[103] A HP model 5340A electronic counter was used as an accurate time base for this calibration. The actual count output of the oscillator was taken from pin 10 of IC3.[103]

In order to check the accuracy of the generating IRQ interrupts from the interrupt timer board over long periods of time, a program was written which accepts and displays hours, minutes, seconds and tenths of a second in a 24 hour format on the control terminal of the computer system. The program works by first allowing the operator to enter the correct time. The MP-T interrupt timer board is configured for a tenth of a second maskable interrupts, and each time an interrupt is generated the program updates and displays the new time. Running this program for long periods of time, the accuracy of interrupt timer was verified.

3.3.5 Signal Conditioning

An electrical noise problem was encountered when the gain of the operation amplifier of the analog input board was set to 100. On thorough testing, this noise was found to be normally distributed and could be eliminated by monitoring, and subsequently averaging, 128 or 256 samples for each data point. The former sampling was compatible with the requirements of scanning at least four input channels every one tenth of second while the latter one was compatible with requirements of scanning three input channels every one tenth of a second.

During the operation of these experiments in the high frequency induction furnace, significant noise was introduced despite the use of shielded cables to the thermocouples. This noise was modulating as an AC signal and consequently demodulation and filtering took place. A network of low-pass filters designed and built for each channel was found to have excellent response to low-frequency signals and at the same time provided a great deal of attenuation at high frequencies. A schematic layout of a low pass filter is presented in Figure 3.15. For this filter network the cut-off frequency may be computed as follows:

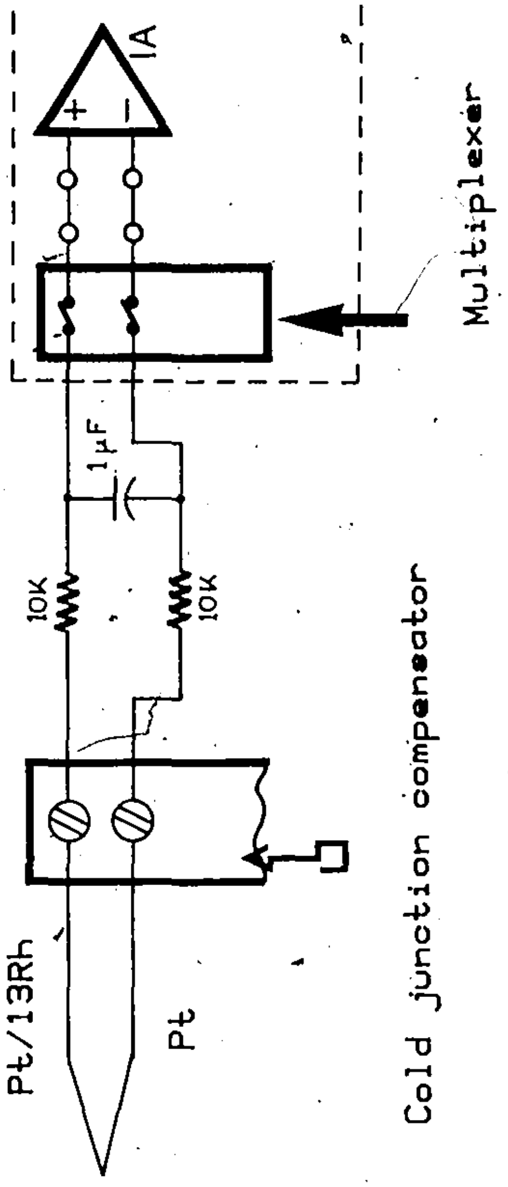

Figure 3.15 Schematic layout of a low pass filter.

$$f = \frac{1}{2\pi RC}$$

where C: size of capacitor in farads;

R: resistance in ohms;

f: the cut-off frequency in Hz above which signals are effectively eliminated.

The noise was reduced to a tolerable level by using a resistance of 10K and capacitance of 1μF. The cut-off frequency of this low-pass filter was 15.9 Hz. Signals of higher frequency were largely eliminated. The filter was placed very close to the analog input board.

3.4 PROCEDURE FOR CYLINDER IMMERSION TESTS

Once the steel bath chemistry had been correctly adjusted and the bath thermocouple had been immersed into the steel bath, the temperature of the steel bath was brought up 20 to 30 K above the specified temperature. The power to the induction furnace was then switched off and the data acquisition started to measure the steel bath temperature. When this temperature was lower or equal to the specified bath temperature, a message was issued on the terminal 'Time of immersion now when you are ready, press R'. The apparatus which carried the load cell was then brought to the top of the steel bath and scanning of the specified channels started a few seconds prior to immersion. When the message 'End of scanning' appeared on the terminal the remaining portion of the cylinder was withdrawn from the steel bath and removed from the load cell.

3.5 INDUCTION HEATING OF COMPOSITE SAMPLES

In order to produce a steel-titanium interface, small cylindrical samples 2.54 cm in diameter and 1.5 cm long were machined and pressed tightly together. Figure 3.16 shows a schematic cross-section parallel to the cylinder vertical axis. A small hole with a diameter of 3 mm was then drilled through the iron up to iron-titanium interface. The composite sample was placed in the induction coil and through it, thermocouple wires were passed until the hot junction met the steel-titanium interface. Figure 3.17 shows the composite sample placed in an induction coil with a thermocouple at the steel-titanium interface.

The composite sample was then heated up inductively and the temperature-time history of the interface was recorded with the data acquisition system described. The electrical noise problem from the induction coil was eliminated by monitoring and subsequently averaging 512 samples for the thermocouple every tenth of a second. A modified version of program KINET was used for this type of experiments.

3.6 CHEMICAL ANALYSIS

The carbon analysis was done with an IR12 carbon analyser manufactured by Leco Corporation. The analyser operates on the principle of oxidizing an inductively melted sample placed in an oxide crucible by passing a stream of pure oxygen over it. The CO_2 thereby produced is analyzed in the oxygen stream by means of a luft cell whose electric signal was electronically

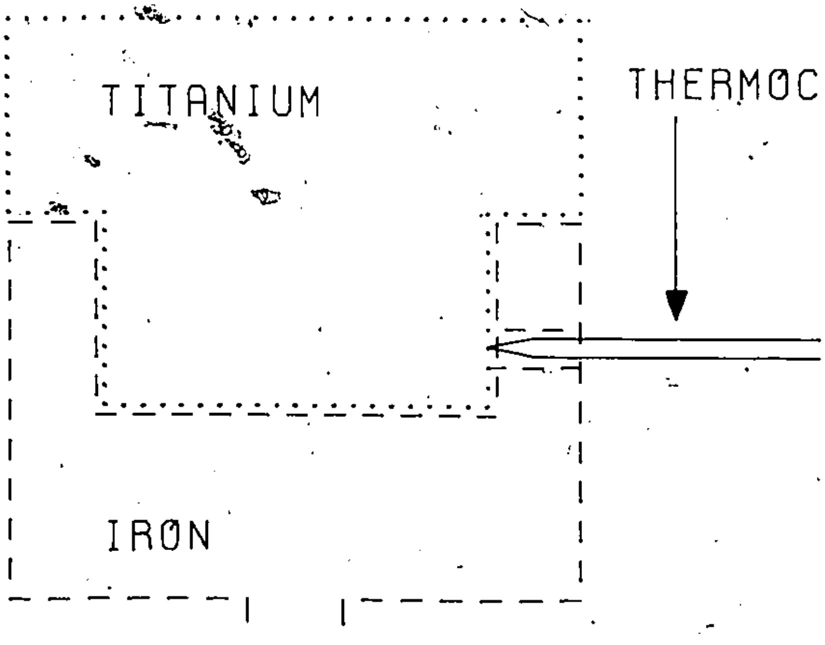

Figure 3.16 Schematic cross-section of the composite sample parallel to the cylinder vertical axis.

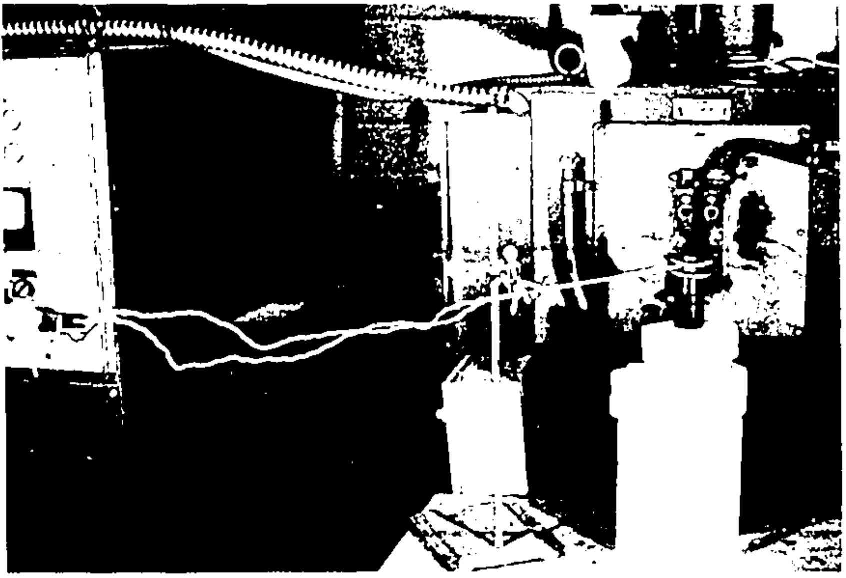

Figure 3.17 Composite sample placed in an induction coil.

integrated so as to give digital carbon weight percent readings.

The oxygen analysis was performed with a Leco RO-17 oxygen determinator. It used the inert gas fusion method. The sample was placed in a previously heated degassed graphite crucible. The crucible was resistance heated to a sufficiently high temperature for the sample to melt. The oxygen in the sample was converted to CO which is analyzed in a luft cell.

The iron, titanium and aluminum analysis was done using wet analytical methods. The samples were treated with aqua regia in order to dissolve their metal contents. The solutions were then diluted and atomic absorption was performed using a Pye-Unican Spectrophotometer SP 190.

In a few samples spectrographic analysis was performed at Sidbec-Dosco in Contrecoeur, Quebec, and iron and titanium wet analysis at QIT, Sorel, Quebec.

CHAPTER 4

MATHEMATICAL MODEL

The mathematical model described in the present text has been developed to predict heat and mass transfer events which occur when a high melting point additive is held motionless below the surface of a steel bath. A cylindrical shaped object was chosen in order to take advantage of prescribed or known heat transfer coefficients reported in the literature for cylinders. Since temperatures within the main body of the cylinder are affected mainly by heat entering in a radial direction from the bath, conduction up through the bottom surface has been ignored. Consequently, the mathematical modelling work presented in this thesis refers to a one dimensional model. The explicit finite difference method was employed to solve the set of steady state differential heat transfer equations and accompanying boundary conditions and equations.

4.1 GENERAL EQUATIONS OF THE MODEL

For an isotropic material, the heat conduction equation may be written in cartesian coördinates as:

$$\alpha\left[\frac{\partial^2\theta}{\partial x^2} + \frac{\partial^2\theta}{\partial y^2} + \frac{\partial^2\theta}{\partial z^2}\right] + \frac{\dot{q}'''(x,y,z)}{\rho\, C_p} = \frac{\partial\theta}{\partial t} \qquad (4.1)$$

where

C_p: heat capacity

ρ: density

k: thermal conductivity

$\alpha = \frac{k}{\rho\, C_p}$: thermal diffusivity

$\dot{q}'''$: heat generation per unit volume

For a cylindrical coordinate system, the spatial variables are the radial distance r, the axial distance z, and the angle ψ. These variables are related to x, y, z as:

$$x = r \cos\psi$$
$$y = r \sin\psi$$
$$z = z$$

Using these relationships equation (4.1) may be written as:

$$\frac{\partial^2 \theta}{\partial r^2} + \frac{1}{r}\frac{\partial \theta}{\partial r} + \frac{1}{r^2}\frac{\partial^2 \theta}{\partial \psi^2} + \frac{\partial^2 \theta}{\partial z^2} + \frac{\dot{q}'''(r,\psi,z)}{k} = \frac{1}{\alpha}\frac{\partial \theta}{\partial t} \qquad (4.2)$$

In the absence of heat conduction in the axial direction, $\partial\theta/\partial z = 0$ and $\partial^2\theta/\partial z^2 = 0$. If in addition, the heat flow is symmetrical with respect to the angular component, ψ (i.e. conditions at r and z, uniform and independent of ψ). Equation (4.2) reduces to:

$$\frac{\partial^2 \theta}{\partial r^2} + \frac{1}{r}\frac{\partial \theta}{\partial r} + \frac{\dot{q}'''(r)}{k} = \frac{1}{\alpha}\frac{\partial \theta}{\partial t} \qquad (4.3)$$

Finally, without any heat generation, this general equation simplifies to that for transient, radial conduction of heat in a cylinder:

$$\frac{\partial^2 \theta}{\partial r^2} + \frac{1}{r}\frac{\partial \theta}{\partial r} = \frac{1}{\alpha}\frac{\partial \theta}{\partial t} \qquad (4.5)$$

or

$$\frac{\partial \theta}{\partial t} = \frac{\alpha}{r}\frac{\partial}{\partial r}\left(r\frac{\partial \theta}{\partial r}\right) \qquad (4.5)$$

Figure (4.1) presents a typical set of circumstances existing during the growth and melt back of a steel shell on a cylindrical additive immersed in liquid steel. The diagram represents a schematic cross section perpendicular to the cylinder's vertical axis. Appropriate expressions for transient conduction in the solid additive and the steel shell are therefore:

Solid additive:

$0 \leq r \leq r_1^*$, $0 \leq t < t_{total}$

$$\frac{\partial \theta}{\partial t} = \frac{\alpha_s}{r}\frac{\partial}{\partial r}\left(r\frac{\partial \theta}{\partial r}\right) \qquad (4.6)$$

Solid steel shell:

$r_1^* \leq r \leq r_2^*$, $0 \leq t \leq t_{total}$

$$\frac{\partial \theta}{\partial t} = \frac{\alpha_{Fe}}{r}\frac{\partial}{\partial r}\left(r\frac{\partial \theta}{\partial r}\right) \qquad (4.7)$$

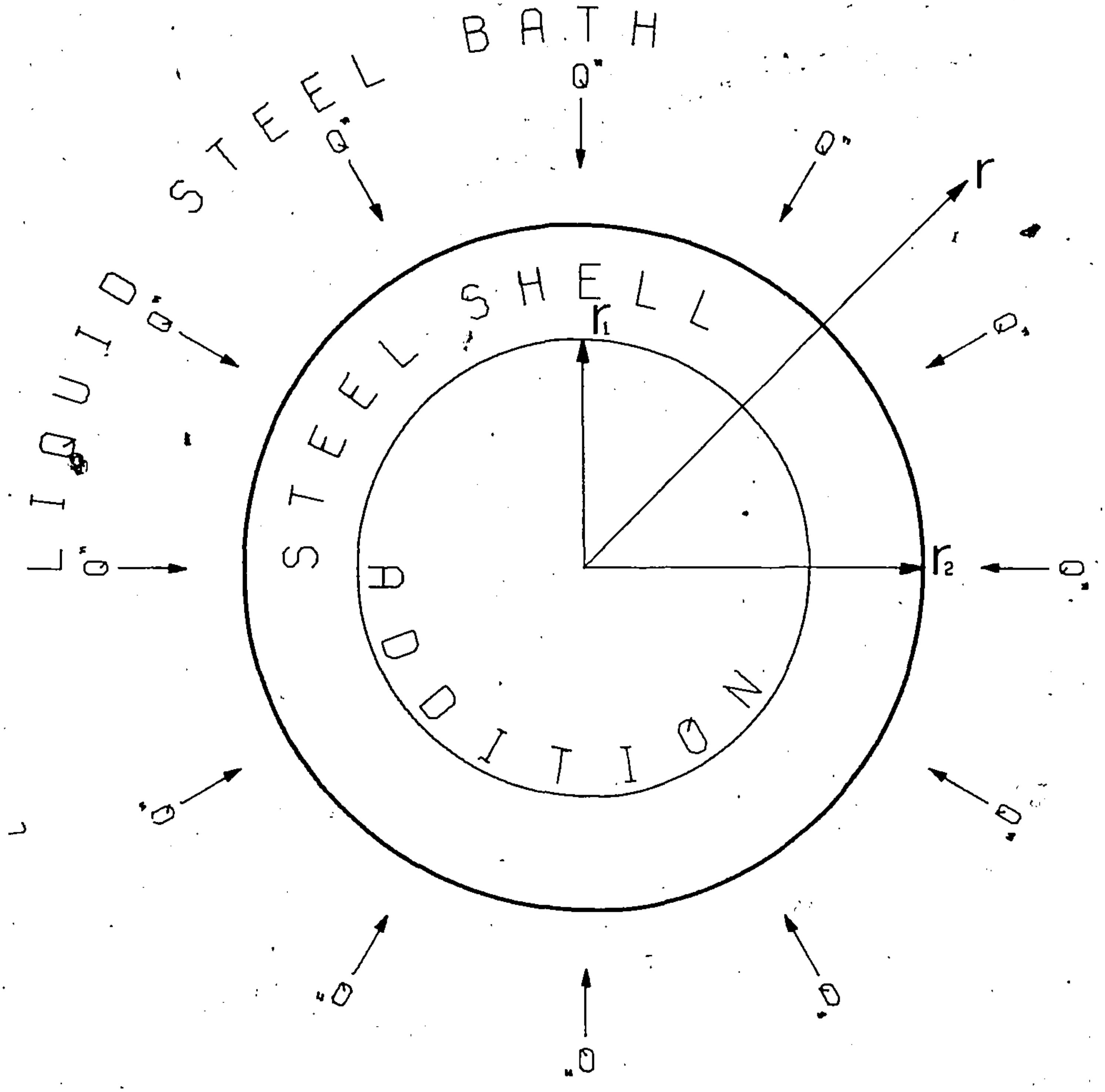

Figure 4.1 Schematic representation of typical melting situation denoting the various interfaces and coordinate systems used in the mathematical model.

For titanium, when the steel shell/titanium interface exceeds a certain threshold temperature, an exothermic reaction is initiated. This phenomenon can be represented (in its most simple form) through a constant heat generation term at the inner steel shell interface, together with associated erosion of the steel shell. This erosion is caused by a constant flux of dissolved titanium, supplied through dissolution of the titanium core. Figure 4.2 presents these phenomena in schematic form.

4.2 INITIAL CONDITIONS

Prior to immersion, the temperature of the cylinder is taken to be uniform at θ_0 and the radius of the cylinder is denoted by r_1^*. Expressing the above conditions mathematically

$$t = 0 \quad \text{and} \quad 0 \leq r \leq r_1^*$$

$$\theta = \theta_0 \tag{4.8}$$

The bulk temperature is taken to be constant prior to immersion:

$$t = 0 \quad \text{and} \quad r > r_1^*$$

$$\theta = \theta_B \tag{4.9}$$

Finally, at time $t = 0$

$$r = r_1 = r_2 \tag{4.10}$$

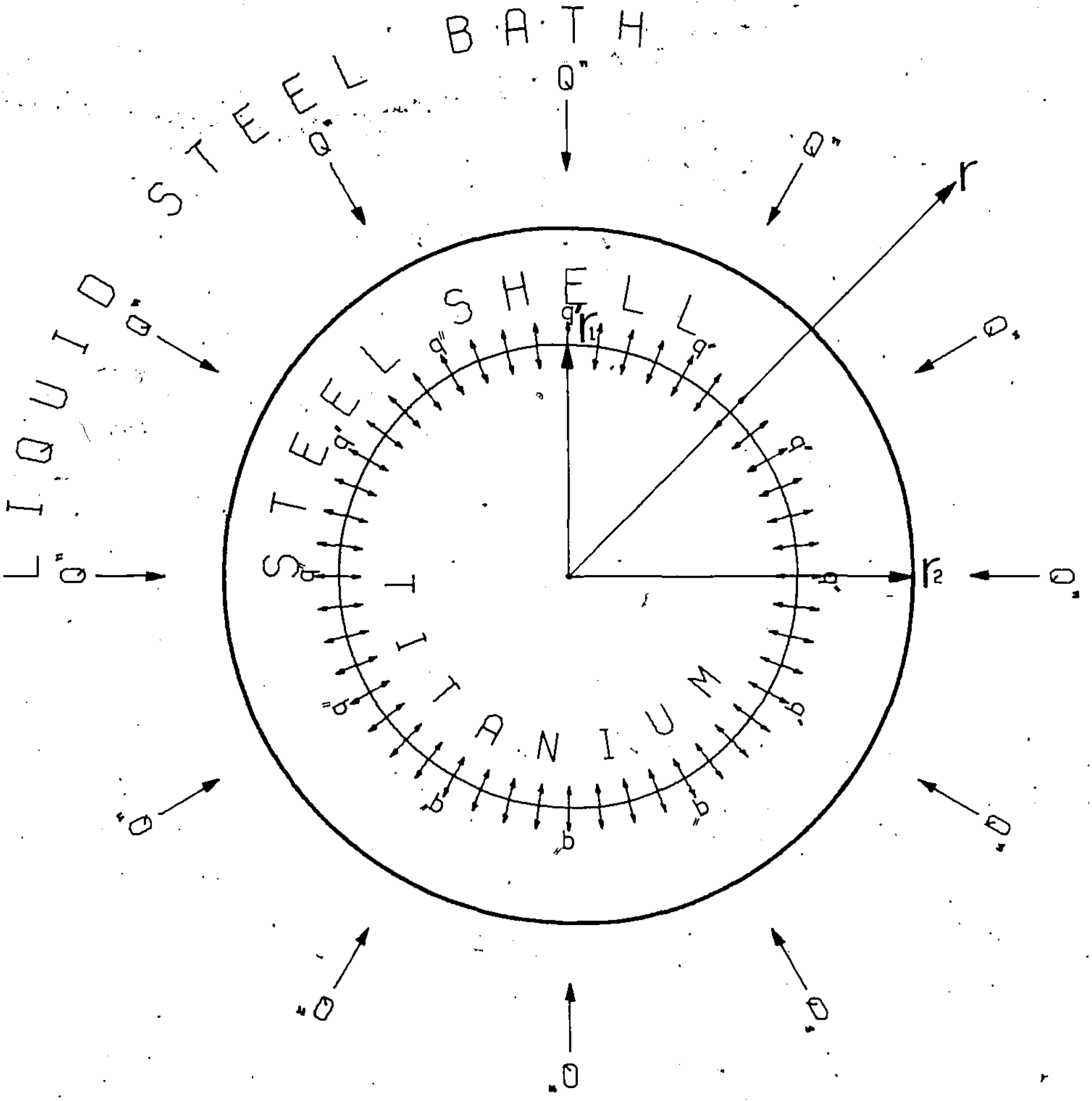

Figure 4.2 Schematic cross section of a dissolving titanium cylinder showing positions, boundaries, and coordinate system chosen for developing the mathematical model.

4.3 BOUNDARY CONDITIONS

In writing boundary conditions, these have been listed in a systematic way starting at the cylinder's centre and time zero and proceeding radially outwards towards the liquid steel bath. Since the phenomena occurring during the dissolution of titanium in molten steel are quite complex, it was decided to present the boundary conditions in two different sections: the first for titanium and the second for vanadium.

4.3.1 Boundary Conditions and Equations for Titanium

As the radial heat flow is assumed to be symmetrical about the cylinder's central axis, the net heat flux at this axis must be zero:

$$\forall t, \quad 0 \leq t \leq t_{total}, \quad r = 0$$

$$\frac{\partial \theta}{\partial r} = 0 \tag{4.11}$$

The interfacial heat fluxes prior to the exothermic reaction between the steel shell and titanium can be taken equal:

$$0 < t < t_R, \quad r = r_1$$

$$-K_{Fe} \frac{\partial \theta}{\partial r} = -K_s \frac{\partial \theta}{\partial r} \tag{4.12}$$

The difference in temperature between the inner surface of the steel shell and the surface of the titanium cylinder depends on R_T, the interfacial thermal resistance.

$$0 < t < t_R, \quad r = r_1$$

$$\dot{q}'' = \frac{\theta^*_{Fe} - \theta^*_s}{R_T}, \tag{4.13}$$

Perfect thermal contact is established at r_1, once a eutectic liquid of iron and titanium has formed ($\theta^* > 1090$°C or 1363 K) at times greater than t_R:

$$t_R < t < t_{total}, \quad r = r_1 \tag{4.14}$$

$$R_T = 0, \quad \theta^* > 1363 \text{ K}$$

When the exothermic reaction starts, the difference between heat fluxes into and out of the interface or reaction zone must be balanced by the heat flux generated from the exothermic reaction. Making the approximation that this zone be treated as acting as the original iron/titanium interface, one can write:

$$t_R \le t \le t_{total}, \quad r = r_1$$

$$-K_{Fe} \frac{\partial \theta}{\partial r} + \dot{N}''_{Ti} \, \dot{Q}''_{Gen} = -K_{Ti} \frac{\partial \theta}{\partial r} \tag{4.15}$$

The temperature at the interface between the steel shell and the liquid steel is constant and equal to the melting point of the steel bath.

$$\forall t, \quad 0 < t < t_{total}$$

$$r = r_2$$

$$\theta = \theta_{M.P.Fe} \tag{4.16}$$

The difference between the heat fluxes from the bulk liquid steel to the interface at r_2, and from this interface into the body of the steel shell is used to freeze or to melt the solid shell. The relevant mathematical statement is thus equation (4.17):

$$\forall t, \quad 0 < t < t_{total}, \quad r = r_2$$

$$\left(K_{Fe} \frac{\partial \theta}{\partial r}\right)_{Fe,shell} = \rho_{Fe} L_{Fe} \frac{\partial r}{\partial t} + \dot{q}''_{conv} \tag{4.17}$$

The heat flux, $\dot{q}_{conv}$, which was used in equation (4.17) will depend on the heat transfer coefficient as well as the temperature 'driving force':

$$\dot{q}''_{conv} = h(\theta_{Bath} - \theta_{M.P.Fe}) \tag{4.18}$$

The mass transfer phenomena occurring at the inner steel shell wall at $r = r_1$ can be expressed by the following:

$$\dot{N}''_{Ti} = K_{Ti}(C_{Fe/Ti} - C_{Ti}) \qquad (4.19)$$

Finally the temperature of the steel bath far from the steel shell can be regarded as being constant:

$$\forall t, \quad 0 < t \leq t_{total}$$

$$r \to \infty, \quad \theta = \theta_{bath} \qquad (4.20)$$

4.3.2 Boundary Conditions for Vanadium

Vanadium follows a more conventional route during steel shell formation and melt back. In this case, there is no exothermic triggering mechanism at the steel shell/ vanadium interface and no equations equivalent to equations (4.14), (4.15) and (4.19). The remaining boundary conditions are applicable, however, during steel shell formation and melt back.

$$\forall t, \quad 0 < t < t_{total} \qquad (4.21)$$

t_{total} is the time during which a frozen steel shell surrounds the addition.

4.4 NUMERICAL MODEL

As the set of partial differential equations (4.6) and (4.7) is too complex for analytical solutions with such boundary conditions, numerical procedures were employed to predict shell thickness, melting rates, etc. as a function of time. The explicit numerical technique was employed for solving the set of partial differential equations and boundary conditions just described.

4.4.1 Assumptions Involved

The technique of numerical integration involves certain simplifying approximations. These are discussed in a later section of this chapter. Assumptions in describing the physical phenomena of a cylinder's dissolution/melting were:

(i) Conduction up through the bottom surface was ignored. Thus temperatures in the main body of the cylinder are affected only by heat entering in a radial direction from the bath.

(ii) The heat transfer was taken to be symmetrical about the cylinder's axis (i.e. slight variations with respect to length are ignored.)

(iii) The immersion of the ferro-alloy cylinder in the liquid steel is assumed to take place instantaneously.

(iv) The cylinder maintains its outer physical dimensions during the freezing and melting process involved (i.e. variations of density were neglected).

(v) The material within each elemental volume or node was assumed to have uniform temperature and thermophysical properties.

(vi) The temperature of the solid-liquid steel interface was constant during the freezing or melting process of steel shell.

4.4.2 Formulation of the Numerical Equations

In order to set up the relevant numerical equations for the solution of the heat transfer problem, it was decided to consider a typical section of the cylinder as shown in figure 4.3. As seen, the section was considered to be composed of equally spaced elemental volumes with nodal points located at their centres. The central nodal point located on the cylinder's axis was designated as number 1, and successive points as 2, 3, 4, etc. The cross-sectional area, A_1 refers to the surface area located halfway between nodal points 1 and 2, and the volume V_1 to the volume of the segment bounded by the cylinder's axis and the surface A_1. Similarly, volume V_2 refers to the volume of the segment bounded by surfaces A_1 and A_2. Thus for the diagram shown in figure 4.3, subtending an angle ψ of 1 radian and of unit length above the cylinder's axis, the relevant cross-sectional area A_1 and volume V_1 are given by:

$$A_1 = \frac{Dx}{2}, \quad V_1 = \frac{Dx^2}{8}$$

Similarly, the cross-sectional area A_2 and volume V_2 are given by:

$$A_2 = \frac{3Dx}{2}, \quad V_2 = Dx^2$$

In general, the cross-sectional area A_N and volume V_N are given by:

DIAGRAM OF HEAT TRANSFER MODEL SHOWING LOCATION OF NODAL POINTS

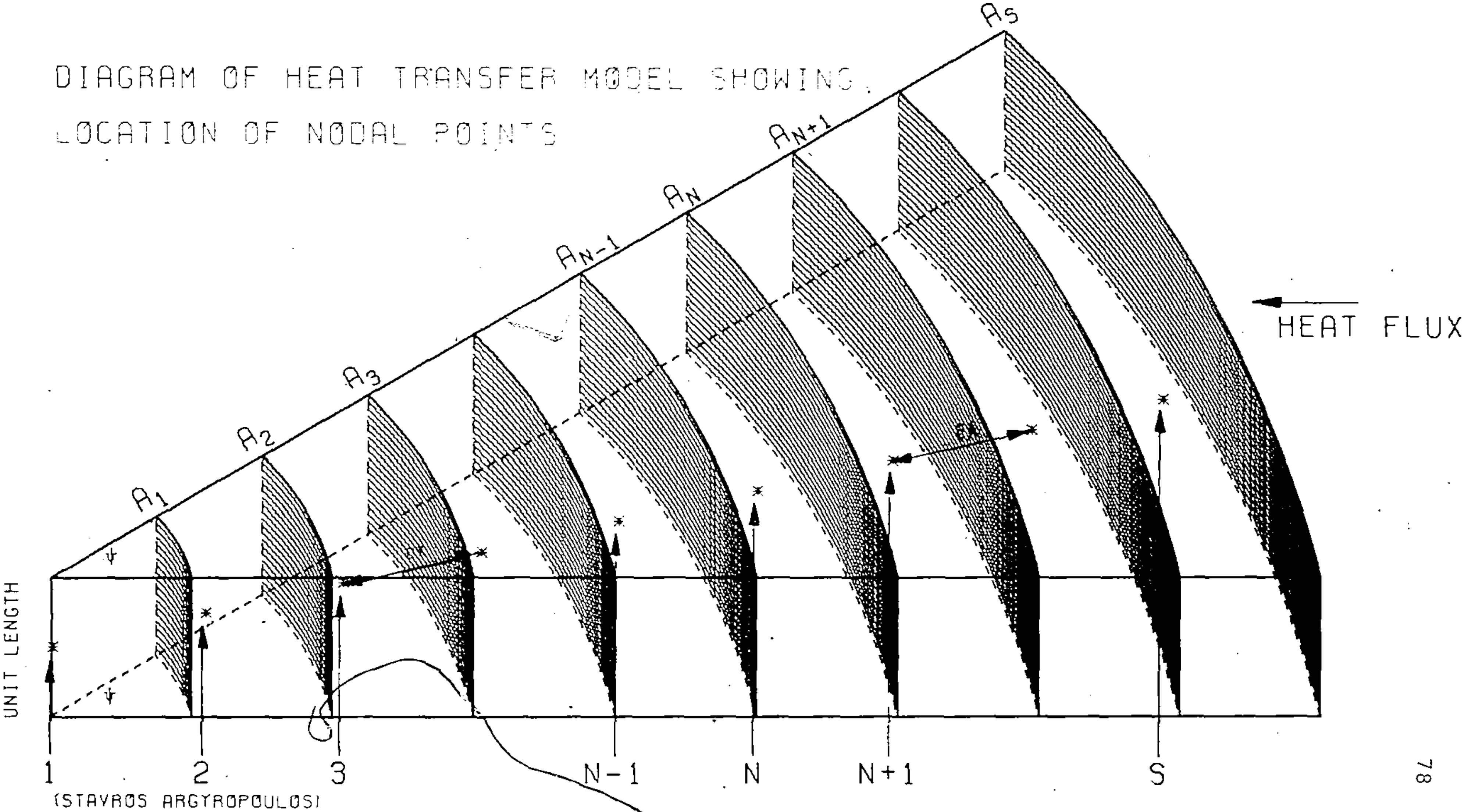

(STAVROS ARGYROPOULOS)

Figure 4.3

$$A_N = \frac{(2N-1)Dx}{2}, \quad V_N = (n-1)Dx^2$$

$$\forall N, \quad N \geqslant 2$$

Thus, writing a heat balance for nodal point N for unsteady-state heat conduction between N and two adjacent nodal points' (N+1) and (N-1) yields the general equation:

$$\theta'_N = \theta_N\{1-M(\frac{2N-1}{2N-2}) - M(\frac{2N-3}{2N-2})\} + M(\frac{2N-1}{2N-2}) \cdot \theta_{N+1}$$

$$+ M(\frac{2N-3}{2N-2}) \cdot \theta_{N-1} \qquad (4.22)$$

where $M = \frac{KDt}{\rho \cdot C_p \cdot Dx^2}$

θ'_N represents the new temperature of nodal point N at time t+δt.

Equation (4.22) is the numerical equivalent of differential equations (4.6) and (4.7) cast in the finite difference explicit form. In Appendix II, equation (4.22) is derived directly from partial differential equations (4.6) and (4.7). As seen, a knowledge of the nodal point temperature at time t allows new nodal point temperatures θ', to be calculated at time t+δt in any region of the cylinder (i.e., addition, steel shell).

The finite difference equation for the central nodal point 1, satisfying boundary condition (4.11) is:

$$\theta_1' = \theta_1(1-4M) + 4M\theta_2 \tag{4.23}$$

Referring to the figure 4.4, let us assume that the solid shell-liquid steel interface at time t is in position A. Let X_t be the distance between the last nodal point N+1 and the liquid-solid steel interface. At time t+δt, the new interface position is given by a dashed line. Then the relevant boundary condition equation (4.17) can be written in finite difference form as follows:

$$\rho_{Fe} \cdot L_{Fe} \cdot \frac{\delta r}{\delta t} = K_{Fe}\left(\frac{\theta_{M.P.Fe} - \theta_{N+1}}{X_t}\right) - h(\theta_{Bath} - \theta_{M.P.Fe}) \tag{4.24}$$

Here, ρ_{Fe}: steel density

L_{Fe}: steel latent heat

K_{Fe}: steel thermal conductivity

h: convective heat transfer coefficient from bath to outer surface of the addition.

When X_t exceeded Dx (radial nodal point distance), a new nodal point was assigned, labelled N+1. The remaining nodes were relabelled, becoming N, etc. Similarly, when δr became negative, the reverse procedure was applied. In the case where a new nodal point was assigned and labelled N+1, the temperature for this new nodal point was calculated, using linear interpolation between the temperature of nodal point N

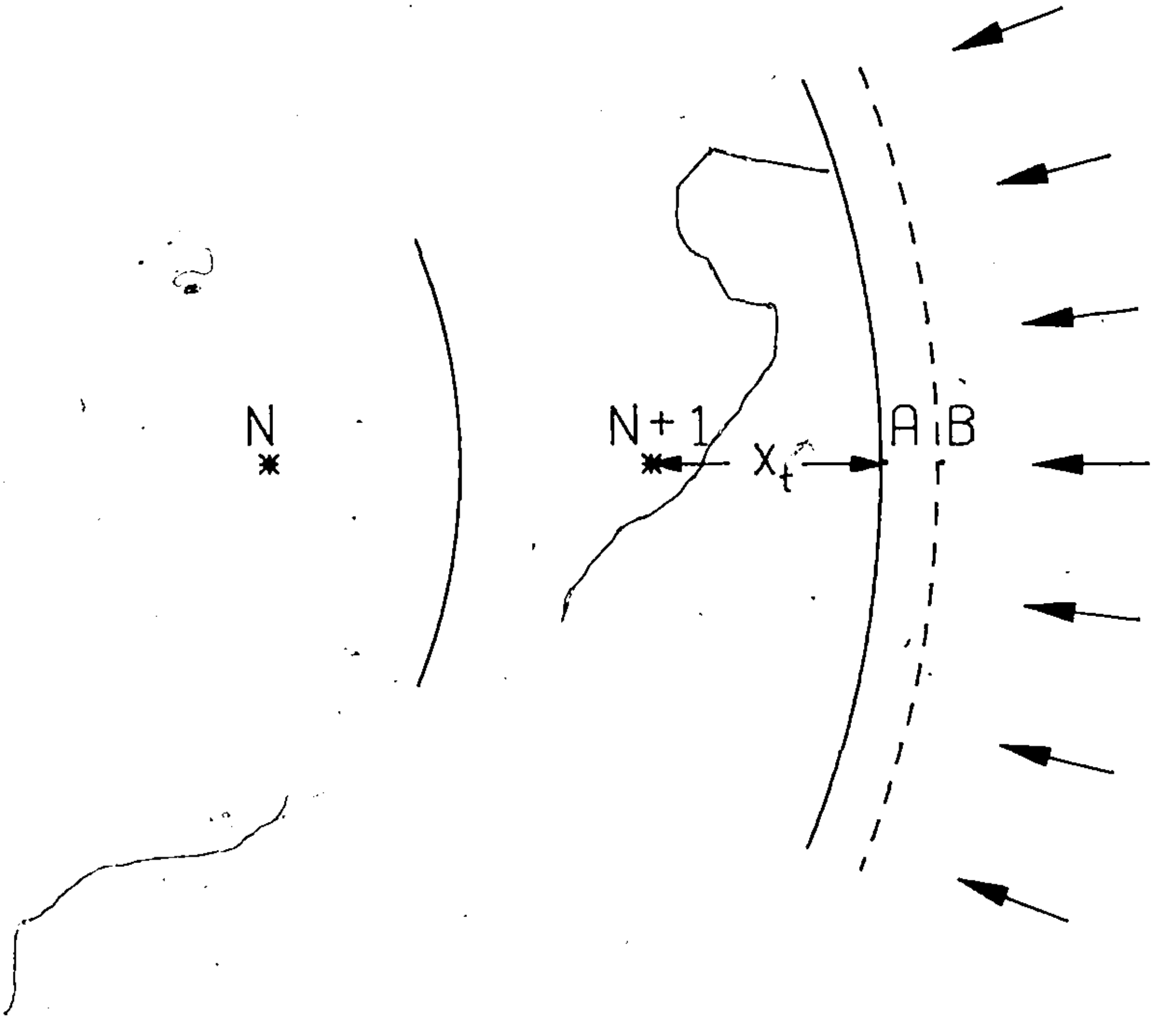

Figure 4.4 Schematic representation of the movement of the steel shell-liquid steel interface X_t is the distance of last nodal point from this interface at time t. The dashed line represents the position for this interface at time t+δt.

and the melting point of steel (temperature of solid-liquid steel interface).

The above notation is illustrated in figure 4.5. The following equation gives the temperature of the newly assigned nodal point, N+1:

$$\theta'_{N+1} = \frac{(\theta_{M.P.Fe} \cdot DLX + X_t \cdot \theta'_N)}{X_t + DLX} \tag{4.25}$$

where θ'_{N+1}: new temperature for new nodal point (N+1)

θ'_N: new temperature for the N nodal point

$\theta_{M.P.Fe}$: steel melting point.

Referring again to figure 4.4 the finite difference equation for the finite element corresponding to nodal point N+1 therefore becomes:

$$\theta'_{N+1} = \theta_{N+1}\left\{1 - \frac{M}{X_t}\,\frac{(2N+1)}{2N}\,Dx - M\,\frac{(2N-1)}{2N}\right\} + M\,\frac{\theta_{M.P.Fe}}{X_t}\,\frac{2N+1}{2N}\,DX + M\,\frac{2N-1}{2N}\,\theta_N \tag{4.26}$$

The M or Fourier Modulus appearing in equations (4.22), (4.23), (4.26) is dimensionless and represents:

$$M = \frac{K \cdot Dt}{\rho \cdot Cp \cdot Dx^2} \tag{4.27}$$

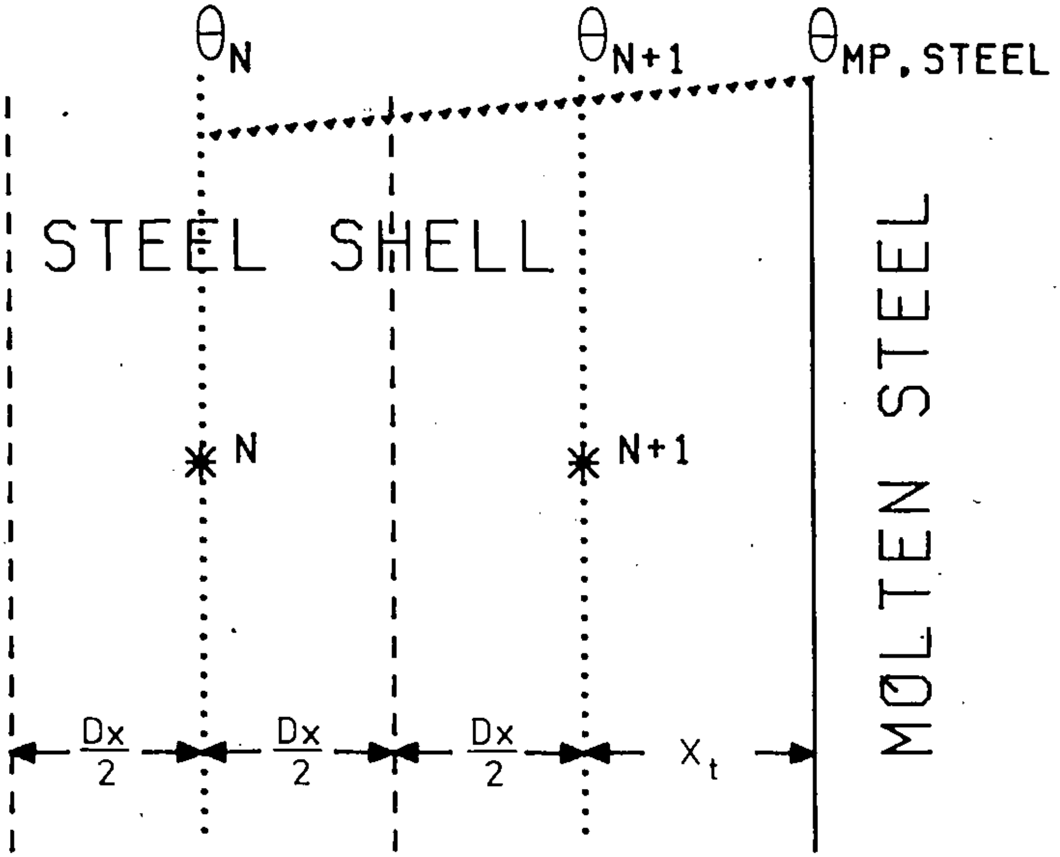

Figure 4.5 Schematic representation of the linear interpolation between the temperature of steel shell-liquid interface $\theta_{M.P.Fe}$ and the temperature of nodal point N (θ_N).

where K: thermal conductivity
ρ: density
Cp: heat capacity at constant pressure
Dx: distance between two adjacent nodal points
Dt: iteration time.

In the case where there is heat generation inside an elemental volume N, this is taken into account through proper modification of the corresponding finite difference equation.

Referring to figure 4.3, let us assume that heat is generated in the nodal point, N, at a rate of $\dot{Q}'''$ per unit volume. Writing a heat balance for nodal point N for unsteady-state heat conduction between N and two adjacent nodal points (N+1) and (N-1) yields the general equation:

$$\theta_N' = \theta_N\{1 - M\frac{2N-1}{2N-2} - M\frac{2N-3}{2N-2}\} + M\frac{(2N-1)}{(2N-2)}\theta_{N+1} + M(\frac{2N-3}{2N-2})\theta_{N-1} + \frac{\dot{Q}'''\,Dt}{\rho \cdot Cp} \tag{4.28}$$

where $\dot{Q}'''$: heat generation per unit volume
ρ: density
Cp: heat capacity (at constant pressure)

Equation (4.28) represents the generalized transformation of equation (4.3) into an equivalent finite difference form.

During the heating of cylindrical additives, phase changes may occur (i.e. titanium α can transform endothermically to β at 1155 K or 882°C).

The numerical model took this transformation into account in the following way. Thus, once the temperature at nodal point N, θ_N, reached the transformation temperature of the addition, θ'_N was computed. The difference between θ'_N and the transformation point temperature θ_{TR}, was then accumulated until it equalled or exceeded the fictitious temperature change given by equation (4.29):

$$\Delta T_{TR} = \frac{L_{TR}}{C_{ps}} \tag{4.29}$$

where ΔT_{TR}: fictitious temperature change

L_{TR}: the latent heat of transformation of the addition

C_{ps}: the heat capacity of the solid cylindrical addition.

During the course of this accumulation process, θ_N was always reinitialized to θ_{TR} after each iteration. Once node N accumulated a temperature increase equivalent to ΔT_{TR} the material comprising nodal point N was considered to be fully transformed (i.e. transformation of titanium α to titanium β).

For a given nodal point N, the M modulus can have two values, $M_{N,N-1}$, $M_{N,N+1}$. The first corresponds to the centrally directed heat flux bearing nodal point N, i.e. the heat flux between nodal point N and N-1. The second value corresponds to the heat flux entering nodal point N, from N+1. The numerical values of these fluxes will depend on the phases existing at the adjacent nodal points (i.e. N and N+1 or N and N-1).

For the α phase of the addition, the value for the M modulus is given by the following formula:

$$M_\alpha = \frac{K_\alpha \; Dt}{\rho \; C_{P\alpha} \; Dx^2} \tag{4.30}$$

where K_α: thermal conductivity of the α phase of the addition

$C_{P\alpha}$: heat capacity of the α phase.

For the β phase of addition the M modulus becomes:

$$M_\beta = \frac{K_\beta \; Dt}{\rho \; C_{P\beta} \; Dx^2} \tag{4.31}$$

where K_β: thermal conductivity of β phase

$C_{P\beta}$: heat capacity of β phase.

For the steel shell region, the M modulus is given by:

$$M_{Fe} = \frac{K_{Fe} \; Dt}{\rho_{Fe} \; C_{PFe} \; Dx^2} \tag{4.32}$$

where K_{Fe}: thermal conductivity of steel

ρ_{Fe}: density of steel

C_{PFe}: heat capacity of steel.

When nodal point N is in the α phase and the adjacent nodal point is in the β phase, the M modulus was assigned the following formula:

$$M_{\alpha-\beta} = \frac{K_{\alpha-\beta}\ Dt}{\rho\ C_{P\alpha}\ Dx^2} \qquad (4.33)$$

where the $K_{\alpha-\beta}$ is the equivalent thermal conductivity taken as:

$$K_{\alpha-\beta} = \frac{2\ K_\alpha\ K_\beta}{K_\alpha + K_\beta} \qquad (4.34)$$

For the case in which a nodal point N is in the β phase and the adjacent nodal point is in the α phase then

$$M_{\beta-\alpha} \quad \frac{K_{\alpha-\beta}\ Dt}{\rho\ C_p\ \ Dx^2} \qquad (4.35)$$

$K_{\alpha-\beta}$ was given in equation (4.34)

The presence of a thermal resistance between the addition and the inner surface of the steel shell necessitates the modification of dimensionless numbers M, which are applied to the relevant numerical equations. This thermal resistance may be a gas layer or a thin oxide film. For modelling purposes it is assumed that this thermal resistance is of negligible thickness and heat capacity. In the solidification or melting of the steel shell there are two distinct situations. The first is depicted schematically in figure 4.6. In this case

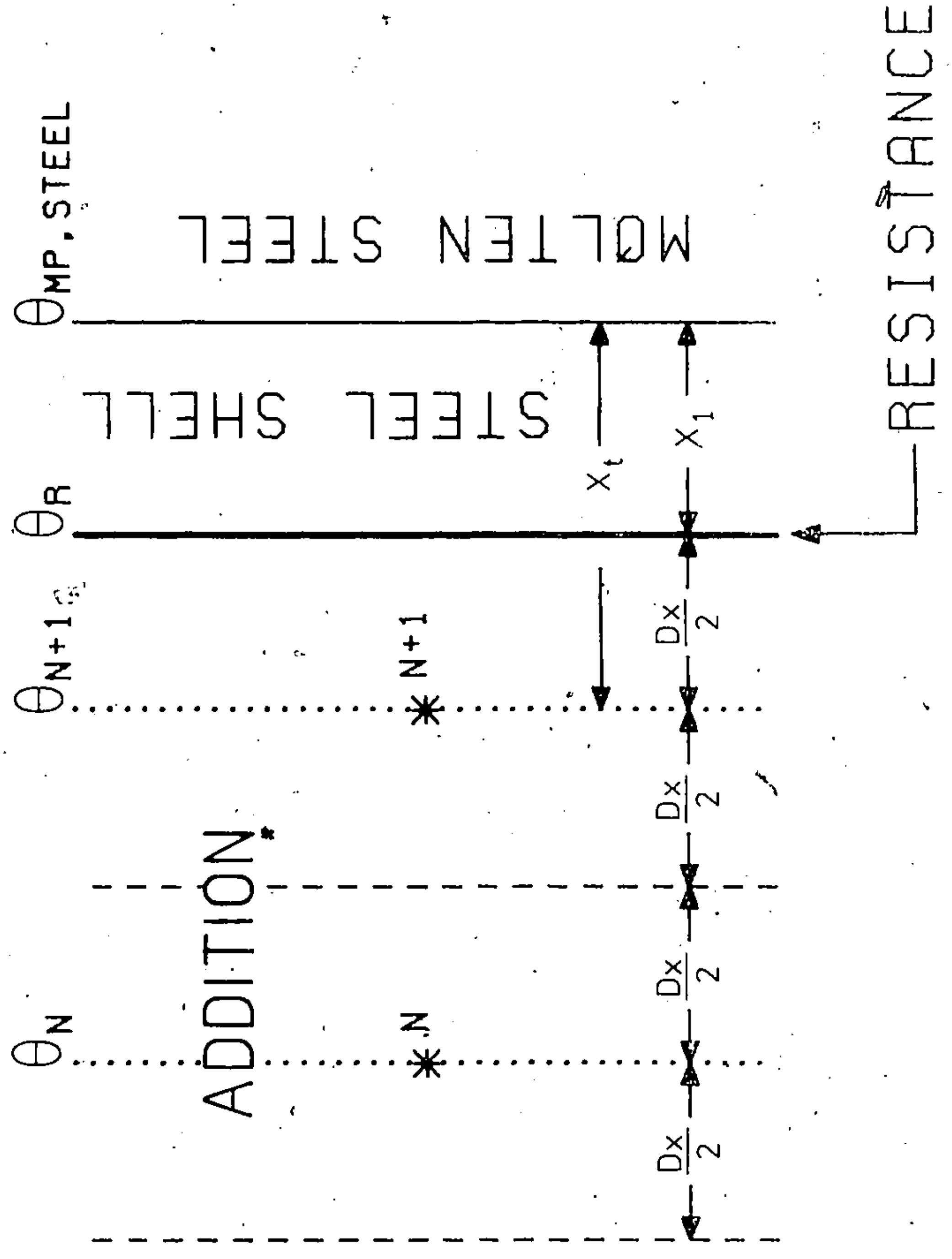

Figure 4.6 A schematic representation of the steel shell interface for a steel shell thickness of less than Dx units.

there is no nodal point in the steel shell, since the shell thickness is smaller than the radial nodal point distance. The latter case is illustrated schematically in figure 4.7. Here, there is a nodal point in the steel shell, since the shell thickness is greater than the radial nodal point distance. Referring to figure 4.6, the heat flux through the steel shell is expressed as:

$$\dot{q}''_{Fe} = \frac{K_{Fe}}{X_1} \Delta\theta_{Fe} \qquad (4.36)$$

where K_{Fe}: thermal conductivity of steel

X_1: steel shell thickness

$\Delta\theta_{Fe}$: temperature difference across the steel shell.

The heat flux through the interfacial resistance is given as

$$\dot{q}''_R = \frac{1}{R} \Delta\theta_R \qquad (4.37)$$

where R: thermal resistance

$\Delta\theta_R$: temperature difference across the thermal resistance.

The heat flux between the steel shell addition interface and the nodal point N+1 was expressed as:

$$\dot{q}''_{N+1} = \frac{K_s}{Dx/2} \Delta\theta_s \qquad (4.38)$$

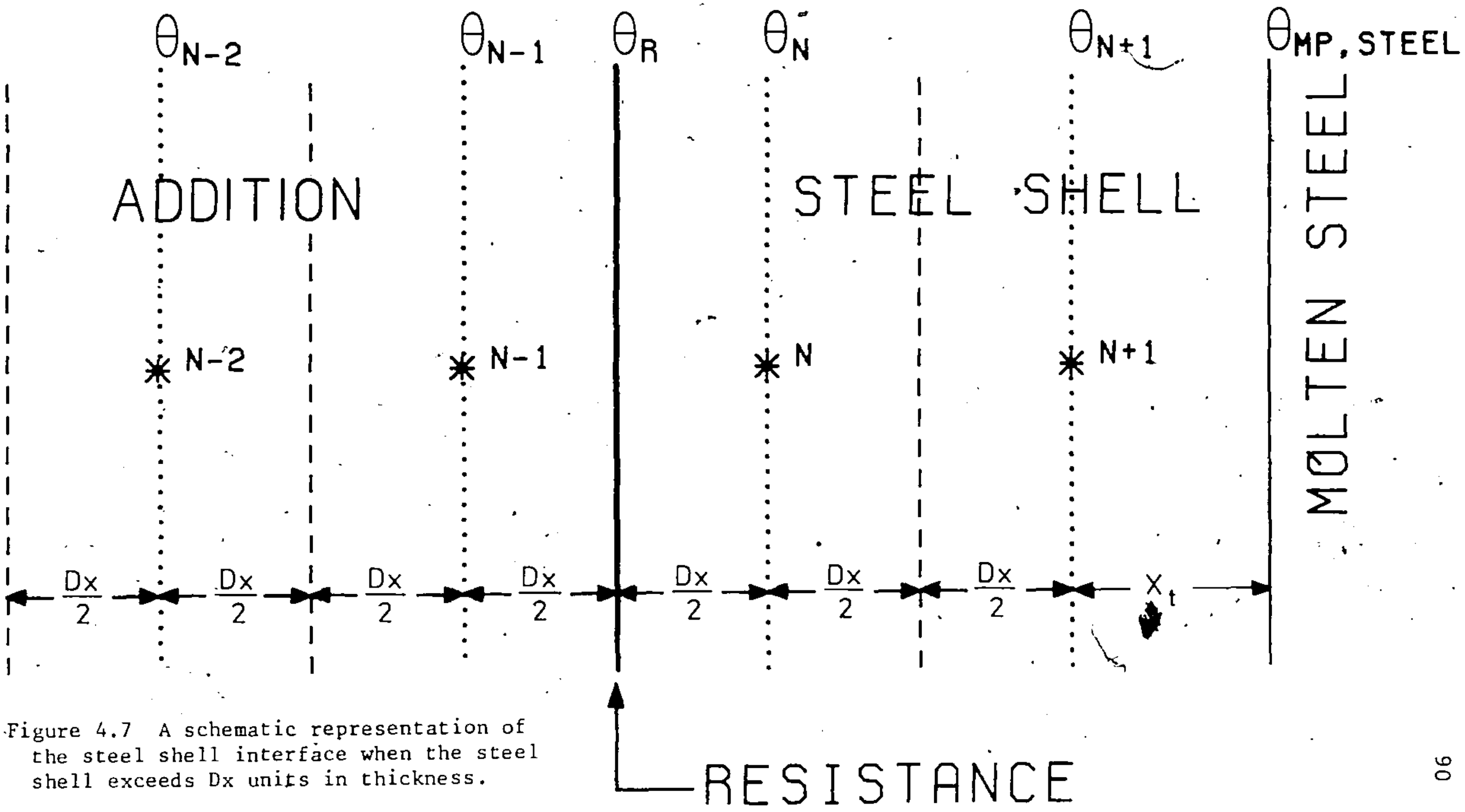

Figure 4.7 A schematic representation of the steel shell interface when the steel shell exceeds Dx units in thickness.

where K_s: thermal conductivity of addition

$\Delta\theta_s$: temperature difference across the steel shell addition interface and the nodal point N+1.

For the heating period during which thermal resistance operates, there is no accumulation or generation of heat across the liquid-solid steel interface and the nodal point N+1, so that heat fluxes must be equal. Hence,

$$\dot{q}''_{Fe} = \dot{q}''_{R} = \dot{q}''_{N+1} = \frac{K_{eq}}{X_t} \Delta\theta_{total} \tag{4.39}$$

where K_{eq}: the equivalent thermal conductivity

X_t: distance between nodal point N+1 and liquid-steel interface

$\Delta\theta_{total}$: temperature difference across liquid-solid steel interface and the nodal point N+1.

From the definition of $\Delta\theta_{total}$ the following relation is obtained:

$$\Delta\theta_{total} = \Delta\theta_{Fe} + \Delta\theta_R + \Delta\theta_s \tag{4.40}$$

From equations (4.36), (4.37), (4.38), (4.39) and (4.40) the following expression is derived:

$$K_{eq} = \frac{2\ K_s\ K_{Fe}\ X_t}{(2\ K_s\ X_1 + 2\ R\ K_s\ K_{Fe} + DX\ K_{Fe})} \tag{4.41}$$

For the case which is depicted schematically in figure 4.7, a similar procedure was followed. Referring to figure 4.7 the equivalent thermal conductivity between nodal points N-1 and N was expressed by:

$$K_{eq} = \frac{2\ K_s\ K_{Fe}\ DX}{(K_s\ DX + 2\ R\ K_s\ K_{Fe} + DX\ K_{Fe})} \tag{4.42}$$

Note that this expression can be derived from (4.41) if $X_1 = DX/2$ and $X_t = Dx$.

4.4.3 Stability and Accuracy

A critical feature of any finite difference technique is its stability and accuracy. For a numerical solution of a finite difference equation to be of any value, it is self-evident that its solution must converge correctly. This occurs (i.e. the accuracy improves) when the finite increments DX (distance between nodal points and Dt (time iteration step)) are decreased in size. Analysis shows[68,69,70] that a restrictive relationship between the size Dx and Dt exists when using the explicit finite difference technique.

For cylinder coordinates, it is readily shown that the modulus ($M = K\ DT/\rho\ Cp\ Dx^2$) should not be greater than 0.25. If this criterion is not satisfied results become unstable and will oscillate from one time step to another, the term (1-4M) in equation (4.23) becoming negative. The value chosen for M in the present calculations was 0.06. It is worth noting that smaller M values made no significant changes in the numerical solutions.

4.4.4 Computer Model

The numerical calculation is performed in the following way. The temperature and the M modules for all nodal points are initially assigned with values corresponding to the initial temperatures and initial M modules for each material used. Then over the next time step, Dt, the temperature of all nodal points are recalculated using the finite difference equations (4.22), (4.23), (4.26). The shell thickness is calculated using equation (4.24). After that, the corresponding M modules for each nodal point are assigned and the calculations for the new temperatures can be repeated over successive time intervals. The above are easily converted in FORTRAN computing language.

A program called DISSOLUTION was written in FORTRAN computing language, compiled with FORTRAN H compiler and executed on an AMDAHL V7 computer. A list of this program along with all symbols appears in Appendix IV.

4.5 COMPARISONS OF NUMERICAL MODEL PREDICTIONS WITH ANALYTICAL SOLUTIONS

In mathematical modelling it is essential to demonstrate general validity by comparing a model's predictions with any cases where analytical solutions might exist. In this section of the thesis, the numerical model was adopted to run under three different limiting conditions for which analytical solutions are available.

4.5.1 Case 1: Infinitely Long Cylinder Subjected to Sudden Temperature Change at Surface

If a cylinder of infinite length and zero initial temperature has its surface maintained at θ_a, a constant, for $t > 0$, the solution for the transient temperature field is given by[71]:

$$\frac{\theta}{\theta_a} = 1 - 2 \sum_{n=1}^{\infty} e^{-\beta_n^2 T} \frac{J_0(r\beta_n/a)}{\beta_n J_1(\beta_n)} \tag{4.43}$$

where a: cylinder radius

k: thermal diffusivity

T: kt/a^2

0: temperature of cylinder at radius r

$J_0(x)$: Bessel function of the first kind of order zero

$J_1(x)$: Bessel function of the first kind of order one

β_n: n 1,2,.... are the roots of $J_o(\beta) = 0$ (4.44)

The sum of the right hand side of equation (4.43) was computed from the first eight terms, the roots for equation (4.44) being obtained from reference 72. The solution to equation (4.43) is given in reference 71 in graphical form. Owing to the uncertainty in reading values from these plots, computer programs were written by the author for equation (4.43). The results are presented in graphical form in Figure 4.8

Figure 4.8 Temperature distribution at various times in a cylinder of radius a with zero initial temperature and surface temperature θ_a. The solid lines show the results of analytical solution (i.e. equation 4.43). The points depict results of the numerical model. The numbers on the curves are the values of $T = Kt/a^2$.

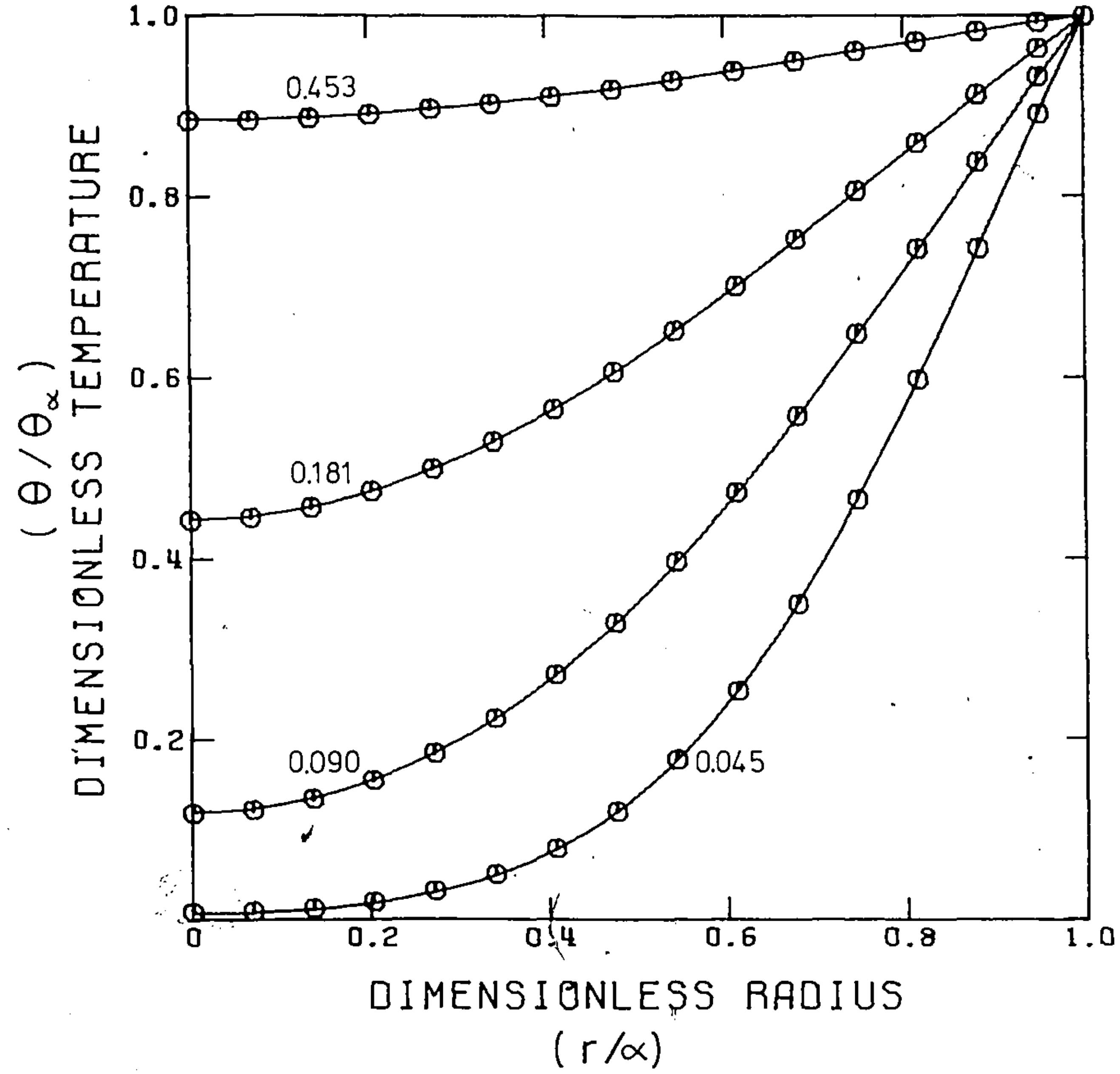

together with predictions from the present model. As seen, there is excellent agreement between the analytical and numerical solutions.

4.5.2 Case 2: Infinite Cylinder with Heat Generated Within It

Consider the case of an infinite cylinder of diameter a, at zero initial temperature with constant heat generation at a rate Q_0 per unit time and per unit volume at $t > 0$. The temperature on the inside of the cylinder is then given by[73]:

$$\theta = \frac{Q_0(a^2 - r^2)}{4K} - \frac{2Q_0}{aK} \sum_{n=1}^{\infty} e^{-k\alpha_n^2 t} \frac{J_0(r\,\alpha_n)}{\alpha_n^3 J_1(a\,\alpha_n)} \qquad (4.45)$$

Substituting $a\,\alpha_n = \beta_n$ and $kt/a^2 = T$,

the following equation is derived:

$$\frac{4\,K\,\theta}{Q_0\,a^2} = 1 - \left(\frac{r}{a}\right)^2 - 8 \sum_{n=1}^{\infty} e^{-\beta_n^2 T} \frac{J_0(r\,\beta_n/a)}{\beta_n^3 J_1(\beta_n)} \qquad (4.46)$$

where K: thermal conductivity

a: cylinder radius

θ: temperature of cylinder at radius r

The solution to equation (4.46) is given in reference 73 in a graphical form. As before, due to uncertainties in reading values from these plots, computer programs were written so that particular solutions to the equation (4.46) could be evaluated more accurately. The results are plotted in figure 4.9 for comparison with equivalent predictions of the present models. Again, the agreement between analytical and numerical solutions is excellent.

4.5.3 Case 3: Exact Solution of Freezing Boundary with Cylindrical Symmetry

Carslaw and Jaeger[74] present an analytical solution for the problem of freezing with cylindrical symmetry. Consider the case where the surface of separation between the solid and liquid phases is at radius $r = R(t)$. The liquid region has the thermal constants ρ, C_{Pl}, K_l, α_l and exists for $r > R$. The solid regions exists for $r < R$ and is assigned thermal constants ρ, C_{Ps}, K_s, α_s. If $\theta_2(r)$ and $\theta_1(r)$ are the temperatures in the liquid and solid regions respectively and θ_{mp} is the melting point, the boundary conditions at $r = R$ are:

$$\theta_1 = \theta_2 = \theta_{mp} \tag{4.45}$$

and

$$K_s \frac{\partial \theta_1}{\partial r} - K_l \frac{\partial \theta_2}{\partial r} = LH\ \rho\ \frac{dR}{dt} \tag{4.46}$$

where LH: latent heat of solidification

ρ: density

For the case of a continuous line source along the axis $r = 0$ which extracts heat at the rate Q per unit time at $t > 0$, the temperature distribution in the solid region is given by

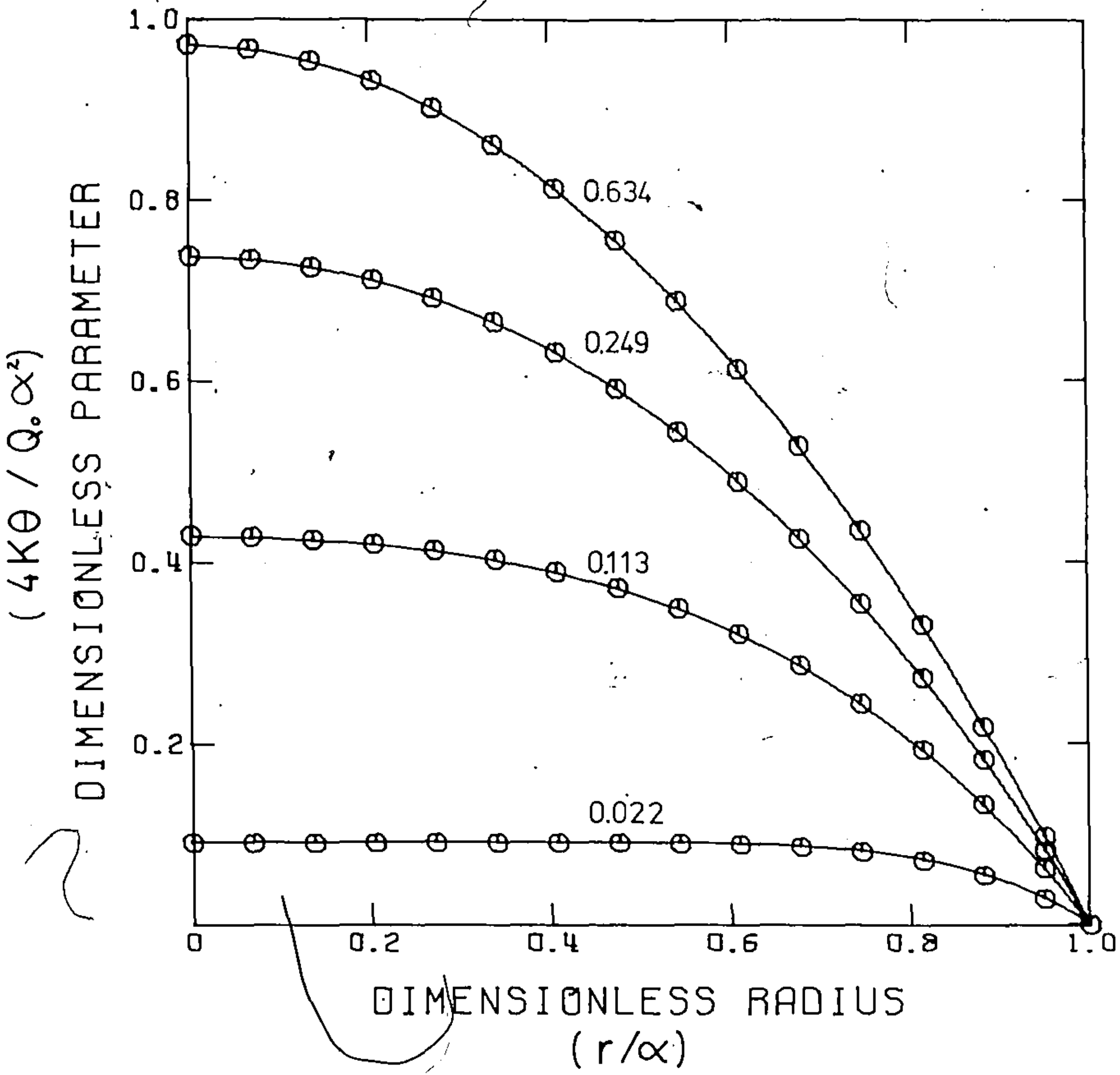

Figure 4.9 Temperature distribution at various times in a cylinder of radius a with zero initial and surface temperatures, and a constant rate of heat generation. The solid lines show the results of analytical solution (i.e. equation 4.46). The points depict results of the numerical model. The numbers on the curves are the values of T = Kt/a².

the following formula:

$$\theta_1(r) = \theta_{mp} + \frac{Q}{4\pi K_s}\{Ei(-\frac{r^2}{4K_s t}) - Ei(-\lambda^2)\} \tag{4.47}$$

for $0 < r < R$

The temperature distribution in the liquid region is given by:

$$\theta_2(r) = \theta_\infty - \frac{(\theta_\infty - \theta_{MP})}{Ei(-\lambda^2 a_s/a_1)} Ei(-\frac{r^2}{4a_1 t}) \tag{4.48}$$

for $r > R$

where

$$R = 2\lambda(a_s t)^{\frac{1}{2}} \tag{4.49}$$

λ is the root of

$$\frac{Q}{4\pi} e^{-\lambda^2} + \frac{K_1(\theta_\infty - \theta_{MP})}{Ei(-\lambda^2 a_s/a_1)} e^{-\lambda^2 a_s/a_1} = \lambda^2 a_s LH \rho \tag{4.50}$$

The function Ei(x) is called exponential integral and is defined as

$$Ei(x) = \int_x^\infty \frac{e^{-u}}{u} du \tag{4.51}$$

LH: the latent heat of solidification.

Initial conditions (t = 0) at the central axis (R = 0) are that $\theta_2 = \theta_\infty$; i.e. at the beginning of freezing, the whole region at $r > 0$ is liquid with a temperature θ_∞. For $t > 0$,

$$\lim_{r \to 0}\{(2\pi r K_s)\frac{\partial\theta_1}{\partial r}\} = Q \qquad (4.52)$$

Equation (4.52) expresses in mathematical terms, that a continuous line source along the axis for t > 0 extracts heat at a rate of Q per unit time.

Paterson has shown[75], that equation (4.50) has only one positive root. The 'secant' method[76] was used in order to find the root of equation (4.50). In this way, the propagation of a fusion boundary can be expressed by equation (4.49).

This solution was also used in order to check the accuracy of the author's numerical model. Thus, by predicting the advance of a solidifying front at the steel shell (radius r_2, figure 4.1), analytically equivalent computations could be checked.

For a given of Q in equation (4.50) a value of λ was computed using the 'secant' method. By using equation (4.49), the time taken, t_{IN}, was then calculated for the case of the solid-liquid interface being at a specified radius R1. The temperature profile in the solid region was calculated using equation (4.47). This profile was then used as initial conditions in the numerical model. In order to simulate precisely the conditions of the line source along the cylinder axis which are expressed in equation (4.52), the temperature of nodal point 1 (figure 4.3) was computed using equation (4.47) at every iteration step. Figure 4.10 presents results from

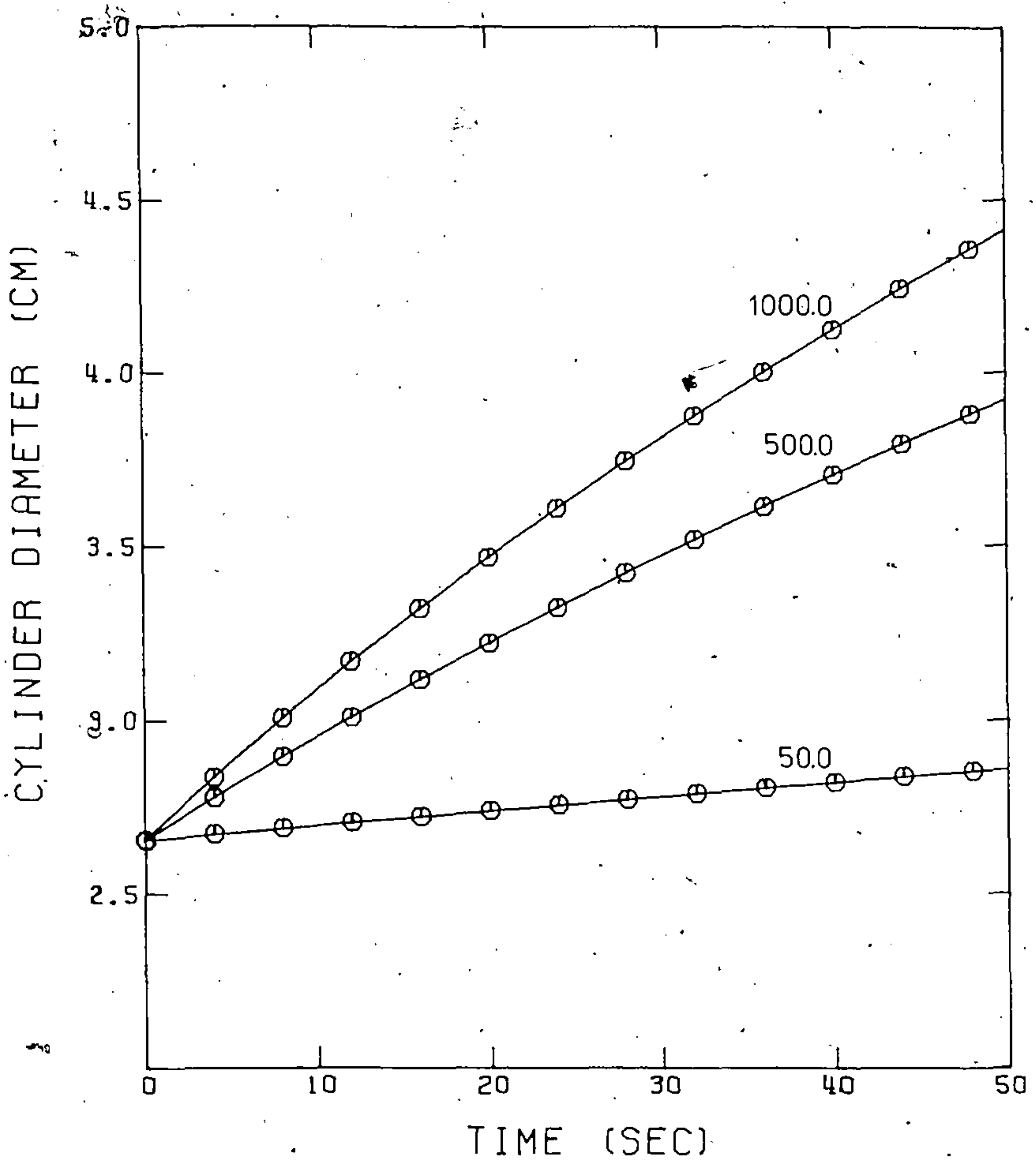

Figure 4.10 The solid lines show results of analytical solution (i.e. equation 4.49). The points depict results of the numerical model. The numbers on the curves are values of Q in cal s^{-1} for the continuous line source (i.e. equation 4.52).

the analytical and numerical solutions for various heat extraction rates, Q. As seen, excellent agreement exists between these two types of solutions.

4.6 NATURAL CONVECTION FROM VERTICAL CYLINDERS

There are two categories in the experimental and theoretical studies of natural convection. The first is uniform heat flux between the convecting fluid and the solid plate, and the second is uniform surface temperature of the solid. The latter case corresponds to conditions for the present study: the constant temperature represents the melting point temperature of the solid in contact with the liquid. It is assumed the laminar flow conditions in liquid metals prevail up to Gr Pr (Rayleigh number) = 10^9, the transition value reported by Holman.[81] Above this value, turbulent flow conditions prevail.

4.6.1 Laminar Flow

The equation for natural laminar convection to a flat plate proposed by Churchill and Usagi[80] for a uniform surface temperature was used.

$$Nu_x\text{, flat plate} = \frac{0.503(Gr_x Pr)^{0.25}}{\left(1 + \left(\frac{0.492}{Pr}\right)^{9/16}\right)^{4/9}} \qquad (4.53)$$

Sparrow and Gregg[77] and Cebeci[78] have computed the deviation that will occur between local Nusselt numbers for cylinders and flat plates, owing to curvature of the former. Cebeci[78] extended the results of Sparrow and Gregg[77] to fluids having Prandtl numbers as low as 0.01. Some of these data of Cebeci[78] was correlated by Mucciárdi[79], using the least square technique, to give:

$$\frac{Nu_x,\text{cylinder}}{Nu_x,\text{flat plate}} = 0.2672\ \varepsilon\ Pr^{-0.42} + 1.011\ Pr^{-0.02} \quad (4.54)$$

where Nu_x,cylinder: the local Nusselt number, x units from the leading edge of a vertical cylinder;

Nu_x,flat plate: the local Nusselt number, x units from the leading edge of a vertical plate;

x: the distance from the leading edge;

r: the radius of the cylinder

Gr_x: the local Grashof number

ε: the dimensionless tranverse-curvature parameter which is defined as:

$$\varepsilon = \frac{2\sqrt{2}}{Gr_x^{0.25}} \left(\frac{x}{r}\right) \quad (4.55)$$

Thus, the appropriate final expression for estimating heat fluxes around cylindrical bodies is arrived at by combining the equations (4.53), (4.54) and (4.55).

$$Nu_x\text{,cylinder} = 0.2672\ Pr^{-0.42}\ \frac{2\sqrt{2}}{Gr_x^{0.25}}\ (\frac{x}{r})$$

$$\times \frac{0.503(Gr_x Pr)^{0.25}}{(1 + (\frac{0.492}{Pr})^{9/16})^{4/9}} + 1.011\ Pr^{-0.02}$$

$$\times \frac{0.503(Gr_x Pr)^{0.25}}{(1 + (\frac{0.492}{Pr})^{9/16})^{4/9}} \qquad (4.56)$$

The reliability of these correlations have been established in independent work[46,47,79] where solid/liquid metal systems were studied that involved natural convective heat transfer to vertical cylindrical surfaces of uniform surface temperature.

4.6.2 Turbulent Flow

Experimental heat transfer data and recommended correlations reported by various authors[84,85,86,87] show significant scatter (i.e. ≈40%). While the present experiments were carried out under conditions dominated by laminar flow, turbulent natural convection heat transfer coefficients can be estimated on the basis of the following correlation:

$$Nu = 0.10(Ra)^{1/3} \qquad (4.57)$$

where Ra: Rayleigh number.

Equation (4.57) was derived from experimental work of Warner and Arpaci[88] and it is in remarkable agreement with the analytical correlation of Bayley.[83] Holman[81] extends the applicability of equation (4.57) to Rayleigh numbers up to 10^{13}.

4.7 HEAT TRANSFER MODEL FOR ESTIMATION OF A CYLINDER'S THERMAL CONDUCTIVITY

A numerical model was developed in order to estimate the thermal conductivity of titanium. In essence, this model solves the differential equation (4.5) for a variable surface temperature with no moving boundary.

In many of the present experiments, two temperatures in the cylinder were measured, one at the center and the other close to the cylinder's edge. It is then possible to solve equation (4.5) numerically using as one boundary condition the measured time-temperature relationship close to the cylinder's edge and the fact that $\partial\theta/\partial r = 0$ at $r = 0$. Thus, the model accepts as an input parameter the near surfaces temperature-time relationship to compute the centerline temperature for a given thermal conductivity. The thermal conductivity best fitting the measured and predicted centerline temperatures then provides a good estimate ($\simeq\pm 5\%$) of the cylinder's thermal conductivity over the temperature range investigated.

CHAPTER 5

RESULTS AND DISCUSSION ON TITANIUM DISSOLUTION IN LIQUID STEEL

5.1 INTRODUCTION

In this chapter, the experimental results obtained for the dissolution of titanium in liquid steel are discussed. Two sets of immersion tests were carried out. The first set involved simple dipping experiments in which titanium cylinders were immersed in liquid steel for different time periods. They were then withdrawn and the steel shell thicknesses and the reaction zones were measured after first cutting the cylinders in half. The total number of titanium cylinders for this set of tests was fifteen. The cylinder diameters ranged from 3.81 cm to 1.905 cm.

The second set of immersion tests involved the dipping of titanium cylinders together with simultaneous monitoring of cylinder and steel bath temperatures, and displaced weight during the dissolution. Thirty-eight cylinders were used for this set. The cylinder diameter ranged from 5.08 cm to 2.54 cm. For the cylinders with a 2.54 cm diameter only the center line temperature was measured while for the larger diameter cylinders (i.e. 3.81 cm and 5.08 cm) temperatures at two locations were measured: one at the centerline, the other at a position close to the edge of the cylinder.

In a further series of tests, the reaction starting temperature between iron and titanium was studied. Five tests were carried out.

Results of titanium thermal conductivity and reaction starting temperature are presented in the first sections of this chapter. In the following section a typical experimental result is analyzed together with model predictions and two periods of dissolution are identified. In the later sections of this chapter, detailed analysis of the two dissolution periods is carried out. Finally, in Appendix I, typical results for the second set of immersion tests are presented in graphical form. At the end of Appendix I a qualitative simulation of titanium dissolution in liquid steel using the Calcomp 663 digital plotter is presented.

5.2 TITANIUM THERMAL CONDUCTIVITY AT ELEVATED TEMPERATURES

The thermal conductivity of titanium used in the present tests (ASTM B 348 Grade 2) is reported[89] to be 0.16 w/cm K at room temperature. However, this property is not known for higher temperatures and the recommended values for thermal conductivity for well-annealed high purity polycrystalline titanium shows considerable change (according to Ho et al.[90]), especially at elevated temperatures. The numerical model described in section 4.7 was used for acquiring the necessary information on metal conductivity.

Figures 5.1 and 5.2 show two typical applications of the numerical model discussed in section 4.7. The heat capacity data was taken from Hultgren et al.[91] The density at room temperature was taken from reference (55). The density at higher temperatures was evaluated from McCoy's[92] thermal expansion data assuming isotropic thermal expansion. Curve 3 in Figure 5.3 shows the results obtained from the present study. The estimated error in these results is ±5% for temperatures up to 1600 K. Unfortunately, no data on thermal expansion at higher temperatures. For the range of 1600 K to 1700 K the thermal diffusivity was evaluated and it was found to be $0.0855 \times 10^{-4}\ \mathrm{m^2/sec} \pm 0.004 \times 10^{-4}\ \mathrm{m^2/sec}$.

Referring to Figure 5.3, the scatter which exists in the literature on titanium thermal conductivity lies between curves 1a and 1b. Line 2 is that recommended by Ho et al.[90] for high purity polycrystalline titanium. The fact that the estimated thermal conductivity is lower than that recommended for high purity titanium can be attributed to the small amount of impurities present in the titanium which was available for use.

5.3 REACTION AT THE STEEL SHELL AND TITANIUM INTERFACE

Preliminary work on dissolution kinetics showed a reaction starting between the titanium and the encasing steel shell during the initial stages of immersion. Figure 5.4 shows a picture of the reaction taking place at the steel shell/titanium interface. In some preliminary tests, efforts

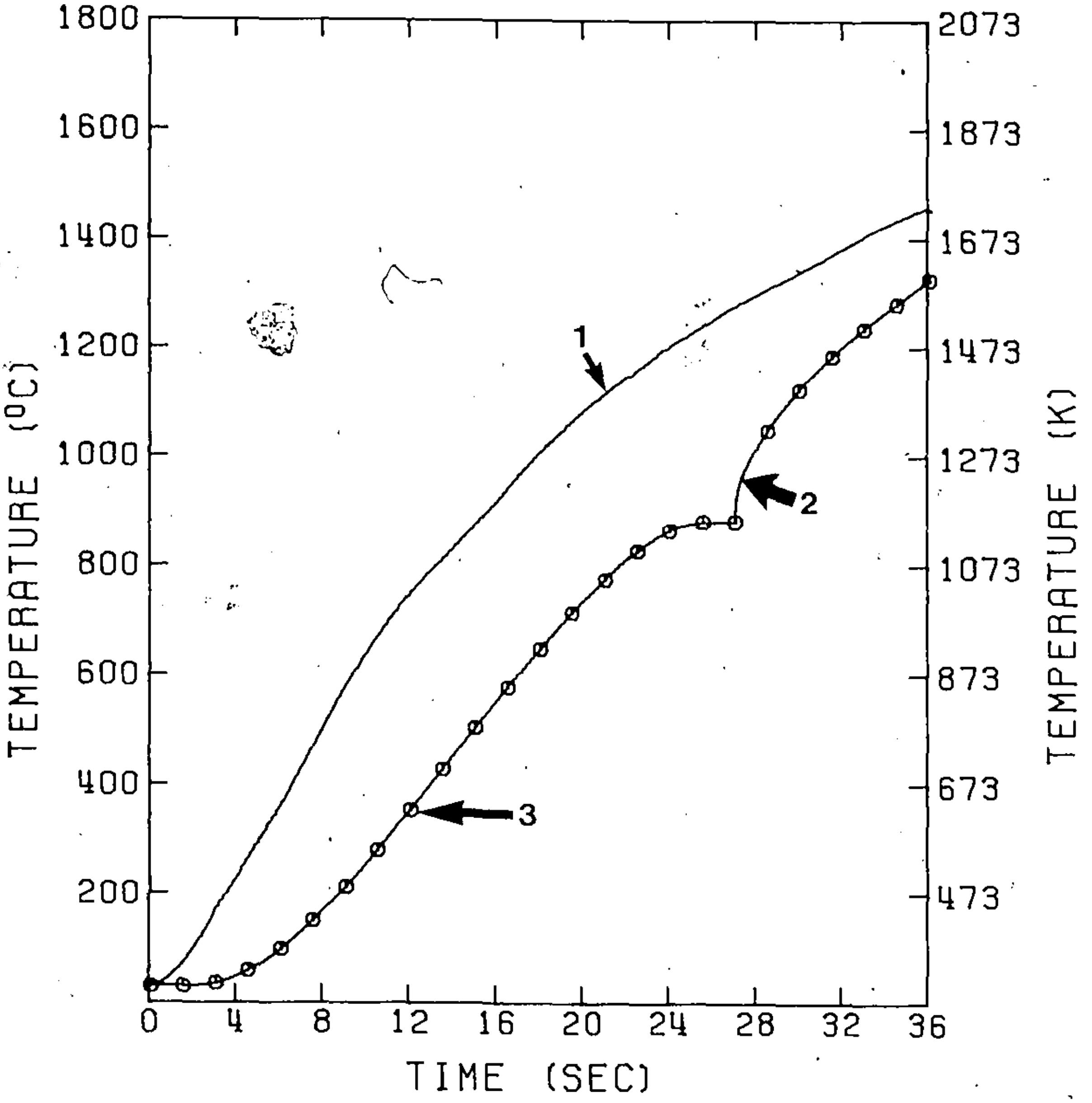

Figure 5.1 1) measured temperature at a point close to the cylinder's edge.
2) predicted temperature at the centerline.
3) measured temperature at the centerline.

Edge thermocouple 1.35 cm from the centerline.
Cylinder diameter 3.81 cm.

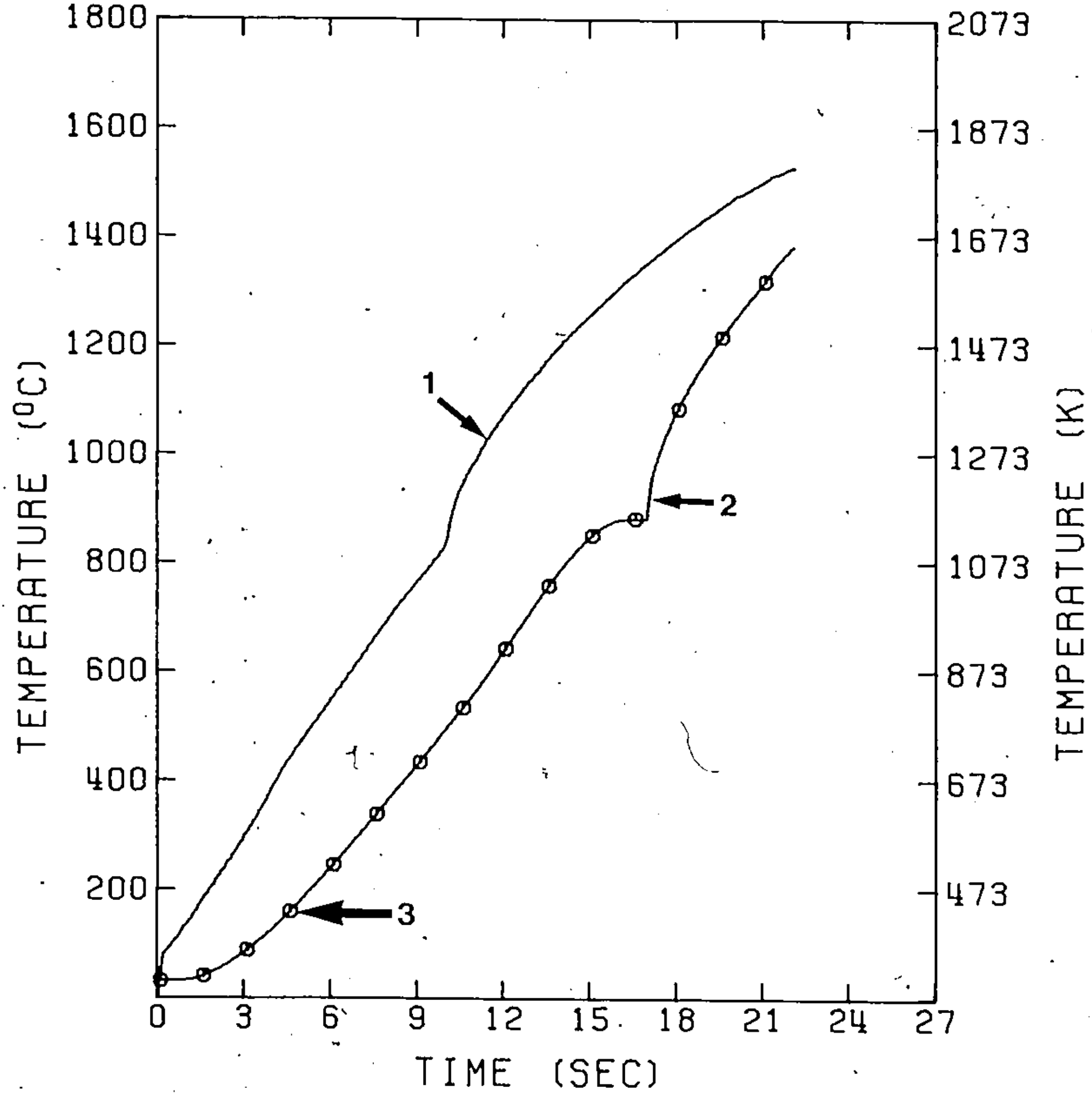

Figure 5.2 1) measured temperature at a point close to the cylinder's edge.
2) predicted temperature at the centerline.
3) measured temperature at the centerline.

Edge thermocouple 1.1 cm from the centerline.
Cylinder diameter 3.81 cm.

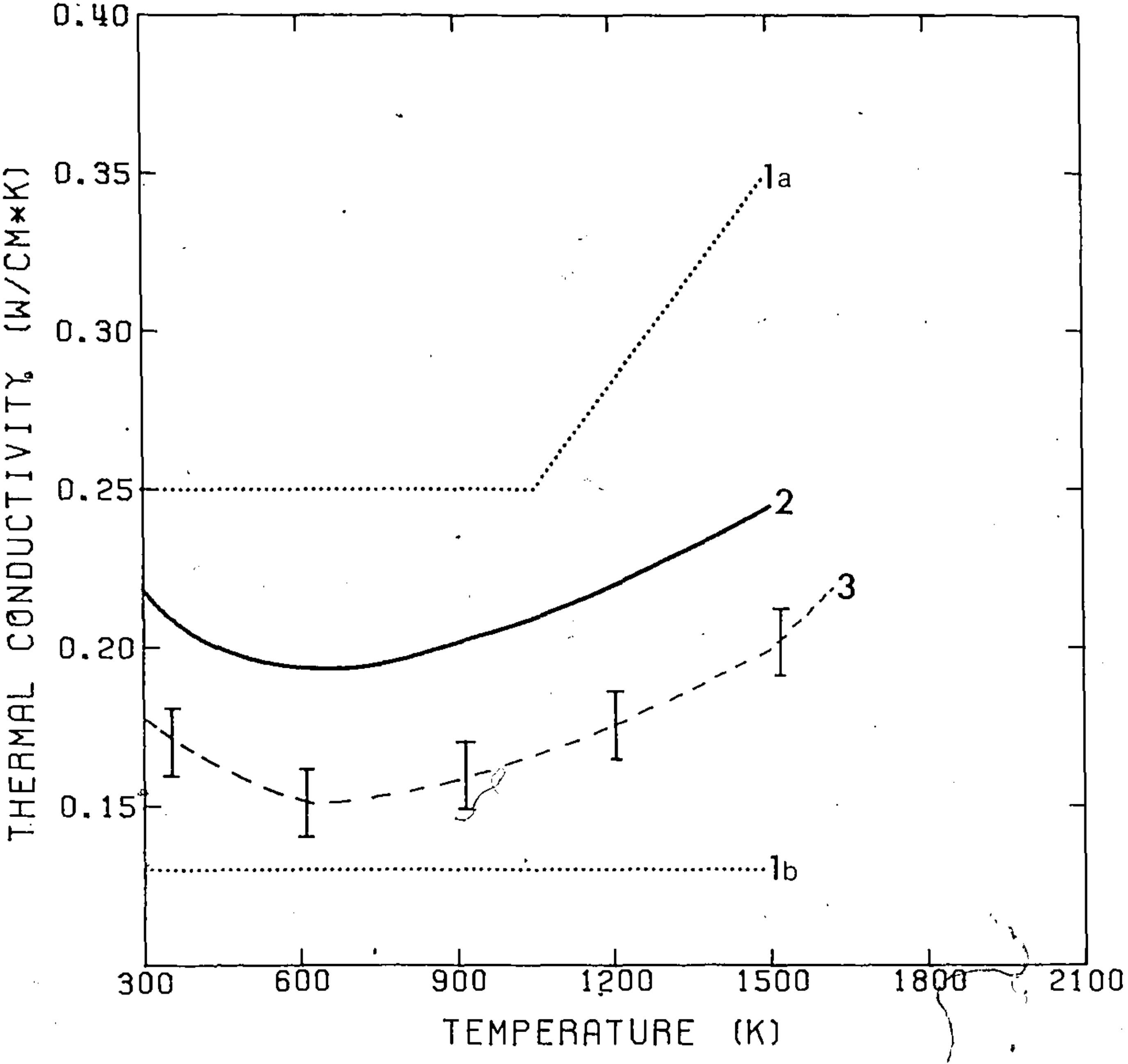

Figure 5.3 The dotted lines 1a and 1b show the scatter existing in the literature on thermal conductivities of titanium. Line 2 depicts the recommended values by Ho et al.[90] The curve 3 shows present results.

Figure 5.4 Cross section of a titanium cylinder (2.54 cm diameter) with surrounding steel shell and the reaction zone sandwiched in between.

were aimed at finding when and how the exothermic reaction between steel and titanium starts.

Composite samples of iron and titanium were heated inductively. The preparation of these samples is described in Chapter 3. The input power to the coil was kept at 9 (kw) throughout the heating history of the sample. The result is presented in Figure 5.5. The slope of the curve decreases with time and after 120 seconds the heating curve becomes horizontal. This is due to the increased radiant heat losses from the specimen. When the input power to the coil was 21 (kw) (Figure 5.6), different characteristics in the heating curve are to be noted. As seen, the slope of the curve tended to decrease. However, after 62 seconds of heating and when the temperature was approximately 1190°C (1463 K), the slope of the heating curve showed an increase and became erratic. During this period a violent reaction between iron and titanium was observed (Figure 5.7).

In an earlier thermodynamic study, Kubaschewski and Dench[93] observed that equi-atomic mixtures of iron and titanium would react at about 1090°C (1363 K), the eutectic temperature. The difference between starting reaction temperatures of the present study and that of Kubaschewski and Dench can be attributed to the different experimental conditions and materials used.

One set of immersion tests involved simple dipping experiments in which titanium cylinders 2.54 cm in diameter

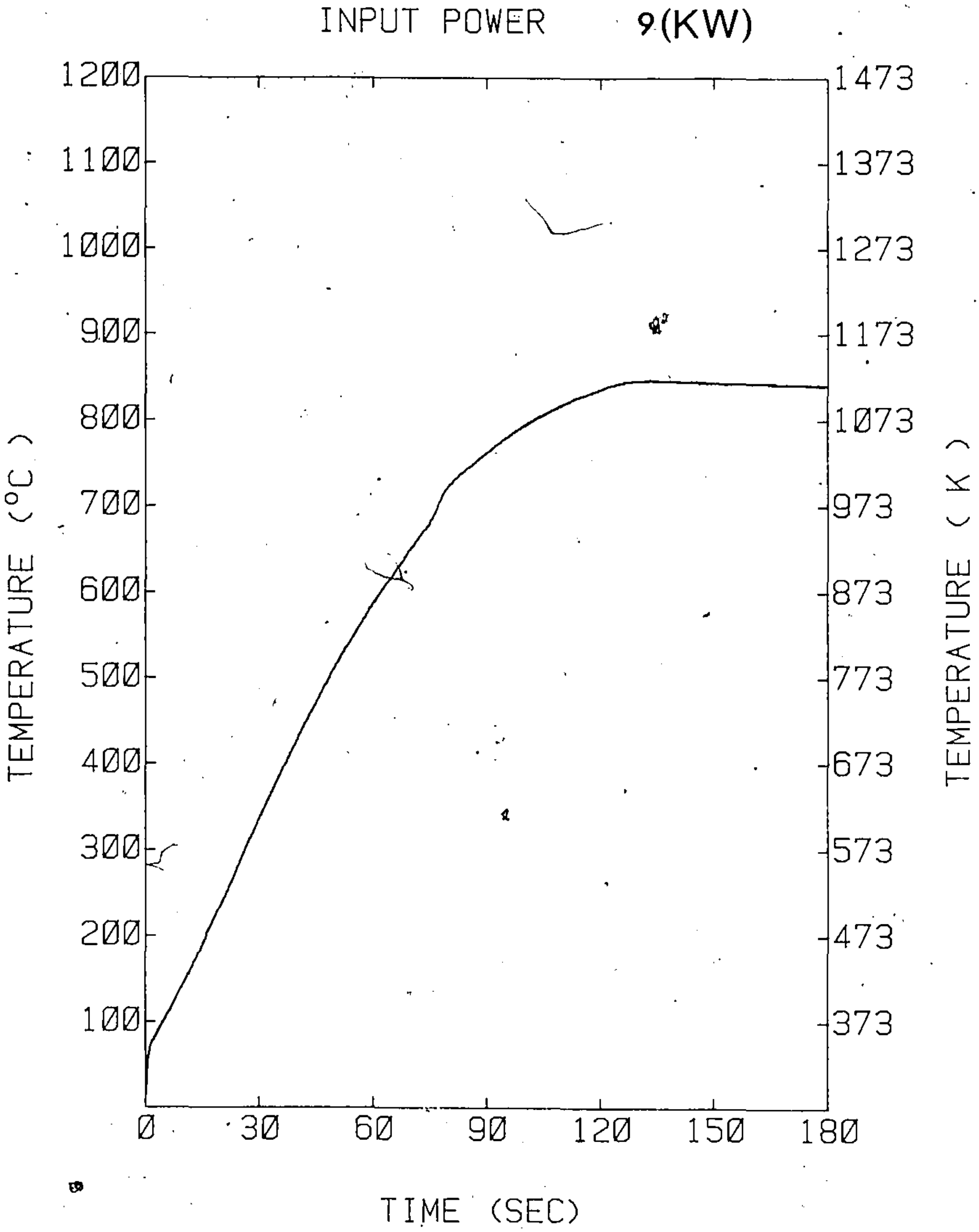

Figure 5.5 Temperature versus time curve for inductively heated composite sample.

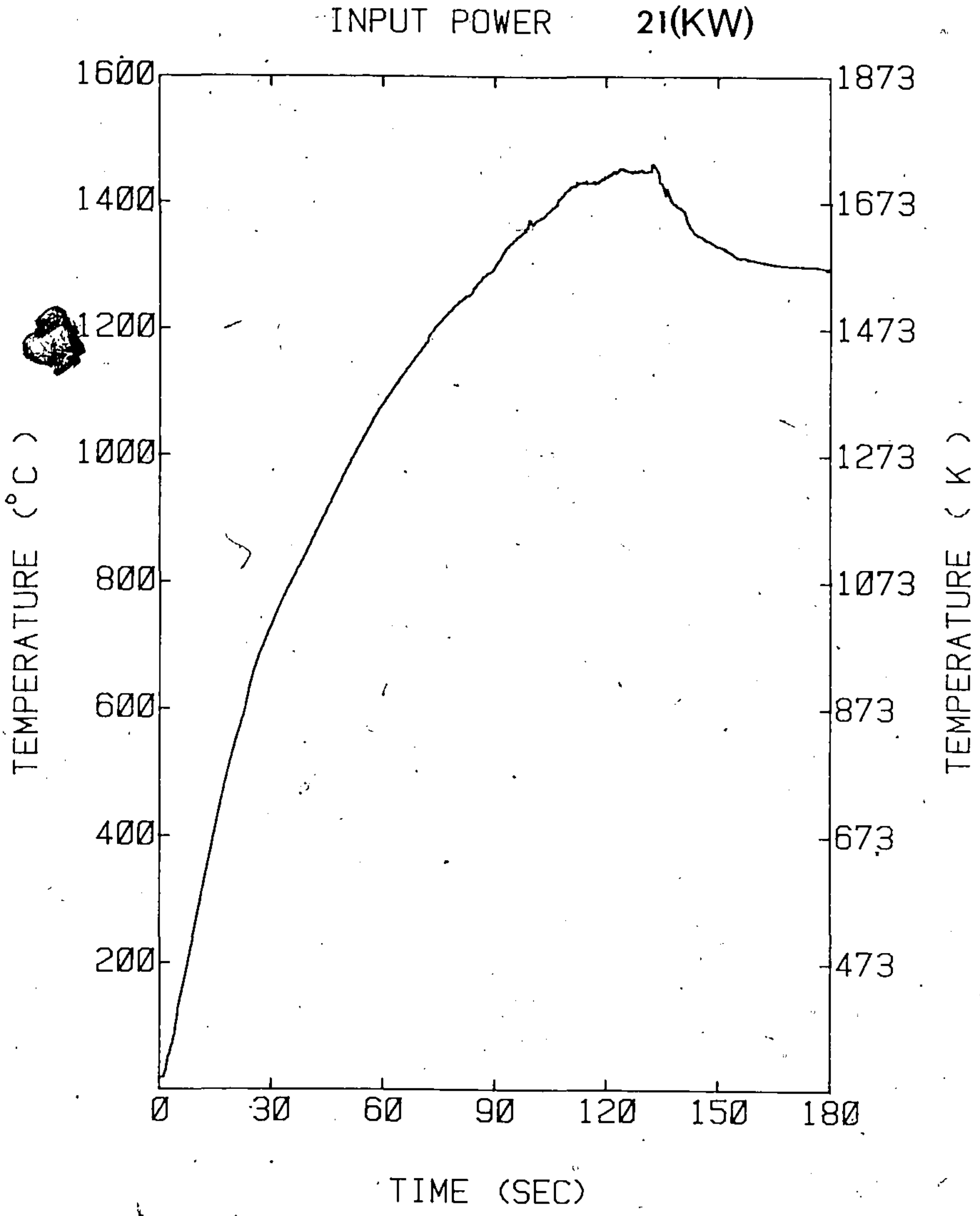

Figure 5.6 Temperature versus time curve for inductively heated composite sample.

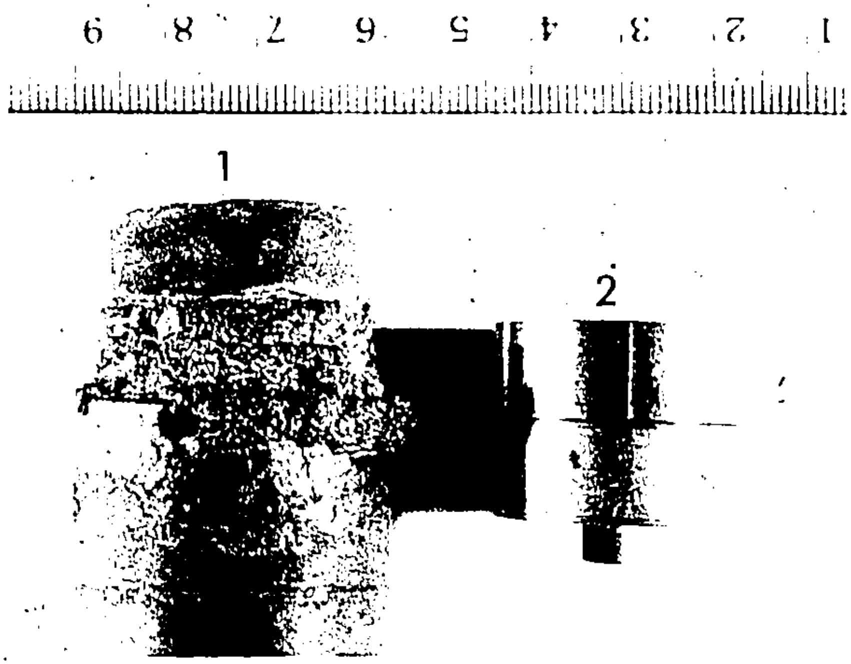

Figure 5.7 Two composite samples
1) After reaction
2) Before reaction

and 15 cm in length were immersed to within 1.0 cm of their top surfaces. Immersion time periods ranged from 5 to 15 seconds. Initial steel bath temperature varied between 1580°C (1853 K) and 1600°C (1873 K). The cylinders were withdrawn and rapidly quenched in water. They were then cut in half and samples from the reaction were taken and analysed. The results are shown in Table 5.1. Referring to Table 5.1, it is clear that the composition of the reaction zone lies around the 60 wt% iron.

The relative volumetric amounts of iron and titanium which had reacted at the original steel shell-titanium interface could be found by measuring final reaction parameters at the inside boundary of the steel shell and at the titanium boundary. An electronic digitizer (Numonics Model 1224) was used for the task. A typical sample can be seen in Figure 5.4. From this analysis it was found that the relative weight of steel shell in the reaction was 60%, with titanium at 40% making up the balance.

Consequently, in interpreting these phenomena, one can conclude that reaction between iron and titanium starts around the eutectic temperature in very pure well-packed mixtures.[93] The same reaction starts at slightly higher temperatures when the interfacial contact is either imperfect or when an oxide film coats the interface. The eutectic liquid provides the necessary trigger for the internal exothermic dissolution reaction to proceed. The composition of

TABLE 5.1

REACTION ZONE ANALYSIS

Steel Bath Temperature 1580°C (1853 K)

Immersion Time - 10 sec.

Fe%	Ti%
59.6	33.2
55.2	36.3
57.0	32.9
59.6	30.7
63.9	28.1
63.0	27.2

Steel Bath Temperature 1580°C (1853 K)

Immersion Time - 15 sec.

Fe%	Ti%
56.5	42.0
72.6	25.8
53.9	42.9

Steel Bath Temperature 1600°C (1873 K)

Immersion Time - 5 sec.

Fe%	Ti%
65.4	28.1
57.2	35.6
63.4	28.3
52.8	40.1
61.4	32.9

Steel Bath Temperature 1600°C (1873 K)

Immersion Time - 10 sec.

Fe%	Ti%
54.1	37.9
51.2	44.3
63.0	31.6

iron and reaction zone during this dissolution remains around 60 wt% Fe and 40 wt% Ti.

5.4 INTERPRETATION OF DATA FROM THE DISSOLUTION EXPERIMENTS

Using the force monitoring equipment described in Chapter 3, the load cell registers an increase in the net downward force. The rate at which the force changes then allows the rate of dissolution to be monitored. Figure 5.8 shows schematically the forces which act on the load cell when a cylinder is immersed in liquid steel.

Mathematically the above can be expressed as follows:

$$F_{NDF} = F_G - F_B \qquad (5.1)$$

where F_{NDF}: Net downward force. This is the force which the load cell registers;

F_G: Gravitational force;

F_B: Buoyancy force.

The gravitational force F_G can be expressed by the following equation:

$$F_G = V_{AIR} \cdot \rho_{Ti,s} \cdot g + V_{IMM} \cdot \rho_{Ti,s} \cdot g \qquad (5.2)$$

where V_{AIR}: The volume of one portion of the cylinder which is outside of the liquid steel during the dissolution in m³;

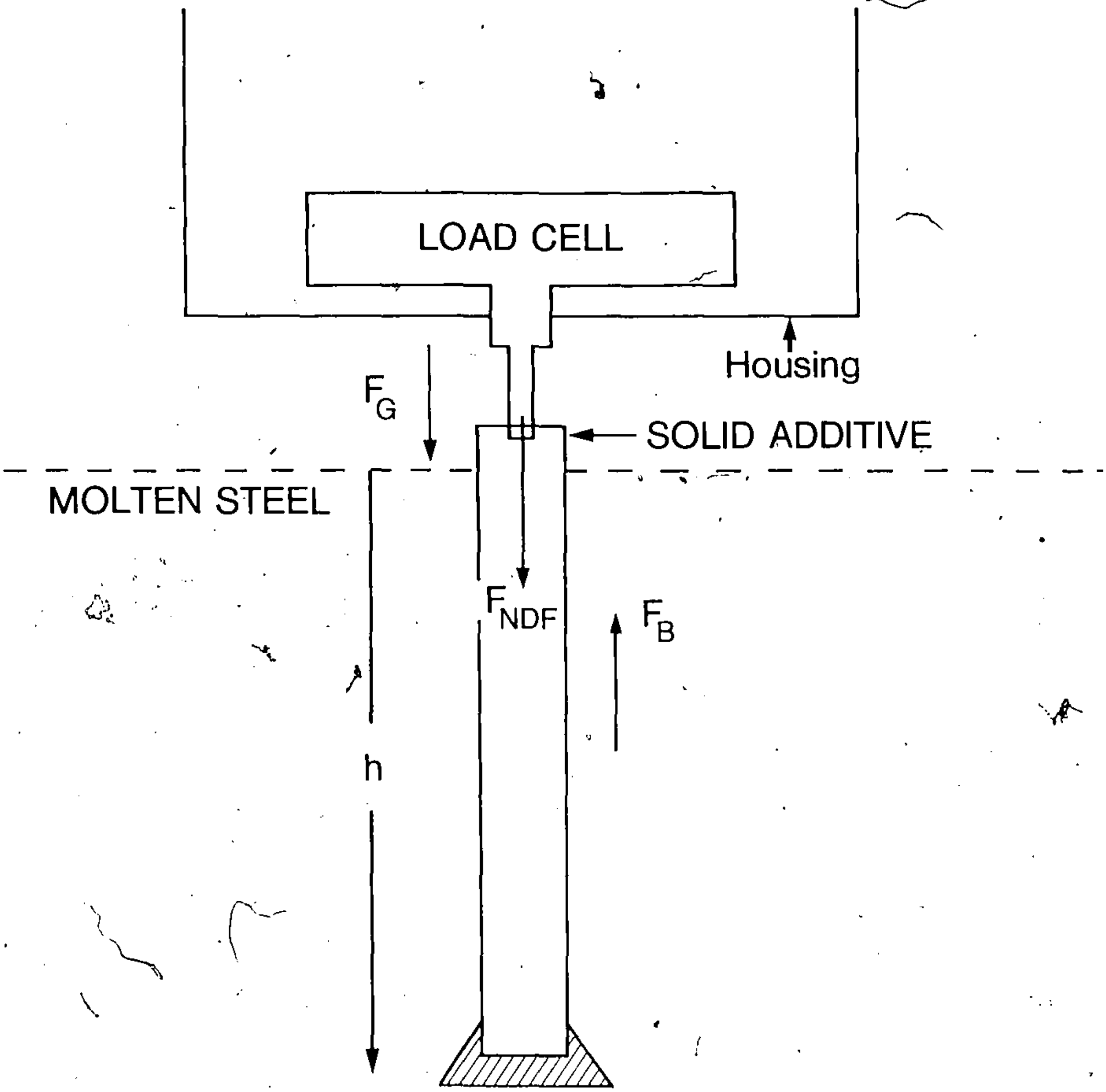

Figure 5.8 Schematic representation of forces which are applied to load cell.

V_{imm}: The volume of the other portion of the cylinder which is inside the liquid steel during the dissolution in m³;

$\rho_{Ti,s}$: Density of the titanium cylinder, kg/m³;

g: Gravitational constant 9.81 m/s²

The term F_B describes the buoyancy forces. According to Archimedes' principle: Any object wholly or partially immersed in a fluid is buoyed up by a force equal to the weight of the displaced fluid. This can be defined as:

$$F_B = V_{imm}\, \rho_{Fe,l}\, g \tag{5.3}$$

where $\rho_{Fe,l}$: Density of the liquid steel.

Combining equations (5.1), (5.2) and (5.3):

$$F_{NDF} = V_{AIR}\, \rho_{Ti,s}\, g + V_{imm}\, \rho_{Ti,s}\, g - V_{imm}\, \rho_{Fe,l}\, g \tag{5.4}$$

Differentiating equation (5.4) with respect to time and assuming that the difference $(\rho_{Ti,s} - \rho_{Fe,l})$ is constant (i.e. independent of time)

$$\frac{dF_{NDF}}{dt} = \frac{dV_{imm}}{dt} (\rho_{Ti,s} - \rho_{Fe,l})\, g \tag{5.5}$$

Figure 5.9 depicts some typical results for the titanium dissolution experiments. The diameter of the cylinder was

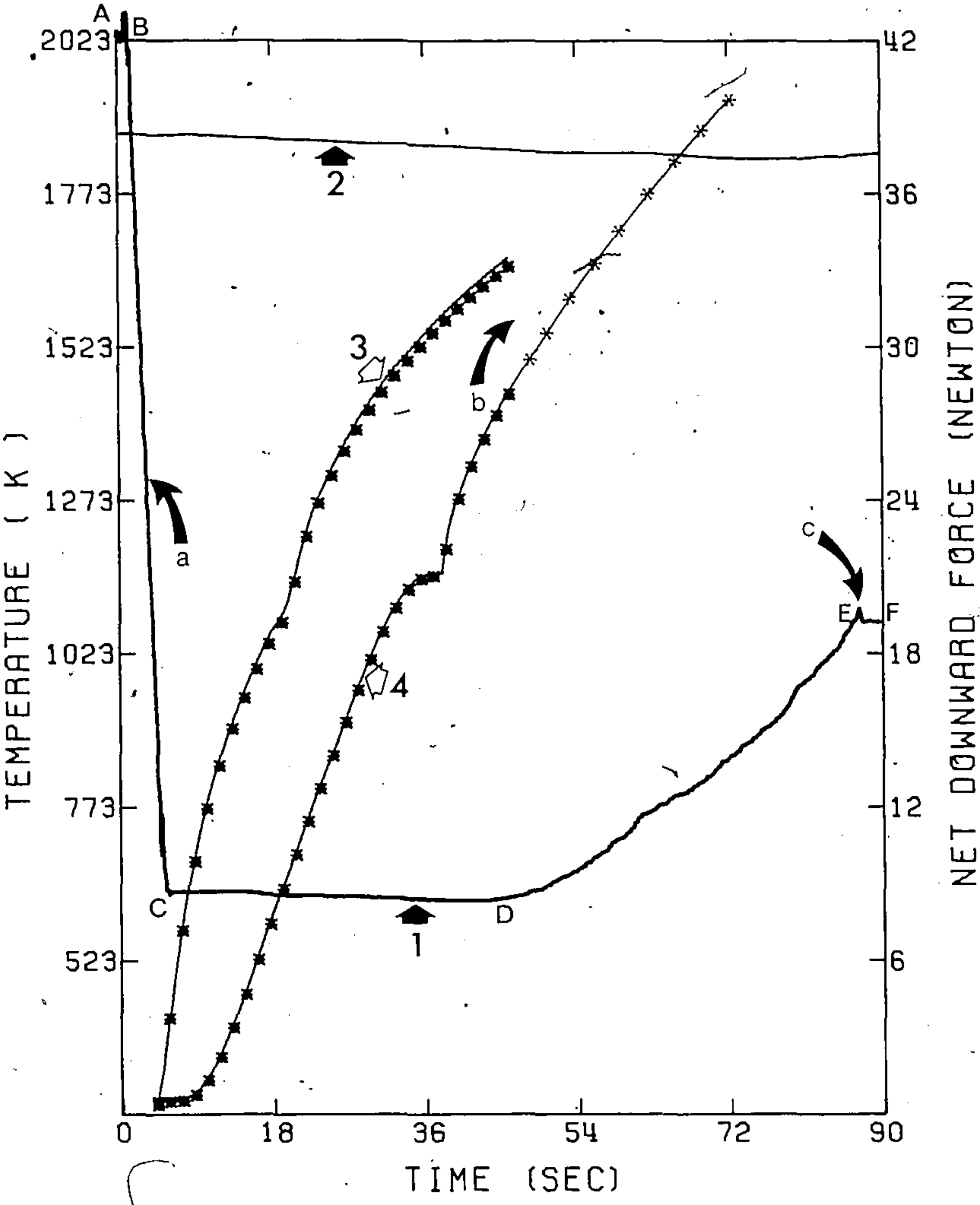

Figure 5.9 Results from a typical titanium dissolution experiment in liquid steel. Cylinder diameter 5.08 cm and 20 cm in length.

1) Registered net downward force;
2) Measured steel bath temperature;
3) Measured and predicted temperature at a point 1.95 cm from cylinder centerline;
4) Measured and predicted centerline temperature.

5.08 cm (2") and its length 20 cm. The two thermocouples were 9 cm away from the cylinder's bottom.

Curve one of figure 5.9 shows the force registered on the load cell during the dissolution experiment. The data acquisition system started monitoring the dissolution parameters a few seconds before the immersion of the titanium cylinder into liquid steel. During the period AB the load cell registers only the gravitational forces. When the leading edge of the titanium cylinder touches the surface of the steel bath the force which the load cell monitors starts to decrease. This is due to the increase in the buoyancy forces and is represented in line one by the segment BC. The subsequent segment CD in line one depicts the steel shell period during which the shell of solid steel freezes around the cylinder. The force registered by the load cell remains constant during this period. It transpires that the expansion of titanium cylinder and the freezing of a solid steel shell tend to compensate each other so that only minor effects are exerted on the overall force balance provided they occur simultaneously.

The segment DE of line one shows the free dissolution period where there is no frozen steel shell around the titanium cylinder. During this period the volume of the titanium cylinder decreases due to dissolution and consequently the buoyancy forces also decrease (Equation 5.3). The net result is that the force which the load cell registers increases during this period. The dissolution of titanium cylinder ends at the point where the segment EF of line one starts.

Curve two of Figure 5.9 shows measured steel bath temperatures. The same line is plotted in Figure 5.10 on an expanded scale. It is clear that the steel bath temperature decreases with time up to 78th second mark and that this must be largely due to heat losses from the steel bath since the power was turned off during an experiment. However, following the 78th second, a sharp increase in the steel bath temperature is to be observed. This fact can only be attributed to the exothermic effects of titanium as it disperses into the liquid steel during dissolution.

Lines three and four show experimental and predictive temperatures in the interior of the titanium cylinder. The solid lines represent predictions while the points show the measured temperatures. Curve four shows the temperature at vertical axis of the cylinder and while curve three represents temperatures at a distance 1.95 cm away from the cylinder's vertical axis. Time zero for the cylinder's temperatures is taken as the half way point between the instant and completion of the initial immersion (i.e. points B and C in the curve one, Figure 5.9).

Referring to Figure 5.9, the centerline temperature (curve four) increases rapidly up to the thirty-fifth second of

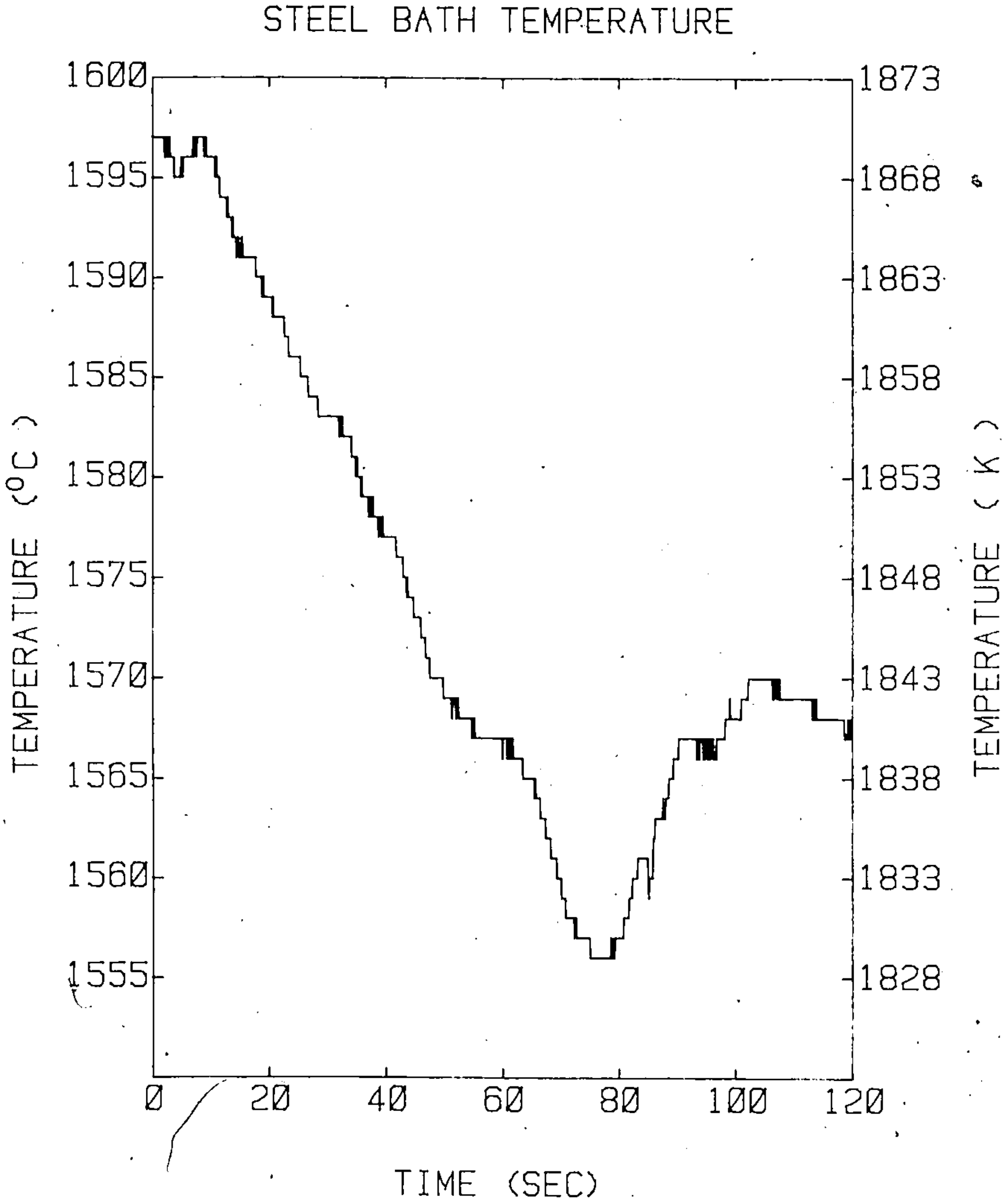

Figure 5.10 Measured steel bath temperature during a typical dissolution experiment.

immersion. A reduction in the rate of temperature rise then follows up to the thirth-seventh second. The cause for this slowed ascent can be explained in terms of the endothermic transformation of α-Ti to β-Ti. This occurs at a temperature of 882°C (1155 K). As seen there is a very good agreement between experimental and predicted temperatures.

Line three of Figure 5.9 shows measured and predicted temperatures at a radial distance of 1.95 cm from the cylinder's vertical axis. An increase in the rate of temperature rise is observed after the eighteenth second, and this can be attributed to the heat which is generated from the exothermic reaction of iron and titanium at the steel shell-titanium interface.

The dissolution of titanium in liquid steel involves two distinct periods. The first is 'the steel shell period' and the second is 'the free dissolution period'. Referring to Figure 5.9, the time coordinate of the curved arrow tips (a,b) show where each one of the above periods start. The steel shell period lies between a and b while the free dissolution period starts at b and ends at c. In the next sections of this chapter these periods are analyzed in more detail.

5.4.1 Tests for Consistency of Results

Consistency tests of the load cell results were performed for each cylinder immersion test. Thus, the immersion length for each cylinder could be found by measuring its length prior to and following immersion. From the immersion length, the volume of the cylinder which had been immersed was found. Then using the equation (5.4), the expected net downward force was calculated. Referring to Figure 5.9, the difference between the net downward force at point B and C of curve one were within 5% of that calculated.

Second, the difference between the registered force at D and E must be equal with that calculated from equation (5.3) within 5% error.

An experimental run was rejected if it failed one of these tests. For these reasons, about 10% of the experimental runs were rejected. Typical causes would be: slag freezing onto the cylinder at the melt line, cylinders hitting or touching the sides of the crucible.

5.4.2 Accuracy of the Method

The accuracy of the method depends upon the difference between the steel bath density and the density of individual element tested. The larger this difference, the higher the accuracy of the displaced weight measurements. In this respect the accuracy of estimation of volumetric change of addition during the dissolution can be found using equation (5.5), data supplied from Table 3.1 and the accuracy of weight sensor. In the case of the titanium cylinders for example, the volumetric change could be estimated within an accuracy of ±1.3 cm^3. For vanadium cylinders, volumes were within ±3.1 cm^3.

Consequently, this method can be applied with greatest accuracy to additions whose densities are most different from that of steel (e.g. Si, Al, Ti, Mg, W, B). Its applicability substantially lessens in those cases where addition densities approaching that of the steel bath.

5.5 APPLICATION OF THE MATHEMATICAL MODEL

From the foregoing discussion it is clear that the phenomena occurring during the dissolution of titanium in molten steel are quite complex. Nevertheless, it will be shown that a semi-empirical heat and mass transfer model of the dissolution process can provide good predictions.

Evidently, any such model must incorporate the essential elements of the phenomena involved. Thus, the model was used to estimate first the internal heat generation during steel shell period and second, the inwards directed heat flux during the free dissolution period.

5.5.1 Estimation of Internal Heat Generation during Steel Shell Period

In the absence of detailed information about the internal heat generation during the steel shell period, it was decided to postulate this in its simplest form by considering that there is a constant rate of heat generation at r_1 in Figure 4.2, the original steel shell interface. This heat generation is caused by the erosion of the steel shell by a constant flux of dissolved titanium supplied by the dissolving titanium core. Equation (4.15) in Chapter 4 represents the relevant mathematical expression. In expressing equation (4.15) numerically, the term $\dot{Q}''_{GEN}$ has to be applied to a small but finite elemental volume DV. In order to estimate an equivalent planar heat source the following equation can be applied:

$$\dot{Q}''_{GEN}\ (DA) \equiv \dot{Q}'''\ (DV) \qquad (5.6)$$

where DV: elemental volume

$\dot{Q}'''$: heat generation term per unit volume and per unit time

DA: surface of elemental volume DV

$\dot{Q}''_{GEN}$: planar heat source per unit surface and per unit time

Figure 5.11 shows temperature time results obtained for a 2.54 cm diameter titanium cylinder placed in a bath of steel at 1590°C (1863 K). For comparison the continuous curve one was generated on the basis of the mathematical model, taking the rate of heat generation at the steel shell titanium interface as zero throughout the dissolution process. The end of the predicted curve one (arrow d) denotes the time at which the encasing steel shell will have entirely melted back to expose solid titanium.

Curve two denotes experimental results and model predictions taking the rate of internal heat generation equal 9.5 cal s^{-1} cm^{-2} (3.97×10^5 w m^{-2}). Arrow a from curve two

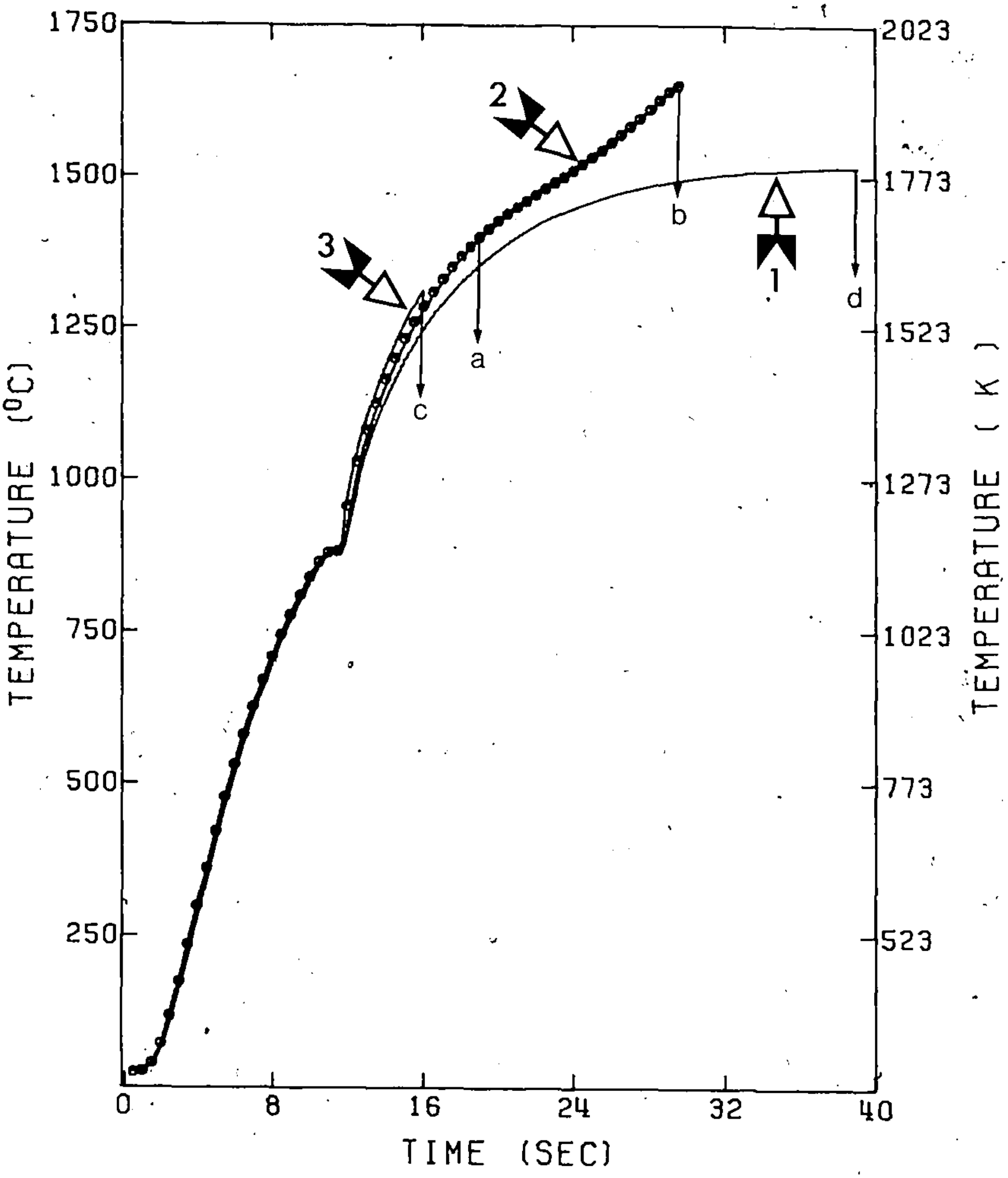

Figure 5.11 Measured and predicted temperatures in a 2.54 cm diameter cylinder.

shows the time at which the steel shell period is predicted to end and marks the start of the free dissolution period. The latter terminates at the time marked by arrow b (i.e. 30 sec). Curve three presents model predictions taking the rate of internal heat generation at the interface equal to 10.5 cal s^{-1} cm^{-2} or (4.39×10^5 w m^{-2}). Arrow c points out the time at which the steel shell period ends at the 10.5 cal s^{-1} cm^{-2} or (4.39×10^5 w m^{-2}).

The results of fifteen different cylinders were analysed in the same way. The rate of heat generation so deduced varied from 8 cal s^{-1} cm^{-2} or (3.34×10^5 w m^{-2}) to 11 cal s^{-1} cm^{-2} or (4.60×10^5 w m^{-2}). From these values an effective mass transfer coefficient for titanium could be estimated. The relevant procedures used are described in Appendix III. In this manner, the estimated mass transfer coefficient of titanium ranged from 0.025 to 0.035 cm s^{-1} or (2.5×10^{-4} to 3.5×10^{-4} m s^{-1}). In a similar way the estimated mass transfer coefficient for iron ranged from 0.024 to 0.033 cm s^{-1} or (2.4×10^{-4} to 3.3×10^{-4} m s^{-1}).

Referring to Figure 5.11, curves one, two and three tend to give different predictions after the ninth second mark. This is due to the fact that the heat generation term is applied only when the interface of titanium steel shell has reached a certain temperature called the reaction starting temperature. According to the analysis presented in Section 5.3, the reaction starting temperature was taken equal to

1090°C (1363 K) for any prediction presented in this chapter. The interfacial thermal resistance was taken equal to 10 cm^2 s °C cal^{-1} (2.39×10^{-4} m^2 K W^{-1}) throughout the analysis. This value is not an arbitrary taken constant but a value which was estimated on the basis of previous work on this subject.[79,49] The convective heat flux from the steel bath to the titanium cylinder was determined on the basis of the experimental dimensionless correlations presented in Section 4.6.

5.5.2 Estimation of Heat Generation during the Free Dissolution Period

During the free dissolution period heat is generated in the vicinity of the dissolving titanium interface. This results from the intermixing of liquid iron with titanium. Under conditions of free dissolution the convective heat flux to the cylinder's surface cannot be evaluated using the correlations presented in Section 4.6. In fact, practically no information is available on heat transfer characteristics for this class of dissolution problem. Szekely and Chaung[95] in some low temperature experimental work studied the accelerated melting of ice spheres in sulfuric acid and provide a qualitative explanation based on a higher temperature within the sulfuric acid close to the surface of the ice sphere. The higher temperature region resulted from the exothermic heat of mixing of water in sulfuric acid.

In the free dissolution period, the interfacial heat flux directed towards the dissolving titanium interface and from this interface into the body of undissolved titanium cylinder must be equal. The relevant mathematical statement is equation 5.7:

$$\left(K_{Ti} \frac{\partial\theta}{\partial r}\right)_{Ti} = \dot{q}''_{IFD} \tag{5.7}$$

where K_{Ti}: thermal conductivity of titanium;

$\dot{q}''_{IFD}$: inwardly directed external heat flux for the free dissolution of titanium in liquid steel.

This heat flux (i.e. $\dot{q}''_{IFD}$) is responsible for the rapid temperature increase which is observed in the center of the titanium cylinder (see Figure 5.9, curve four) during the free dissolution period. It is clear from this curve that the temperature in the cylinder center exceeds the steel bath temperature after a certain time. In the absence of any information about the magnitude of $\dot{q}''_{IFD}$ it was decided to postulate this in its simplest form by considering that there is a constant heat flux inwardly directed from the heat which is generated in the vicinity of the dissolving interface into the body of undissolved titanium cylinder. The rate at which the dissolving interface moves can be easily calculated as follows. Referring to Figure 5.8, the volume of the immersed portion of the titanium cylinder can be expressed as:

$$V_{imm} = \pi r^2 h \tag{5.8}$$

where r: cylinder radius

h: immersed cylinder length

Substituting equation (5.8) into (5.5), equation (5.5) can be written:

$$\frac{dF_{NDF}}{dt} = \frac{d(\pi r^2 h)}{dt} (\rho_{Ti,s} - \rho_{Fe,l}) g \tag{5.9}$$

assuming that the dissolution takes place in the radial direction only. This assumption is valid in view of special precautions which were taken to that effect (see Chapter 3). Consequently, equation (5.9) can be written as:

$$\frac{dF_{NDF}}{dt} = \pi h \frac{d(r^2)}{dt} (\rho_{Ti,s} - \rho_{Fe,l}) g$$

or

$$\frac{dF_{NDF}}{dt} = 2\pi hr \frac{dr}{dt} (\rho_{Ti,s} - \rho_{Fe,l}) g \tag{5.10}$$

Equation 5.10 shows how the radial velocity of the dissolving interface varies in relation to the rate at which the net downward force the load changes. The mathematical model in the free dissolution period runs in a coupled heat and mass transfer manner as follows: From the measured change in the net downward force (Figure 5.9 curve one) the rate at which the dissolving interface moves can be calculated using equation (5.10). For a given $\dot{q}''_{IFD}$, the centerline temperatures can be predicted. The value of $\dot{q}''_{IFD}$ which gives predictions providing the best fit for the measured centerline temperatures provides $\dot{q}''_{IFD}$ for the given experimental conditions. It is important to note that $\dot{q}''_{IFD}$ relates solely to the inwardly directed heat flux.

The rate of inwardly directed external heat generation during the free dissolution period was found to lie between 6.5 and 10 cal s^{-1} cm^{-2} or (2.72×10^5 and 4.186×10^5 w m^{-2}).

5.6 STEEL SHELL PERIOD

In order to study the steel shell period in a more detailed manner, three sets of immersion tests were carried out using titanium cylinders. These tests involved simple dipping experiments of titanium cylinders for specific times. The cylinders were then withdrawn, cross-sectioned, and steel shell thicknesses and internal reaction zones measured.

The first set of immersion tests involved titanium cylinders 2.54 cm in diameter and 20 cm in length. These cylinders were immersed to within 1.5 cm of their top surface. Immersion time periods ranged from 5 to 20 seconds. The initial steel bath temperature during these experiments was 1580°C (1853 K) and the bath cooling rate was equal to 0.3°C/sec. Figure 5.12 shows photographs of the cylinder's cross-sections following immersion. As seen, cylinder D had only a steel shell in its upper part. This was due to the steel

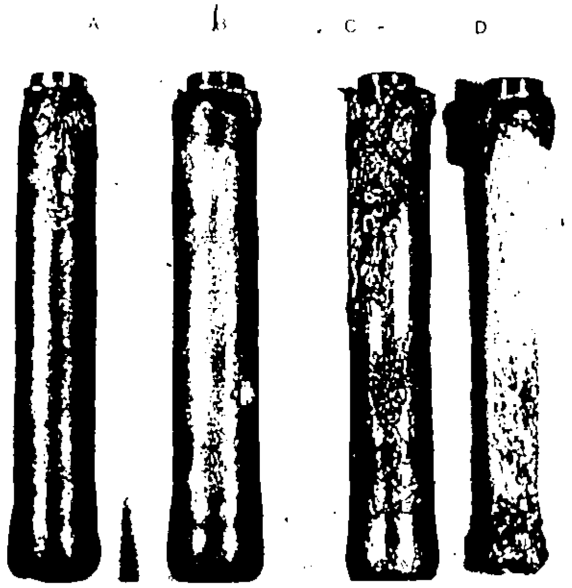

Figure 5.12 Titanium cylinders 2.54 cm in diameter immersed in steel bath of initial temperature 1580°C (1853 K) for different time periods. A = 5 sec, B = 10 sec, C = 15 sec, D = 20 sec.

shell breaking and slipping off during withdrawal. Nevertheless, the diameter of the steel shell was measured from the part which remained around the cylinder. It is worth noting at this point that the cylindrical shape is maintained for long immersion periods (i.e. cylinder D). This justifies the adoption of a one dimensional model.

Experimental and theoretical (i.e. predicted) results are shown in Figure 5.13. Line one shows how the outer radius of the cylinder changed with time. The dotted line two depicts the initial radius of the cylinder. The dashed lines three and four present the predicted extent of the internal exothermic dissolution reaction and gives the location of the steel shell and titanium interfaces, respectively. As seen, the predicted location of the steel shell/liquid steel interface and that of the inner steel shell boundary agree very well with the experimental data indicating that heat flux estimates at the outer and inner steel shell surfaces are both independently correct.

In the second set of immersion tests, cylinders 1.905 cm in diameter and 16.5 cm in length were immersed in liquid steel to within 1.0 cm of their top surface. Immersion periods ranged from 5 to 15 sec. The initial steel bath temperature during these experiments was 1580°C (1853 K) with a steel bath cooling rate equal to 0.23°C/sec. Figure 5.14 shows cross sections of these cylinders after immersion while Figure 5.15 depicts experimental and theoretical results for this set of experiments.

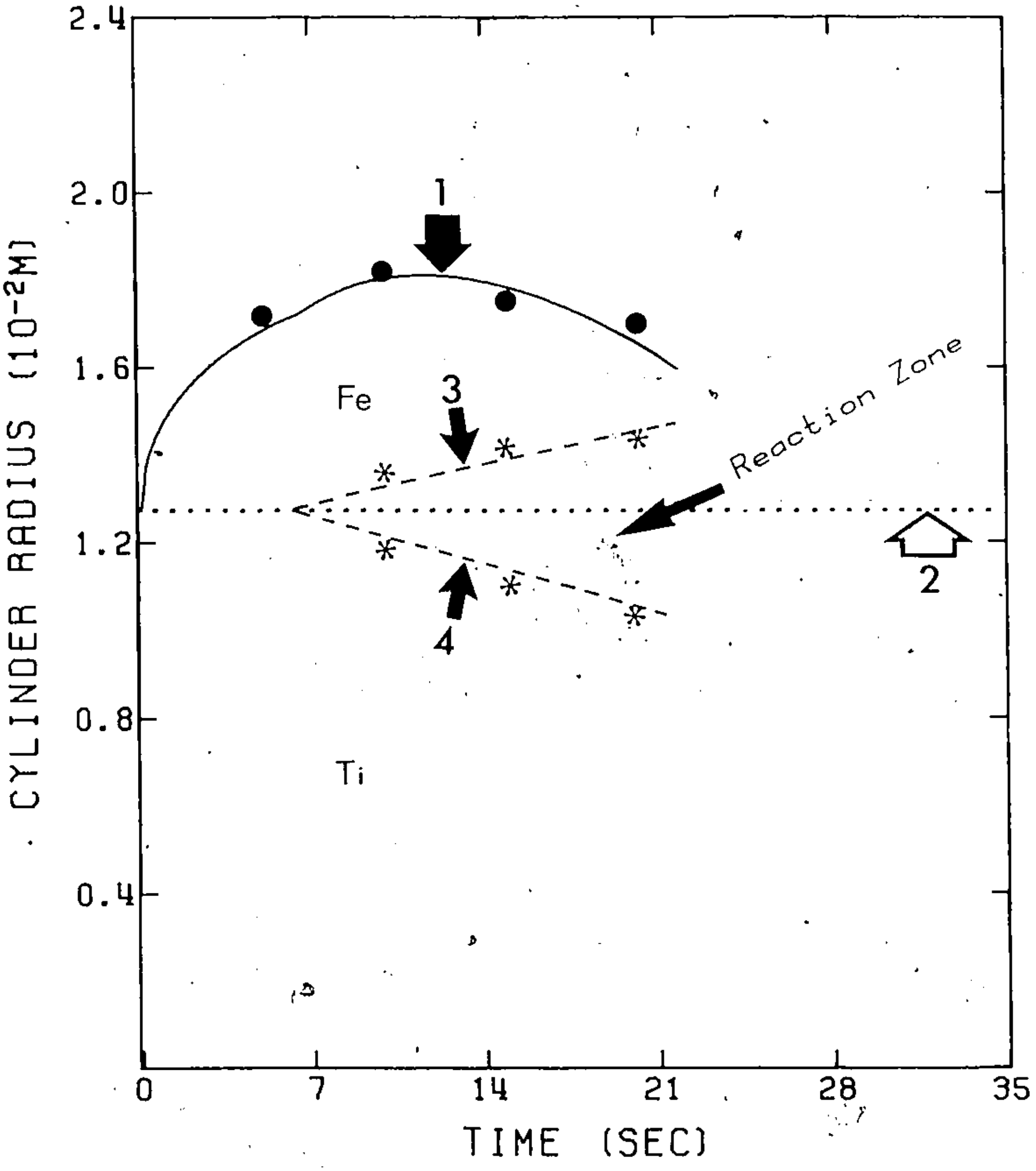

Figure 5.13 Experimental and predicted results obtained from the first set of immersion tests.

1) Predicted radius;
2) Initial radius;
3) Predicted reaction line in the steel shell;
4) Predicted reaction line in the titanium.

Figure 5.14 Titanium cylinders 1.905 cm in diameter immersed in steel bath. Pictures A and B show sectioned titanium cylinders. Picture C depicts the whole cylinder.

A

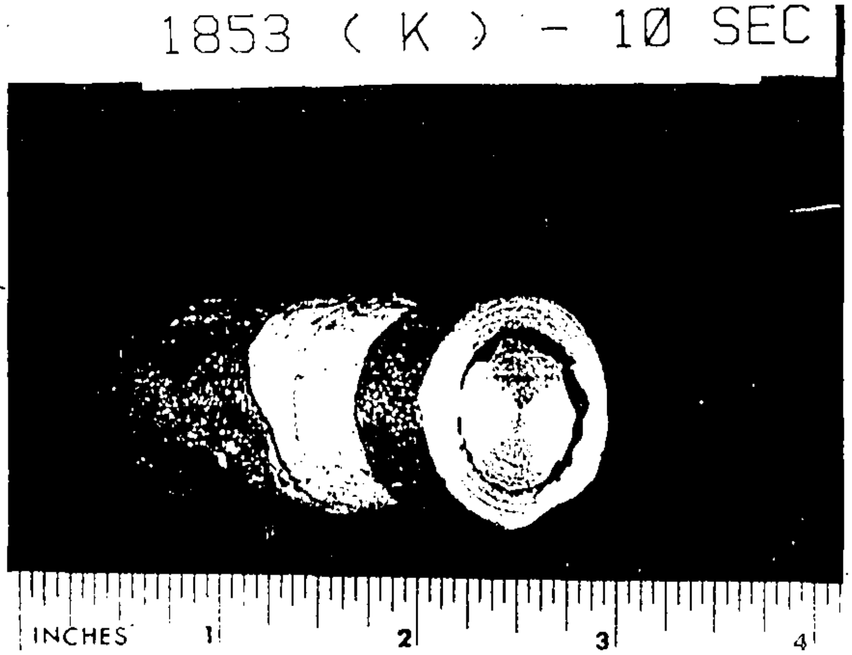

B

C

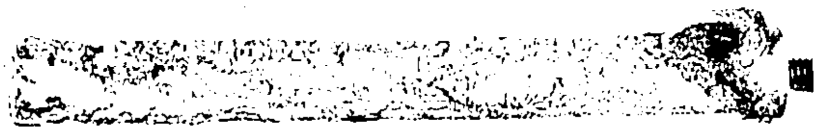

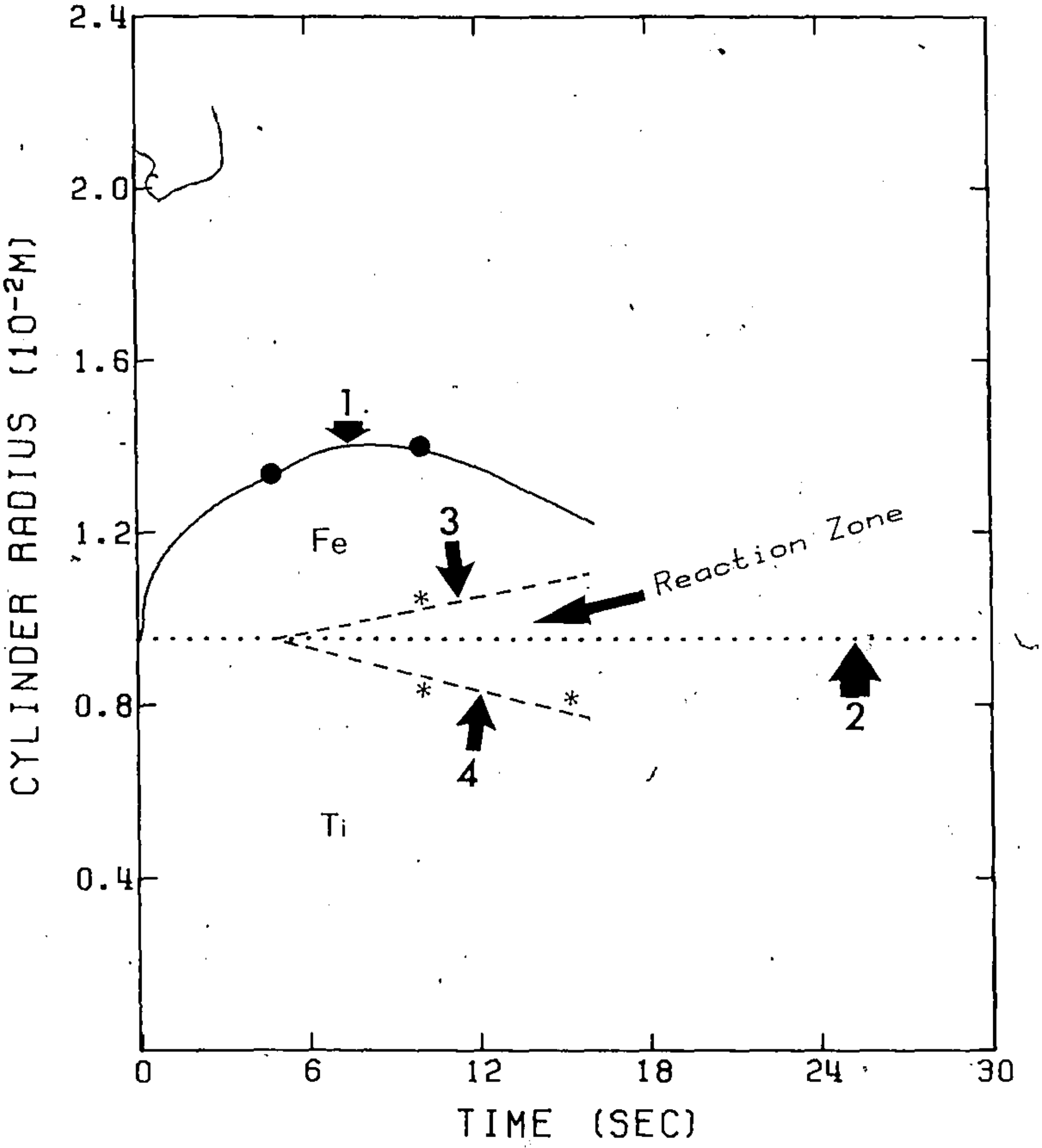

Figure 5.15 Experimental and theoretical results obtained from the second set of immersion tests.

1) Predicted cylinder radius;
2) Initial cylinder radius;
3) Predicted reaction line in the steel shell;
4) Predicted reaction line in the titanium.

In the third set of immersion tests, cylinders 3.81 cm in diameter and 16.5 cm in length were immersed in liquid steel to within 1.0 cm of their top surface. Immersion time periods ranged from 5 to 10 sec. The initial steel bath temperature during these experiments was 1580°C (1853 K) with a steel bath cooling rate of 0.32°C/sec. Figure 5.16 presents cross sections of these cylinders while figure 5.17 shows predicted and experimental results.

The fourth set of immersion tests involved titanium cylinders 3.81 cm in diameter and 16.5 cm in length. These cylinders were immersed to within 1.0 cm of their top surface. Immersion time periods ranged between 5 to 15 sec. The initial steel bath temperature during these experiments was 1600°C (1873 K) with a steel bath cooling rate equal to 0.32°C/sec. Figure 5.18 shows cross sections of these cylinders while Figure 5.19 presents the experimental and theoretical results obtained in a graphical form.

5.7 FREE DISSOLUTION PERIOD

Referring to Figure 5.9, the radius of the titanium cylinder during the free dissolution period (i.e. from D to E, curve one) was deduced on the basis of equation (5.10). These results are plotted in Figure 5.20. Line two shows the initial cylinder diameter. The steel shell period starts at A and finishes at B, while the free dissolution period commences at B and ends at D. A very important feature to be

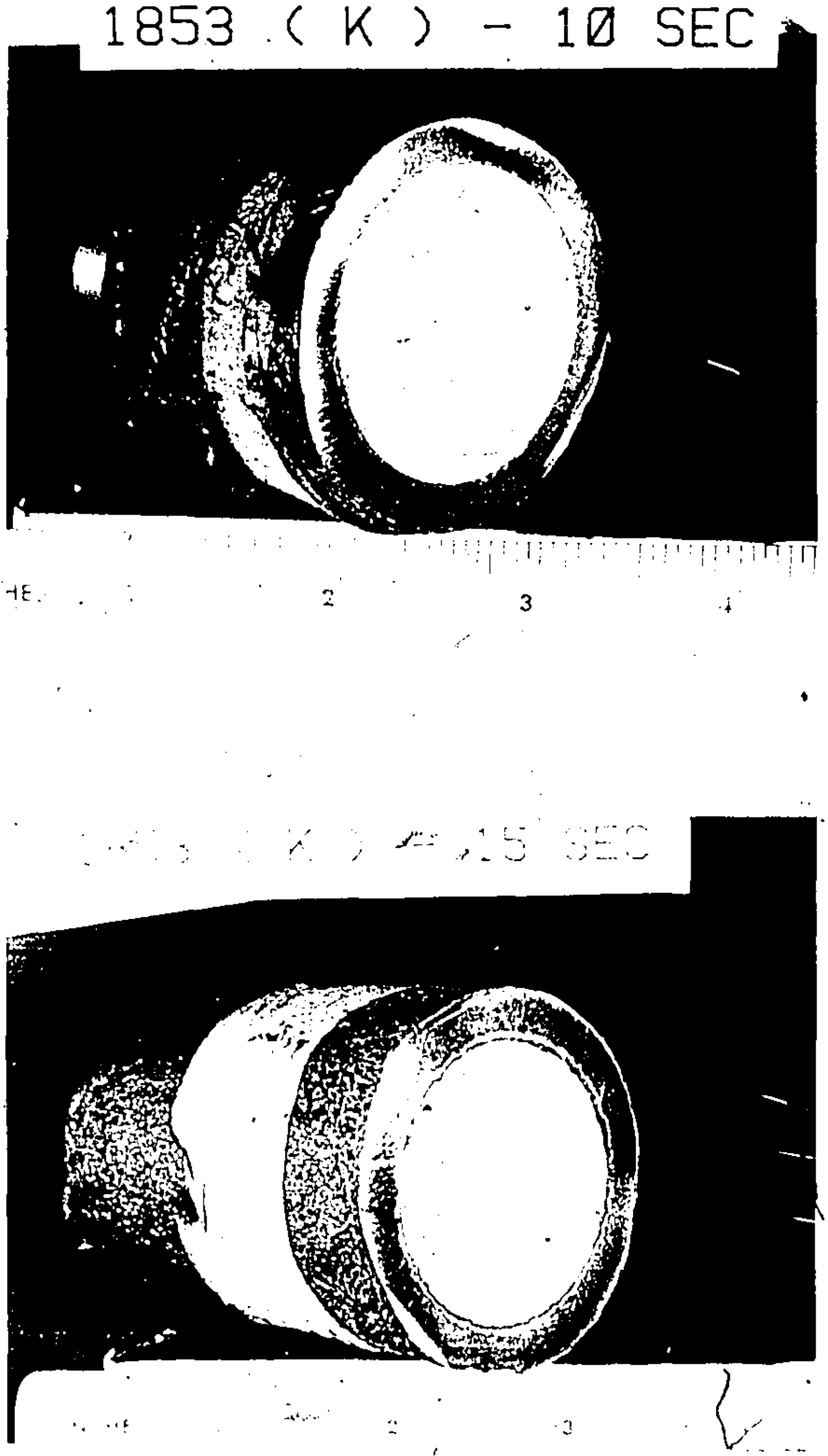

Figure 5.16 Cross sections of titanium cylinders 3.81 cm in diameter immersed in steel bath from the third set of immersion tests.

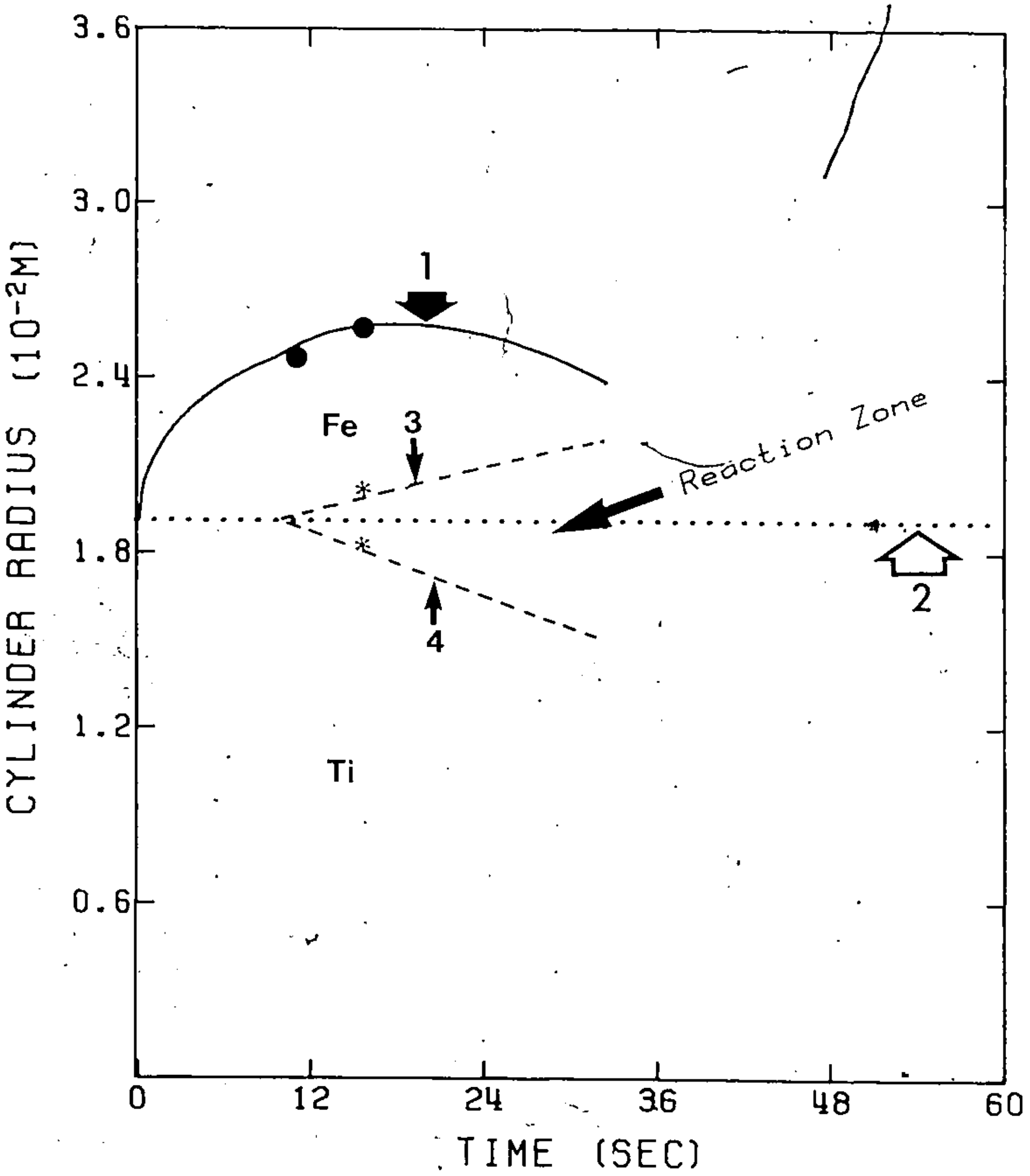

Figure 5.17 Experimental and theoretical results obtained from the third set of immersion tests.

1) Predicted cylinder radius;
2) Initial cylinder radius;
3) Predicted reaction line in the steel shell;
4) Predicted reaction line in the titanium.

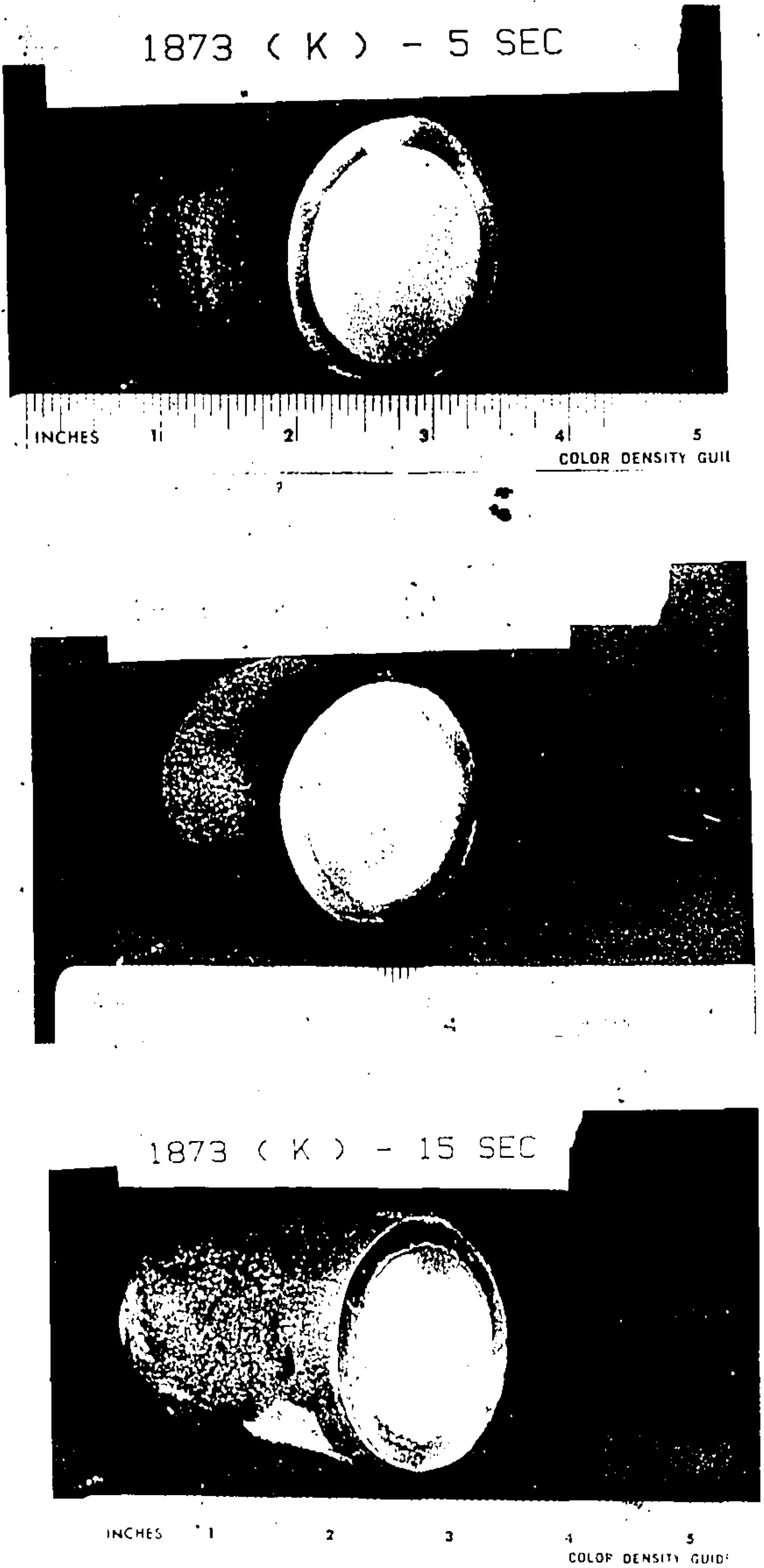

Figure 5.18 Cross sections of titanium cylinders 3.81 cm in diameter immersed in steel bath.

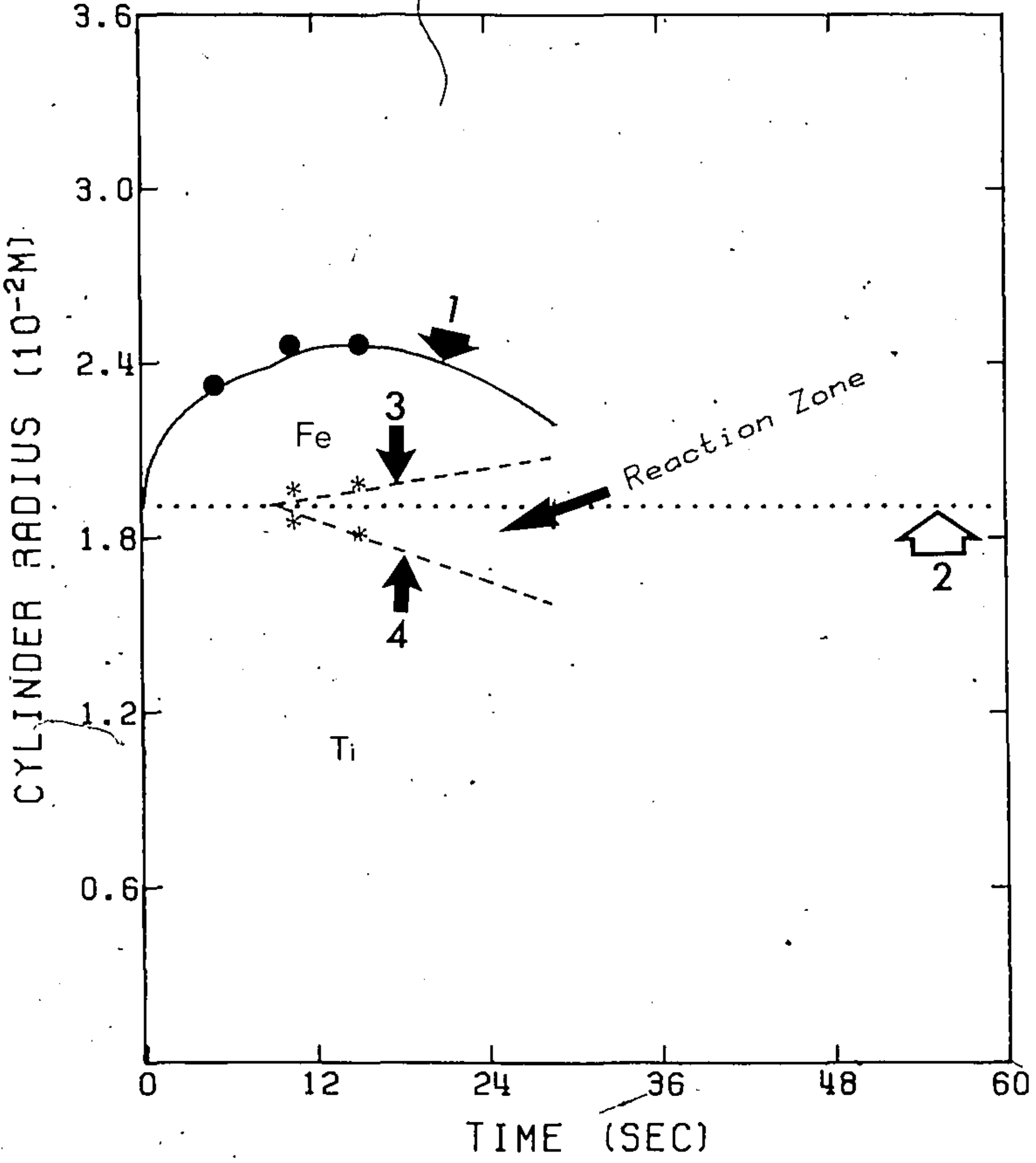

Figure 5.19 Experimental and theoretical results obtained from the fourth set of immersion tests.

1) Predicted cylinder radius;
2) Initial cylinder radius;
3) Predicted reaction line in the steel shell;
4) Predicted reaction line in titanium

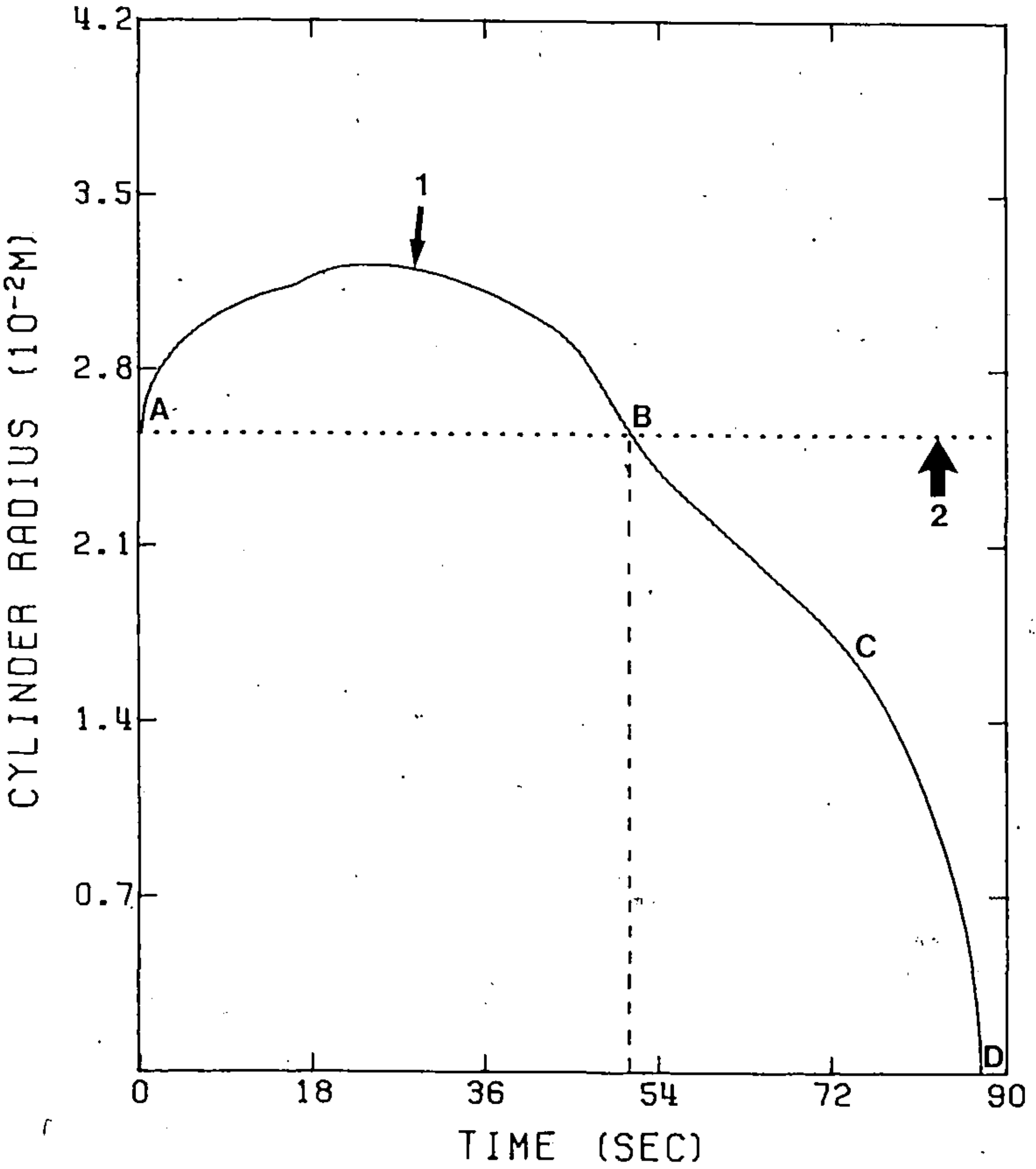

Figure 5.20 Predicted cylinder radius for a typical titanium dissolution experiment.

1) Predicted cylinder radius;
2) Initial cylinder radius;
AB) Steel shell period;
BCD) Free dissolution period;
BC) Dissolution;
CD) Melting.

observed from Figure 5.20 is the definite increase in -dr/dt, the radial velocity of the cylinders retreating surface during the free dissolution period. This rate could change quite dramatically during the final stages of free dissolution as is evident from Figure 5.20. Examination of the temperature profiles computed during the free dissolution period has shown that the temperature of the dissolving titanium interface increases. During the early stages of 'free dissolution' the temperature of the dissolving Ti interface is lower than titanium's melting temperature. As the free dissolution proceeds, the calculated surface temperatures at the dissolving interface approach the melting point temperature of titanium. Referring to Figure 5.20, the computed temperature at the dissolving interface increases between points B and C, approaching titanium's melting point at C. It is for this reason that the rate of decrease in cylinder radius increases dramatically (Section CD on curve one). It is emphasized that these high temperatures refer strictly to local phenomena.

From the foregoing observations it is clear that the free dissolution of titanium may sometimes be subdivided into both dissolution and melting periods. It is worth noting at this point that during the free dissolution period an increasing degree of turbulence is to be observed in the plume of rising steel surrounding the cylinder.

In the free dissolution period the heat which is generated in the vicinity of the dissolving titanium interface results from the intermixing of liquid iron with titanium. In order to quantify this phenomenon, it is of interest to recall that since a small amount of titanium is being mixed with a large quantity of liquid steel, the heat of mixing should closely approximate the partial molar enthalpy of the system. This partial molar enthalpy was calculated from reference 61 to be equal 14.9 k cal/mole of titanium.

Referring to Figure 5.20, an average molar flux during the free dissolution was deduced at discrete time intervals during the dissolution period. From these values, the total heat generated at the vicinity of dissolving titanium interface was estimated using the following formula:

$$\dot{Q}''_{Total} = \Delta\bar{H}_{Ti} \cdot \dot{N}''_{FD} \tag{5.11}$$

where $\Delta\bar{H}_{Ti}$: partial molar enthalpy of mixing of titanium with liquid steel.

$\dot{N}''_{FD}$: molar flux of dissolving titanium.

The $\dot{Q}''_{Total}$ term contains two components: the first is the inwards directed heat flux $\dot{q}''_{IFD}$ (i.e. towards to dissolving titanium interface) and the second is the outwards directed heat flux $\dot{q}''_{OFD}$ (i.e. towards the steel bath). The term $\dot{q}''_{IFD}$ was estimated in section 5.5.2 to be:

$$8.25 \pm 1.75 \text{ cal s}^{-1} \text{ cm}^{-2} \ (3.45 \times 10^5 \text{ w m}^{-2})$$

The outwards directed heat flux can therefore be derived on the basis of the following formula:

$$\dot{q}''_{OFD} = \dot{Q}''_{Total} - \dot{q}''_{IFD} \qquad (5.12)$$

The results are summarized in Table 5.2. As seen, the proportion of heat flux which is directed into the liquid steel increases with time and this fact can explain the accelerated turbulence which was observed during the free dissolution period.

5.8 THE INFLUENCE OF OXYGEN ON DISSOLUTION KINETICS

Figures 5.21 and 5.22 present results for titanium dissolution into liquid steel with oxygen contents of 600 ppm and 350 ppm respectively. No significant change was to be observed in any of the dissolution times.

5.9 DISCUSSION

Estimated heat and molar fluxes in the steel shell/titanium reaction zone are presented in Table 5.3. The agreement found between predicted and experimentally measured reaction zones determines the consistency of the estimated values. The reaction at the steel shell/titanium reaction zone must be largely responsible for at least halving shell melt back times for the conditions chosen. Naturally, at superheats

TABLE 5.2

HEAT AND MASS FLUXES AT DISCRETE TIME INTERVALS DURING THE FREE DISSOLUTION PERIOD

Time (sec)	$\dot{N}''_{FD}$ mole $s^{-1}cm^{-2}$	$\dot{Q}''_{Total}$ cal $cm^{-2}s^{-1}$	$\dot{q}''_{IFD}$ cal $cm^{-2}s^{-1}$	$\dot{q}''_{OFD}$ cal $cm^{-2}s^{-1}$
54.0	0.0013	19.3	8.25	11.05
64.0	0.0033	49.1	8.25	40.85
74.0	0.0036	53.6	8.25	45.35
84.0	0.0077	114.0	8.25	105.75

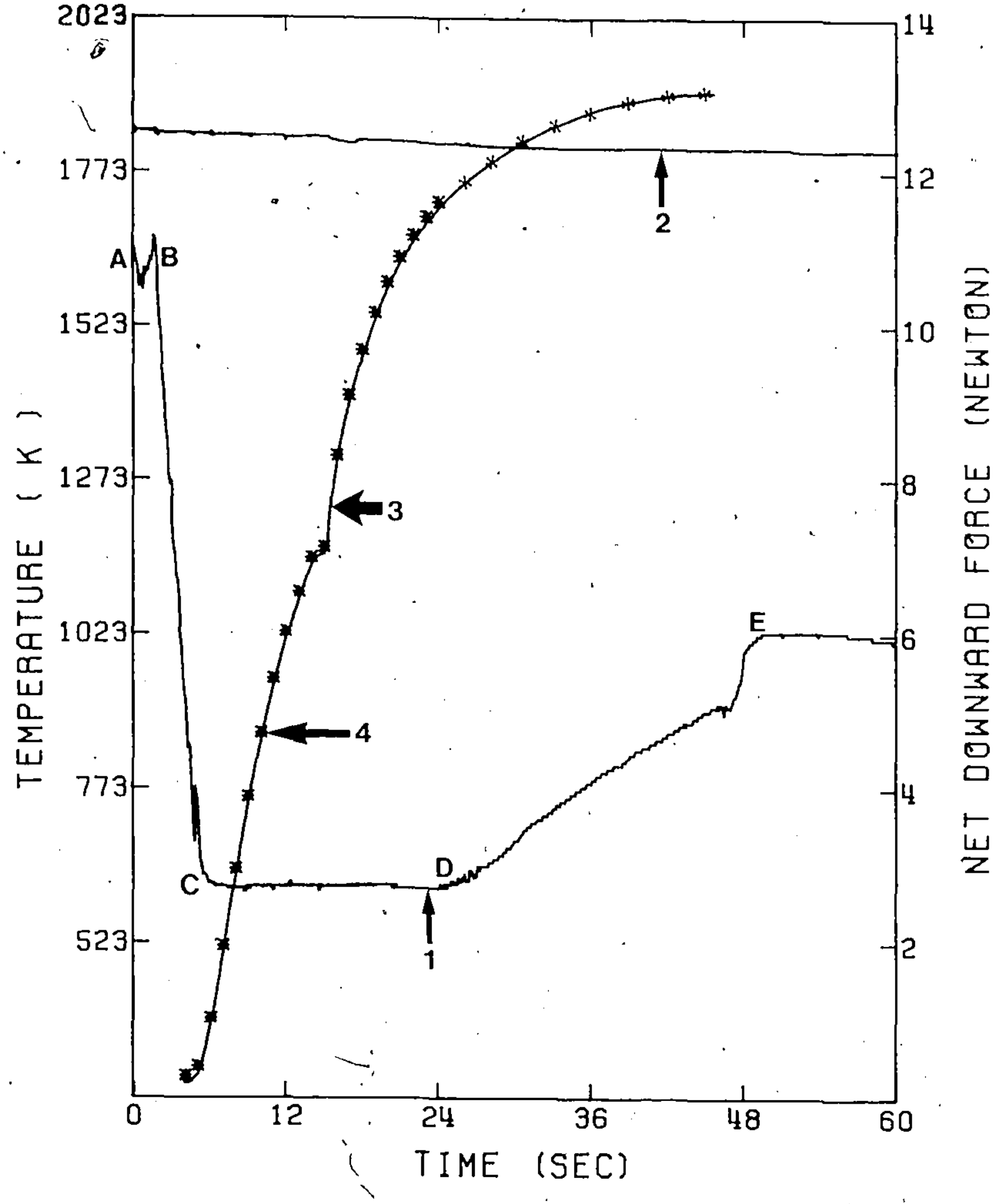

Figure 5.21 Results from titanium dissolution experiment. Cylinder diameter 2.54 cm. Steel bath oxygen content 600 ppm.

1) Registered net downward force;
2) Measured steel bath temperature;
3) Predicted centerline temperature;
4) Measured centerline temperature.

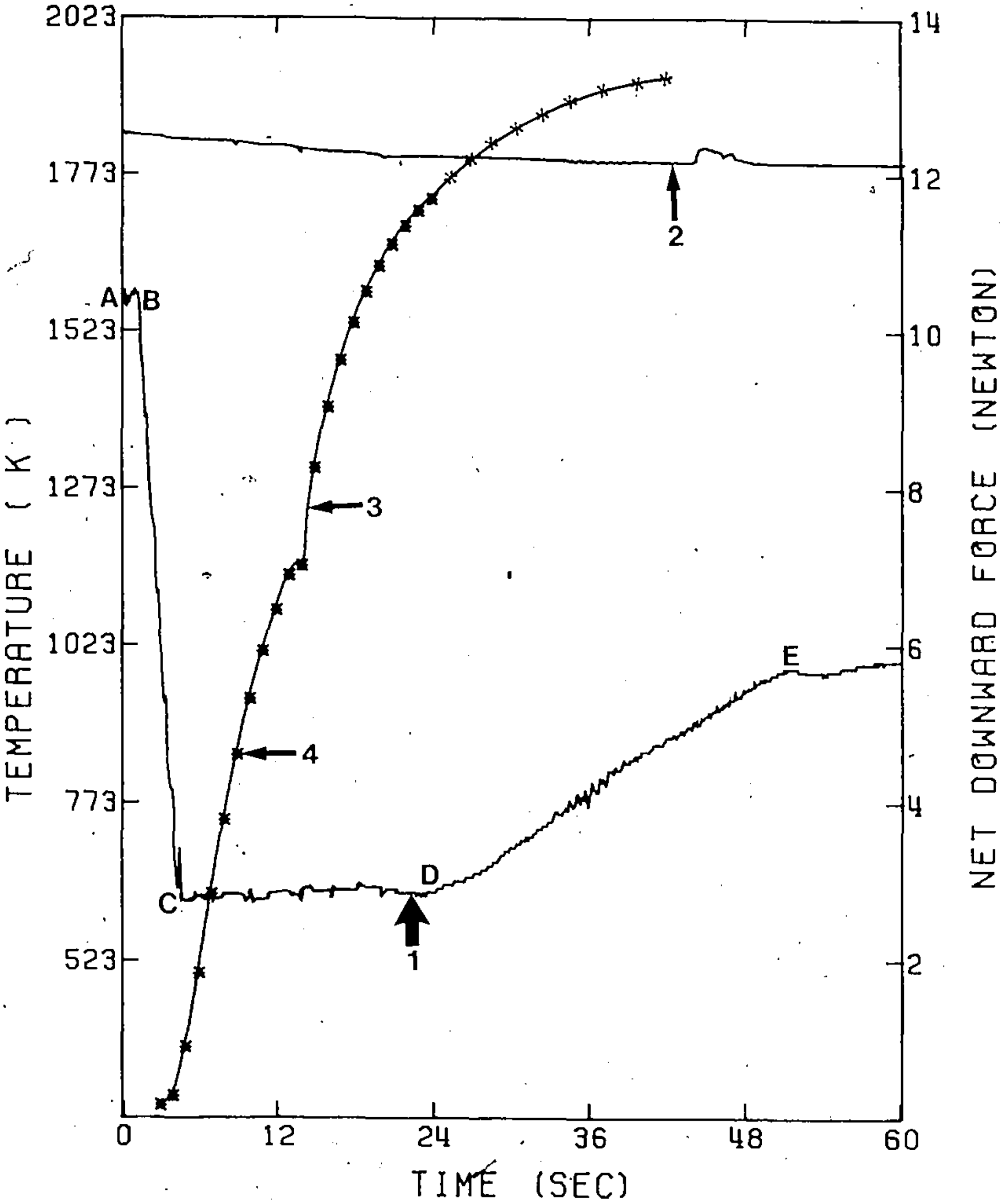

Figure 5.22 Results from titanium dissolution experiment. Cylinder diameter 2.54 cm. Steel bath oxygen content 350 ppm.

1) Registered net downward force;
2) Measured steel bath temperature;
3) Predicted centerline temperatures;
4) Measured centerline temperatures.

TABLE 5.3

ESTIMATED HEAT AND MASS FLUXES DURING STEEL SHELL PERIOD AND FREE DISSOLUTION PERIOD

		CGS Units	SI Units
Steel Shell Period	Heat flux at the interface	9.5 ± 1.5 cal $cm^{-2}s^{-1}$	3.97 ± 0.63 w m^{-2}
	Molar flux of iron	0.0018 ± 0.0002 mol $cm^{-2}s^{-1}$	18.05 ± 2 mol $m^{-2}s^{-1}$
	Molar flux of titanium	0.0013 ± 0.0002 mol $cm^{-2}s^{-1}$	13.62 ± 2 mol $m^{-2}s^{-1}$
	Mass transfer coefficient of iron	0.028 ± 0.004 cm s^{-1}	2.8×10^{-4} ± 0.4×10^{-4} m s^{-1}
	Mass transfer coefficient of titanium	0.030 ± 0.004 cm s^{-1}	3.0×10^{-4} ± 0.4×10^{-4} m s^{-1}
Free Dissolution Period	Heat flux during free dissolution	8.25 ± 1.75 cal $cm^{-2}s^{-1}$	3.44 ± 0.73 w m^{-2}

approaching zero the enhancement would become far greater since the convective heat inputs from the steel bath would be drastically reduced. As seen in section 5.6, the predicted locations of the steel shell/liquid steel interface and that of the inner steel shell boundary agree rather well with the experimental data. This indicates that the heat flux estimated at the outer and inner steel shell surfaces are both independently correct. The starting time for the reaction at the steel shell titanium interface depends mainly upon two factors: first is the cylinder diameter and second is the steel bath superheat.

The semi-empirical method of estimating heat fluxes generated during the steel shell period involves errors ~ ±15%. The error results from two factors; the first derives from the convective heat transfer correlations used at the outer surface of the steel shell while the second arises from the fact that steel shell melt back and exposure of titanium in liquid steel must be somewhat stochastic in nature. Thus, any slight imperfections in a hot, rapidly thinning shell will lead to premature exposure of titanium in liquid steel.

As pointed out in section 5.4, free dissolution commences once the steel shell period ends. In general, one can expect the free dissolution of titanium cylinders to be controlled by mass transport of dissolved titanium through a titanium rich boundary layer adjacent to the cylinder out into the liquid steel bath. Thus, continuity at the dissolving interface dictates that:

> Net moles of titanium lost from cylinder per unit time = Net moles of titanium diffusing into steel bath per unit time, i.e.

$$-\frac{d}{dt}(\pi r^2 h\rho_{Ti}/M_{Ti}) = K_{Ti}2\pi rh(C_{Ti}^{*L} - C_{Ti}^{B}) \qquad (5.13)$$

where r: cylinder radius

h: cylinder immersion length

ρ_{Ti}: density of titanium

M_{Ti}: titanium molecular weight

C_{Ti}^{*L}: liquidus concentration of titanium at the temperature of steel bath

C_{Ti}^{B}: bulk concentration of titanium in the steel

K_{Ti}: experimental mass transfer coefficient

Since h, ρ_{Ti}, and M_{Ti} are independent of time and C_{Ti}^{B} is equal to zero, equation (5.13) reduces to:

$$-\frac{dr}{dt} = \frac{K_{Ti} * C_{Ti}^{*L}}{\rho_{Ti}/M_{Ti}} \qquad (5.14)$$

Based on this expression, an experimental mass transfer coefficient can be estimated.

Ravoo et al.[96] suggested the following correlation for turbulent mass transfer from vertical plates:

$$Sh_L = 0.13\ (Gr_L\ Sc)^{1/3} \qquad (5.15)$$

where * Sh_L: Sherwood number

Sc: Schmidt number

Gr_L: Grasshof mass transfer number

Mass transfer coefficients experimentally measured and predicted from equation (5.15) during the early stages of free dissolution of titanium are presented in Table 5.4.

The features to be observed from table 5.4 are first that the experimentally measured mass transfer coefficients are higher than the predicted ones from equation (5.15) and second is the strong influence of bath temperature on measured mass transfer coefficients. This trend was observed in every experiment. The strong dependency of the mass transfer coefficient on temperature cannot be explained solely on the basis of liquid phase diffusion. It is proposed that the accelerating degree of turbulence which was to be observed during the free dissolution period altered fluid flow patterns in the vicinity of the dissolving titanium interface.

Thus, on observing the bath surface during the course of an experiment, the steel surrounding the addition was relatively quiescent during the steel shell period and the first part of the free dissolution period. However, visual examin-

---

* More explanations about these dimensionless numbers can be found in Reference 97.

TABLE 5.4

MASS TRANSFER COEFFICIENTS DURING TITANIUM FREE DISSOLUTION

Temperature	Mean Experimental Mass Transfer Coefficient cm s^{-1}	Predicted Mass Transfer Coefficient from Eq. 5.15 cm s^{-1}
1580°C	0.0183 ± 0.0015	0.0127
1630°C	0.0391 ± 0.002	0.0137

ation of the surface of the bath close to the addition showed it becoming much hotter and turbulent, with the upwelling plume of liquid becoming faster during the later stages of free dissolution. Recalling Levich's[98] proposal that the thickness of the mass transfer boundary layer δ is related to velocity:

$$\delta = f(\frac{1}{\upsilon^n}) \qquad (5.16)$$

where υ: velocity of moving liquid

n: exponent ranging from 0.5 to 1

One can expect changes in the recirculation rate of liquid steel to increase the effective mass transfer coefficient.

During the free dissolution period the relative proportions of dissolution and melting depend upon the steel bath temperature; that is, the higher the steel bath temperature, the larger the proportion of cylinder which is molten when it is dispersed in liquid steel. From the analysis of the experimental results, it was found that when the inward radial velocity of the titanium interface was less than 0.045 cm s^{-1}, dissolution dominated, while above this figure melting occurred.

An average dr/dt and an average steel bath temperature during the free dissolution period was estimated for the 17 different runs. Table 5.5 summarizes this data. Using equation (5.14), an average mass transfer coefficient was also computed. Linear regression analysis of these results was

TABLE 5.5

EXPERIMENTALLY MEASURED dr/dt DURING TITANIUM FREE DISSOLUTION

Run No.	Average Temp.	Average dr/dt
1	1564.0	0.058
2	1573.0	0.062
3	1580.0	0.057
4	1600.0	0.098
5	1625.0	0.127
6	1625.0	0.141
7	1606.5	0.082
8	1568.0	0.054
9	1551.0	0.042
10	1560.0	0.045
11	1571.6	0.066
12	1569.6	0.051
13	1570.0	0.049
14	1570.0	0.048
15	1572.5	0.049
16	1572.5	0.049
17	1580.0	0.060

performed for a relationship between log K and the reciprocal value of absolute temperature shown in Figure 5.23. The equation for the curve one is:

$$\log K = \frac{15481.54}{T} + 7.2846 \qquad (5.17)$$

with a correlation coefficient of 0.887 at 16 degrees of freedom, and a standard error of estimate 0.051. According to these data, the apparent activation energy for the solution of titanium in liquid steel was found to be 296.3 kJ/mol or (70.5 k cal/mole). The reason for this surprisingly high activation energy is twofold. First the average steel bath temperature during the free dissolution period does not represent the temperature of the dissolving interface which is higher. Second, the exothermic reaction alters the fluid flow patterns in the vicinity of the dissolving interface and makes the effective boundary layer thinner, thereby increasing the sensitivity of experimental mass transfer coefficients to changes in temperature.

While the mathematical model developed can easily predict thermal events during the steel shell period for any given set of conditions (i.e. steel bath temperature, cylinder diameter), the free dissolution period is more complex. Thus, molar fluxes cannot be evaluated from existing dimensionless mass transfer correlations, due to the complex hydrodynamic phenomena associated with this class of dissolution problem.

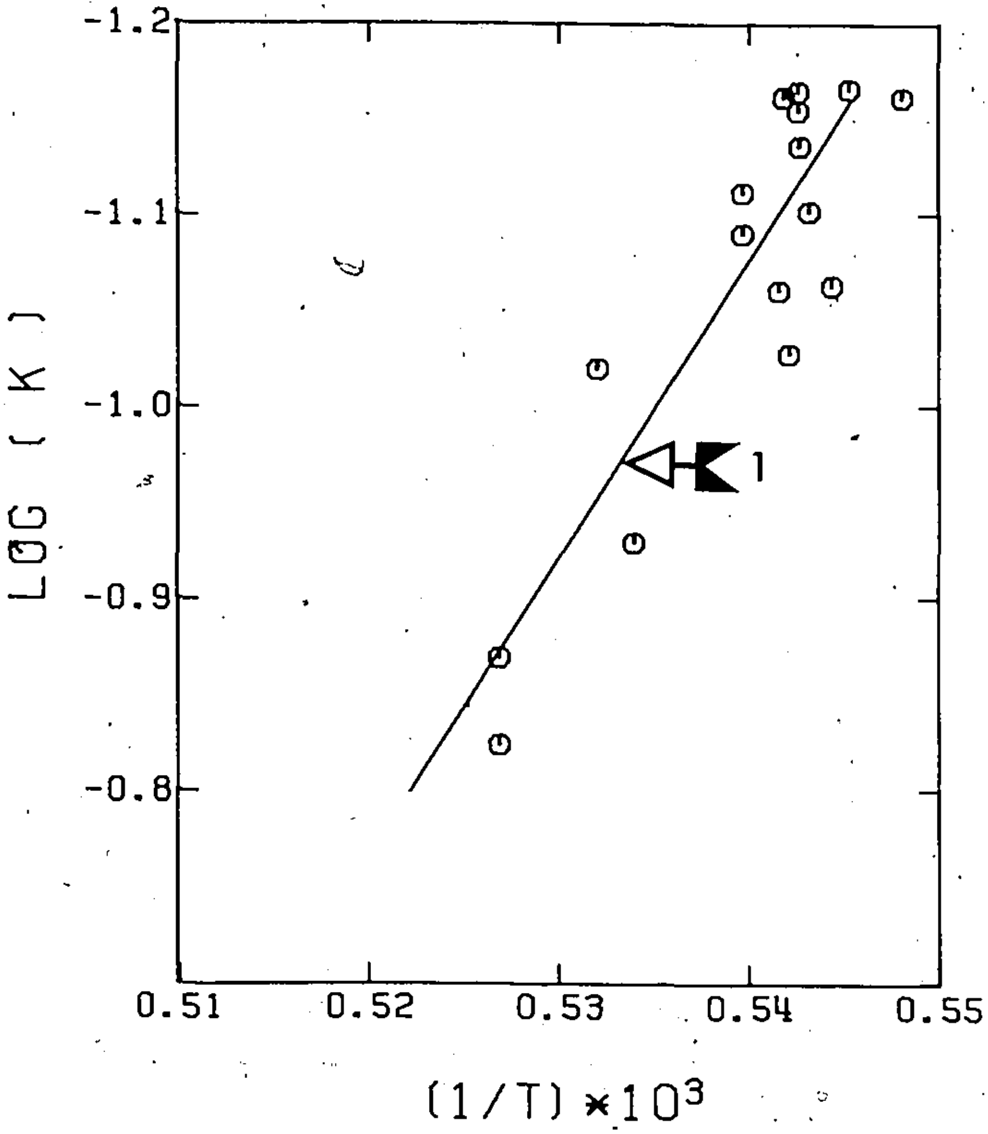

Figure 5.23 Logarithm of mass transfer coefficient versus reciprocal of absolute temperature.

In view of this difficulty, which is left for future work, a statistical approach has been adopted to predict free dissolution times.

Referring to Table 5.5, a linear regression was performed between the average steel bath temperature and the average radial velocity of the cylinder during the free dissolution period. This procedure yielded to the equation:

$$\left(\frac{dr}{dt}\right)_{mean} = -1.96 + 0.00128\ \theta \tag{5.18}$$

where θ: degree celsius

The correlation coefficient was found to be 0.945 at 16 degrees of freedom with a standard error of estimate equal to 0.01.

For a given set of conditions the mathematical model was used to predict the time for steel shell period, while equation (5.18) was used to predict the free dissolution time. The sum of these two periods represents the total dissolution time. The results are presented in Figure 5.24.

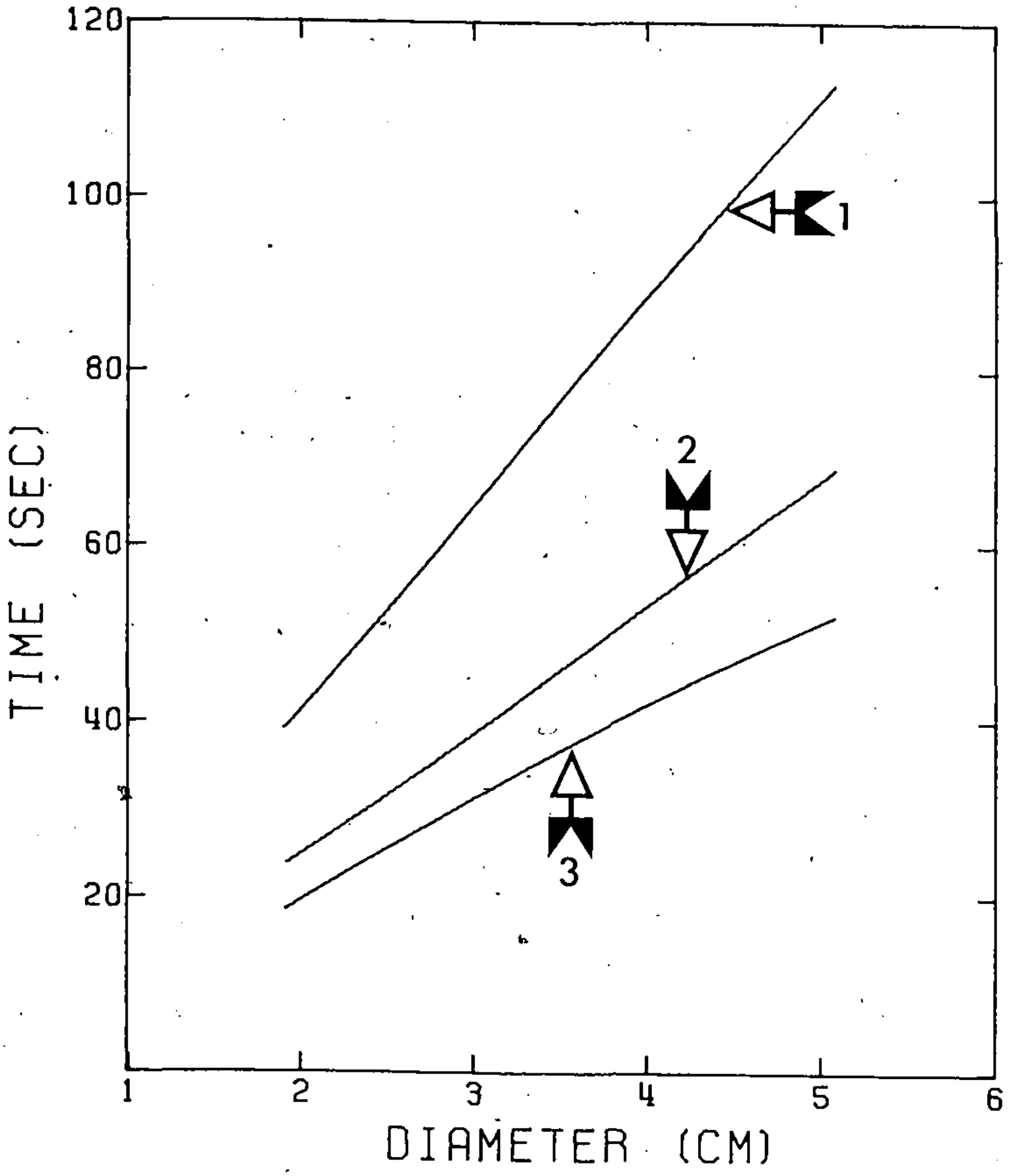

Figure 5.24 Predicted total dissolution times versus diameter for different steel bath temperatures.
1) liquid steel at 1570°C (or 1843 K)
2) liquid steel at 1600°C (1873 K)
3) liquid steel at 1630°C (1903 K)

CHAPTER 6

RESULTS AND DISCUSSION ON VANADIUM DISSOLUTION IN LIQUID STEEL

6.1 INTRODUCTION

In this chapter, the experimental results obtained for the solution of pure vanadium and ferrovanadium alloys are presented and discussed. Referring to the iron-vanadium phase diagram in Chapter 2, ferrovanadium alloys with vanadium grades lower than 60 wt% have a melting range which is lower than the steel melting point. Consequently, one can expect different solution patterns between ferrovanadium alloys of different grade. For this reason it was decided that the effect of vanadium content on the solution of ferrovanadium alloys in liquid steel should be investigated.

Four pure vanadium cylinders and ten ferrovanadium cylinders with grades varying between 30 wt% and 80 wt% vanadium were therefore prepared for immersion tests in liquid steel. The reason for the relatively small number of tests on pure vanadium cylinders were their prohibitive cost (≃$800/cylinder).

6.2 VANADIUM DISSOLUTION IN LIQUID STEEL

6.2.1 Tests with Pure Vanadium

Figure 6.1 presents results for the dissolution of a pure vanadium cylinder 2.48 cm in diameter and 20 cm in length.

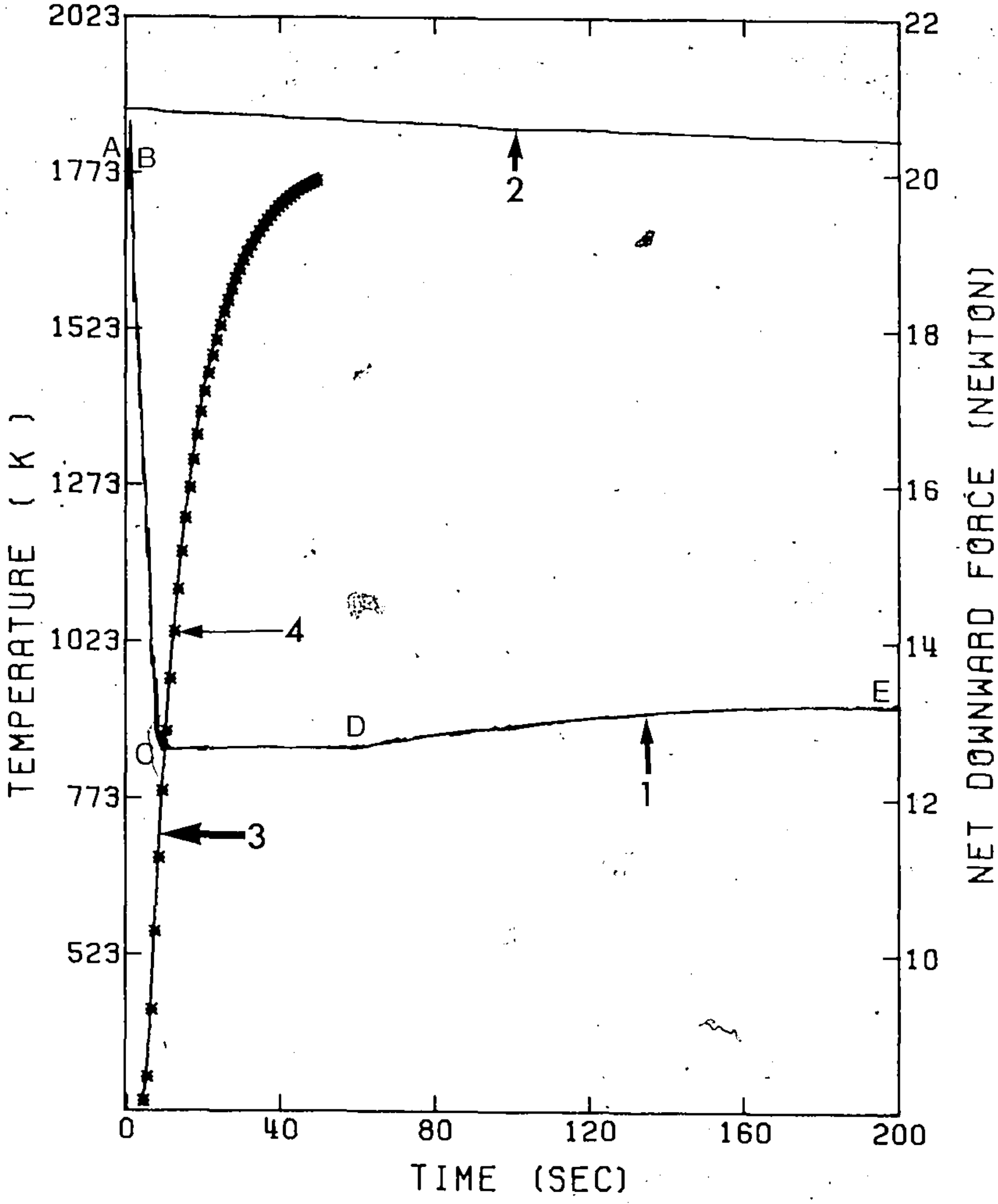

Figure 6.1 Test #1 Results from a vanadium dissolution experiment in liquid steel cylinder 2.48 cm, length 20 cm.

1) Registered net downward force;
2) Steel bath temperature;
3) Predicted centerline temperature;
4) Measured centerline temperature.

The vanadium cylinder was immersed to within 3.0 cm of its top surface. Curve one depicts the net downward force which the load cell registers. During the period AB the load cell registered only the gravitational forces. When the leading edge of the cylinder touched the surface of the steel bath the force which the load cell monitored started to decrease. Segment BC represents this period. The subsequent segment CD of curve one depicts the steel shell period (i.e. when a shell of solid steel was frozen around the cylinder). The force registered by the load cell remains constant during this period. Segment DE of line one shows the free dissolution period where there is no frozen steel shell around the vanadium cylinder. During this period, pure dissolution took place at a steady rate as evidenced by the upward slope of the force-time curve. Thus, as more of the submerged cylinder dissolved, the buoyancy force term decreased and the pull on the load cell increased. Line two in Figure 6.1 shows the measured steel bath temperature. The initial steel bath temperature for this experiment was 1600°C (1873 K). Line three presents experimental results and model predictions for the centerline temperature during the steel shell period. Time zero for the temperature of the cylinder is taken as the half way point between the times which correspond to the beginning and end of initial immersion (i.e. points B and C in curve one, Figure 6.1). As seen, very good agreement between experimental and predicted centerline temperatures is achieved.

Similar results for a vanadium cylinder 2.61 cm in diameter are presented in Figure 6.2. For this experimental run the initial steel bath temperature was 1620°C (1893 K).

Figure 6.3 shows experimental results and model predictions for the dissolution of a pure vanadium cylinder 1.36 cm in diameter and 17.5 cm in length. The vanadium cylinder was immersed to within 30 cm of its top surface. The initial steel bath temperature for this experimental run was 1636°C (1909 K).

Results for the fourth pure vanadium cylinder are presented in Figure 6.4. In this experimental run, the cylinder had a diameter of 1.38 cm and a length of 14.0 cm and was immersed to within 2.0 cm of its top surface. The initial steel bath temperature was 1643°C (1916 K). This fourth cylinder had no centerline thermocouple.

In the first three tests, the temperatures measured at the centerline of the cylinder during the free dissolution period tended to be higher than the steel bath temperature. This fact is clear in test number three (Figure 6.3). In tests one and two, the recorded centerline temperatures exhibited erratic behaviour during the free dissolution period. For this reason, centerline temperatures are not plotted during the free dissolution periods in Figures 6.1 and 6.2 respectively.

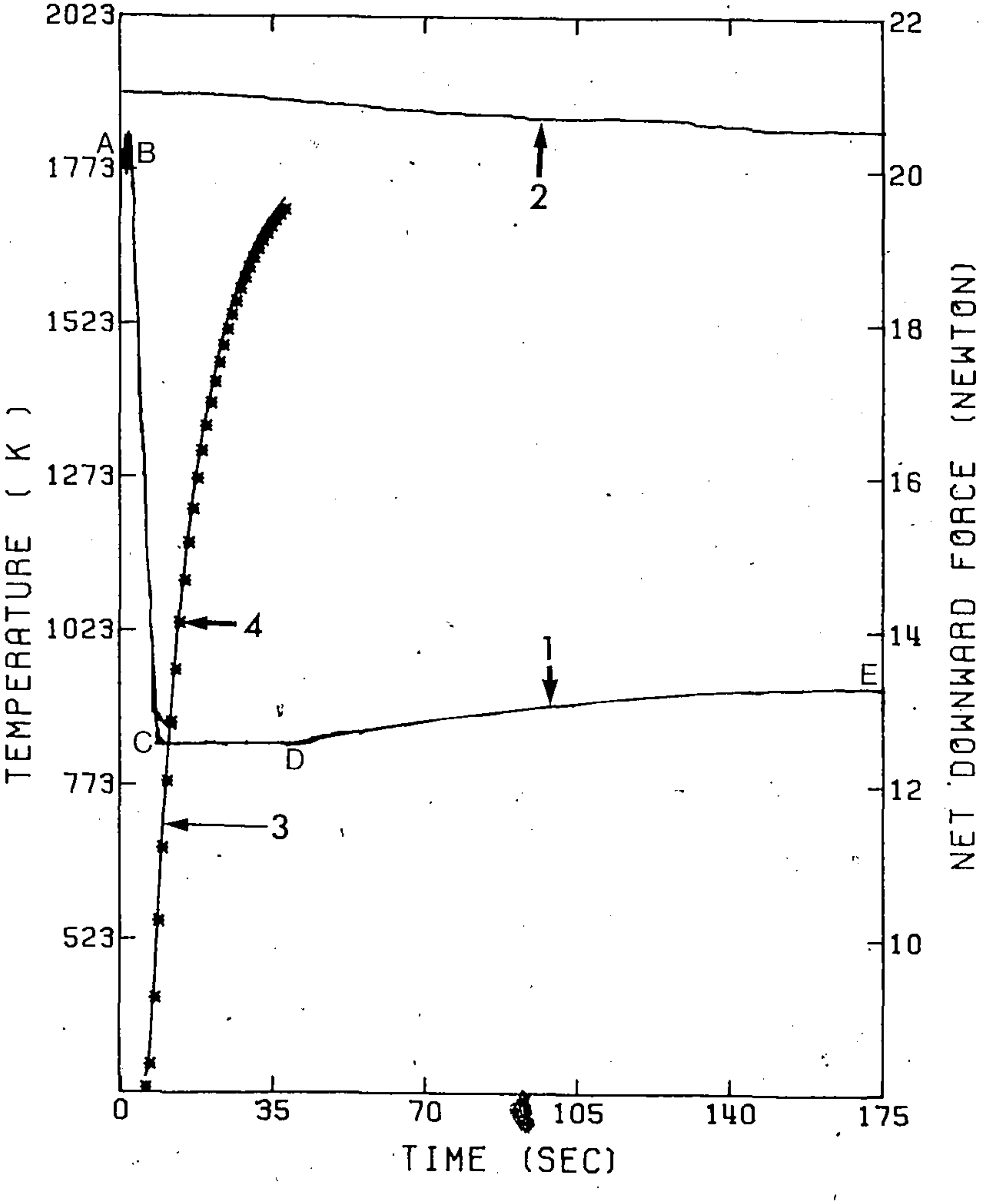

Figure 6.2 Test #2 Results from a vanadium dissolution experiment in liquid steel. Cylinder diameter 2.61 cm, length 20 cm.

1) Registered net downward force;
2) Steel bath temperature;
3) Predicted centerline temperature;
4) Measured centerline temperature.

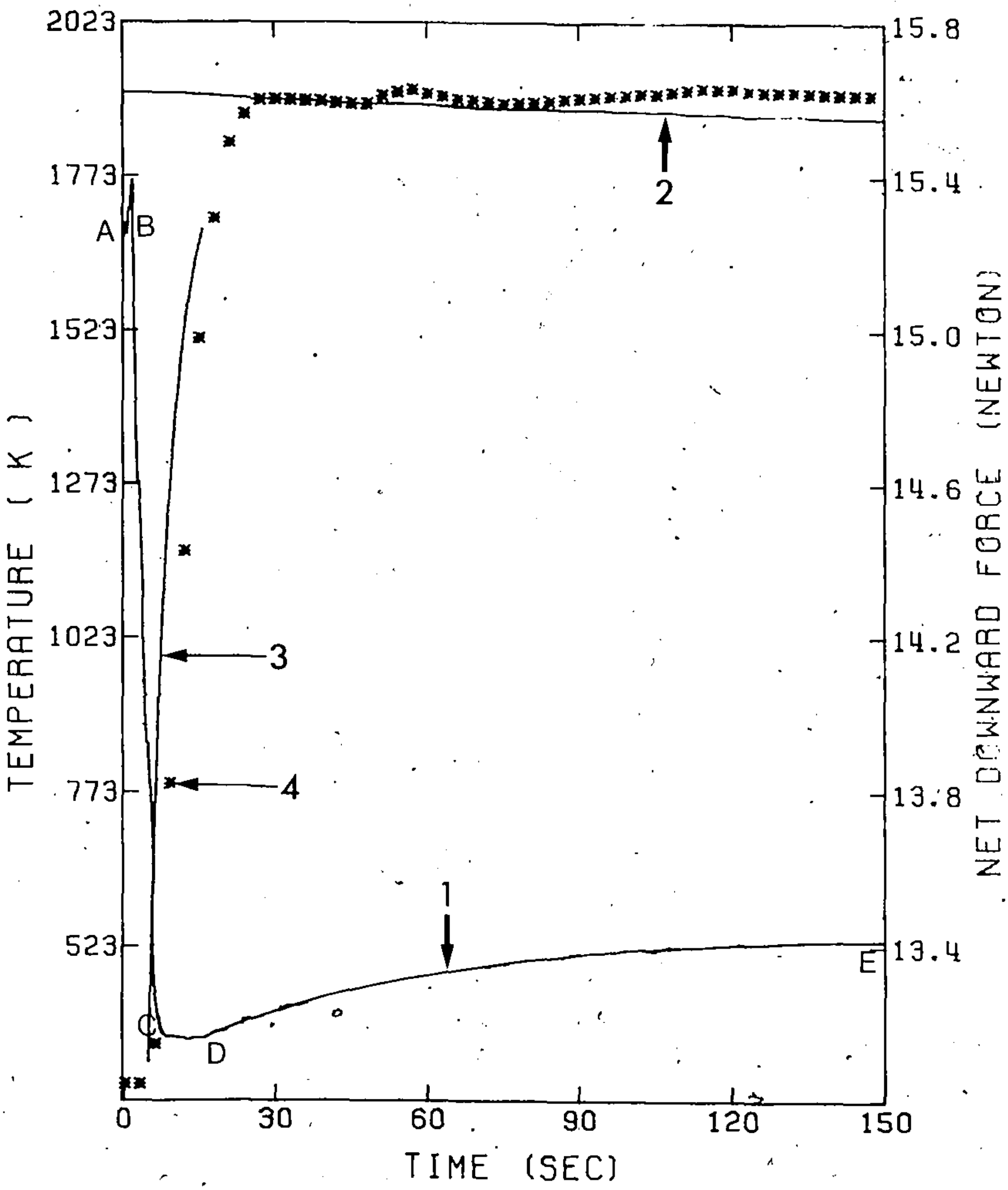

Figure 6.3 Test #3 Results from a vanadium dissolution experiment in liquid steel. Cylinder diameter 1.36 cm, length 17.5 cm.

1) Registered net downward force;
2) Steel bath temperature;
3) Predicted centerline temperature;
4) Measured centerline temperature.

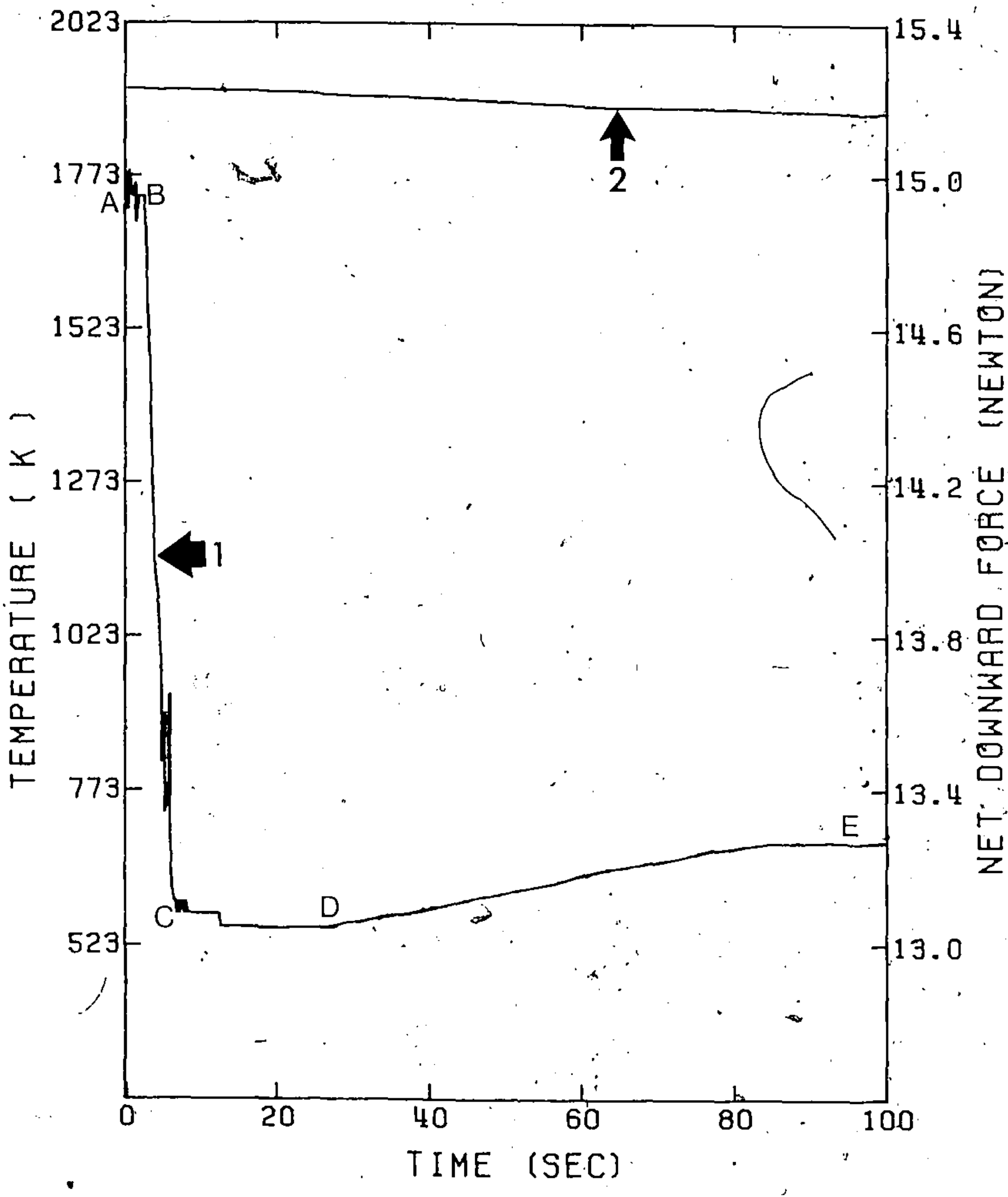

Figure 6.4 Test #4 Results from a vanadium dissolution experiment in liquid steel cylinder diameter 1.38 cm, length 1.40 cm.

1) Registered net downward force;
2) Measured steel bath temperature.

6.2.2 Tests with Different Ferro-Vanadium Grades

In some preliminary tests, Fe-V cylinders of 30, 40, 50 and 80 wt% vanadium and 2.54 cm in diameter and 10 cm in length, were immersed in liquid steel at 1600°C (1873 K). It was observed that the Fe-V cylinders with 30, 40 and 50 wt% vanadium became 'spongy' and close to collapse as they were pulled out of the steel bath after immersion times of 30 to 40 sec. On the other hand, this did not seem to be the case for Fe-V cylinders with 80% vanadium which appeared to be strong as they were withdrawn from the steel bath after extended immersion times (≈60-70 sec.).

Figure 6.5 shows results for one test with a 50 wt% Fe-V cylinder immersed in steel at 1600°C (1873 K). Line one of Figure 6.5 shows the force registered by the load cell while line two shows the measured steel bath temperature during the experiment. The feature to be noted in curve one is the sharp increase in load at the 42nd second (arrow A). This was followed by a plateau marking the sudden release of the molten alloy into the steel bath. It is worth noting at this point that under these conditions, the mathematical model predicts steel shell melt back time at 39 seconds.

6.3 INTERPRETATION OF DATA

Following similar reasoning to that explained in the previous chapter, an experimental mass transfer coefficient was computed for the free dissolution of vanadium in liquid

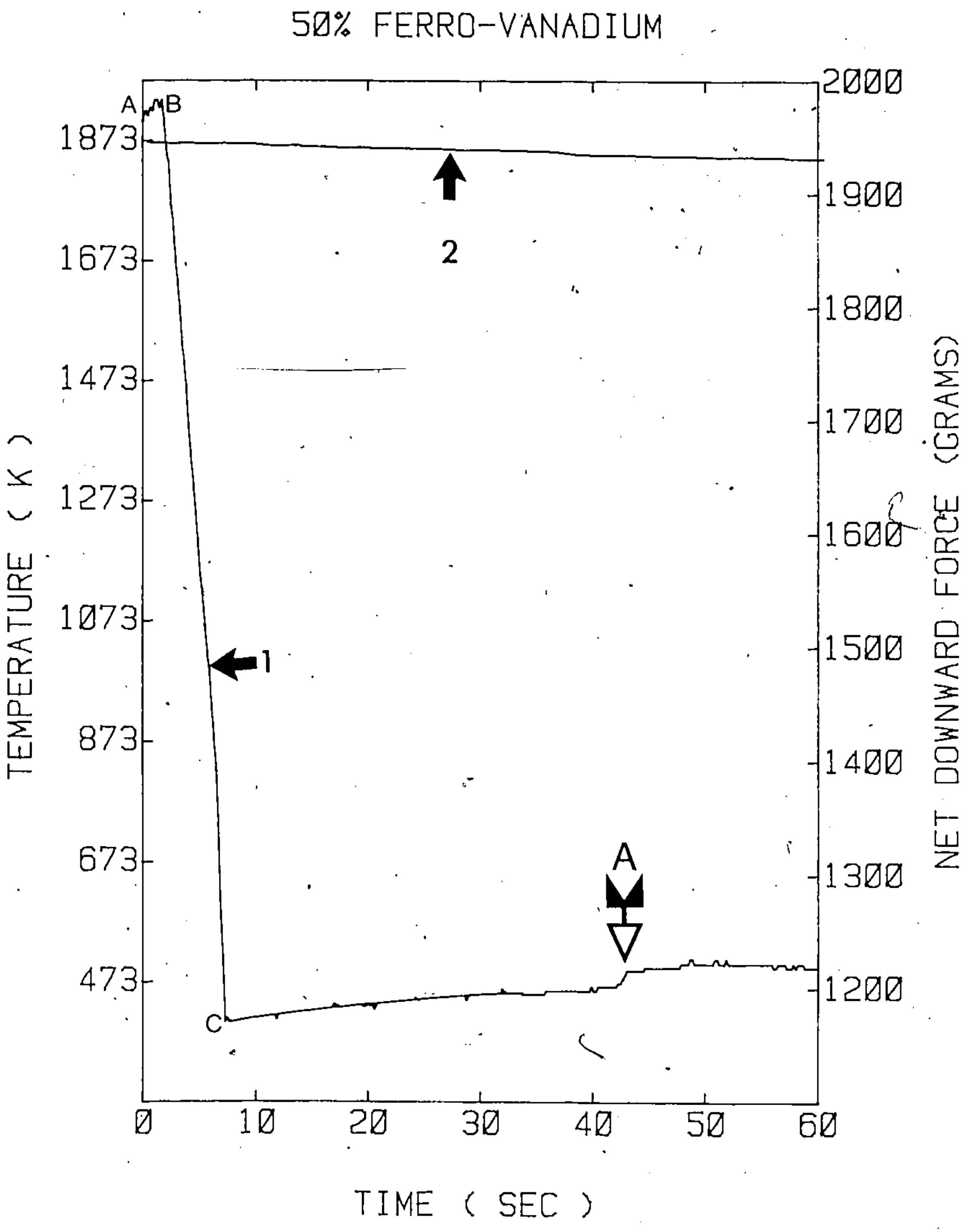

Figure 6.5 50% Ferro-vanadium cylinder: diameter 2.54 cm, 20 cm length.

1) Net downward force;
2) Measured steel bath temperature.

steel. The temperature used in these computations was the average measured steel bath temperature during free dissolution. For comparison, mass transfer coefficients may be predicted on the basis of empirical correlations available in the literature for condition of natural convection to vertical cylinders. Thus, the vanadium cylinders, on dissolving, release material which is less dense than the surrounding steel. This will generate upward currents around the dissolving cylinder. One proven relationship for dissolution of vertical cylinders is equation (5.15) presented in the previous chapter. Table 6.1 shows a comparison of predicted and experimental results.

Referring to Table 6.1, two aspects are to be noted. Firstly, the experimental mass transfer coefficients are in reasonable agreement but tend to be higher than those predicted by equation (5.15). Secondly, the inward radial velocity of the interface tended to increase during the course of the free dissolution of vanadium in liquid steel. The latter aspect is demonstrated quite clearly in Figure 6.6 where the radius of the cylinder for test number three is plotted versus time.

Theoretically, however, dr/dt is expected to be constant for normal isothermal dissolution phenomena. Also it is to be noted that the steel shell period is quite short in comparison with the free dissolution period.

TABLE 6.1

EXPERIMENTAL AND PREDICTED MASS TRANSFER COEFFICIENTS FOR VANADIUM

Test No.	Average Temperature	Experimental Average Mass Transfer Coefficient cm s^{-1}	Predicted Mass Transfer Coefficient cm s^{-1}	Experimental $(dr/dt)_{mean}$ cm s^{-1}	Experimental molar flux mole $cm^{-2}s^{-1}$	Period (sec)
1	1580°C or 1853 K	0.0038 ± 0.0003	0.0043	0.0026	0.00023	59.4 - 99.2
	1570°C or 1843 K	0.0029 ± 0.0003	0.0043	0.0020	0.00022	99.2 - 150
2	1590°C or 1863 K	0.0047 ± 0.0002	0.0043	0.0033	0.00037	50 - 100
	1576°C or 1849 K	0.0057 ± 0.0003	0.0042	0.0039	0.00044	100 - 150
3	1625°C or 1898 K	0.0061 ± 0.001	0.0046	0.0047	0.00053	16.5 - 50.1
	1615°C or 1888 K	0.0076 ± 0.001	0.0045	0.0057	0.00064	50.1 - 95.1
4	1634°C or 1907 K	0.0071 ± 0.0015	0.0047	0.0056	0.00063	22.0 - 41.2
	1625°C or 1898 K	0.010 ± 0.002	0.0046	0.0084	0.00091	41.0 - 75.0

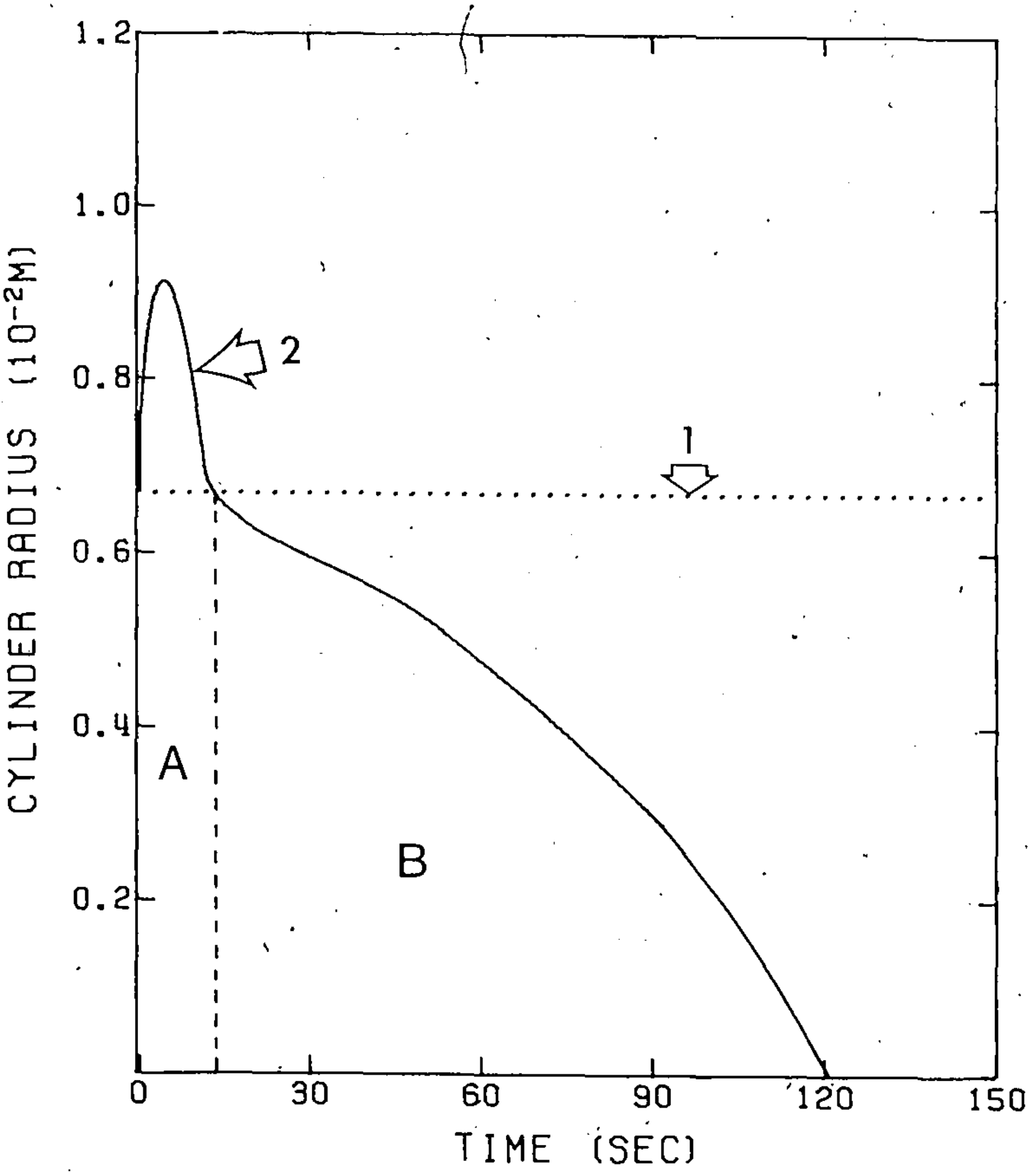

Figure 6.6 Dynamics of dissolution of pure vanadium in liquid steel.

1) Original diameter;
2) Predicted and calculated diameter;
A) Steel shell period;
B) Free dissolution period.

One common feature which was observed in all the ferrovanadium alloys tested, is that the steel shell which freezes around the cylinder melts back in a conventional way. That is, no reaction was observed at the steel shell-ferrovanadium interface.

6.4 DISCUSSION

As pointed out in section 2.7, the mixing of vanadium with liquid steel is somewhat exothermic. This may be the reason for the experimental mass transfer coefficients being higher than those predicted. Furthermore, the 'exothermicity' of mixing is stronger at higher steel bath temperatures.

Another feature to be observed from Table 6.1 is that the experimental mass transfer coefficient generally increases in the later stages of free dissolution. This may be caused by the exothermic reaction in the vicinity of the dissolving vanadium interface enhancing natural convection, thereby thinning the effective mass transfer boundary layer and enhancing mass transfer coefficients.

In Figure 6.7, the logarithm of the experimental mass transfer coefficients measured during the early stages of free dissolution are plotted against the reciprocal of absolute temperature. By regression analysis, one obtains:

$$\text{Log } K = -\frac{15707.7}{T} + 6.082 \qquad (6.1)$$

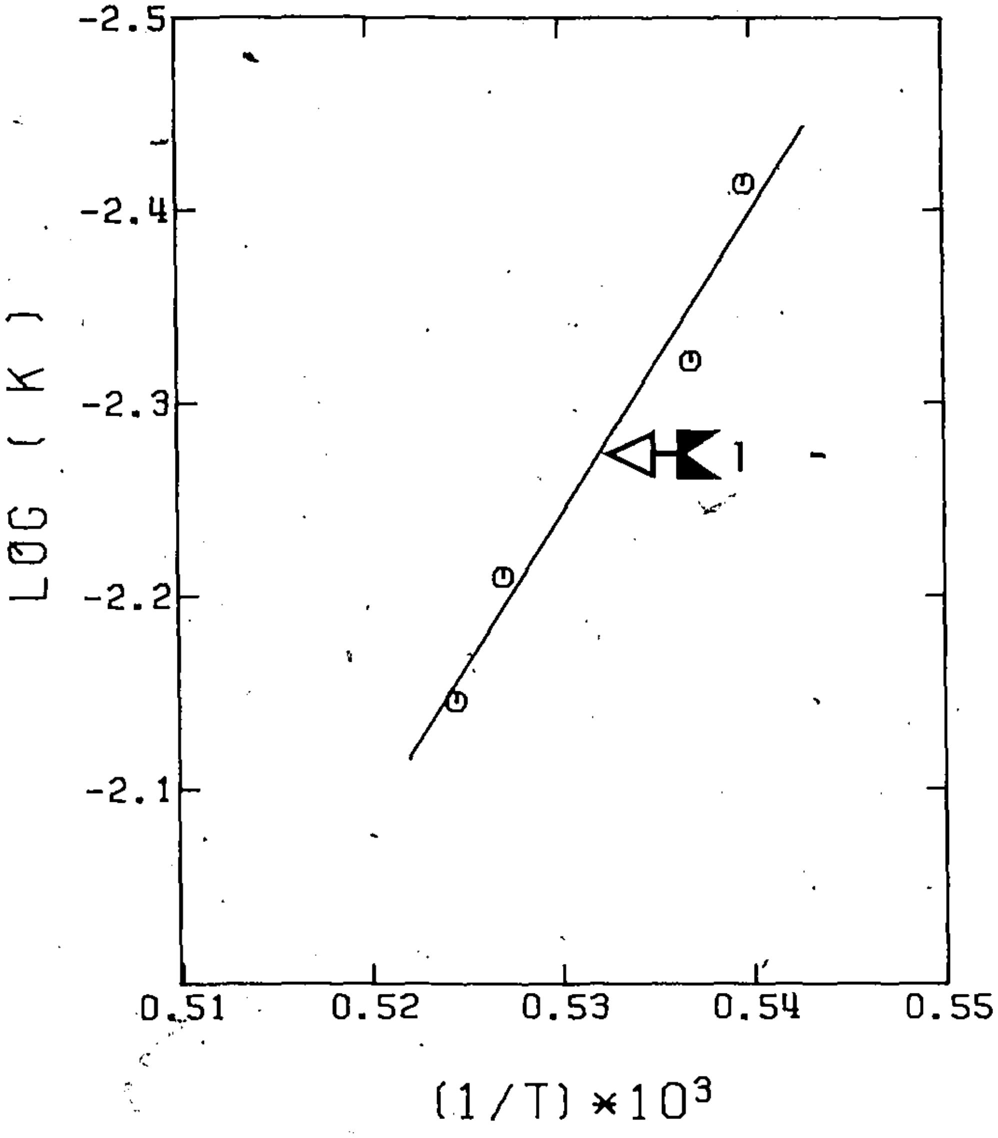

Figure 6.7 · Logarithm of experimental mass transfer coefficients for vanadium versus the reciprocal of absolute temperature.

Equation (6.1) is plotted as curve one of Figure 6.7. The slope of this line represents an Arrhenius-type apparent activation energy for the solution of vanadium in liquid steel. The value was found to equal 71.5 kcal/mole or (300.6 kJ/mole). This large apparent activation energy for the dissolution of vanadium in liquid steel is close to that obtained by the author for titanium dissolution in liquid steel.

Krupman et al.[37] also measured a large apparent activation energy for the dissolution of molybdenum in liquid steel. They report values in the order of 65.1 kcal/mole (273.4 kJ/mole). These uncommonly high values for vanadium, titanium and molybdenum are most likely explained on the basis of the exothermic reactions taking place as they dissolve in liquid steel. For such elements, the temperature at the dissolving interface is higher than the temperature of the bulk steel and tends to increase during the course of dissolution. Consequently, one can regard their dissolution as being non-isothermal. Therefore, the high activation energy reported by Krupman et al.[37] for molybdenum dissolution can be explained on a similar basis to the systems studied in the present work.

Based on all the experimental work carried out on the behaviour of pure vanadium and Fe-V alloy additions in steel baths, it is concluded that the dissolution proceeds via a heat transfer or melting dominated mechanism for alloys containing less than 68% vanadium and by a mass transfer mechanism for all alloys containing more than this amount.

From the results presented in Table 6.1, an average rate of radius decrease $(dr/dt)_{mean}$ and an average steel bath temperature during the free dissolution was calculated for each dissolution test on pure vanadium. A regression between $(dr/dt)_{mean}$ and bath temperature yielded:

$$(dr/dt)_{mean} = -0.11 + (0.75 \times 10^{-4})\ \theta \qquad (6.2)$$

where θ: temperature in °C.

At 1600°C (1873 K) equation (6.2) gives:

$$(dr/dt)_{mean} = 0.0045 \qquad (6.3)$$

From this equation and from equation (5.14) an average molar flux of vanadium during free dissolution was found to be:

$$\dot{N}''_{mean} = 0.0005\ \frac{\text{mole}}{\text{cm}^2\ \text{sec}} \quad \text{or}$$

$$N_{mean} = 0.025\ \frac{\text{gr of V}}{\text{cm}^2\ \text{sec}} \qquad (6.4)$$

Shantarin et al.[38] have found that solution rates of ferro-alloys are higher than the corresponding solution rates of pure metals. They proposed the following equation:

$$N_{FeMe} = \frac{N_{Me}}{(\%Me)_{FeMe}} \; 100\% \qquad (6.5)$$

where N_{Me}: pure metal solution rate in (gr cm^{-2} s^{-1})

$(\%Me)_{FeMe}$: percentage of element in the ferro-alloy

N_{FeMe}: solution rate of ferro-alloy in (gr cm^{-2} s^{-1})

According to Shantarin et al., they feel that equation (6.5) implies that the concentration gradients are identical to pure metals and ferro-alloys and consequently a greater loss of specimen weight is necessary in the solution of ferro-alloys to maintain the same concentration gradient. Since Santarin et al.[38] were able to apply this ratio satisfactorily in the solution of pure W and FeW and the solution of pure Mo and FeMo, equation (6.5) has been adopted as a first estimate to the Fe-V system.

Thus, Figure 6.8 shows the predicted melting/dissolution times required for 2.54 cm diameter cylinders of ferrovanadium to dissolve into a steel bath at 1600°C (1873 K) versus ferro-alloy grade. As seen, all alloys below 68% V require approximately 33 seconds while those above need a minimum of 240 seconds. Pure vanadium requires the maximum time of 316 seconds. It is important to note that vanadium would start dissolving in the bath at all compositions once the steel shell freezing on them had remelted.

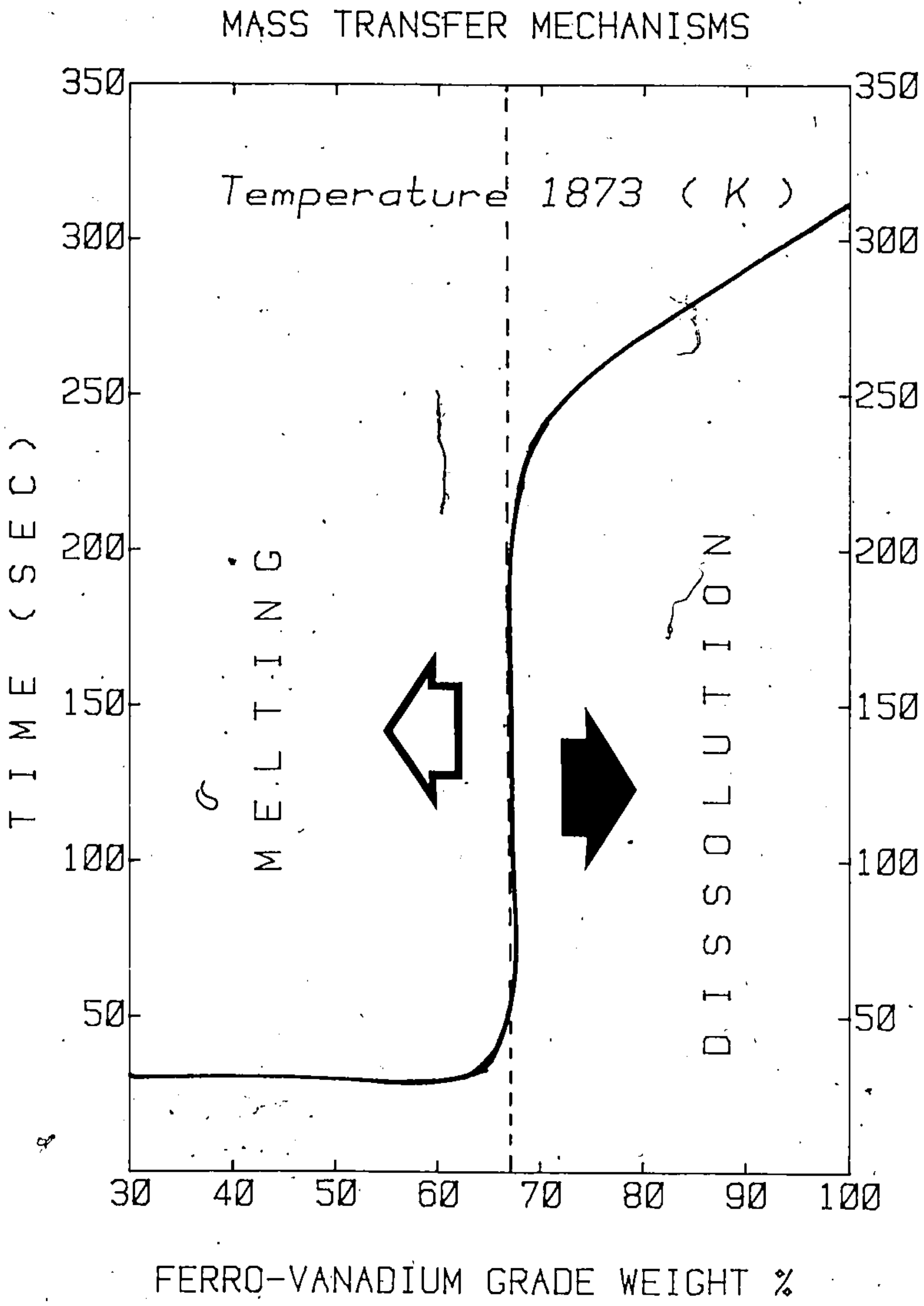

Figure 6.8 Predicted melting/dissolution times required for 2.54 cm diameter cylinders of ferrovanadium to dissolve into a steel bath at 1600°C (1873 K) versus ferrovanadium grade.

Figure 6.8 demonstrates clearly the significant difference in solution times between the different grades of ferrovanadium. In grades where melting occurs, the kinetics is about seven times faster than in grades where dissolution dominates. Consequently, improved consistency and efficiency of alloy additions to steel baths can be expected for steelplant practises calling for the use of the low grade ferrovanadium alloys.

CHAPTER 7

CONCLUSIONS

The purpose of this work was to investigate the dissolution of high melting point additives to liquid steel. For this reason, titanium and vanadium were chosen as representative cases for study. Conclusions resulting from the present investigation are outlined below.

1) An experimental technique for measuring the dissolution of cylindrical shaped specimens in liquid steel has been developed. The dissolution can be monitored by measuring a) the apparent weight of the specimen, b) temperatures of the specimen at various locations and c) the temperature of the steel bath.

2) During the dissolution of titanium in liquid steel, two distinct periods were identified. The 'steel shell period' and the 'free dissolution period'.

3) In the steel shell period, a steel shell is first formed when a titanium addition is immersed in liquid steel. The dissolution reaction starts at the steel shell solid titanium interface, once the temperature at this interface reaches about 1190°C or 1463 K. A liquid film of eutectic composition then forms and an exothermic reaction is initiated. A 'double heat effect' is applied to the steel shell and the steel shell melting times are decreased. It was estimated that the net heating effect (heat flux) during exothermic

reaction was (3.97 ± 0.63 w m^{-2}) or (9.5 ± 1.5 cal cm^{-2} s^{-1}) under nominal conditions of natural convection.

4) During the 'free dissolution period', the temperature at the surface of the dissolving titanium increases causing the dissolution to accelerate. In the early stages of 'free dissolution', the temperature of the dissolving interface is lower than melting point of Ti and dissolution occurs. In the later stages of 'free dissolution', the temperature of the dissolving interface approached titanium's melting point and melting occurred. The relative proportions of dissolution and melting during free dissolution depend upon cylinder diameter, steel bath superheat and hydrodynamic conditions.

5) A simplified mathematical model of the dissolution process has been developed to describe the coupled heat and mass transfer phenomena taking place. The model was shown to be capable of providing a good quantitative representation of the processes studied.

6) Pure vanadium and ferrovanadium alloys dissolve in a more conventional manner: that is, no reaction product is observed between the steel shell and solid vanadium. The kinetics of dissolution of vanadium in liquid steel is significantly lower than that of titanium.

7) The dissolution of ferrovanadium alloy additions in steel baths proceeds via a heat transfer or melting dominated mechanism for alloys containing less than 60% vanadium and by

a mass transfer mechanism for all alloys containing more than this amount.

CHAPTER 8

FUTURE WORK

It is suggested that the turbulence generated during the free dissolution of titanium in liquid steel would be well worth further hydrodynamic investigation. The dissolution of ice cylinders in a 93 wt% H_2SO_4 at temperatures of -25°C (or 248 K) could serve as a low temperature model for this purpose. At higher temperatures, the dissolution of iron in a ferrosilicon bath with 50 wt% silicon could prove to be an appropriate model.

Another area where future work is called for is in the quantitative analysis of exothermic heats of mixing and dissolution rates. This problem could be tackled experimentally by studying the behaviour of iron cylinders in ferrosilicon baths of differing silicon contents.

CHAPTER 9

CLAIM TO ORIGINALITY

Many aspects of this work are, in the author's opinion, contributions to original knowledge.

Thus, an experimental 'direct' method for studying the dissolution of solid alloy additions in molten steel has been developed which is capable of yielding data of high accuracy.

In terms of developing the data acquisition system, the interface of SS-50 bus* with the MOTOROLA EXORciser bus* is new.

In the metallurgical context, the reaction between steel shell and titanium is a novel phenomenon which has been observed and explained. Similarly, a detailed analysis of heat and mass transfer phenomena associated with the dissolution of titanium in liquid steel has been carried out that is entirely novel.

This work contains the first experimental data on the dissolution kinetics of pure vanadium and ferrovanadium alloys in liquid steel.

---

*bus is a standardized combination of microprocessor signals which are common in many subsystems.

ACKNOWLEDGEMENTS

The author would like to express his sincere appreciation to Professor R.I.L. Guthrie, for his guidance and assistance during the course of this work.

The author wishes to express his special gratitude to his friend Dr. Kasi Ananthanarayanan for his valuable help during the development of the data acquisition system.

The author wishes to thank the Quebec Ministry of Education and the Steel Company of Canada for their financial support.

Last but not least, the author would like to express his deep appreciation to his wife Angie, who had to bear with the special moods of a graduate student husband and for her patience and love throughout the long years of graduate studies and research work.

APPENDIX I

PART 1: TYPICAL RESULTS OF THE SECOND SET OF TITANIUM IMMERSION TESTS

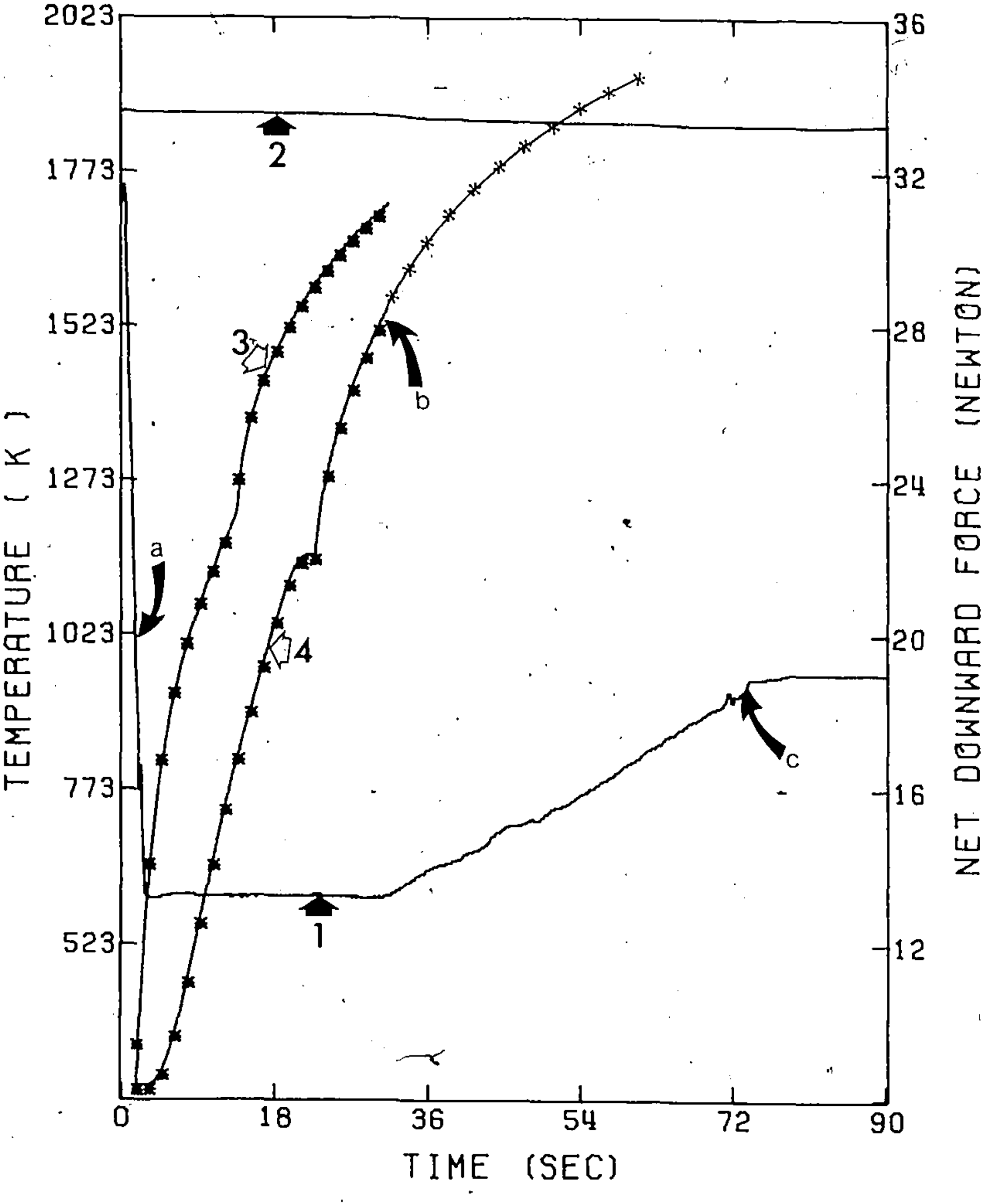

Figure I-1 Results from a titanium dissolution experiment in liquid steel. Cylinder diameter 3.81 cm and 20 cm in length:

1) Registered net downward force;
2) Measured steel bath temperature;
3) Measured and predicted temperatures at a point 1.62 cm from cylinder centerline;
4) Measured and predicted temperatures at the cylinder's centerline.

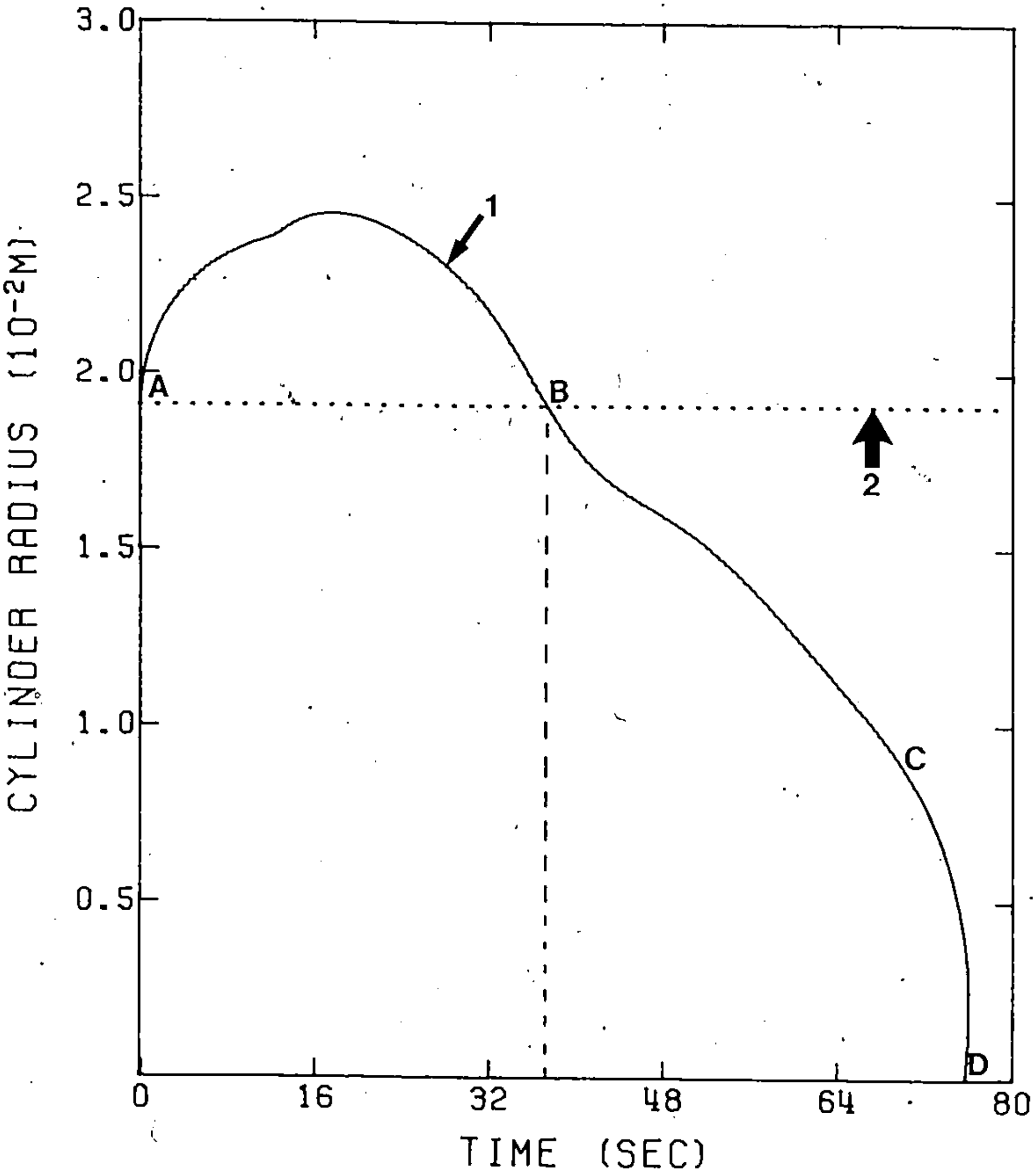

Figure I-2 Predicted cylinder radius versus time for the experimental results presented in Figure I-1:

AB: steel shell period
BCD: free dissolution period
BC: dissolution
CD: melting
1: cylinder radius
2: initial cylinder radius

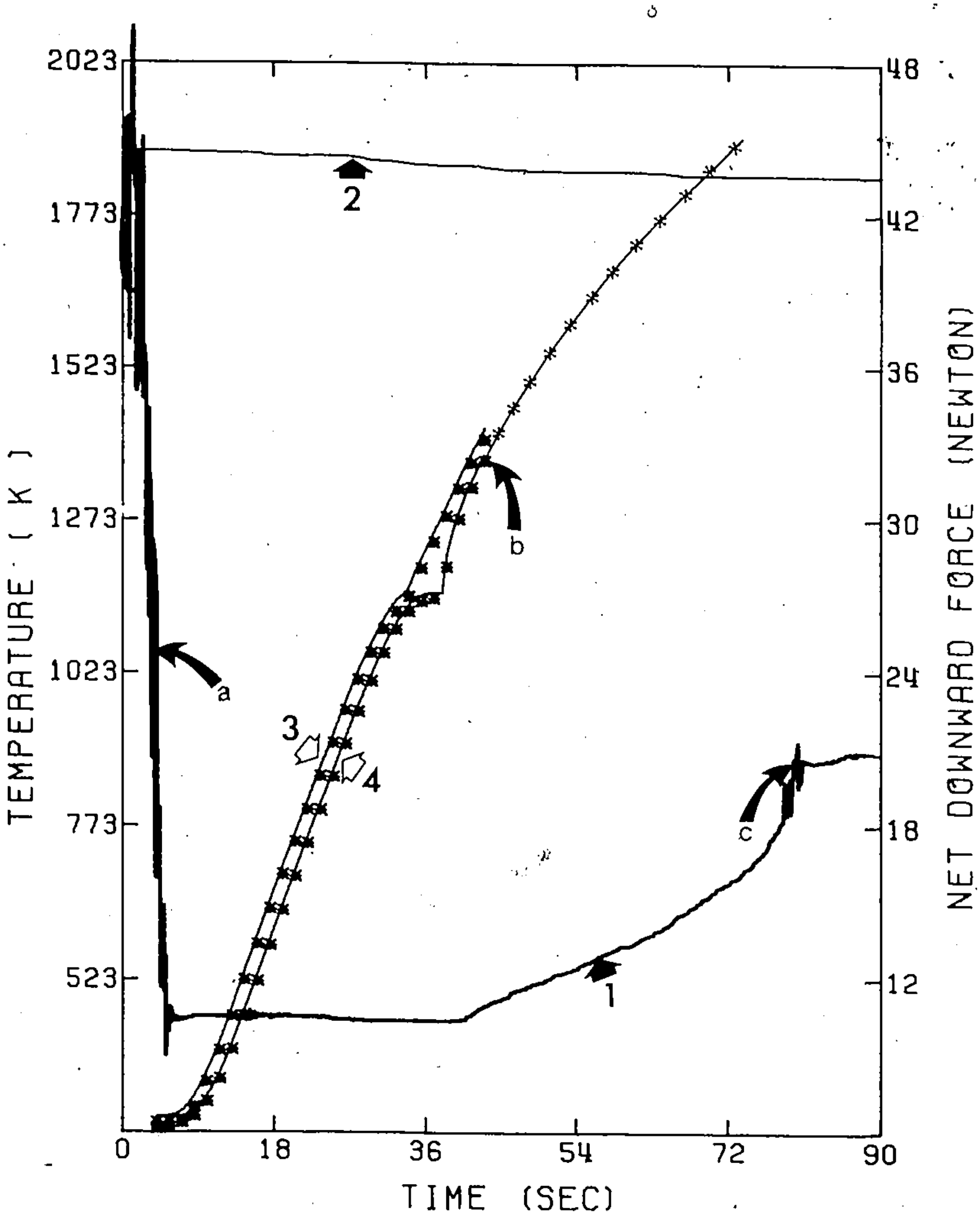

Figure I-3 Results from a titanium dissolution experiment in liquid steel. Cylinder diameter 5.08 cm and 22 cm in length:

1) Registered net downward force;
2) Measured steel bath temperature;
3) Measured and predicted temperatures at a point 0.7 cm from cylinder centerline;
4) Measured and predicted temperatures at the cylinder's centerline.

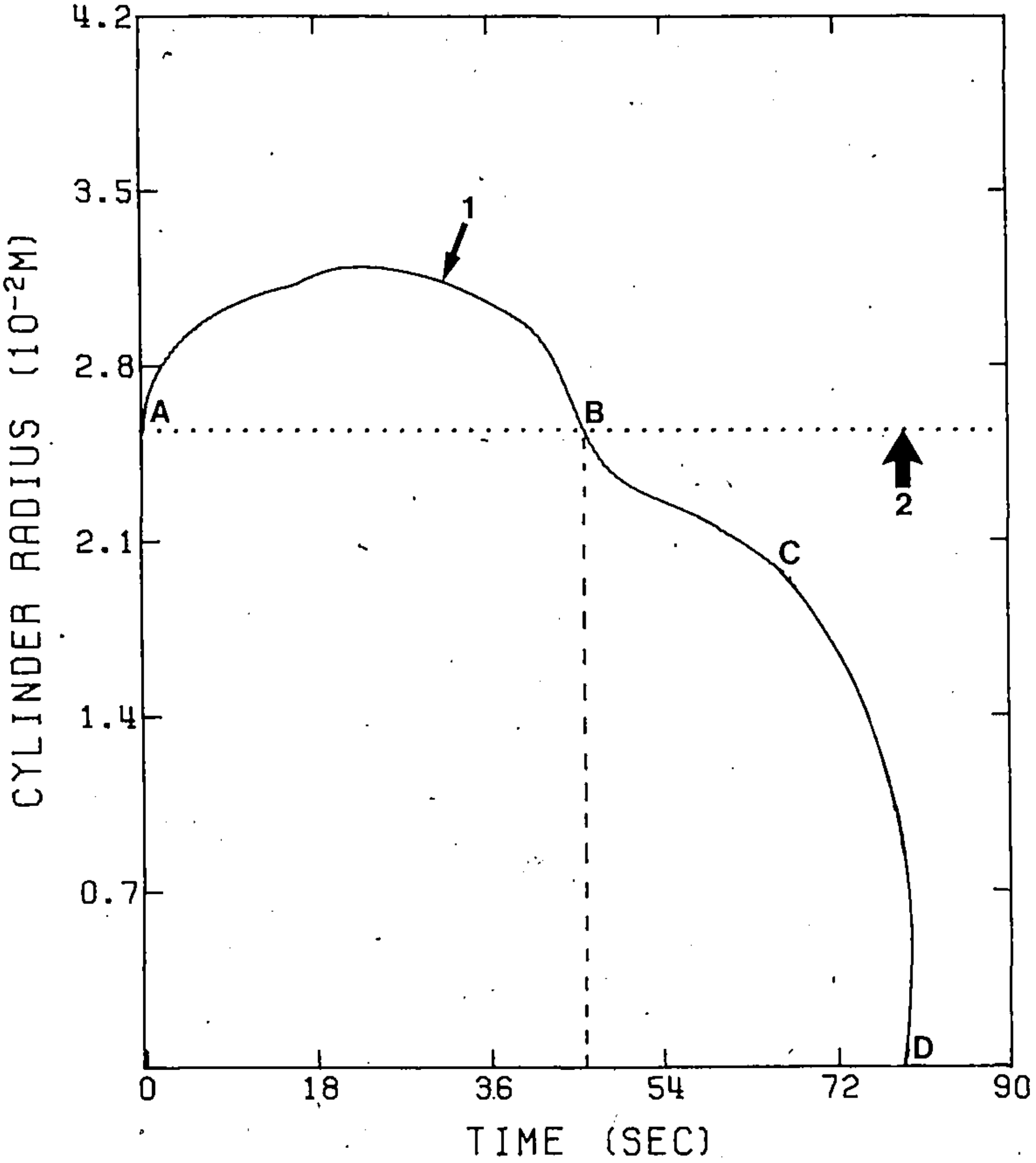

Figure I-4 Predicted cylinder radius versus time for the experimental results presented in Figure I-3:

1: Predicted cylinder radius
2: Initial cylinder radius
AB: Steel shell period
BCD: Free dissolution period
BC: Dissolution
CD: Melting

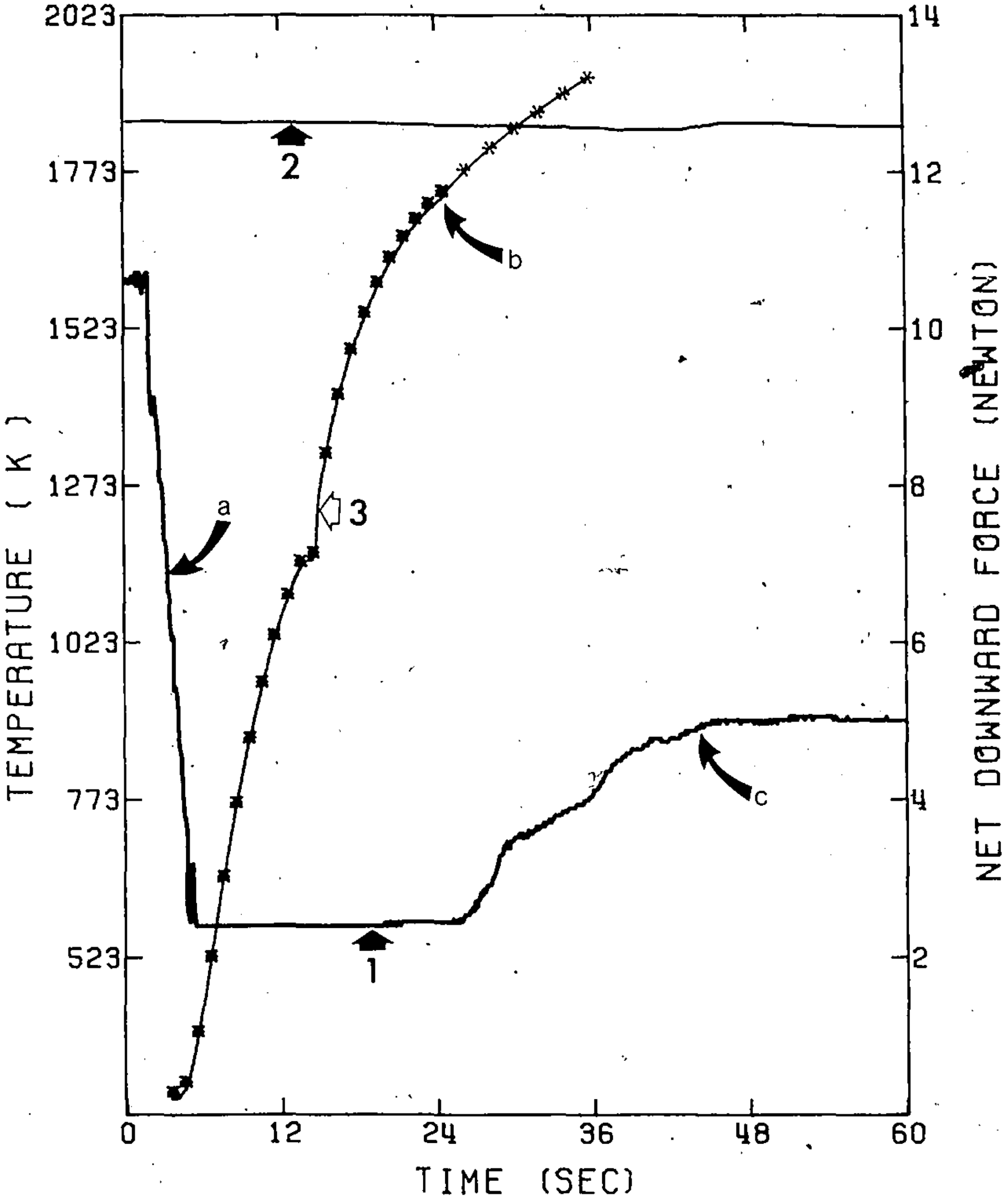

Figure I-5 Results from a titanium dissolution experiment in liquid steel. Cylinder diameter 2.54 cm and 21.0 cm in length:

1) Registered net downward force;
2) Measured steel bath temperature;
3) Measured and predicted temperatures at the cylinder's centerline.

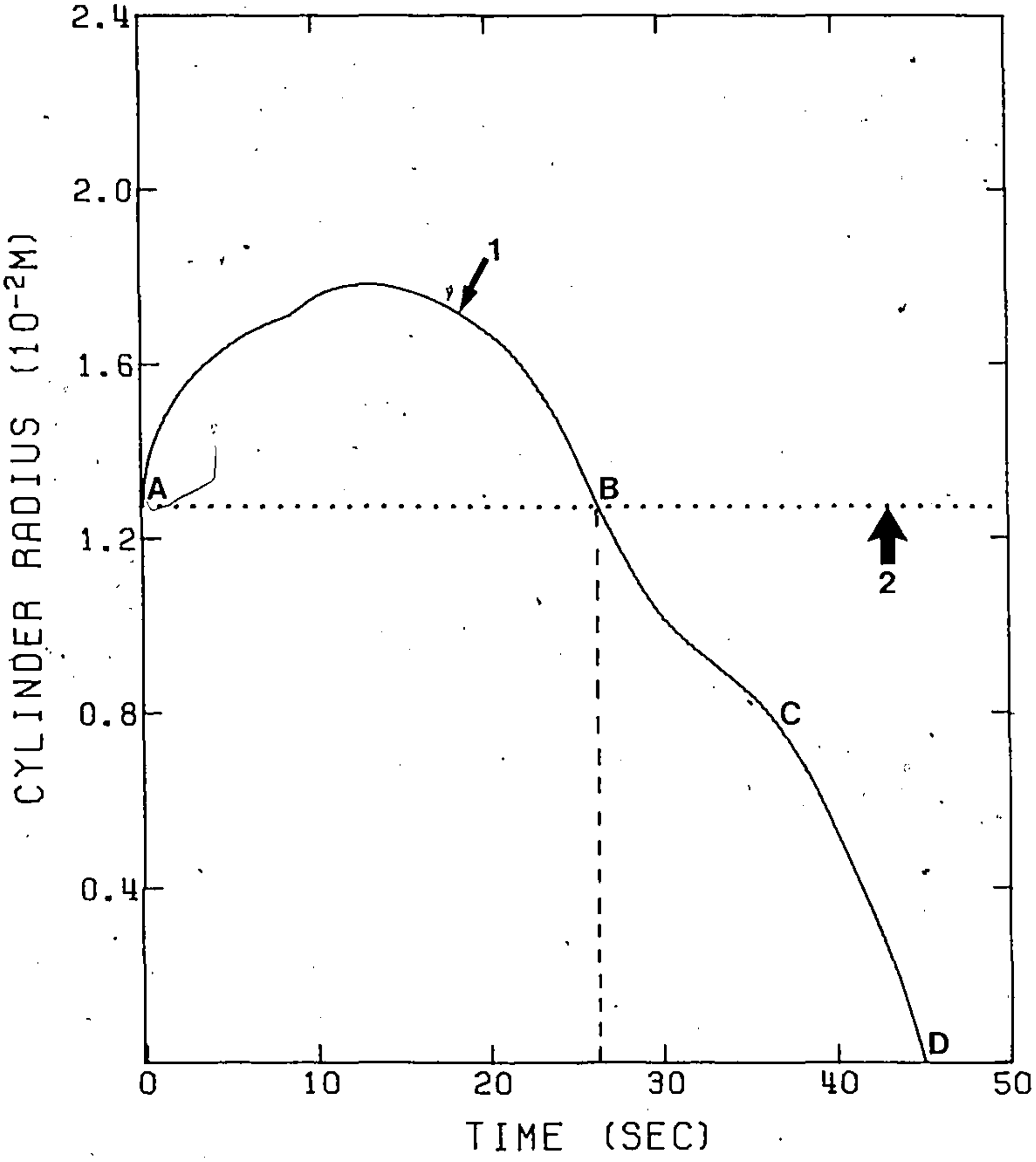

Figure I-6 Predicted cylinder radius versus time for the experimental results presented in Figure I-5:

1: Predicted cylinder radius;
2: Initial cylinder radius;
AB: Steel shell period;
BCD: Free dissolution period;
BC: Dissolution;
CD: Melting

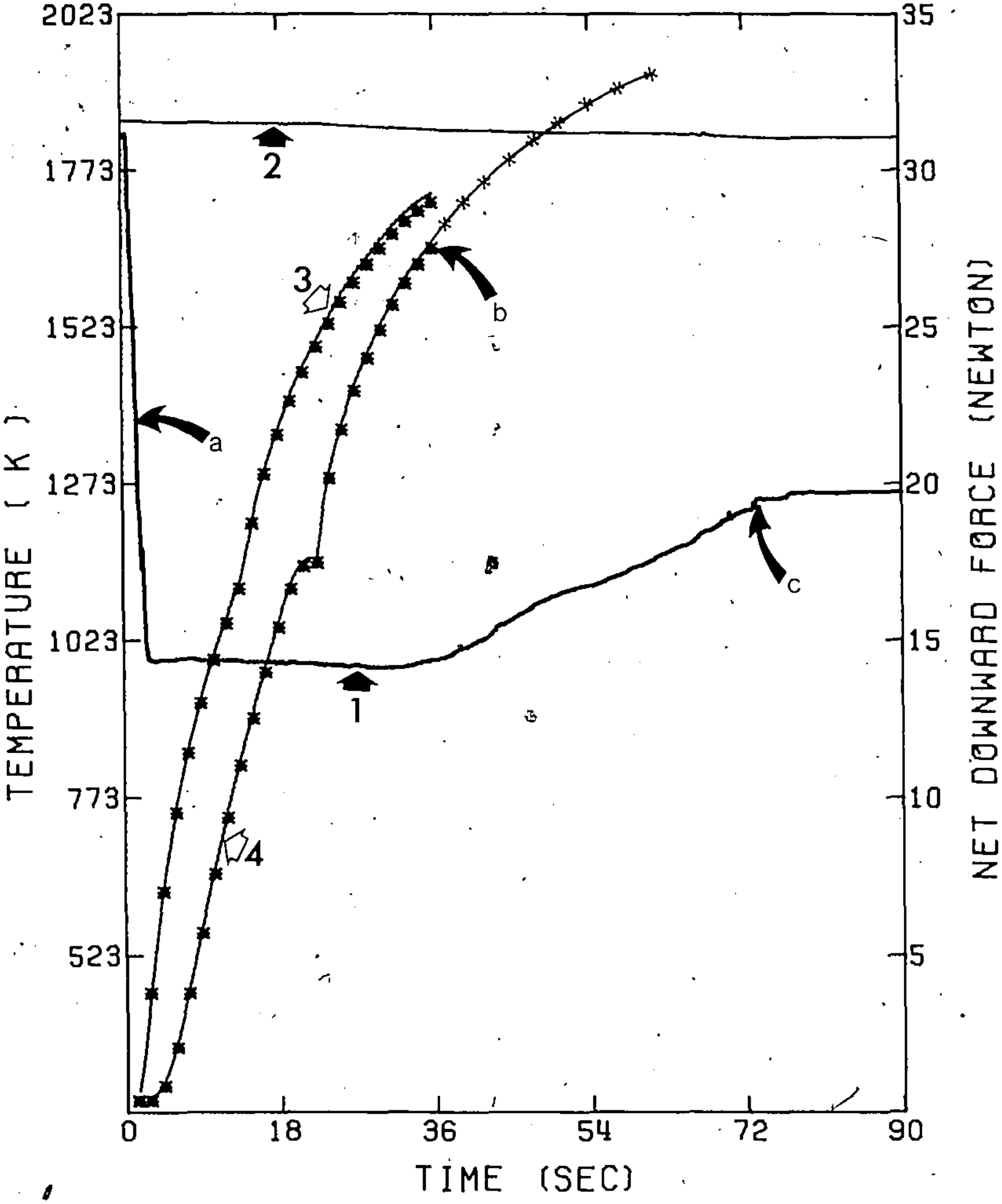

Figure I-7 Results from a titanium dissolution experiment in liquid steel. Cylinder diameter 3.81 cm and 21 cm in length:

1) Registered net downward force;
2) Measured steel bath temperature;
3) Measured and predicted temperatures at a point 1.35 cm from cylinder centerline;
4) Measured and predicted temperatures at the cylinder's centerline.

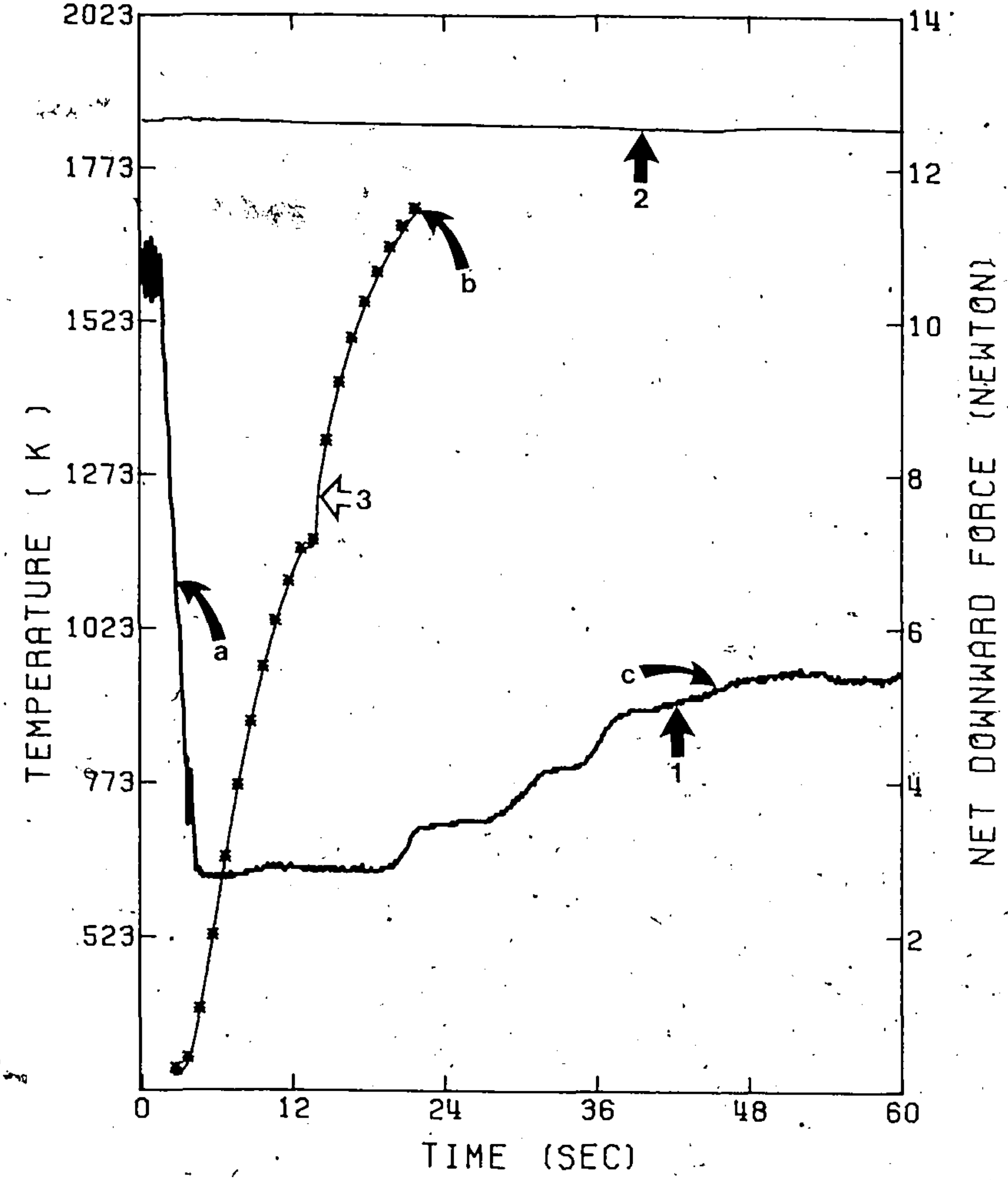

Figure I-8 : Results from a titanium dissolution experiment in liquid steel. Cylinder diameter 2.54 cm and 20 cm in length:

1) Registered net downward force;
2) Measured steel bath temperature;
3) Measured and predicted temperatures at the cylinder's centerline.

APPENDIX I

PART 2: QUALITATIVE SIMULATION OF TITANIUM DISSOLUTION IN LIQUID STEEL USING A CALCOMP 663 DIGITAL PLOTTER

Events which occur in the cross-section of a titanium cylinder perpendicular to the cylinder vertical axis are presented sequentially.

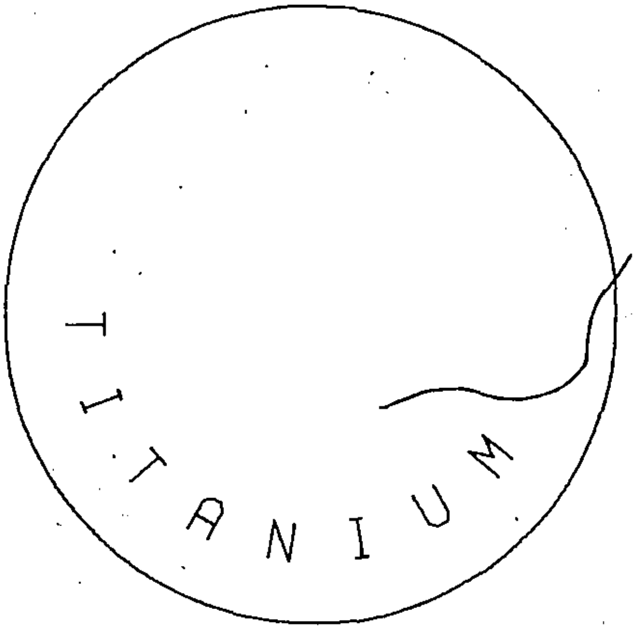

Figure I-9 Time t = 0. Prior to immersion.

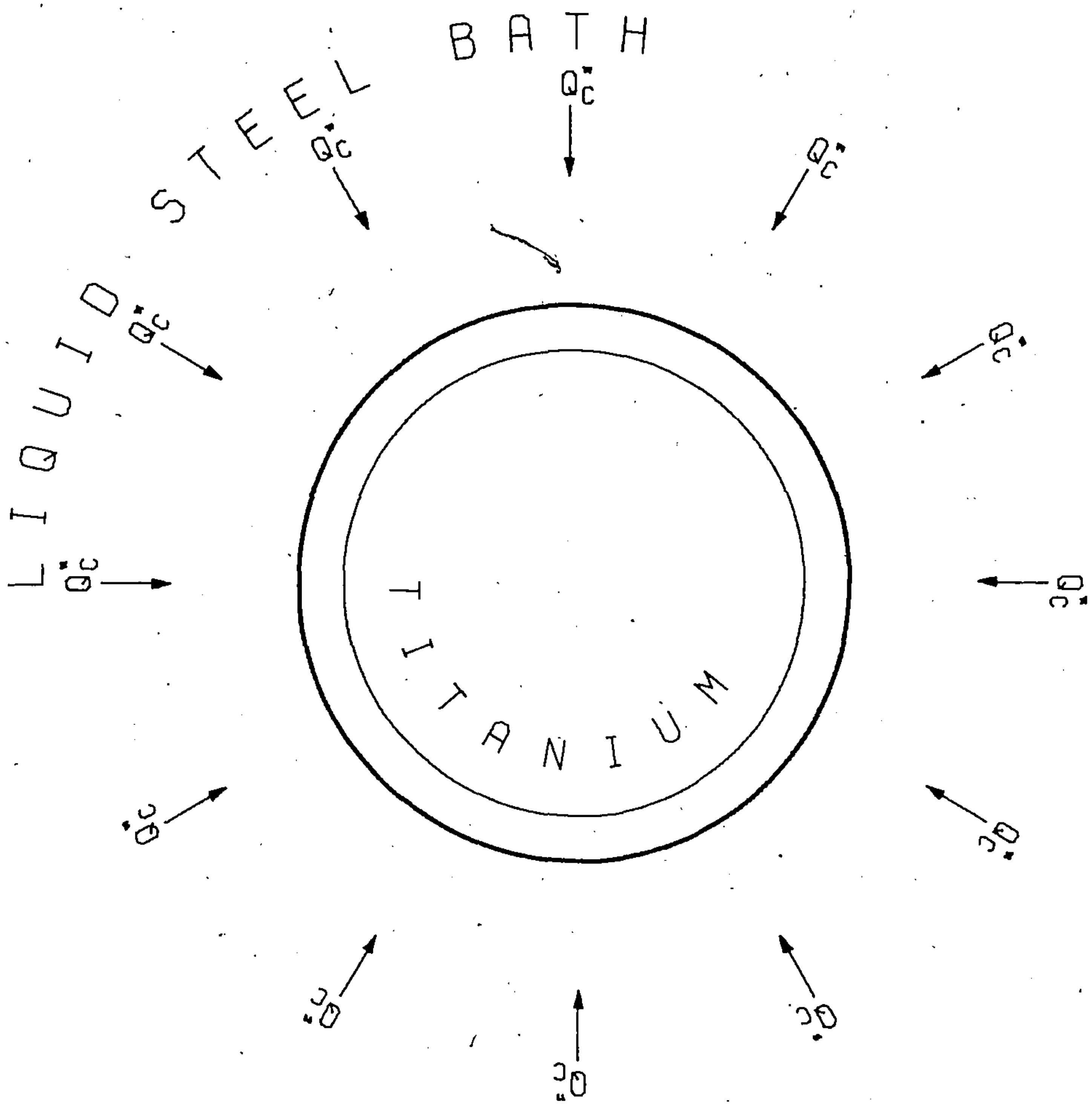

Figure I-10 Time t > 0. Immediately after immersion steel freezes around the cylinder.

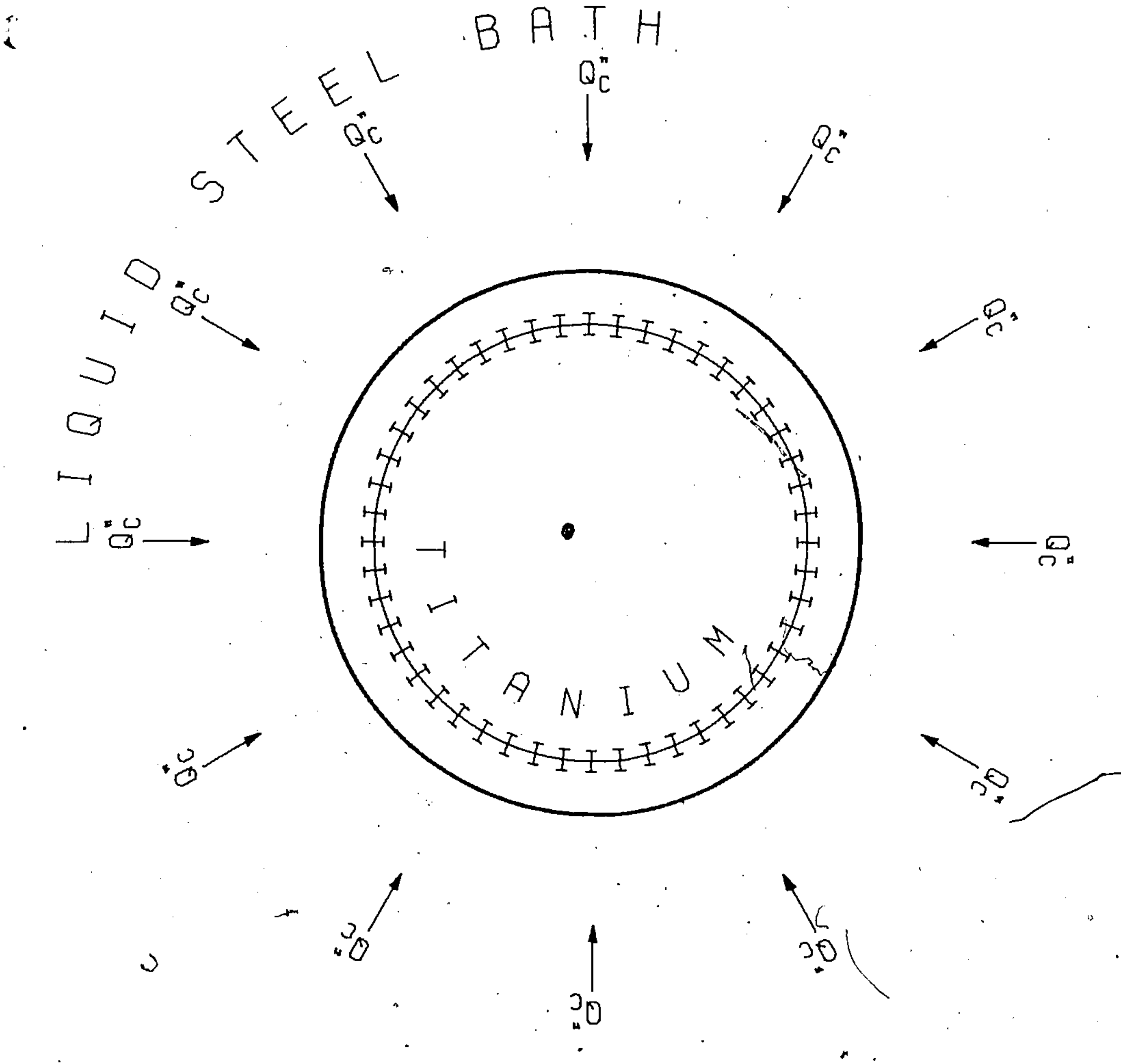

Figure I-11 Reaction starts at the steel shell/titanium interface.

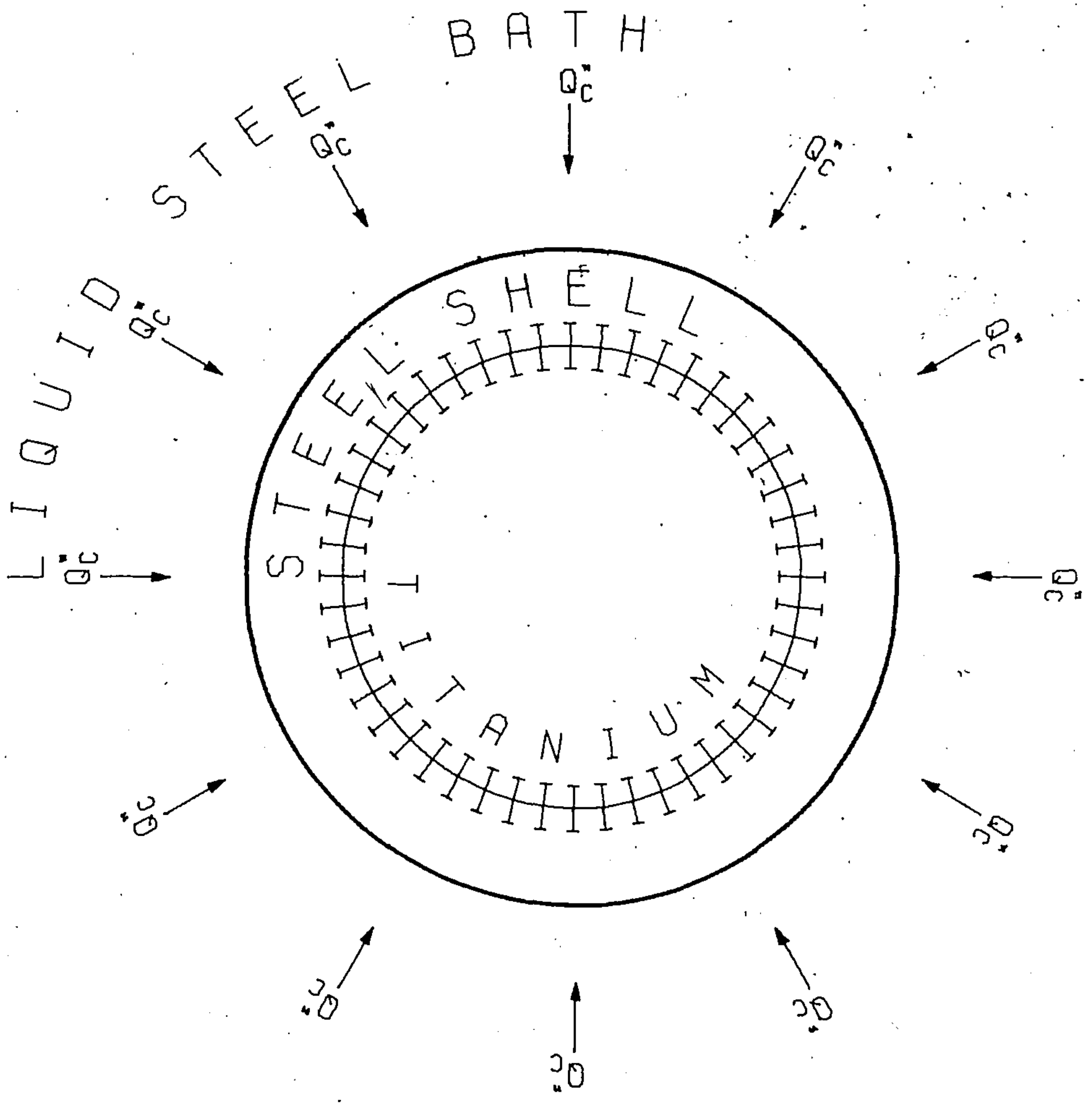

Figure I-12 The thickness of the steel shell and reaction zone increases.

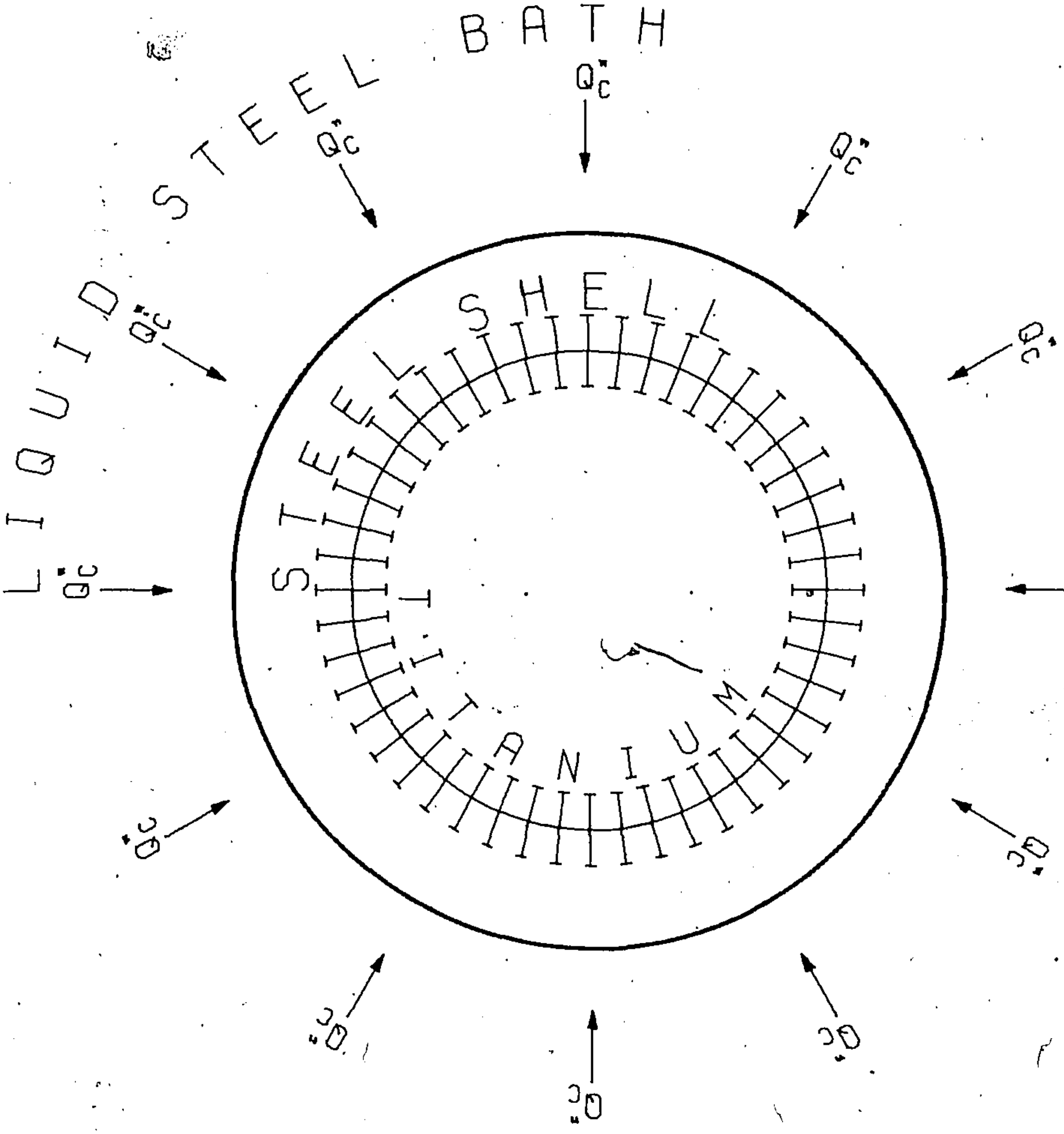

Figure I-13 The thickness of the steel shell and reaction zone continues to increase.

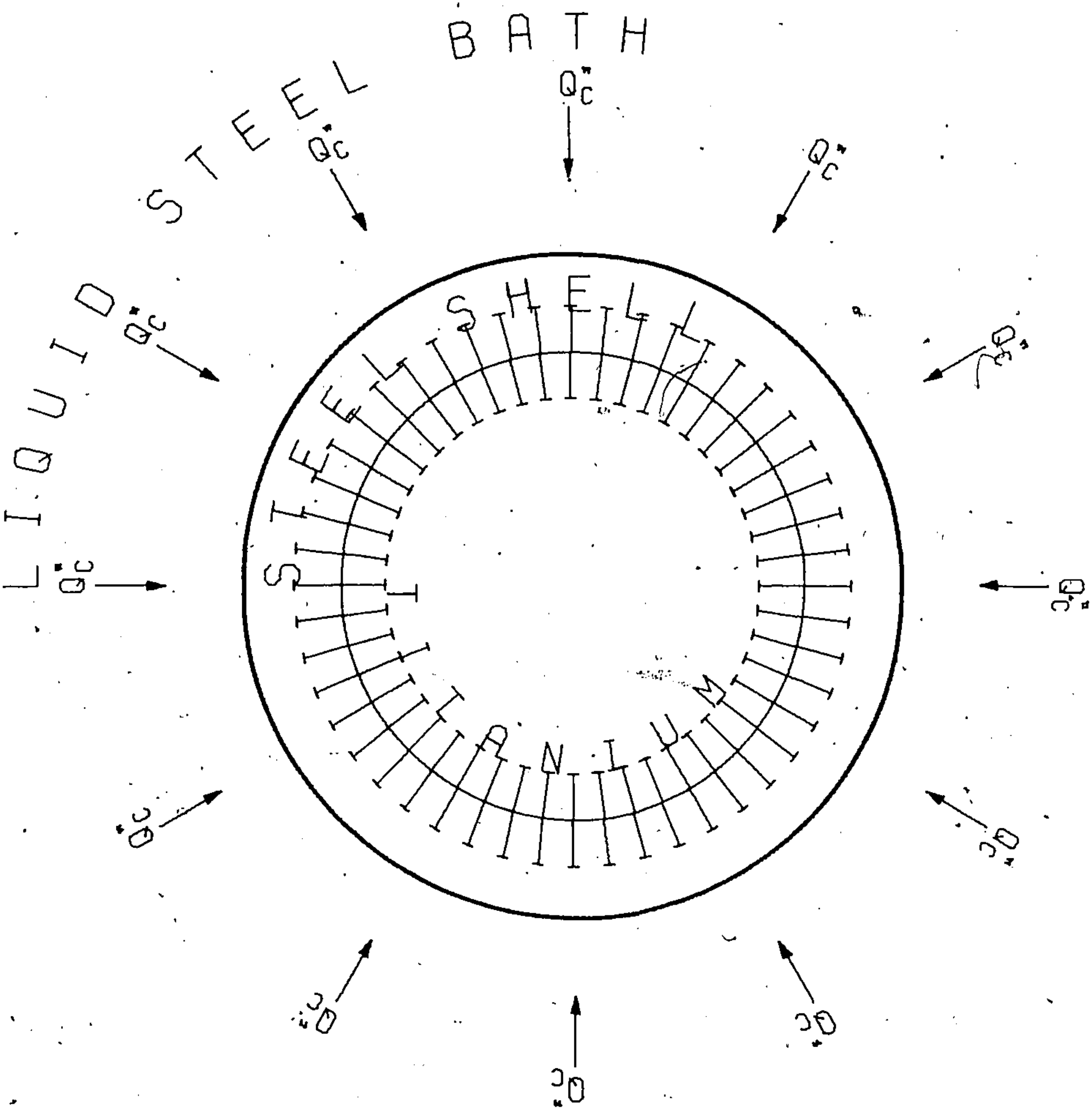

Figure I-14 Steel shell starts melting back. The reaction zone becomes thicker.

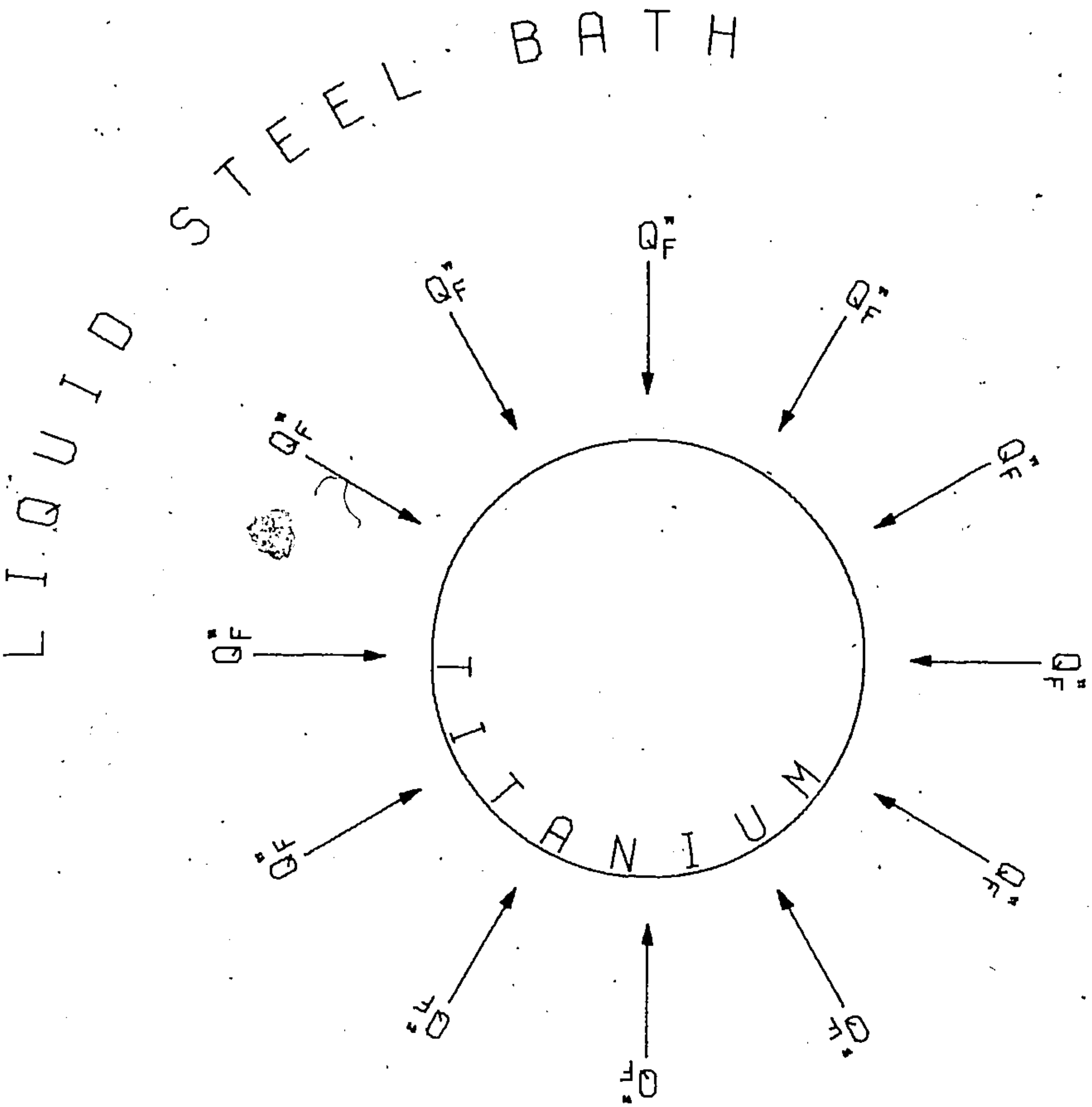

Figure I-15 Steel shell disappears and free dissolution starts.

APPENDIX II

TRANSFORMATION OF PARTIAL DIFFERENTIAL EQUATIONS INTO THE FINITE DIFFERENCE EQUATIONS

The equation:

$$\frac{a}{r}\frac{\partial}{\partial r}\left(r\,\frac{\partial\theta}{\partial r}\right) = \frac{\partial\theta}{\partial t}$$

can be written as:

$$\frac{\partial^2\theta}{\partial r^2} + \frac{1}{r}\frac{\partial\theta}{\partial r} = \frac{1}{a}\frac{\partial\theta}{\partial t} \qquad \text{(II-1)}$$

From Taylor series with proper substitution, the following expressions can be obtained.[68]

$$\left(\frac{d\theta}{dr}\right)_N = \frac{\theta_{N+1} - \theta_N}{\Delta r} - \left(\frac{d^2\theta}{dr^2}\right)\frac{\Delta r}{2!} - \left(\frac{d^3\theta}{dr^3}\right)_N\frac{(\Delta r)^2}{3!}\ \ldots \qquad \text{(II-2)}$$

$$\left(\frac{d^2\theta}{dr^2}\right)_N = \frac{\theta_{N+1} - 2\theta_N + \theta_{N-1}}{(\Delta r)^2} - \left(\frac{d^4\theta}{dr^4}\right)_N\frac{(\Delta r)^2}{12}\ \ldots \qquad \text{(II-3)}$$

Similarly,

$$\left(\frac{d\theta}{dt}\right)_N = \frac{\theta_{N+1} - \theta_N}{\Delta t} - \left(\frac{d^2\theta}{dt^2}\right)_N\frac{\Delta t}{2!} - \left(\frac{d^3\theta}{dt^3}\right)_N\frac{\Delta x^2}{3!}\ \ldots \qquad \text{(II-4)}$$

Keeping the first term on the right hand side of equations (II-1), (II-2), (II-3) and truncating the rest the following equations can be obtained:

$$\left(\frac{\partial\theta}{\partial r}\right)_N \simeq \frac{\theta_{N+1} - \theta_N}{\Delta r} \qquad \text{(II-5)}$$

$$\left(\frac{\partial^2\theta}{\partial r^2}\right)_N \simeq \frac{\theta_{N+1} - 2\theta_N + \theta_{N-1}}{(\Delta r)^2} \qquad \text{(II-6)}$$

$$\left(\frac{\partial\theta}{\partial t}\right)_N \simeq \frac{\theta'_N - \theta_N}{\Delta t} \qquad \text{(II-7)}$$

Substituting equations (II-6) and (II-7) into equation (II-1) we obtain:

$$\frac{\theta_{N+1} - 2\theta_N + \theta_{N+1}}{(\Delta r)^2} + \frac{1}{r}\,\frac{\partial\theta}{\partial r} = \frac{1}{a}\,\frac{\theta'_N - \theta_N}{\Delta t} \qquad \text{(II-8)}$$

The second term on the left hand side of equation (II-8) can be written as:

$$\frac{1}{r}\,\frac{\partial\theta}{\partial r} \simeq \frac{1}{(N-1)\Delta r}\,\frac{\theta_{N+1} - \theta_{N-1}}{2\Delta r} \qquad \text{(II-9)}$$

Substituting (II-9) into (II-8) we obtain the equation (4.22).

APPENDIX III

ESTIMATION OF EXOTHERMIC HEATS OF MIXING AND TITANIUM MASS TRANSFER COEFFICIENT DURING STEEL SHELL PERIOD

At the steel shell-titanium interface, solid steel at a temperature below its melting point is dissolving and mixing with solid titanium. It was found experimentally (section 5.3) that the relative amounts of Fe and Ti in the reaction zone are 60 wt% Fe and 40 wt% Ti. The product we assume is a mixture of FeTi and Fe_2Ti. Consequently, the exothermic dissolution reaction can be represented by:

$$0.57Fe(S) + 0.43Ti(S) \rightarrow 0.29FeTi(L) + 0.14Fe_2Ti(L) \qquad \text{(III-1)}$$

where

$$-\frac{1}{0.57}\dot{N}''_{Fe} = \frac{1}{0.43}\dot{N}''_{Ti} \qquad \text{(III-2)}$$

This intermixing results in an enthalpy change ΔH_m

$$\Delta H_m = 0.57H_{Fe} + 0.43H_{Ti} - 0.29H_{FeTi} - 0.14H_{Fe_2Ti} \qquad \text{(III-3)}$$

The study of the above enthalpy change was done using the facility for the analysis of chemical thermodynamics.[94] The data were taken from reference 61. It was found that:

$$\Delta H_m = -6.97 \text{ kcal/mole of titanium} \qquad \text{(III-4)}$$

The semi-empirically determined heat flux fitting the dissolution data was found to be in the range of 8 to 11 cal cm^{-2} sec^{-1} (or 3.34×10^5 to 4.60×10^5 w m^{-2}).

Consequently, the molar flux is given by:

$$\dot{N}'' = \frac{\text{Heat flux}}{\Delta H_m}$$

which can range from 1.14×10^{-3} to 1.57×10^{-3} g mole cm^{-2} s^{-1}

The mass transfer coefficient can be defined as:

$$k_{Ti} = \frac{\text{molar flux of Ti}}{\text{net concentration driving force}}$$

where the driving force: $C_1 - C_2$ and

C_1: mole of Ti in (Pure Ti)/cm^3 = 0.09556
C_2: mole of Ti in (mixture 40 wt% Ti)/cm^3 = 0.0511

Consequently for the system studied, the mass transfer coefficient of titanium varied from 0.025 to 0.035 cm sec^{-1} or (2.5 to 3.5 m s^{-1}). In a similar way the mass transfer of iron was calculated and found to range from 0.024 to 0.033 cm s^{-1}.

The thickness of the reaction zone could therefore be deduced based on a knowledge of the heat released and the stoichiometry of the reaction (Equation III-1).

APPENDIX IV

LIST OF PROGRAMS

PART 1: PROGRAM KINET WRITTEN IN MOTOROLA 6809 ASSEMBLER

DEVELOPED BY
STAVROS A. ARGYROPOULOS
McGILL UNIVERSITY
1981

```
                                NAM   MEASUR
7000                            ORG   $7000
7000 10FF 7474                  STS   STACK
7004 1A   10                    SEI            SET INTERRUPT MASK BIT
7006 8E   70EB                  LDX   #BASIC
7009 BF   BFFB                  STX   $BFFB
700C 7F   7450         ARXH     CLR   V        INITIALIZATION
700F 7F   745E                  CLR   D        FOR IMMERSION TIME
7012 8E   7204                  LDX   #IN1
7015 BD   F09E                  JSR   PDATA1
7018 BD   F0BA         START    JSR   INEEE    INSERT A NUMBER
701B 81   00                    CMPA  #$00     COMPARE WITH C R
701D 27   1A                    BEQ   TEL      IF EQUAL GO TO TEL
701F 80   30                    SUBA  #$30     CHANGE FROM ASCII
                       *                       TO STRAIGHT BINARY
7021 78   7450                  ASL   V        MULTIPLY BY TWO
7024 F6   7450                  LDAB  V        STORE THE RESULT
7027 78   7450                  ASL   V        MULTIPLY BY FOUR
702A 78   7450                  ASL   V        MULTIPLY BY EIGHT
702D FB   7450                  ADDB  V        ADD THE RESULT
7030 34   04 ABE0               ABA            ADD B AND A KEEP
                       *                       THE RESULT AT A
7034 B7   7450                  STAA  V        STORE RESULT AT V
7037 20   0F                    BRA   START    GO TO START
7039 B6   7450         TEL      LDAA  V
703C B7   7461                  STAA  ST2
703F 8E   72FA                  LDX   #IN2     WRITE IN2
7042 BD   F09E                  JSR   PDATA1
7045 7F   7450                  CLR   V
7048 7F   745E                  CLR   D
704B BD   F0BA         START1   JSR   INEEE    INSERT A NUMBER
704E 81   00                    CMPA  #$00     INITIALIZATION
                       *                 FOR NUMBER OF MEASUREMENTS
7050 27   1A                    BEQ   TEL1     PER SECOND
7052 80   30                    SUBA  #$30     CHANGE FROM ASCII
                       *                       TO STRAIGHT BINARY
7054 78   7450                  ASL   V        MULTIPLY BY TWO
7057 F6   7450                  LDAB  V        STORE THE RESULT
705A 78   7450                  ASL   V        MULTIPLY BY FOUR
705D 78   7450                  ASL   V        MULTIPLY BY EIGHT
7060 FB   7450                  ADDB  V        ADD THE RESULT
7063 34   04 ABE0               ABA            ADD B AND A KEEP
                       *                       THE RESULT AT A
7067 B7   7450                  STAA  V        STORE
706A 20   0F                    BRA   START1   GO TO START1
                       *                 MULTIPLICATION SUBROUTINE
706C 4F                TEL1     CLRA           CALCULATING
                       *                       THE LENGTH OF TIME
706D 5F                         CLRB           TEMPERATURES
                       *                       ARE READ FOR DO LOOP
706E 8E   0008                  LDX   #$08     MULTIPLY V
7071 58                SHIFT    ASLB
7072 49                         ROLA           BY ST2
7073 78   7450                  ASL   V        THE RESULT
7076 24   05                    BCC   DECA     IS IN THE
7078 FB   7461                  ADDB  ST2      TWO ACCUMULATORS
707B 89   00                    ADCA  #0       A AND B
707D 30   1F           DECA     DEX
707F 26   F0                    BNE   SHIFT
7081 8E   745F                  LDX   #ST1     COUNTER ADDRESS
7084 A7   84                    STAA  0,X      STORE FIRST BYTE
7086 E7   01                    STAB  1,X      STORE SECOND BYTE
7088 8E   7324                  LDX   #LINE    OUTPUT A LINE
```

```
7088 BD   FD9E             JSR   PDATA1
708E 8E   734A             LDX   #IN3      OUTPUT INSERT
                    *                      BATH TEMPERATURE
7091 BD   FD9E             JSR   PDATA1
7094 BD   7250             JSR   DECIMA
                    *                 JUMP TO SUBROUTINE DECIMA
7097 8E   7426             LDX   #CHAN     OUTPUT LINE WRITING
709A BD   FD9E             JSR   PDATA1    HOW MANY CHANNELS
709D BD   FDBA             JSR   INEEE     INSERT A NUMBER
70A0 80   30               SUBA  #$30      CONVERT TO BINARY
70A2 48                    ASLA            MULTIPLY BY TWO
70A3 8B   20               ADDA  #$20      ADD THE RESULT TO 20
70A5 8E   746A             LDX   #CHA1     FIND THE ADDRESS OF CHA1
70A8 C6   E0               LDAB  #$E0      E0 IS THE FIRST BYTE
                    *                      OF CHANNEL ADDRESS
70AA E7   84               STAB  0,X       STORE AT CHA1
70AC A7   01               STAA  1,X       STORE AT CHA1+1
70AE 8E   7328             LDX   #TSEK     OUTPUT A LINE IS THE
70B1 BD   FD9E             JSR   PDATA1    ABOVE DATA CORRECT
70B4 BD   FDBA             JSR   INEEE     INSERT A CHARACTER
70B7 81   59               CMPA  #'Y       IF YES
70B9 27   03               BEQ   TELOS     GO TO TELOS
70BB 7E   700C             JMP   ARXH      OR GO TO ARXH
70BE 8E   737B      TELOS  LDX   #IN4      OUTPUT A LINE
70C1 BD   FD9E             JSR   PDATA1    DO YOU WANT TO WAIT
70C4 BD   FDBA      TELOS1 JSR   INEEE     INSERT A CHARACTER
70C7 81   59               CMPA  #'Y       IF YES
70C9 27   F9               BEQ   TELOS1    GO TO TELOS1
70CB 8E   71CB             LDX   #BATH     GET ADDRESS
                    *                      OF THE BATH SCANNING
70CE BF   DFC8             STX   $DFC8     SUBROUTINE
                    *                AND STORE FOR IRQ INTERRUPTS
                    *               CONFIGURATION FOR INTERRUPT TIMER
70D1 8E   E010             LDX   #$E010
70D4 86   FF               LDAA  #$FF
70D6 A7   02               STAA  2,X
70D8 86   3D               LDAA  #$3D
70DA A7   03               STAA  3,X
70DC 86   80               LDAA  #$80
70DE A7   02               STAA  2,X
70E0 86   06               LDAA  #$06     SET INTERRUPTS
70E2 A7   02               STAA  2,X      EVERY SECOND
70E4 3C   EF        LL     CWAI  #$EF
                    *                 CLEAR INTERRUPT MASK BIT
                    *                 AND WAIT FOR INTERRUPT
70E6 10FE 7474             LDS   STACK
70EA 39                    RTS
                    *                 RETURN CONTROL TO BASIC
70EB 10FF 7474      BASIC  STS   STACK
                    *                AT THIS POINT B ACCUMULATOR
                    *           CARRIES THE RESULT OF THE COMPARISON
                    *           IF B 0 OR + THEN THE BATH TEMPERATURE
                    *           IS     EQUAL      OR
                    *           LOWER THAN THE SPECIFIED TEMPERATURE
70EF F6   745C             LDAB  KAPOU
70F2 5D                    TSTB            TEST FOR TEMPERATURE
70F3 2D   EF               BLT   LL        IF NEGATIVE GO TO LL
70F5 86   3C               LDAA  #$3C
70F7 B7   E013             STAA  $E013     DISABLE FURTHER INTERRUPTS
70FA 8E   7397             LDX   #INS      WRITE INS
70FD BD   FD9E             JSR   PDATA1
7100 108E 0000             LDY   #$00
7104 8E   7144             LDX   #SCAN
7107 BF   DFC8             STX   $DFC8
```

```
7108 BE   745F            LDX    ST1
710D BD   F0BA     LL1    JSR    INEEE      WAIT LOOP
                   *                        TO START SCANNING
7110 81   52              CMPA   #'R        IF R THEN START
7112 26   F9              BNE    LL1
                   *      CONFIGURATION FOR SCANNING ROUTINE
7114 1A   10              SEI
7116 CC   FF30            LDD    #$FF30
7119 FD   E012            STD    $E012
711C 86   80              LDAA   #$80
711E B7   E012            STAA   $E012      RESET OSCILLATOR/DIVIDER
7121 86   05              LDAA   #$05       SET UP TIMING-INTERVAL
                   *                    EVERY TENTH OF A SECOND
7123 B7   E012            STAA   $E012
7126 3C   EF       SC1    CWAI   #$EF
                   *               CLEAR INTERRUPT MASK BIT AND
                   *               WAIT FOR IRQ INTERRUPTS
7128 30   1F              LEAX   -1,X
                   *                        DECREASE COUNTER
712A 26   FA              BNE    SC1
712C 86   3C              LDAA   #$3C
712E B7   E013            STAA   $E013      DISABLE
                   *                        FURTHER INTERRUPTS
7131 8E   7303            LDX    #END1
7134 BD   F09E            JSR    PDATA1
7137 CC   0FFF            LDD    #$0FFF
                   *                        ARTIFICIAL DATA
713A ED   A0              STD    0,Y+
713C 1E   21              EXG    Y,X
713E BD   F06A            JSR    OUT4HS     WRITE THE LAST ADDRESS
7141 7E   C003            JMP    $C003
                   *                        SCANNING ROUTINE
7144 B6   E012     SCAN   LDAA   $E012
                   *          NO MORE INTERRUPTS DURING EXECUTION
                   *          OF INTERRUPT SERVICE ROUTINE
7147 CE   E020            LDU    #$E020     A/D BOARD BASE ADDRESS
714A 8E   0000     SCANN  LDX    #$00       CLEAR MEMORY LOCATIONS
714D BF   746C            STX    VAL        FROM VAL TO
7150 BF   746E            STX    VAL+2
7153 BF   7470            STX    VAR+1      VAR+2
7156 8E   0080            LDX    #$0080
7159 A7   C4       SCAN1  STAA   0,U        CHANNEL ADDRESS
                   *                        TO BE CONVERTED
715B BD   7288            JSR    STATIS     ADDITION SUBROUTINE
715E 86   02              LDAA   #$02
7160 4A            DELAY  DECA
7161 26   FD              BNE    DELAY
7163 B6   E020     CC1    LDAA   $E020      CHECK
                   *               IF THE CONVERSION IS COMPLETED
7166 85   10              BITA   #$10
7168 27   F9              BEQ    CC1
716A B6   E020            LDAA   $E020      GET MOST SIGNIFICANT BYTE
716D F6   E021            LDAB   $E021      GET LEAST SIGNIFICANT BYTE
7170 85   08              BITA   #$08       CHECK IF THERE IS NEGATIVE
                   *                        VOLTAGE
7172 27   0C              BEQ    SKATA      IF YES
7174 8A   F0              ORAA   #$F0       PUT F IN THE MOST
                   *                        SIGNIFICANT BITS
7176 B7   7470            STAA   VAR+1
7179 86   FF              LDAA   #$FF       DO THE SAME
717B B7   746F            STAA   VAR        AND STORE AT VAR
717E 20   0A              BRA    STAVR
7180 84   0F       SKATA  ANDA   #$0F       PUT 0 IN THE MOST
                   *                        SIGNIFICANT BITS
```

```
7182 B7   7470          STAA   VAR+1     STORE AT VAR+1
7185 86   00            LDAA   #$00      PUT 00 AND STORE
7187 B7   746F          STAA   VAR       AT VAR
718A F7   7471   STAVR  STAB   VAR+2
718D 30   1F            LEAX   -1,X      DECREMENT CONVERSIONS
                 *                       COUNTER
718F 26   C8            BNE    SCAN1
7191 FB   746E          ADDB   VAL+2     SIMILAR INSTRUCTIONS
                 *                      WITH SUBROUTINE STATIS
7194 F7   746E          STAB   VAL+2
7197 B6   7470          LDAA   VAR+1
719A B9   746D          ADCA   VAL+1     SUBROUTINE FOR THE
719D B7   746D          STAA   VAL+1     FINAL ADDITION
71A0 B6   746F          LDAA   VAR
71A3 B9   746C          ADCA   VAL
71A6 B7   746C          STAA   VAL
                 *             THIS SECTION FINDS THE AVERAGE
                 *                            OF THE CONVERSIONS
71A9 86   07            LDAA   #$07
71AB 77   746C   DAVID  ASR    VAL
71AE 76   746D          ROR    VAL+1
71B1 76   746E          ROR    VAL+2
71B4 4A                 DECA
71B5 26   F4            BNE    DAVID
71B7 FC   746D          LDD    VAL+1     GET THE CONVERSION RESULT
71BA ED   A1            STD    0,Y++     STORE IN THE MEMORY AND
                 * INCREMENT INDEX REGISTER BY TWO
71BC 33   42            LEAU   2,U
71BE 11B3 746A          CMPU   CHA1
                 *  CHECK IF ALL CHANNELS HAVE BEEN CONVERTED
71C2 27   03            BEQ    RET1
>71C4 7E  714A          JMP    SCANN     CONVERSION
71C7 10AF 66     RET1   STY    6,S
71CA 3B                 RTI              RETURN FROM INTERRUPT
                 *      INTERRUPT SERVICE ROUTINE FOR INITIAL
                 *      BATH MEASUREMENTS
71CB B6   E012   BATH   LDAA   $E012     NO MORE INTERRUPTS DURING
                 *     THE EXECUTION OF INTERRUPT SERVICE  ROUTINE
71CE 108E 0100          LDY    #$0100    DO 256 CONVERSIONS
71D2 8E   0000          LDX    #$00      CLEAR MEMORY
71D5 BF   746C          STX    VAL       LOCATIONS
71D8 BF   746E          STX    VAL+2     VAL
71DB BF   7470          STX    VAR+1     TO VAR+2
71DE B7   E020   BATH1  STAA   $E020     INITIATE CONVERSION
71E1 BD   72B8          JSR    STATIS    JUMP TO STATIS
71E4 86   05            LDAA   #$05
71E6 4A          DELAY1 DECA
71E7 26   FD            BNE    DELAY1
71E9 B6   E020   BATH2  LDAA   $E020
71EC 85   10            BITA   #$10
71EE 27   F9            BEQ    BATH2
71F0 B6   E020          LDAA   $E020     FIRST BYTE OF CONVERSION
71F3 F6   E021          LDAB   $E021     SECOND BYTE OF CONVERSION
71F6 85   08            BITA   #$08      LOGICAL AND FOR + OR -
71F8 27   0C            BEQ    BATH3     IF + GO TO BATH3
71FA 8A   F0            ORAA   #$F0      PUT F FOR TWO'S COMPLEMENT
71FC B7   7470          STAA   VAR+1     STORE AT VAR+1
71FF 86   FF            LDAA   #$FF      LOAD FF
7201 B7   746F          STAA   VAR       STORE FOR TWO'S COMPLEMENT
7204 20   0A            BRA    BATH4     GO TO BATH4
7206 84   0F     BATH3  ANDA   #$0F      PUT 0 FOR TWO'S COMPLEMENT
7208 B7   7470          STAA   VAR+1     STORE AT VAR+1
720B 86   00            LDAA   #$00
720D B7   746F          STAA   VAR       STORE 00 AT VAR
```

```
 7210 F7   7471      BATH4    STAB   VAR+2
 7213 31   3F                 LEAY   -1,Y         LOAD CONVERSION'S NUMBER
 7215 27   03                 BEQ    NEXT         IF 0 GO TO NEXT
>7217 7E   710E               JMP    BATH1        JUMP TO BATH1
                     *        CONVERSION'S AVERAGE
 721A FB   746E      NEXT     ADDB   VAL+2
 721D F7   746E               STAB   VAL+2
 7220 B6   7470               LDAA   VAR+1
 7223 B9   746D               ADCA   VAL+1
 7226 B7   746D               STAA   VAL+1
 7229 B6   746F               LDAA   VAR
 722C B9   746C               ADCA   VAL
 722F B7   746C               STAA   VAL
                     *        AT THIS POINT VAL AND VAL+1 HAVE
                     *        THE CONVERSION'S AVERAGE
 7232 BE   746C               LDX    VAL          LOAD CONVERSION AVERAGE AND
 7235 BF   BFF9               STX    $BFF9        MOVE CONVERSION RESULT
                     *  TO BASIC
 7238 1E   10                 EXG    X,D
 723A 10B3 7462               CMPD   SACE1
 723E 2F   04                 BLE    DONE
 7240 C6   FF                 LDAB   #$FF
 7242 20   02                 BRA    OUT
 7244 C6   01        DONE     LDAB   #$01
 7246 F7   745C      OUT      STAB   KAPOU
 7249 8E   7324               LDX    #LINE
 724C BD   FD9E               JSR    PDATA1
 724F 3B                      RTI                 RETURN FROM INTERRUPT
                     *  THE SUBROUTINE DECIMA ACCEPTS
                     *  DATA FOR THE
                     *  BATH THERMOCOUPLE IN DECIMAL
                     *  FORM AND
                     *  MODIFIES IT IN HEXADECIMAL FORM
                     *  THIS DATA IS TREATED AS ADDRESS
                     *  AND THE CONTENT OF THIS
                     *  ADDRESS IS THE HEXADECIMAL FORM OF THE
                     *  BATH  THERMOCOUPLE WHICH IS COMPARED WITH
                     *  THE MEASURED BATH TEMPERATURE
 7250 7F   7456      DECIMA   CLR    VV
 7253 7F   7457               CLR    VV+1
 7256 BD   FDBA      STARTD   JSR    INEEE
 7259 81   0D                 CMPA   #$0D         IF THIS IS  C R
 725B 27   48                 BEQ    FIN          GO TO FIN
 725D 80   30                 SUBA   #$30         CHANGE FROM ASCII
 725F B7   745C               STAA   KAPOU
 7262 78   7457               ASL    VV+1
 7265 79   7456               ROL    VV
 7268 BE   7456               LDX    VV
 726B BF   7458               STX    ALPHA
 726E 78   7457               ASL    VV+1
 7271 79   7456               ROL    VV
 7274 78   7457               ASL    VV+1
 7277 79   7456               ROL    VV
 727A BE   7456               LDX    VV
 727D BF   745A               STX    BETA
 7280 B6   7459               LDAA   ALPHA+1
 7283 F6   7458               LDAB   ALPHA
 7286 BB   745B               ADDA   BETA+1
 7289 F9   745A               ADCB   BETA
 728C B7   7457               STAA   VV+1
 728F F7   7456               STAB   VV
 7292 C6   00                 LDAB   #$00
 7294 B6   745C               LDAA   KAPOU
 7297 BB   7457               ADDA   VV+1
```

```
320    729A F9    7456                 ADCB   VV
321    729D B7    7457                 STAA   VV+1
322    72A0 F7    7456                 STAB   VV
323    72A3 20    81                   BRA    STARTO
324    72A5 B6    7456        FIN      LDAA   VV
325    72A8 8A    70                   ORAA   #$70       PUT 7 AT THE HIGH
326                           *                           ORDER BITS
327    72AA B7    7456                 STAA   VV
328    72AD BE    7456                 LDX    VV         VV CONTAINS THE ADDRESS
329                           *                           OF THE TABLE
330    72B0 A6    84                   LDAA   0,X        GET THE HIGH ORDER BYTE
331    72B2 E6    01                   LDAB   1,X        GET THE LOW ORDER BYTE
332    72B4 FD    7462                 STD    SRCE1      SRCE1 CONTAINS THE
333                           *    CONTENT OF THE
334                           *    ABOVE ADDRESS OF THE TABLE
335    72B7 39                         RTS
336                           *    THIS SUBROUTINE ADDS A THREE BYTE
337                           *    TWO'S COMPLEMENT NUMBER
338                           *    NUMBER DURING THE CONVERSION
339    72B8 F6    7471        STATIS   LDAB   VAR+2
340    72BB FB    746E                 ADDB   VAL+2
341    72BE F7    746E                 STAB   VAL+2
342    72C1 B6    7470                 LDAA   VAR+1
343    72C4 B9    746D                 ADCA   VAL+1
344    72C7 B7    746D                 STAA   VAL+1
345    72CA B6    746F                 LDAA   VAR
346    72CD B9    746C                 ADCA   VAL
347    72D0 B7    746C                 STAA   VAL
348    72D3 39                         RTS
349    72D4 00 0A             IN1      FCB    $00,$0A
350    72D6 49 4E 53 45                FCC    /INSERT IMMERSION TIME/
       72DA 52 54 20 49
       72DE 4D 4D 45 52
       72E2 53 49 4F 4E
       72E6 20 54 49 4D
       72EA 45
351    72EB 20 49 4E 20                FCC    / IN SECONDS/
       72EF 53 45 43 4F
       72F3 4E 44 53
352    72F6 00 0A 0A 04                FCB    $00,$0A,$0A,$04
353    72FA 00 0A             IN2      FCB    $00,$0A
354    72FC 49 4E 53 45                FCC    /INSERT NUMBER OF /
       7300 52 54 20 4E
       7304 55 4D 42 45
       7308 52 20 4F 46
       730C 20
355    730D 4D 45 41 53                FCC    /MEASUREMENTS PER SECOND/
       7311 55 52 45 4D
       7315 45 4E 54 53
       7319 20 50 45 52
       731D 20 53 45 43
       7321 4F 4E 44
356    7324 00 0A 0A 04       LINE     FCB    $00,$0A,$0A,$04
357    7328 00 0A 0A          TSEK     FCB    $00,$0A,$0A
358    732B 49 53 20 54                FCC    /IS THE ABOVE DATA CORRECT ?/
       732F 48 45 20 41
       7333 42 4F 56 45
       7337 20 44 41 54
       733B 41 20 43 4F
       733F 52 52 45 43
       7343 54 20 3F
359    7346 00 0A 0A 04                FCB    $00,$0A,$0A,$04
360    734A 00 0A 0A          IN3      FCB    $00,$0A,$0A
361    734D 49 4E 53 45                FCC    /INSERT BATH TEMPERATURE/
```

```
         7351 52 54 20 42
         7355 41 54 48 20
         7359 54 45 4D 50
         735D 45 52 41 54
         7361 55 52 45
362      7364 20 49 4E 20              FCC    / IN DEGREES CELSIUS/
         7368 44 45 47 52
         736C 45 45 53 20
         7370 43 45 4C 53
         7374 49 55 53
363      7377 0D 0A 0A 04              FCB    $0D,$0A,$0A,$04
364      737B 0D 0A 0A         IN4     FCB    $0D,$0A,$0A
365      737E 44 4F 20 59              FCC    /DO YOU WISH TO WAIT ?/
         7382 4F 55 20 57
         7386 49 53 48 20
         738A 54 4F 20 57
         738E 41 49 54 20
         7392 3F
366      7393 0D 0A 0A 04              FCB    $0D,$0A,$0A,$04
367                     F0BA   INEEE   EQU    $F0BA
368                     F09E   PDATA1  EQU    $F09E
369                     F00F   OUTEE1  EQU    $F00F
370                     F06A   OUT4HS  EQU    $F06A
371                     F02B   BADDR   EQU    $F02B
372      7397 0D 0A 07 0A      INS     FCB    $0D,$0A,$07,$0A
373      739B 54 49 4D 45              FCC    /TIME OF IMMERSION NOW/
         739F 20 4F 46 20
         73A3 49 4D 4D 45
         73A7 52 53 49 4F
         73AB 4E 20 4E 4F
         73AF 57
374      73B0 0D 0A 07                 FCB    $0D,$0A,$07
375      73B3 57 48 45 4E              FCC    /WHEN YOU ARE READY , PRESS  R/
         73B7 20 59 4F 55
         73BB 20 41 52 45
         73BF 20 52 45 41
         73C3 44 59 20 2C
         73C7 20 50 52 45
         73CB 53 53 20 20
         73CF 52
376      73D0 0D 0A 04                 FCB    $0D,$0A,$04
377      73D3 0D 0A            END1    FCB    $0D,$0A
378      73D5 45 4E 44 20              FCC    /END OF SCANNING/
         73D9 4F 46 20 53
         73DD 43 41 4E 4E
         73E1 49 4E 47
379      73E4 0D 0A 0D 0A              FCB    $0D,$0A,$0D,$0A,$0A
         73E8 0A
380      73E9 46 49 52 53              FCC    /FIRST DATA WAS STORED AT  0000/
         73ED 54 20 44 41
         73F1 54 41 20 57
         73F5 41 53 20 53
         73F9 54 4F 52 45
         73FD 44 20 41 54
         7401 20 20 30 30
         7405 30 30
381      7407 0D 0A 0D 0A              FCB    $0D,$0A,$0D,$0A
382      740B 4C 41 53 54              FCC    /LAST DATA WAS STORED AT   /
         740F 20 44 41 54
         7413 41 20 57 41
         7417 53 20 53 54
         741B 4F 52 45 44
         741F 20 41 54 20
         7423 20 20
```

```
383    7425 04                       FCB    $04
384    7426 00 0A           CHAN     FCB    $00,$0A
385    7428 48 4F 57 20              FCC    /HOW MANY CHANNELS ARE GOING /
       742C 4D 41 4E 59
       7430 20 43 48 41
       7434 4E 4E 45 4C
       7438 53 20 41 52
       743C 45 20 47 4F
       7440 49 4E 47 20
386    7444 54 4F 20 42              FCC    /TO BE SCANNED/
       7448 45 20 53 43
       744C 41 4E 4E 45
       7450 44
387    7451 20 3F                    FCC    / ?/
388    7453 00 0A 04                 FCB    $00,$0A,$04
389    7456                 VV       RMB    2
390    7458                 ALPHA    RMB    2
391    745A                 BETA     RMB    2
392    745C                 KAPOU    RMB    1
393    745D                 V        RMB    1
394    745E                 D        RMB    1
395    745F                 ST1      RMB    2
396    7461                 ST2      RMB    1
397    7462                 SACE1    RMB    2
398    7464                 STORE    RMB    2
399    7466                 SACE     RMB    2
400    7468                 DEST     RMB    2
401    746A                 CHA1     RMB    1
402    746B                 CHA2     RMB    1
403    746C                 VAL      RMB    3
404    746F                 VAR      RMB    3
405    7472                 VVV      RMB    2
406    7474                 STACK    RMB    2
407                         * TABLE FOR COMPARISONS
408    750C                          ORG    $750C
409    750C 05 95                    FCB    $05,$95
410    75E1                          ORG    $75E1
411    75E1 05 9A                    FCB    $05,$9A
412    75E6                          ORG    $75E6
413    75E6 05 A0                    FCB    $05,$A0
414    75EB                          ORG    $75EB
415    75EB 05 A6                    FCB    $05,$A6
416    75F0                          ORG    $75F0
417    75F0 05 AC                    FCB    $05,$AC
418    75F5                          ORG    $75F5
419    75F5 05 B1                    FCB    $05,$B1
420    75FA                          ORG    $75FA
421    75FA 05 B7                    FCB    $05,$B7
422    75FF                          ORG    $75FF
423    75FF 05 BD                    FCB    $05,$BD
424    7604                          ORG    $7604
425    7604 05 C3                    FCB    $05,$C3
426    7609                          ORG    $7609
427    7609 05 C8                    FCB    $05,$C8
428    760E                          ORG    $760E
429    760E 05 CE                    FCB    $05,$CE
430    7613                          ORG    $7613
431    7613 05 D4                    FCB    $05,$D4
432    7618                          ORG    $7618
433    7618 05 D9                    FCB    $05,$D9
434    761D                          ORG    $761D
435    761D 05 DF                    FCB    $05,$DF
436    7622                          ORG    $7622
437    7622 05 E5                    FCB    $05,$E5
```

```
438   7627                        ORG    $7627
439   7627 05 EB                  FCB    $05,$EB
440   762C                        ORG    $762C
441   762C 05 F0                  FCB    $05,$F0
442   7631                        ORG    $7631
443   7631 05 F6                  FCB    $05,$F6
444   7636                        ORG    $7636
445   7636 05 FC                  FCB    $05,$FC
446   763B                        ORG    $763B
447   763B 06 01                  FCB    $06,$01
448   7640                        ORG    $7640
449   7640 06 07                  FCB    $06,$07
450   7645                        ORG    $7645
451   7645 06 00                  FCB    $06,$00
452   764A                        ORG    $764A
453   764A 06 12                  FCB    $06,$12
454   764F                        ORG    $764F
455   764F 06 18                  FCB    $06,$18
456   7654                        ORG    $7654
457   7654 06 1E                  FCB    $06,$1E
458   7659                        ORG    $7659
459   7659 06 23                  FCB    $06,$23
460   765E                        ORG    $765E
461   765E 06 29                  FCB    $06,$29
462   7663                        ORG    $7663
463   7663 06 2F                  FCB    $06,$2F
464   7668                        ORG    $7668
465   7668 06 34                  FCB    $06,$34
466   766D                        ORG    $766D
467   766D 06 3A                  FCB    $06,$3A
468   7672                        ORG    $7672
469   7672 06 40                  FCB    $06,$40
470   7677                        ORG    $7677
471   7677 06 45                  FCB    $06,$45
472   767C                        ORG    $767C
473   767C 06 4B                  FCB    $06,$4B
474   7681                        ORG    $7681
475   7681 06 50                  FCB    $06,$50
476   7686                        ORG    $7686
477   7686 06 56                  FCB    $06,$56
478                               END

0 ERROR(S) DETECTED

SYMBOL TABLE:

ALPHA   7458   ARXH    700C   BADDR   FD2B   BASIC   70EB   BATH    71CB
BATH1   710E   BATH2   71E9   BATH3   7206   BATH4   7210   BETA    745A
CC1     7163   CHA1    746A   CHA2    746B   CHAN    7426   D       745E
DAVID   71AB   DECIMA  7250   DECR    7070   DELAY   7160   DELAY1  71E6
DEST    7468   DONE    7244   END1    7303   FIN     72A5   IN1     7204
IN2     72FA   IN3     734A   IN4     737B   INS     7397   INEEE   F0BA
KAPOU   745C   LINE    7324   LL      70E4   LL1     710D   NEXT    721A
OUT     7246   OUT4HS  F06A   OUTEE1  F0DF   PORTA1  FD9E   RET1    71C7
SC1     7126   SCAN    7144   SCAN1   7159   SCANN   714A   SHIFT   7071
SKATA   7180   SACE    7466   SACE1   7462   ST1     745F   ST2     7461
STACK   7474   START   7018   START1  704B   STARTO  7256   STATIS  7288
STAVA   718A   STORE   7464   TEL     7039   TEL1    706C   TELOS   70BE
TELOS1  70C4   TSEK    7328   V       7450   VAL     746C   VAR     746F
VV      7456   VVV     7472
```

APPENDIX IV

LIST OF PROGRAMS

PART 2: PROGRAM TEMP WRITTEN IN BASIC

PROGRAM TEMP RUNS
SIMULTANEOUSLY WITH
PROGRAM KINET

DEVELOPED BY
STAVROS A. ARGYROPOULOS
McGILL UNIVERSITY
1981

```
10 LET M=50000./4096.
20 LET A0=3.4238682E+2
30 A1=6.1485536E-2
40 A2=2.7924100E-7
50 DPOKE HEX("BFFB"),HEX("7000")
60 M1=M*USA(0)
70 M2=M1*M1
80 TE=A0+A1*M1+A2*M2
90 PRINT USING '****.*',TE
100 M1=M*USA(0)
110 M2=M1*M1
120 TE=A0+A1*M1+A2*M2
130 PRINT USING '****.*',TE
140 GO TO 100
150 END
```

APPENDIX IV

LIST OF PROGRAMS

PART 3: PROGRAM OFFSET WRITTEN IN MOTOROLA 6809 ASSEMBLER

PROGRAM OFFSET IS USED
FOR A/D CALIBRATION

DEVELOPED BY
STAVROS A. ARGYROPOULOS
McGILL UNIVERSITY
1981

```
  1                                    NAM    OFFSET
  2   B000                             ORG    $B000
  3   B000 108E F800                   LDY    #$F800
  4   B004 86   64         START       LDAA   #$64
  5   B006 B7   B1B0                   STAA   COUNT
  6   B009 4F                          CLRA
  7   B00A 7F   B1AF                   CLR    BHTA
  8   B00D B7   D3E0       CONV        STAA   $D3E0
  9   B010 8E   B01A                   LDX    #$B01A
 10   B013 BD   E2C5                   JSR    DELAY1
 11   B016 B6   D3E0       CC1         LDAA   $D3E0
 12   B019 85   10                     BITA   #$10
 13   B01B 27   F9                     BEQ    CC1
 14   B01D B6   D3E0                   LDAA   $D3E0
 15   B020 F6   D3E1                   LDAB   $D3E1
 16   B023 85   08                     BITA   #$08
 17   B025 27   04                     BEQ    SKATA
 18   B027 8A   F0                     ORAA   #$F0
 19   B029 20   02                     BRA    STAVR
 20   B02B 84   0F         SKATA       ANDA   #$0F
 21   B02D FD   B1B1       STAVR       STD    STORE
 22   B030 10BC B1B1                   CMPY   STORE
 23   B034 26   03                     BNE    AA
 24   B036 7C   B1AF                   INC    BHTA
 25   B039 7A   B1B0       AA          DEC    COUNT
 26   B03C 26   CF                     BNE    CONV
 27   B03E B6   B1AF                   LDAA   BHTA
 28   B041 B7   B1B3                   STAA   STRO
 29   B044 8E   B1B3                   LDX    #STRO
 30   B047 BD   E0BF                   JSR    OUT2H
 31   B04A 8E   B1B5                   LDX    #LINE
 32   B04D BD   E07E                   JSR    PDATA1
 33   B050 BD   E1AC                   JSR    INEEE
 34   B053 81   46                     CMPA   #'F
 35   B055 27   09                     BEQ    TELOS
 36   B057 8E   B1B5                   LDX    #LINE
 37   B05A BD   E07E                   JSR    PDATA1
 38  >B05D 7E   B004                   JMP    START
 39   B060 3F                  TELOS   SWI
 40   B1AF                             ORG    $B1AF
 41   B1AF                     BHTA    RMB    1
 42   B1B0                     COUNT   RMB    1
 43   B1B1                     STORE   RMB    2
 44   B1B3                     STRO    RMB    2
 45   B1B5 20 20 04            LINE    FCB    $20.$20.$04
 46                     E2C5   DELAY1  EQU    $E2C5
 47                     E0BF   OUT2H   EQU    $E0BF
 48                     E07E   PDATA1  EQU    $E07E
 49                     E101   OUTEEE  EQU    $E101
 50                     E1AC   INEEE   EQU    $E1AC
 51                                    END

0 ERROR(S) DETECTED

SYMBOL TABLE:

AA      B039    BHTA    B1AF    CC1     B016    CONV    B00D    COUNT   B1B0
DELAY1  E2C5    INEEE   E1AC    LINE    B1B5    OUT2H   E0BF    OUTEEE  E101
PDATA1  E07E    SKATA   B02B    START   B004    STAVR   B02D    STORE   B1B1
STRO    B1B3    TELOS   B060
```

APPENDIX IV

LIST OF PROGRAMS

PART 4: PROGRAM GAIN WRITTEN IN MOTOROLA 6809 ASSEMBLER

PROGRAM GAIN IS USED
FOR A/D CALIBRATION

DEVELOPED BY
STAVROS A. ARGYROPOULOS
McGILL UNIVERSITY
1981

```
 1                                    NAM    GAIN
 2    B000                            ORG    $B000
 3    B000 108E 07FF                  LDY    #$07FF
 4    B004 86   64         START      LDAA   #$64
 5    B006 B7   B1B0                  STAA   COUNT
 6    B009 4F                         CLRA
 7    B00A 7F   B1AF                  CLR    BHTA
 8    B00D B7   03E0       CONV       STAA   $03E0
 9    B010 8E   B01A                  LDX    #$B01A
10    B013 BD   E2C5                  JSR    DELAY1
11    B016 B6   03E0       CC1        LDAA   $03E0
12    B019 85   10                    BITA   #$10
13    B01B 27   F9                    BEQ    CC1
14    B01D B6   03E0                  LDAA   $03E0
15    B020 F6   03E1                  LDAB   $03E1
16    B023 85   08                    BITA   #$08
17    B025 27   04                    BEQ    SKATA
18    B027 8A   F0                    ORAA   #$F0
19    B029 20   02                    BRA    STAVR
20    B02B 84   0F         SKATA      ANDA   #$0F
21    B02D FD   B1B1       STAVR      STD    STORE
22    B030 10BC B1B1                  CMPY   STORE
23    B034 26   03                    BNE    AA
24    B036 7C   B1AF                  INC    BHTA
25    B039 7A   B1B0       AA         DEC    COUNT
26    B03C 26   CF                    BNE    CONV
27    B03E B6   B1AF                  LDAA   BHTA
28    B041 B7   B1B3                  STAA   STRO
29    B044 8E   B1B3                  LDX    #STRO
30    B047 BD   E0BF                  JSR    OUT2H
31    B04A 8E   B1B5                  LDX    #LINE
32    B04D BD   E07E                  JSR    PDATA1
33    B050 BD   E1AC                  JSR    INEEE
34    B053 81   46                    CMPA   #'F
35    B055 27   09                    BEQ    TELOS
36    B057 8E   B1B5                  LDX    #LINE
37    B05A BD   E07E                  JSR    PDATA1
38   >B05D 7E   B004                  JMP    START
39    B060 3F                  TELOS      SWI
40    B1AF                            ORG    $B1AF
41    B1AF                     BHTA   RMB    1
42    B1B0                     COUNT  RMB    1
43    B1B1                     STORE  RMB    2
44    B1B3                     STRO   RMB    2
45    B1B5 20 20 04            LINE   FCB    $20,$20,$04
46                  E2C5       DELAY1 EQU    $E2C5
47                  E0BF       OUT2H  EQU    $E0BF
48                  E07E       PDATA1 EQU    $E07E
49                  E1D1       OUTEEE EQU    $E1D1
50                  E1AC       INEEE  EQU    $E1AC
51                                    END

0 ERROR(S) DETECTED

SYMBOL TABLE:

AA      B039   BHTA    B1AF   CC1     B016   CONV    B00D   COUNT  B1B0
DELAY1  E2C5   INEEE   E1AC   LINE    B1B5   OUT2H   E0BF   OUTEEE E1D1
PDATA1  E07E   SKATA   B02B   START   B004   STAVR   B02D   STORE  B1B1
STRO    B1B3   TELOS   B060
```

APPENDIX IV

LIST OF PROGRAMS

PART 5: PROGRAM DISSOLUTION

WRITTEN IN FORTRAN

DEVELOPED BY
STAVROS A. ARGYROPOULOS
McGILL UNIVERSITY
1981

```
C       PROGRAM  ---  DISSOLUTION
        REAL*4 T(2,185),M(185,2),LHTI,LHTR,MTI1,MTI2
        REAL*4 MFE,MFETI1,MT1FER,MT2FE,MTLFE,MT2L,MTL2,QQ(185)
        REAL*4 DTA(185),DTLH(185),Q(185),MFET2R,MFET2,MFETL,MT12,MT21
        REAL*4 MPFE,LENGTH,ITA,KT1,KT2,KTIL,LHFE,KFE,MTIL
        REAL*4 MT2FER,MTL1,MT1L
        REAL*4 RADIUS,RAD,R0,R1
        REAL*4 KT,KEQ,KFETI1,KFETI2
        INTEGER CI,INDEX(20)
        COMMON /PART1/ DLX,DLX5,X,A,KFE,Q,TRE,TT,TR,TL,M,T
        COMMON /PART2/ MT1FER,MT2FER,MT2FE,MTLFE,MT2L,MT1,MT2
        COMMON /PART3/ MTIL,MFE,MT12,MT21,MFET2R,MFETL,DEAD,RAD1
        COMMON /PART4/ DEFE,CPFE,QMTI1,QMTI2,QMTIL,MPFE,KT1
        COMMON /PART5/ DLX22,KT2,KTIL,MFET2,QGEN
        COMMON /PART6/ DTA,DTLH,QG1,DAT,DX,CPTI1,CPTI2,CPTIL,DLT
        COMMON /PART7/ L0,N,CI,N3
C
C            SECTION 1  ---
C            INPUT DATA
C
        READ(5,10)(INDEX(II),II=1,20)
10      FORMAT(20A4)
        READ(5,1)L0
C           L0:NUMBER OF NODAL POINTS
1       FORMAT(I2)
        READ(5,3)ITER
C            ITER: NUMBER OF ITERATIONS
3       FORMAT(I6)
2       FORMAT(F12.5)
        READ(5,2)DLT
C         DLT:ITERATION TIME
        READ(5,2)COUL
C           COUL:COOLING RATE OF THE BATH
        READ(5,2)LENGTH
C            LENGTH:CYLINDER IMMERSION LENGTH
        READ(5,2)ITA
C            ITA:INITIAL TEMPERATURE OF THE CYLINDER
        READ(5,2)MPFE
C             MPFE:STEEL MELTING POINT
        READ(5,2)TR
C             TR:TRANSFORMATION TEMPERATURE
        READ(5,2)TL
C            TITANIUM MELTING POINT
        READ(5,2)CPTI1
C          CPTI1:CP FOR THE FIRST RANGE
        READ(5,2)CPTI2
C         CPTI2:CP FOR THE SECOND RANGE
        READ(5,2)CPTIL
C        CPTIL:CP FOR LIQUID TITANIUM
        READ(5,2)KT1
C         KT1:CONDUCTIVITY FOR THE FIRST RANGE
        READ(5,2)KT2
C       KT2:CONDUCTIVITY FOR THE SECOND RANGE
        READ(5,2)KTIL
C         KTIL:CONDUCTIVITY FOR THE LIQUID TITANIUM
        READ(5,2)DLX
C          DISTANCE BETWEEN NODAL POINTS
        READ(5,2)CPFE
C         CPFE:CP FOR IRON
        READ(5,2)KFE
C         KFE:CONDUCTIVITY FOR IRON
        READ(5,2)DEAD
C         DEAD:DENSITY OF TITANIUM
```

```
      READ (5,2) DEFE
C        DEFE:DENSITY OF IRON
      READ (5,2) B
      READ (5,2) QGEN
      READ (5,2) LHFE
C        LHFE:LATENT HEAT OF IRON
      READ (5,2) LHTI
C        LHTI:LATENT HEAT OF TITANIUM
      READ (5,2) LHTA
C        LHTA:LATENT HEAT OF TRANSFORMATION
      READ (5,3) I1
C        COUNTER FOR OUTPUT
      READ (5,2) SPH
C        SPH:SUPERHEAT
      READ (5,2) R
C        R:RESISTANCE
      READ (5,2) TRE
      READ (5,3) LL
      READ (5,2)  DAT
      READ (5,2)  QG1
      READ (5,3)  NUMBER
      READ (5,3)  LAST
C
C          SECTION 2 ---
C          CALCULATIONS OF DIFFERENT M VALUES
C          AND INITIAL CONDITIONS
C
      DTTA=LHTA/CPTI1
      JJ1=0
      DTTLH=LHTI/CPTI2
      DTTFE=LHFE/CPFE
      DLX22=DLX**2.0
      CPFEE=CPFE*DLX22
      MTI1= (KT1*DLT)/(DEAD*CPTI1*DLX22)
      MTI2= (KT2*DLT)/(DEAD*CPTI2*DLX22)
      MTIL= (KTIL*DLT)/(DEAD*CPTIL*DLX22)
      MFE= (KFE*DLT)/(DEFE*CPFEE)
      MFETI1= (2*KFE*KT1*DLX*DLT)/((KFE*DLX+2.*R*KFE*KT1+KT1*DLX)*
     1CPFEE*DEFE)
      KFETI1= (2*KFE*KT1*DLX)/(KFE*DLX+2.*R*KFE*KT1+KT1*DLX)
      KFETI2= (2*KFE*KT2*DLX)/(KFE*DLX+2.*R*KFE*KT2+KT2*DLX)
      MFET2R= (2*KFE*KT2*DLX*DLT)/((KFE*DLX+2.*R*KFE*KT2+KT2*DLX)*
     1CPFEE*DEFE)
      MFET2= (2.0*KFE*KT2*DLT)/((KFE+KT2)*CPFEE*DEFE)
      MFETL= (2*KFE*KTIL*DLT)/((KFE+KTIL)*CPFEE*DEFE)
      MT12= (2*KT1*KT2*DLT)/((KT1+KT2)*CPTI1*DEAD*DLX22)
      MT21= (2.0*KT2*KT1*DLT)/((KT1+KT2)*CPTI2*DEAD*DLX22)
      MT1FER= (2*KT1*KFE*DLX)*DLT/((KT1*DLX+2.0*R*KFE*KT1+KFE*
     1DLX)*CPTI1*DEAD*DLX22)
      MT2FER= (2*KT2*KFE*DLX)*DLT/((KT2*DLX+2.0*R*KFE*KT2+KFE*
     1DLX)*CPTI2*DEAD*DLX22)
      MT2FE= (2*KT2*KFE*DLT)/((KT2+KFE)*CPTI2*DEAD*DLX22)
      MTLFE= (2.0*KTIL*KFE*DLT)/((KTIL+KFE)*CPTIL*DEAD*DLX22)
      MT2L= (2.0*KT2*KTIL*DLT)/((KT2+KTIL)*CPTI2*DEAD*DLX22)
      MT1L= (2.0*KT1*KTIL*DLT)/((KT1+KTIL)*CPTI1*DEAD*DLX22)
      MTL2= (2.0*KT2*KTIL*DLT)/((KT2+KTIL)*CPTIL*DEAD*DLX22)
      MTL1= (2.0*KT1*KTIL*DLT)/((KT1+KTIL)*CPTIL*DEAD*DLX22)
      QMTI1=DLT/(CPTI1*DEAD)
      QMTI2=DLT/(CPTI2*DEAD)
      QMTIL=DLT/(CPTIL*DEAD)
      SMTI1=QMTI1/DLX22
      SMTI2=QMTI2/DLX22
      SMTIL=QMTIL/DLX22
      WRITE (6,34) (INDEX(II),II=1,20)
```

```
34    FORMAT('1',//,1X,20A4)
      WRITE(6,35)LO
35    FORMAT(3X,'NUMBER OF NODAL POINTS =',I5)
      WRITE(6,36)ITER
36    FORMAT(3X,'NUMBER OF ITERATIONS =',I8)
      WRITE(6,37)DLT
37    FORMAT(3X,'DLT =',F10.4)
      WRITE(6,38)COUL
38    FORMAT(3X,'BATH COULING RATE =',F12.4)
      WRITE(6,39)LENGTH
39    FORMAT(3X,'CYLINDER LENGTH =',F12.4)
      WRITE(6,40)ITA
40    FORMAT(3X,'INITIAL TEMPERATURE OF THE CYLINDER =',F12.4)
      WRITE(6,41)MPFE
41    FORMAT(3X,'STEEL MELTING POINT =',F12.4)
      WRITE(6,42)TR
42    FORMAT(3X,'TRANSFORMATION TEMPERATURE =',F12.4)
      WRITE(6,43)TL
43    FORMAT(3X,'TITANIUM MELTING POINT =',F12.4)
      WRITE(6,44)CPTI1
44    FORMAT(3X,'CP FOR THE FIRST RANGE =',F12.4)
      WRITE(6,45)CPTI2
45    FORMAT(3X,'CP FOR THE SECOND RANGE =',F12.4)
      WRITE(6,46)CPTIL
46    FORMAT(3X,'CP FOR THE LIQUID TITANIUM =',F12.4)
      WRITE(6,47)KT1
47    FORMAT(3X,'THERMAL CONDUCTIVITY FOR THE FIRST RANGE =',F12.4)
      WRITE(6,48)KT2
48    FORMAT(3X,'THERMAL CONDUCTIVITY FOR THE SECOND RANGE =',F12.4)
      WRITE(6,49)KTIL
49    FORMAT(3X,'THERMAL CONDUCTIVITY FOR THE LIQUID TI =',F12.4)
      WRITE(6,50)DLX
50    FORMAT(3X,'NODAL POINTS DISTANCE =',F12.4)
      WRITE(6,51)CPFE
51    FORMAT(3X,'CP FOR IRON =',F12.4)
      WRITE(6,52)KFE
52    FORMAT(3X,'THERMAL CONDUCTIVITY FOR IRON =',F12.4)
      WRITE(6,53)DEAD
53    FORMAT(3X,'TITANIUM DENSITY =',F12.4)
      WRITE(6,54)DEFE
54    FORMAT(3X,'IRON DENSITY =',F12.4)
      WRITE(6,55)B
55    FORMAT(3X,'   B =',F12.4)
      WRITE(6,56)QGEN
56    FORMAT(3X,'   HEAT GENERATINON =',F12.5)
      WRITE(6,57)LHFE
57    FORMAT(3X,'LATENT HEAT OF IRON =',F12.4)
      WRITE(6,58)LHTI
58    FORMAT(3X,'LATENT HEAT OF TITANIUM =',F12.4)
      WRITE(6,59)LHTR
59    FORMAT(3X,'LATENT HEAT OF TRANSFORMATION =',F12.4)
      WRITE(6,60)I1
60    FORMAT(3X,'FREQUENCY OF OUTPUT =',I6)
      WRITE(6,61)SPH
61    FORMAT(3X,'STEEL BATH SUPERHEAT =',F12.4)
      WRITE(6,62)R
62    FORMAT(3X,'RESISTANCE =',F12.4)
      WRITE(6,63)TRE
63    FORMAT(3X,'REACTION STARTING POINT =',F12.4)
      WRITE(6,64)MTI1
64    FORMAT(3X,'   MTI1 =',F12.4)
      WRITE(6,65)MTI2
65    FORMAT(3X,'   MTI2 =',F12.4)
      WRITE(6,66)MTIL
```

```
66     FORMAT(3X,'  MTIL   =',F12.4)
       WRITE(6,67)MFE
67     FORMAT(3X,'   MFE =',F12.4)
       WRITE(6,68)MFETI1
68     FORMAT(3X,'     MFETI1 =',F12.4)
       WRITE(6,69)MFET2A
69     FORMAT(3X,'  MFET2A =',F12.4)
       WRITE(6,70)MFET2
70     FORMAT(3X,'    MFET2 =',F12.4)
       WRITE(6,71)MFETL
71     FORMAT(3X,'  MFETL =',F12.4)
       WRITE(6,72)MT12
72     FORMAT(3X,'  MT12 =',F12.4)
       WRITE(6,73)MT21
73     FORMAT(3X,'  MT21 =',F12.4)
       WRITE(6,74)MT1FEA
74     FORMAT(3X,'  MT1FEA =',F12.4)
       WRITE(6,75)MT2FE
75     FORMAT(3X,'     MT2FE =',F12.4)
       WRITE(6,76)MTLFE
76     FORMAT(3X,'  MTLFE =',F12.4)
       WRITE(6,77)MT2L
77     FORMAT(3X,' MT2L =',F12.4)
       WRITE(6,78)MTL2
78     FORMAT(3X,'  MTL2 =',F12.4)
       WRITE(6,79)SMTI1
79     FORMAT(3X,'  SMTI1 =',F12.4)
       WRITE(6,80)SMTI2
80     FORMAT(3X,'    SMTI2 =',F12.4)
       WRITE(6,81)SMTIL
81     FORMAT(3X,'  SMTIL =',F12.4)
       WRITE(6,82) QMTI1
82     FORMAT(3X,'  QMTI1 =',F12.4)
       WRITE(6,83) QMTI2
83     FORMAT(3X,'    QMTI2 =',F12.4)
       WRITE(6,84) QMTIL
84     FORMAT(3X,'    QMTIL =',F12.4)
       WRITE(6,85)LL
85     FORMAT(3X,' LL =',I3)
       WRITE(6,86)MT2FEA
86     FORMAT(3X,'MT2FEA =',F12.4)
       WRITE(6,87) MTL1
87     FORMAT(3X,' MTL1 =',F12.4)
       WRITE(6,88) MT1L
88     FORMAT(3X,' MT1L =',F12.4)
       WRITE(6,8900) DAT
8900   FORMAT(10X,'DISSOLUTION FRONT MOVING RATE=',F12.3)
       WRITE(6,8910) QG1
8910   FORMAT(10X,'FREE DISSOLUTION HEAT GENERATION RATE=',F12.3)
       WRITE(6,8920) NUMBER
8920   FORMAT(10X,'ITERATION NUMBER WHERE FREE DISSOLUTION',
      *1X,'STARTS=',I6)
       WRITE(6,8930) LAST
8930   FORMAT(10X,'LAST NODAL POINT FOR ITERATIONS',I6)
       N=LO-1
C          N:  MOVEABLE NODAL POINT
       L1=LO+1
C          L1: FIRST NODAL POINT  IN THE STEEL SHELL
       L2=3*LO
       DLX5=DLX*0.5
       DLX15=DLX*1.5
       X=DLX5
       H1=-TA+ITA
       H2=-TL+TA
```

```
      H3=-MPFE+ITA
      DO 90 J=1,LO
      T(1,J)=ITA
      M(J,2)=MTI1
      M(J,1)=MTI1
      DTA(J)=H1
      DTLH(J)=H2
      QQ(J)=QMTI1
      Q(J)=0.0
 90   CONTINUE
      DO 100 J=L1,L2
      M(J,2)=MFE
      Q(J)=0.0
      QQ(J)=0.0
      DTA(J)=H3
      DTLH(J)=0.0
 100  CONTINUE
      M(L1,1)=MFETI1
      CALL SMTIFE
C:        CALL SMTIFE IN ORDER TO SET THE PROPER M(LO,2)
      N2=LO-1
      L3=L1+1
      DO 101 J=L3,L2
      M(J,1)=MFE
101   CONTINUE
      RAD=(N2+0.5)*DLX
      COUL=COUL*DLT
      RAD1=(2.*LO-1)*DLX5
      RAD2=RAD1**2.0
      TLEN=2.0*(2**0.5)*(LENGTH)
      CI=0
      TAA=TA-DTTA
      TLL=TL-DTTLH
      TFFE=MPFE-DTTFE
      N4=L1
      HH1=41400.0/8.3144
      HH2=CPFE/KFE
      HH3=8*981.0*(LENGTH**3)
      HH4=0.678044*KFE/LENGTH
      HH5=0.38*KFE
      E916=9./16.
      E49=-4./9.
C
C            SECTION 3 ---
C            CALCULATES NEW TEMPERATURES
C            AND THE POSITION OF STEEL SHELL INTERFACE
C
      DO 3000 I=1,ITER
      TT=I*DLT
      IF(JJ1.NE.0) GO TO 105
      SPH=SPH-COUL
      TV=1809.15+SPH
      TVA=HH1/TV
      V=0.003699*EXP(TVA)
      DEFE1=7.015-0.000883*SPH
      PA=V*HH2
      GA=SPH*(DEFE1**2*HH3)/(V**2)
      H1=(0.492/PA)**(E916)
      H2=(1+H1)**(E49)
      H4=HH4*(PA**0.23)*H2
      H3=HH5*(PA**(-0.17))*H2
      H5=H3/RAD
      H=H5+H4*(GA**0.25)
      E=(TLEN)/((GA**0.25)*RAD)
```

```
C
C          T(2,1) :   NEW TEMPERATURE AT THE FIRST NODAL POINT
C
105    T(2,1)=T(1,1)*(1-4.*M(1,2))+4.0*M(1,2)*T(1,2)+Q(1)*QQ(1)
       H1=T(2,1)-T(1,1)
       DTA(1)=DTA(1)+H1
       IF(1.GE.N4)DTLH(1)=DTLH(1)+H1
       AN=N-1
       DO 102 J=2,N
       A=J-1
C
C          T(2,J) :NEW TEMPERATURES FROM THE SECOND NODAL POINT
C          UNTIL THE ONE BEFORE LAST NODAL POINT
C
       T(2,J)=T(1,J)*(1- M(J,2)*((2.0*A+1)/(2.0*A))
      o- M(J,1)*((2.0*A-1)/(2.0*A)))
      o+ M(J,1)*((2.0*A-1)/(2.0*A))*T(1,J-1)+
      oM(J,2)*((2.0*A+1)/(2.0*A))*T(1,J+1)+Q(J)*QQ(J)
       H1=T(2,J)-T(1,J)
       DTA(J)=DTA(J)+H1
       IF(J.GE.N4)DTLH(J)=DTLH(J)+H1
102    CONTINUE
C
C          T(2,N+1): NEW TEMPERATURE AT THE LAST NODAL POINT
C
       IF(JJ1.NE.0) CALL FREE
       IF(JJ1.NE.0) GO TO 140
       AN1=((2*N+1)/2.0)*DLX+X-DLXS
       AN=((2*N-1)/2.0)*DLX
       VN1X=(2*X*N*DLX+X**2.0+N*DLX22-(DLX22/4.0))/2.0
       IF(N+1.GT.LO) GO TO 114
       VN1=N*DLX22
       VFE=VN1X-VN1
       WFE=VFE*DEFE
       WN1=VN1*DEAD
       AMEAN=(WFE+WN1)/VN1X
       IF(T(1,LO).LE.TA) GO TO 110
       IF(T(1,LO).GT.TA.AND.T(1,LO).LT.TL)GO TO 112
       CP=CPTIL
       KT=KTIL
       GO TO 115
110    CP=CPTI1
       KT=KT1
       GO TO 115
112    CP=CPTI2
       KT=KT2
       GO TO 115
114    KEQ=KFE
       CPMEAN=CPFE
       AMEAN=DEFE
       KT=KFE
       IF(N+1.EQ.L1.AND.T(1,LO).LE.TA)KT=KFETI1
       IF(N+1.EQ.L1.AND.T(1,LO).GT.TA)KT=KFETI2
       GO TO 120
115    P=X-DLXS
       KEQ=(DLX+2.0*P)*(KT*KFE/(DLX*KFE+2.0*A*KT*KFE+2.0*KT*P))
       CPMEAN=(CPFE*WFE+CP*WN1)/(WFE+WN1)
120    FIRST=(MPFE-T(1,N+1))*AN1*KEQ*DLT/(X*AMEAN*CPMEAN*VN1X)
       SECOND=(T(1,N+1)-T(1,N))*AN*KT*DLT/(DLX*AMEAN*CPMEAN*VN1X)
       T(2,N+1)=T(1,N+1)+FIRST-SECOND+Q(N+1)*QQ(N+1)
       H1=T(2,N+1)-T(1,N+1)
       DTA(N+1)=DTA(N+1)+H1
       IF(N+1.GE.N4)DTLH(N+1)=DTLH(N+1)+H1
C          DX:CALCULATION OF THE MOVEMENT OF THE INTERFACE
```

```
C         IN THE ITERATION STEP
      IF(N+1.GT.LO)  GO TO 130
      KT=KT1
      IF(T(1,LO).GT.TR)  KT=KT2
      P=X-DLX5
      KEQ=(DLX+2.0*P)*(KT*KFE/(DLX*KFE+2.0*R*KT*KFE+
     @2.0*KT*P))
      GO TO 132
130   KEQ=KFE
132   DX=(MPFE-T(1,N+1))*KEQ*DLT/(DEFE*LHFE*X)-
     @(H*SPH*DLT)/(DEFE*LHFE)
C          X: DISTANCE OF THE SHELL INTERFACE FROM THE LAST NODAL POINT
140   X=X+DX
      N3=N+1
C         RAD :  RADIUS OF CYLINDER IN EVERY ITERATION STEP
      RAD=((2.*N+1)*DLX)/2.+X-DLX5
      NDIF=N-LAST
      IF(NDIF)3100,3100,153
C
C         SECTION  4----
C         THE PROGRAM CHECKS FOR THE POSITION OF STEEL SHELL
C         LIQUID STEEL INDERFACE
C
153   IF(X-DLX5)155,160,160
155   N=N-1
      N3=N+1
      X=X+DLX
      GO TO 165
160   IF(X-DLX15)165,161,161
161   N=N+1
      N3=N+1
      X=X-DLX
      T(1,N+1)=(MPFE*DLX+X*T(2,N))/(X+DLX)
      DTR(N+1)=T(1,N+1)-MPFE
C
C         SECTION 5 ---
C         CALCULATION OF LATENT HEAT OF TRANSFORMATION
C
165   DO 250 J=1,LO
      IF(J.GE.N4)  GO TO 190
      IF(DTR(J).GT.0.0)  GO TO 170
      T(1,J)=DTR(J)+TR
      GO TO 250
170   IF(DTR(J).GT.DTTR)  GO TO 180
      T(1,J)=TR
      GO TO 250
180   T(1,J)=TRR+DTR(J)
      DTLH(J)=DTLH(J)+(CPTI1*(T(1,J)-TR)/CPTI2)
      N4=J
190   IF(DTLH(J).GT.0.0)  GO TO 200
      T(1,J)=DTLH(J)+TL
      GO TO 250
200   IF(DTLH(J).GT.DTTLH)  GO TO 210
      T(1,J)=TL
      GO TO 250
210   T(1,J)=TLL+DTLH(J)
250   CONTINUE
      IF(L1.GT.N3)  GO TO 270
      DO 260 J=L1,N3
      IF(DTR(J).GT.0.0)  GO TO 262
      T(1,J)=DTR(J)+MPFE
      GO TO 260
262   IF(DTR(J).GT.DTTFE)  GO TO 264
      T(1,J)=MPFE
```

```
      GO TO 260
264   T(1,J)=TFFE+DTA(J)
260   CONTINUE
270   IF(LL.EQ.0) GO TO 365
      IF(CI.EQ.0) CALL TEMPER
      IF(CI.NE.0) CALL REACTI
C
C          SECTION 6 ---
C          SETS PROPER M VALUES
C
365   IF(T(1,1).GT.TL)GO TO 400
      IF(T(1,1).GT.TA.AND.T(1,1).LE.TL)GO TO 420
      IF(T(1,1).LE.TA)GO TO 425
400   DO 405 J=1,LO
      M(J,1)=MTIL
405   CONTINUE
      DO 410 J=1,N2
      M(J,2)=MTIL
410   CONTINUE
      CALL SMTLFE
      GO TO 500
420   IF(T(1,2).GT.TL)M(1,2)=MT2L
      IF(T(1,2).GT.TA.AND.T(1,2).LE.TL)M(1,2)=MTI2
      GO TO 430
425   IF(T(1,2).GT.TL)M(1,2)=MTI2L
      IF(T(1,2).GT.TA.AND.T(1,2).LE.TL)M(1,2)=MT12
      IF(T(1,2).LE.TA)M(1,2)=MTI1
430   DO 460 J=2,N2
      IF(T(1,J).GT.TL)GO TO 435
      IF(T(1,J).GT.TA.AND.T(1,J).LE.TL)GO TO 440
      IF(T(1,J).LE.TA)GO TO 450
435   M(J,2)=MTIL
      IF(T(1,J-1).GT.TL)M(J,1)=MTIL
      IF(T(1,J-1).GT.TA.AND.T(1,J-1).LE.TL)M(J,1)=MTL2
      IF(T(1,J-1).LE.TA)M(J,1)=MTL1
      GO TO 460
440   IF(T(1,J+1).GT.TL)M(J,2)=MT2L
      IF(T(1,J+1).GT.TA.AND.T(1,J+1).LE.TL)M(J,2)=MTI2
      IF(T(1,J-1).GT.TA.AND.T(1,J-1).LE.TL)M(J,1)=MTI2
      IF(T(1,J-1).LE.TA)M(J,1)=MT21
      GO TO 460
450   IF(T(1,J+1).GT.TL)M(J,2)=MT1L
      IF(T(1,J+1).GT.TA.AND.T(1,J+1).LE.TL)M(J,2)=MT12
      IF(T(1,J+1).LE.TA)M(J,2)=MTI1
      M(J,1)=MTI1
460   CONTINUE
      IF(T(1,LO).GT.TL)GO TO 470
      IF(T(1,LO).GT.TA.AND.T(1,LO).LE.TL)GO TO 480
      IF(T(1,LO).LE.TA)GO TO 490
470   CALL SMTLFE
      IF(T(1,N2).GT.TL)M(LO,1)=MTIL
      IF(T(1,N2).GT.TA.AND.T(1,N2).LE.TL)M(LO,1)=MTL2
      IF(T(1,N2).LE.TA)M(LO,1)=MTL1
      GO TO 500
480   CALL SMT2FE
      IF(T(1,N2).GT.TA.AND.T(1,N2).LE.TL)M(LO,1)=MTI2
      IF(T(1,N2).LE.TA)M(LO,1)=MT21
      GO TO 500
490   CALL SMT1FE
      M(LO,1)=MTI1
500   IF(N+1.GT.LO)GO TO 510
      GO TO 1200
510   IF(T(1,LO).GT.TL)M(L1,1)=MFETL
      IF(T(1,LO).GT.TA.AND.T(1,LO).LE.TL)M(L1,1)=MFET2A
```

```
      IF(T(1,LO).LE.TA)M(L1,1)=MFETI1
1200  DO 1210 J=1,LO
      IF(T(1,J).LE.TA) QQ(J)=QMTI1
      IF(T(1,J).GT.TA.AND.T(1,J).LE.TL) QQ(J)=QMTI2
      IF(T(1,J).GT.TL) QQ(J)=QMTIL
1210  CONTINUE
      IF(JJ1.EQ.0) GO TO 2900
      IF(MOD(I,I1).EQ.0) GO TO 1300
      GO TO 2900
1300  WRITE(6,1301)TT,(T(1,J),J=1,N3)
1301  FORMAT(1X,F12.4,10(1X,F10.4),/6X,10(1X,F10.4),
     1/6X,10(1X,F10.4),/6X,10(1X,F10.4),/6X,10(1X,F10.4),
     1/6X,10(1X,F10.4),/6X,10(1X,F10.4),/6X,10(1X,F10.4),
     1/6X,10(1X,F10.4),/6X,10(1X,F10.4),/6X,10(1X,F10.4),
     1/6X,10(1X,F10.4),/6X,10(1X,F10.4),/6X,10(1X,F10.4),
     1/6X,10(1X,F10.4),/6X,10(1X,F10.4))
      WRITE(6,1302)X,RAD
1302  FORMAT('0','DISTANCE FROM LAST NODAL POINT=',F10.5,
     $10X,'RADIUS OF CYLINDER=',F10.5)
2900  IF(I.EQ.NUMBER) GO TO 2910
      GO TO 3000
2910  N3=LO-1
      N=N3-1
      X=DLX15
      JJ1=1
      T(1,LO)=MPFE+SPH
3000  CONTINUE
3100  WRITE(6,3101)
3101  FORMAT('0',20X, ' L A S T  T E M P E R A T U R E')
      WRITE(6,1301)TT,(T(1,J),J=1,N3)
      STOP
      END
C
      SUBROUTINE TEMPER
      REAL*4 T(2,185),M(185,2),LHTI,LHTR,MTI1,MTI2
      REAL*4 MFE,MFETI1,MT1FER,MT2FE,MTLFE,MT2L,MTL2,QQ(185)
      REAL*4 DTA(185),DTLH(185),Q(185),MFET2R,MFET2,MFETL,MT12,MT21
      REAL*4 MPFE,KT1,KT2,KTIL,KA,MT2FER,KFE
      REAL*4 MTIL,MTL1,MT1L
      INTEGER CI,INDEX(20)
      COMMON /PART1/ DLX,DLX5,X,A,KFE,Q,TAE,TT,TA,TL,M,T
      COMMON /PART2/ MT1FER,MT2FER,MT2FE,MTLFE,MT2L,MT1,MT2
      COMMON /PART3/ MTIL,MFE,MT12,MT21,MFET2R,MFETL,DEAD,RAD1
      COMMON /PART4/ DEFE,CPFE,QMTI1,QMTI2,QMTIL,MPFE,KT1
      COMMON /PART5/ DLX22,KT2,KTIL,MFET2,QGEN
      COMMON /PART7/ LO,N,CI,N3
      IF(T(1,LO).LT.TA) KA=KT1
      IF(T(1,LO).GE.TA.AND.T(1,LO).LT.TL) KA=KT2
      IF(T(1,LO).GT.TL) KA=KTIL
      IF(N+1.GT.LO) GO TO 5
      Y=X
      TPFE=MPFE
      GO TO 6
5     Y=DLX
      TPFE=T(1,LO+1)
6     F1=TPFE*KFE/(Y-DLX5)
      F2=(1+(KA*A/DLX5))*A
      F3=KA*T(1,LO)*A/DLX5
      F4=KFE/(Y-DLX5)
      F4=F4+1./A
      F4=1./F4
      F5=F4/F2
      F6=F3*F4/F2
      F7=F1*F4
```

```
      TSHEL=(F7+F6)/(1.-F5)
      F8=F2/R
      TADD=(TSHEL+F3)/F8
      IF(TSHEL.GT.TRE.AND.TADD.GT.TRE)  GO TO 20
      GO TO 40
20    CI=CI+1
      WRITE(6,25)  TT
25    FORMAT('0',////,20X,30('*'),///,20X,'THE REACTION STARTS AT  =',
     $F10.5,2X,'SEC',///,20X,30('*'),/////)
      MFET2R=MFET2
      MT2FER=MT2FE
      R=0.0
40    RETURN
      END
C
      SUBROUTINE SMT1FE
      REAL*4 T(2,185),M(185,2),LHTI,LHTR,MTI1,MTI2
      REAL*4 MFE,MFETI1,MT1FER,MT2FE,MTLFE,MT2L,MTL2,QQ(185)
      REAL*4 DTR(185),DTLH(185),Q(185),MFET2R,MFET2,MFETL,MT12,MT21
      REAL*4 MPFE,MT2FER,KT1,KT2,KTIL,KA,KEQ,KFE
      REAL*4 MTIL,MTL1,MT1L
      INTEGER CI,INDEX(20)
      COMMON /PART1/ DLX,DLX5,X,R,KFE,Q,TRE,TT,TR,TL,M,T
      COMMON /PART2/ MT1FER,MT2FER,MT2FE,MTLFE,MT2L,MT1,MT2
      COMMON /PART3/ MTIL,MFE,MT12,MT21,MFET2R,MFETL,DEAD,RAD1
      COMMON /PART4/ DEFE,CPFE,QMTI1,QMTI2,QMTIL,MPFE,KT1
      COMMON /PART5/ DLX22,KT2,KTIL,MFET2,QGEN
      COMMON /PART7/ LO,N,CI,N3
      IF(N+1.GT.LO)  GO TO 10
      GO TO 20
10    M(LO,2)=MT1FER
      GO TO 100
20    P=X-DLX5
      KEQ=(DLX+2.0*P)*(KT1*KFE/(DLX*KFE+2.0*R*KT1*KFE+2.0*KT1*P))
      M(LO,2)=(QMTI1/((DLX5+X)**2.000))*KEQ
100   RETURN
      END
C
      SUBROUTINE SMT2FE
      REAL*4 T(2,185),M(185,2),LHTI,LHTR,MTI1,MTI2
      REAL*4 MFE,MFETI1,MT1FER,MT2FE,MTLFE,MT2L,MTL2,QQ(185)
      REAL*4 DTR(185),DTLH(185),Q(185),MFET2R,MFET2,MFETL,MT12,MT21
      REAL*4 MPFE,MT2FER,KT1,KT2,KTIL,KA,KEQ,KFE
      REAL*4 MTIL,MTL1,MT1L
      INTEGER CI,INDEX(20)
      COMMON /PART1/ DLX,DLX5,X,R,KFE,Q,TRE,TT,TR,TL,M,T
      COMMON /PART2/ MT1FER,MT2FER,MT2FE,MTLFE,MT2L,MT1,MT2
      COMMON /PART3/ MTIL,MFE,MT12,MT21,MFET2R,MFETL,DEAD,RAD1
      COMMON /PART4/ DEFE,CPFE,QMTI1,QMTI2,QMTIL,MPFE,KT1
      COMMON /PART5/ DLX22,KT2,KTIL,MFET2,QGEN
      COMMON /PART7/ LO,N,CI,N3
      IF(N+1.GT.LO) GO TO 10
      GO TO 20
10    M(LO,2)=MT2FER
      GO TO 100
20    P=X-DLX5
      KEQ=(DLX+2.0*P)*(KT2*KFE/(DLX*KFE+2.0*R*KT2*KFE+2.0*KT2*P))
      M(LO,2)=(QMTI2/((DLX5+X)**2.000))*KEQ
100   RETURN
      END
C
      SUBROUTINE SMTLFE
      REAL*4 T(2,185),M(185,2),LHTI,LHTR,MTI1,MTI2
      REAL*4 MFE,MFETI1,MT1FER,MT2FE,MTLFE,MT2L,MTL2,QQ(185)
```

```
      REAL*4 DTR(185),DTLH(185),Q(185),MFET2R,MFET2,MFETL,MT12,MT21
      REAL*4 MPFE,MT2FER,KT1,KT2,KTIL,KA,KFE,KEQ
      REAL*4 MTIL,MTL1,MT1L
      INTEGER CI,INDEX(20)
      COMMON /PART1/ DLX,DLX5,X,R,KFE,Q,TRE,TT,TA,TL,M,T
      COMMON /PART2/ MT1FER,MT2FER,MT2FE,MTLFE,MT2L,MT1,MT2
      COMMON /PART3/ MTIL,MFE,MT12,MT21,MFET2R,MFETL,DEAD,RAD1
      COMMON /PART4/ DEFE,CPFE,QMTI1,QMTI2,QMTIL,MPFE,KT1
      COMMON /PART5/ DLX22,KT2,KTIL,MFET2,QGEN
      COMMON /PART7/ LO,N,CI,N3
      IF(N+1.GT.LO) GO TO 10
      GO TO 20
10    M(LO,2)=MTLFE
      GO TO 100
20    P=X-DLX5
      KEQ=(DLX+2.0*P)*(KTIL*KFE/(DLX*KFE+2.0*KTIL*P))
      M(LO,2)=(QMTIL/((DLX5+X)**2.000))*KEQ
100   RETURN
      END
C
      SUBROUTINE REACTI
      REAL*4 T(2,185),M(185,2),LHTI,LHTR,MTI1,MTI2
      REAL*4 MFE,MFETI1,MT1FER,MT2FE,MTLFE,MT2L,MTL2,QQ(185)
      REAL*4 DTR(185),DTLH(185),Q(185),MFET2R,MFET2,MFETL,MT12,MT21
      REAL*4 MPFE,MT2FER,KT1,KT2,KTIL,KA
      REAL*4 MTIL,MTL1,MT1L,KFE
      INTEGER CI,INDEX(20)
      COMMON /PART1/ DLX,DLX5,X,R,KFE,Q,TRE,TT,TA,TL,M,T
      COMMON /PART2/ MT1FER,MT2FER,MT2FE,MTLFE,MT2L,MT1,MT2
      COMMON /PART3/ MTIL,MFE,MT12,MT21,MFET2R,MFETL,DEAD,RAD1
      COMMON /PART4/ DEFE,CPFE,QMTI1,QMTI2,QMTIL,MPFE,KT1
      COMMON /PART5/ DLX22,KT2,KTIL,MFET2,QGEN
      COMMON /PART7/ LO,N,CI,N3
      DO 10 J=1,N3
      Q(J)=0.0
10    CONTINUE
      Q(LO)=QGEN
      RETURN
      END
C
      SUBROUTINE FREE
      REAL*4 T(2,185),M(185,2),LHTI,LHTR,MTI1,MTI2
      REAL*4 MFE,MFETI1,MT1FER,MT2FE,MTLFE,MT2L,MTL2,QQ(185)
      REAL*4 DTR(185),DTLH(185),Q(185),MFET2R,MFET2,MFETL,MT12,MT21
      REAL*4 MPFE,LENGTH,ITA,KT1,KT2,KTIL,LHFE,KFE,MTIL
      REAL*4 MT2FER,MTL1,MT1L
      REAL*4 KT,KEQ,KFETI1,KFETI2
      INTEGER CI,INDEX(20)
      COMMON /PART1/ DLX,DLX5,X,R,KFE,Q,TRE,TT,TA,TL,M,T
      COMMON /PART2/ MT1FER,MT2FER,MT2FE,MTLFE,MT2L,MT1,MT2
      COMMON /PART3/ MTIL,MFE,MT12,MT21,MFET2R,MFETL,DEAD,RAD1
      COMMON /PART4/ DEFE,CPFE,QMTI1,QMTI2,QMTIL,MPFE,KT1
      COMMON /PART5/ DLX22,KT2,KTIL,MFET2,QGEN
      COMMON /PART6/ DTR,DTLH,QG1,DRT,DX,CPTI1,CPTI2,CPTIL,DLT
      COMMON /PART7/ LO,N,CI,N3
      AN1=((2*N+1)/2.0)*DLX+X-DLX5
      AN=((2*N-1)/2.0)*DLX
      VN1X=(2*X*N*DLX+X**2.0+N*DLX22-(DLX22/4.0))/2.0
      IF(T(1,N+1).LT.TA) GO TO 10
      IF(T(1,N+1).GE.TA.AND.T(1,N+1).LE.TL)GO TO 20
      GO TO 30
10    CP=CPTI1
      KT=KT1
      GO TO 50
```

```
 20     CP=CPTI2
        KT=KT2
        GO TO 50
 30     CP=CPTIL
        KT=KTIL
 50     F1=(DEAD*CP*VN1X)
        F2=QG1*AN1*DLT/F1
        F3=F1*DLX
        F4=KT*AN*(T(1,N+1)-T(1,N))*DLT
        F5=F4/F3
        T(2,N+1)=T(1,N+1)+F2-F5
        F1=T(2,N+1)-T(1,N+1)
        DTA(N+1)=DTA(N+1)+F1
        DTLH(N+1)=DTLH(N+1)+F1
        DX=-DAT*DLT
        RETURN
        END
```

REFERENCES

1. V.O. Dahlke and O. Knacke, 'Die Auflösung von Kohlenstoff in Flüssigem Eisen', Arch. Eisenhüttenw., 26, 373, 1955.
2. R. Krzeszewski, 'Kinetics of Dissolving Stable Carbon in Liquid Iron', Prace Inst. Odlewnictwa, 13, 1, 1963.
3. M. Kosaka and S. Minowa, 'Mass Transfer from Graphite Cylinder into Liquid Fe-C Alloy', Tetsu-to-Hagane, 53, 1467, 1967.
4. R.G. Olsson, V. Koump, and T.F. Perzak, 'Rate of Dissolution of Carbon in Molten Iron-Carbon Alloys', Trans. AIME, 236, 426, 1966.
5. V.D. Shantarin, V.V. Utochkin, and V.S. Kubryavtsev, 'Diffusion of Carbon in Manganese-Base Melts', Izv. VUZ chernaya Met., No. 6, 5, 1968.
6. V.P. Karshin and V.A. Grigoryan, 'Kinetics of the Dissolution of Graphite in an Iron-Carbon Melts', Izv. VUZ chernaya Met., No. 11, 16, 1970.
7. V.M. Surovsky and N.K. Nekrasov, 'Kinetics of Solution of Carbon in Iron', Izv. VUZ chernaya Met., No. 1, 164, 1971; Steel in the USSR, No. 1, 75, 1971.
8. P.M. Shurygin and V.I. Kryuk, 'The Kinetics of Dissolving Carbon in Iron-Carbon Solutions', Izv. VUZ chernaya Met., 6, No. 12, 14, 1963.
9. V.P. Cherevko, B.M. Boichenko, V.M. Dusha, B.M. Korkin, 'Kinetics of Dissolution of Carbon Materials in Iron-

Carbon Melts', Metallurgiya Koksokhimiya. Resp. Mezhred. Nauch.-tekhn. sb 1977, 52, 36-39.

10. A.K. Biletskii, V.S. Shumikhin, 'Dissolution of Solid Spherical Particles in a Liquid', Protessy Plavki Liteinykh Splavov, 65-70, 1979.

11. A. Mihajlovic, B. Marincek, 'Dissolution Kinetics of Technical Graphites in Iron Melts', Arch. Eisenhuettenw 44(7), 507-512, 1973.

12. V.M. Surovskii, N.K. Nekrasov, 'Kinetics of the Dissolution of Carbon in a High-Carbon Melt', Sb. Tr., Mosk. Vech. Metall. Inst., 1972, No. 12, 13-16 (in Russian).

13. P.M. Shurygin and V.D. Shantrin, 'Diffusion in the Fe-C System', Fiz. Met. Metallovdenie, 17, 471, 1964

14. P.M. Shurygin and V.D. Shantrin, 'Solubility of Metals in Fe-C Solutions', Izv. VUZ. chernaya Met., 6, No. 10, 5, 1963.

15. J.W. Robison, A.B. Draper, 'Dissolution of Silicon Carbide in Liquid Gray Irons', Paper No. A 78-21, 107th AIME Annual Meeting, Denver, February, 1978.

16. R.D. Pehlke, P.D. Goodell and R.W. Dunlap, 'Kinetics of Steel Dissolution in Molten Pig Iron', Trans. AIME, 233, 1420, 1965.

17. R.G. Olsson, V. Koump, and T.F. Perzak, 'Rate of Dissolution of Carbon-Steel in Molten Iron-Carbon Alloys', Trans. AIME, 233, 1654, 1965.

18. K. Niwa, M. Shimei and R. Shina, 'A Kinetic Study on the Reaction of the Alumina Crucible with Carbon Dissolved in Molten Iron', Nippon Kinzok Gakkai-Si, 30, 329, 1966.

19. M. Kosaka and S. Minowa, 'Dissolution of Steel Cylinder into Liquid Fe-C Alloy', Tetsu-to-Hagane, 52, 1429, 1966.

20. M. Kosaka and S. Minowa, 'Mass Transfer from Solid Metal Cylinder into Liquid Metal', Tetsu-to-Hagane, 52, 1429, 1966.

21. A.V. Klibus, B.M. Lepinskikh, and A.A. Gorshkov, 'Kinetics of the Dissolution of a Copper-Magnesium Alloy in Molten Cast Iron', Dop. Akad. Ukrain. R.S.R., 6A, 536, 1967.

22. M. Kosaka and S. Minowa, 'Dissolution of Steel Cylinder into Liquid Fe-C Alloy', Tetsu-to-Hagane, 53, 983, 1967.

23. A.V. Kaibichev, B.M. Lepinskikh, E.E. Shretsov and B.I. Sergin, 'Kinetics of Dissolution of Cerium in Cast Iron', Russian Casting Production, No. 3, 108, 1968.

24. A.A. Vostryakov and B.M. Lepinskikh, 'Kinetics of Dissolution of Iron in Oxide Melts', Izv. Akad. Nauk SSSR Met., No. 4, 33, 1968; Russ. Met., No 4, 23, 1968.

25. B.M. Lepinskikh, A.V. Kaibichev, and V.A. Pankratov, 'Kinetics of Dissolution of Magnesium Alloys in Iron-Carbon Melts', Trudy Inst. Met. Sverdlorsk, No. 20, 160, 1969.

26. A. Simkovich, K. Li, and C.L. McCabe, 'Dissolution of Alumina in Carbon-Saturated Liquid Iron', Trans. AIME, 245, 897, 1969.

27. H. Nomura and K. Mori, 'The Rate of Dissolution of Iron into Liquid Fe-C Alloy', Tetsu-to-Hagane, 55, 1134, 1969.

28. G.N.K. Iyengar and R.D. Pehlke, 'Dissolution of Boron Nitride in Liquid Iron', Met. Trans. 1, 2235, 1970.

29. H. Ooi, Y. Oguchi, and H. Nakato, 'Rate of Desulfurization of Carbon-Saturated Iron Melts by a Rotating Cylinder of Calcium Carbide', Tetsu-to-Hagane, 56, 991, 1970.

30. J. Szekely, Y.K. Chuang, and J.W. Hlinka, 'The Melting and Dissolution of Low-Carbon Steels in Iron-Carbon Melts', Met. Trans., 3, 2825, 1972.

31. R.I.L. Guthrie and P. Stubbs, 'Kinetics of Scrap Melting in Baths of Molten Pig Iron', Canadian Metallurgical Quarterly, vol. 12, no. 4, 465-473, 1973.

32. Yeong-Ukim, R.D. Pehlke, 'Mass Transfer during Dissolution of a Solid into Liquid in the Iron-Carbon System', Met. Trans. AIME, Vol. 5, 2527-2532, 1974.

33. R.B. Gundlash and R.D. Pehlke, 'Rate of Molybdenum Solution in Carbon-Saturated Liquid Iron', Met. Trans. AIME, 3, 2337-2342, 1972.

34. A.A. Vostryakov, B.M. Lepinskikh and L.N. Shibanova, 'Kinetics of Dissolution of Iron in its Sulfide Melts', Deposited Dec. 1975; VINITI 2013-75, 15 pp.

35. R. Ohno, 'Rates of Dissolution of Rotating Iron Cylinders in Liquid Copper and Copper-Iron Alloys', (Res. Inst. Iron, Steel Other Met., Tohoku Univ., Sendai, Japan). Met. Trans., 4(4), 909-915, 1973 (Eng.).

36. V.D. Shantarin and P.M. Shurygin and V.V. Utochkin, 'Kinetics of the Dissolution of Niobium in Iron-Carbon Melts', Izvest. Akad. Nauk SSSR, Metally, 3, 31-33, 1966.

37. L.I. Krupman and V.I. Yavoiskii, 'Kinetics of Ferroalloy Dissolution in a Steel-Teeming Ladle', Izv. Vysshikh Uchebn. Zavedenii, Chern. Met., 7(9), 35-42, 1964.

38. V.D. Shantarin and P.M. Shurygin, 'Kinetics of Alloying Cast Iron and Steel with Pure Metals and Ferroalloys', Liteinoe Proizv (7), 19-21, 1964; Russian Castings Production, No. 7, 309-311, 1964.

39. K. Bungardt, K. Wiebking, H. Brandis and H. Schmalzried, 'The Dissolution of Molybdenum and Tungsten in Iron Melts as a Contribution to the Process of Dissolution of Solid in Liquid Materials. I.-Dissolution of Solid Metallic Bodies in Metal Melts Unaffected by Convection. II-Dissolution of Solid Metallic Bodies in Metal Melts Influenced by Convection', DEW. Techn. Ber., 9(3), Sept. 1969, 407-438; discussion 431-437 (in German).

40. I.P. Kazachkov and I.B. Parimonchik, 'Kinetics of Fusion of Ferro-Alloys', Steel in USSR, 123-124, February 1973.

41. P.G. Terziyan, 'The Kinetics of the Solution of Ferroalloys in Molten Steel', Stal', 2, 126-127, 1973.

42. G.S. Ershov and V.M. Bychev, 'Kinetics of the Dissolution of Titanium Nitride and Diffusion of Oxygen in Molten Iron', Izvest. Akad. Nauk SSSR, Metally, 1, 62-63, 1975 (in Russian).

43. I.P. Kazachkov and I.B. Parimonchik, 'Factors Determining the Rate of Dissolution of Alloys in Molten Steel', Metall. Koksokhim., 49, 56-60, 1976 (in Russian).

44. S.A. Argyropoulos, 'The Kinetics of Ferro-Alloy Solution in Liquid Steel', Master's Thesis, Department of Mining and Metallurgical Engineering, McGill University, Montreal, Canada, 1977.

45. R.I.L. Guthrie, 'Addition Kinetics in Steelmaking', Electric Furnace Proceedings, AIME, 1977.

46. S.A. Argyropoulos and R.I.L. Guthrie, 'The Exothermic Dissolution of 50 wt% Ferro-Silicon in Molten Steel', Canadian Metallurgical Quarterly, 18, 267-281, 1979.

47. S.A. Argyropoulos and R.I.L. Guthrie, 'The Influence of High Exothermic Heats of Dissolution to Molten Steel', 1979 Inter. Seminar Heat and Mass Transfer in Metallurgical Systems, Sept. 3-7, Dubrovnik, Yugoslavia, 1979.

48. L. Gourtsoyannis, H. Henein, and R.I.L. Guthrie, 'Some Kinetic and Hydrodynamic Aspects of Making Aluminum and Ferro-Alloy Additions to Steel Baths', Physical Chemistry of Production or Use of Alloy Additives, Proceedings of Sessions from the 103rd AIME Annual Meeting, Edited by John Farrel, 45-67, 1974.

49. F.A. Mucciardi, 'A Study of Light Alloy Addition Techniques in Steelmaking', Ph.D. Thesis, Dept. of Mining and Metallurgical Engineering, McGill University, Montreal, October, 1980.

50. G.S. Ershov, A.A. Kasatkin, I.V. Gavrilin, 'Diffusion of Various Alloying Elements in Liquid Fe in the Temperature Range 1550-1700°C', Izv. Akad. Nauk SSSR, Met., 2, 76-79, 1978; Diffusion and Defect Data, 195-196, 1978.

51. Y. Ono and T. Shigematsu, 'Diffusion Coefficients of Vanadium, Cobalt and Molybdenum in Molten Iron', Journal Japan Inst. Metallurgy, 41(1), 62-68, 1977.

52. J.F. Elliot, M. Gleiser, V. Ramakrishna, 'Thermochemistry for Steelmaking', Addison-Wesley Publishing Company Inc.

53. L.D. Lucas, in 'Physiochemical Measurements in Metals Research', (R.A. Rapp, ed), p. 219, Wiley (Interscience), New York, 1970.

54. K.W. Lange, 'Zur Temperaturleitfähigkeit des Eisens', Arch. Eisenhüttenw., 41, 559, 1970.

55. C.J. Smithels, 'Metals Reference Book', Fifth edition, Butterworths, 1976.

56. E.T. Turkdogan, 'Physical Chemistry of High Temperature Technology', Academic Press, 1980.

57. T. Iida and Z. Morita, 'Estimation of Some Physical Properties of Liquid Steel Near the Liquidus Temperature', Proceedings of the International Iron and Steel Congress, Chicago, April 1978.

58. D.Y. Povolotskii, V.E. Roshchin, and A.N. Keis, 'Diffusion of Deoxidants in Molten Iron', Steel in the USSR, 2(4), 289-291,

59. E. Ence and H. Margolin, 'Re-Examination of Ti-Fe and Ti-Fe-O Phase Relations', Trans. AIME, 206, 572-577, May 1956.

60. E.K. Molchanova, 'Phase Diagrams of Titanium Alloys', Daniel Davey and Co., Inc., New York, . Phase Diagram.

61. L. Kaufman and H. Nesor, 'Coupled Phase Diagrams and Thermochemical Data for Transition Metal Binary Systems', CALPHAD, 2, no. 1, 55-80, Pergamon Press, 1978.

62. O. Kubaschewski and W.A. Dench, 'The Heats of Formation in the Systems Titanium-Aluminium and Titanium-Iron', Acta Met., 3, 339, 1955.

63. S. Wagner and G. St. Pierre, 'Thermodynamics of the Liquid Binary Iron-Titanium by Mass Spectrometry', Metal. Trans., 5, 887, April 1974.

64. J. Chipman, 'The Deoxidation Equilibrium of Titanium in Liquid Steel', Transactions of the Metallurgical Society of AIME, 218, 767, August 1960.

65. R.J. Fruehan, Met. Trans., 1, 3403-3410, 1970.

66. I.I. Kornilov and V.S. Mikheev, Doklady Akad. Nauk SSSR, 104, No. 1, 88, September 1955.

67. D.A.R. Kay and A. Kontopoulos, 'Determination of Deoxidation Thermodynamics in the Fe-V-O System Using Solid Electrolytes', Proceedings of the International Symposium on Metallurgical Chemistry-Applications in Ferrous Metallurgy', held in the University of Sheffield, 19-21 July, 1971, pp. 178-183.

68. Dale U. von Rosenberg, '<u>Methods for the Numerical Solution of Partial Differential Equations</u>', American Elsevier Publishing Co., Inc., New York, 1969.

69. B. Carnahan, H.A. Luther, and J. Wilkes, '<u>Applied Numerical Methods</u>', John Wiley and Sons, Inc.

70. G.M. Dusinberre, '<u>Heat-Transfer Calculations by Finite Differences</u>', International Textbook Company, 1961.

71. H.S. Carslaw and J.C. Jaeger, '<u>Conduction of Heat in Solids</u>', Oxford University Press, 1959, Second Edition, page 199.

72. N.W. Mclachlan, '<u>Bessel Functions for Engineers</u>', Oxford at the Clarendon Press, Second edition, 1961.

73. H.S. Carslaw and J.C. Jaeger, '<u>Conduction of Heat in Solids</u>', Oxford University Press, 1959, Second edition, p. 204.

74. H.S. Carslaw and J.C. Jaeger, '<u>Conduction of Heat in Solids</u>', Oxford University Press, 1959, Second edition, p. 295.

75. S. Paterson, 'Propagation of a Boundary of Fusion', Proc. <u>Glasgow Math. Ass</u>., <u>1</u>, 42-47, 1952-1953.

76. G.G. Bach, 'Computing Methods I, II', Dept. of Mechanical Engineering, McGill University, September 1971.

77. E.M. Sparrow and J.L. Gregg, 'Laminar Free Convection Heat Transfer from the Outer Surface of a Vertical Circular Cylinder', <u>Transactions of ASME</u>, November 1956, pp. 1823-1829.

78. T. Cebeci, 'Laminar Free Convection Heat Transfer from the Outer Surface of a Vertical Slender Circular Cylinder', Proceedings of the Fifth International Heat Transfer Conference, Tokyo, Vol. 3, 15-19, September 1974.

79. F.A. Mucciardi, 'Heat Flow to Cylinders Submerged in Liquid Metal Baths', Master's Thesis, Dept. of Mining and Metallurgical Engineering, McGill University, Montreal, January 1977.

80. S.W. Churchill and R. Usagi, 'A General Expression for the Correlation of Rates of Transfer and Other Phenomena', AIChE Journal, 18, 1121-1128, November 1972.

81. J.P. Holman, 'Heat Transfer', Fourth edition, McGraw-Hill, 1976.

82. E.R.G. Eckert and T.W. Jackson, 'Analysis of Turbulent Free-Convection Boundary Layer on a Flat Plate', NACA TR 1015, 1951.

83. F.J. Bayley, 'An Analysis of Turbulent Free-Convection Heat Transfer', Proc. Instn. Mech. Engrs, 169(20), 361, 1955.

84. T. Fujii, 'Experimental Studies of Free Convection Heat Transfer', Bull. J.S.M.E., 2(8), 555, 1959.

85. O.A. Saunders, 'Effect of Pressure upon Natural Convection in Air', Proc. R. Soc. A127, 278, 1936.

86. M. Jakob and W. Linke, 'Heat Transfer in Boiling Water', Forsch. Ceb. Ing. Wes. 4, 75, 1933.

87. W.H. McAdams, '<u>Heat Transmission</u>', Third Edition, McGraw-Hill, New York, 1954.

88. C.Y. Warner and V.S. Arpaci, 'An Experimental Investigation of Turbulent Natural Convection in Air at Low Pressure Along a Vertical Heated Flat Plate', <u>Int. J. Heat Mass Transfer</u>, <u>11</u>, 397-406,

89. <u>Metals Handbook</u>, Volume 3, Ninth Edition, American Society for Metals, p. 375, 1980.

90. G.Y. Ho, R.W. Powell, P.E. Liley, 'Thermal Conductivity of the Elements: A Comprehensive Review', <u>Journal of Physical and Chemical Reference Data</u>, volume 3, 1974; Supplement No. 1, pp. 682-688, Published by the American Chemical Society and the American Institute of Physics.

91. R. Hultgren, P.D. Desai, D.T. Hawkins, M. Gleiser, K.K. Kelly, and D.D. Wagman, 'Selected Values of the Thermodynamic Properties of the Elements', <u>American Society for Metals</u>,

92. H.E. McCoy, 'Thermal Expansion of Iodide Titanium', <u>Trans. Amer. Soc. of Metals</u>, <u>57</u>, 743-746, 1964.

93. O. Kubaschewski, and W.A. Dench, 'The Heats of Formation in the Systems Titanium-Aluminum and Titanium-Iron', <u>Acta Metallurgica</u>, <u>3</u>, 339-346, July 1955.

94. C.W. Bale, A.D. Pelton, W.T. Thompson, 'Facility for the Analysis of Chemical Thermodynamics', <u>FACT User's Guide</u>, Edition 1, June 1979, McGill University, Ecole Polytechnique.

95. J. Szekely and Y.K. Chuang, 'On the Melting and Dissolution of a Solid in a Liquid with a Strong Exothermic Heat of Solution', Chemical Engineering Science, 27, 2300-2304, 1972.

96. E. Ravoo, J.W. Rotte and F.W. Levenstern, 'Theoretical and Electrochemical Investigation of Free Convection Mass Transfer at Vertical Cylinders', Chemical Engineering Science, 25, 1637-1652, 1970.

97. J. Szekely and N. Themelis, 'Rate Phenomena in Process Metallurgy', Wiley-Interscience, 1971.

98. V.G. Levich, 'Physicochemical Hydrodynamics', Prentice-Hall, p. 42, 1962.

99. An. N. Nesmeyanov and G. Trapp, Zh. Fiz. Khim. 39(2), 356-9, 1965 (in Russian).

100. Metals Handbook, Volume 1, Ninth Edition, American Society for Metals,

101. Instruction Manual: Microcomputer Analog Input System MP7218, Burr-Brown Research Corporation, P.O. Box 11400, Tucson, Arizona, U.S.A.

102. FLEX 09^{TM} Disk Operating System, Technical Systems Consultants Inc., P.O. Box 2574, West Lafayette, Indiana 47906, U.S.A

103. MP-T Interrupt Timer Instruction Manual, Southwest Technical Products Corporation, San Antonio, Texas, U.S.A.

104. S.A. Argyropoulos, R.I.L. Guthrie and K. Ananthanaraynan, 'Microprocessor Studies in Process Metallurgy', The Canadian Mining and Metallurgical Bulletin, August 1980.